Array Manifold Calibration for Multichannel SAR Sounders

By

Theresa Moore

Submitted to the graduate degree program in the Department of Electrical Engineering and Computer Science and the Graduate Faculty of the University of Kansas in partial fulfillment of the requirements for the degree of Doctor of Philosophy.

James Stiles, Chair

John Paden, Co-Chair

Committee members

Shannon Blunt

Carl Leuschen

Leigh Stearns

Date defended:

The Dissertation Committee for Theresa Moore certifies
that this is the approved version of the following dissertation:

Array Manifold Calibration for Multichannel SAR Sounders

James Stiles, Chair

Date approved: _____

Abstract

This dissertation demonstrates airborne synthetic aperture radar (SAR) sounder array manifold calibration to improve outcomes in two-dimensional and three-dimensional image formation of ice sheet and glacier subsurfaces. The methodology relies on the creation of snapshot databases that aid in both the identification of calibration pixels as well as the validation of proposed calibration strategies. A parametric estimator of nonlinear SAR sounder manifold parameters is derived given a superset of statistically independent and spatially diverse subsets, assuming knowledge of the manifold model. Both measurements-based and computational electromagnetic modeling (CEM) approaches are pursued in obtaining a parametric representation of the manifold that enables the application of this estimator. The former relies on a principal components based characterization of SAR sounder manifolds. By incorporating a subspace clustering technique to identify pixels with a single dominant source, the algorithm circumvents an assumption of single source observations that underlies the formulation of nonparametric methods and traditionally limits the applicability of these techniques to the SAR sounder problem. Three manifolds are estimated and tested against a nominal manifold model in angle estimation and tomography. Measured manifolds on average reduce angle estimation error by a factor of 4.8 and lower vertical elevation uncertainty of SAR sounder derived digital elevation models by a factor of 3.7. Application of the measured manifolds in angle estimation produces 3-D images with more focused scattering signatures and higher intensity pixels that improve automated surface extraction outcomes. Measured manifolds are studied against Method of Moments predictions of the array's response to plane wave excitation obtained with a detailed model of the sounder's array that includes the airborne platform and fairing housing. CEM manifolds reduce angle estimation uncertainty off nadir on average by a factor of 3 when applied to measurements, providing initial

confirmation of the utility of the CEM model in predicting angle estimation performance of the sounder's airborne arrays. The research findings of this dissertation indicate that SAR sounder manifold calibration will significantly increase the scientific value of legacy ice sheet and glacier sounding data sets and lead to optimized designs of future remote sensing instrumentation for surveying the cryosphere.

Acknowledgements

It is with overwhelming emotion and great humility that I compose the acknowledgments of this dissertation. I wish to first express my deepest gratitude to the gifted members of my committee who I hold in the highest esteem, who have guided me through this journey, and who have all served in developing me as a researcher and contributor in my field. I wish to thank my chair Dr. Stiles who opened my eyes to the power of statistical signal processing and whose deep knowledge across all aspects of our discipline continues to be awe-inspiring. I thank Dr. Blunt for building my strong foundation as a graduate student at the University of Kansas and whose adaptive signal processing course changed my life. I thank Dr. Leuschen for always making it look easy and inspiring me to approach my craft with pragmatism. I thank Dr. Stearns for anchoring me in the science and helping me to understand how my work serves the glaciology community. I wish to express my deepest appreciation for Dr. Paden who introduced me to the beauty of SAR and array signal processing, who mentored me over many years in ice sheet imaging, who gave me space to grow as an investigator, who pushed me to do great work, and who always showed up with kindness. This work is the product of the many years of his continual training and teaching for which I will be forever grateful. I wish to give special thanks to the School of Engineering and the Electrical Engineering and Computer Science Department at the University of Kansas for supporting my remote completion of the dissertation research. I am especially grateful to Joy Grisafe-Gross for being my touchstone at KU and for her deep sincerity and support as I navigated the challenges of finishing this work on the heels of my father's passing.

I owe an equal amount of gratitude to my talented leadership at The Johns Hopkins University Applied Physics Laboratory whose technical expertise raised the bar for the research documented here and all of whom offered encouragement and insight at different points over

the course of the dissertation. I am extremely grateful to Matthew Sharp for encouraging me to dissect problems with different lenses, ask questions, and bring curiosity to my problem space. I wish to thank Vince Karasack for helping me wade through the difficult times, for never turning down an antennas question and for offering feedback on the EM model. I am extremely grateful to Gerald Ricciardi who made me start defending the work from day one, who was always willing to delve into the gory math, who imparted pieces of his deep knowledge in antenna theory, and who taught me the art of making a technical argument. Many hours spent at his white board have inarguably enriched me as an engineer. Finally I wish to express my deepest gratitude for the grace and talent of Jenny Sue Hollenbeck who opened the door to computational electromagnetics last spring following my dad's death, providing a technical outlet to help channel my grief. The sixth chapter of this dissertation would not have been possible without her mentorship and teaching in CEM. I am in awe of her technical spirit; she is a true pioneer and an incredible human being who has empowered me tremendously and who continually inspires me to trust my instincts as an engineer.

None of this work would have been possible without the love, support, and commitment of my family. I wish to express my gratitude and honor for my father Robert who never lost his sense of wonder in the chaos of this mortal coil and who always sought to move through his life with goodness. I am grateful for my brilliant brother Matthew who taught me that failures anneal my character and who helped me summon my courage in many dark hours. I thank my sister Katie for her persistent loyalty and well-timed sense of humor that has broken many tense moments. I thank God for making me in the image of my mother Anna and breathing her strength, guts, and technical aptitude into me at inception. I thank my amazing daughters Shuri and Kyleigh for their patience over the last two years. Most importantly I wish to express my deepest gratitude and affection for my husband Kevin who has been my champion, my shield, and my rock throughout the journey. This dissertation is as much a song of his devotion as it is the embodiment of my research and it would have never come to fruition without his unwavering commitment to the completion of my work.

The purpose of life is to be defeated by greater and greater things.

Rainer Maria Rilke

Contents

List of Figures

List of Tables

List of Abbreviations

RDS	Radar Depth Sounder
SAR	Synthetic Aperture Radar
SLC	Single Look Complex
NSF	National Science Foundation
CRLB	Cramér-Rao Lower Bound
DOA	Direction of Arrival
MLE	Maximum Likelihood Estimator
MVDR	Minimum Variance Distortionless Response
MPDR	Minimum Power Distortionless Response
MUSIC	MUltiple Signal Classification
RMSE	Root mean squared error
FCS	Flight coordinate system
LUT	Lookup table
DEM	Digital elevation model
CEM	Computational electromagnetics
EM	Electromagnetic
SIR	Signal to interference ratio

Chapter 1

Introduction

Airborne, ice-penetrating synthetic aperture radar (SAR) sounders profile ice thickness and leverage cross-track phase center diversity to map basal morphology in three dimensions (3-D) with tomography; the remote sensing measurements collected by these sensors are important for understanding and predicting the response of the cryosphere to warming. In their sixth assessment report on climate change, the Intergovernmental Panel on Climate Change (IPCC) reports with high confidence that the Greenland and Antarctic Ice Sheets are losing mass [10]. The *likely* range of sea level rise projected for the year 2,100 ranges from 0.28-0.44 meters under a very low emissions scenario (SSP1-1.9). Under the very high greenhouse gas emissions scenario (SSP5-8.5), sea level rise projections range from 0.63 to 1.01 meters. Projected increases in global mean sea level for 2,150 under very high emissions scenarios are reported with medium to low confidence and changes exceeding 2 meters are not ruled out due to deep uncertainties in ice sheet processes [10]. SAR sounder derived ice thickness estimates and bed elevations contribute to large continental scale digital elevation models (DEMs) of the subsurfaces of Greenland and Antarctica, [11], [12], needed to constrain the estimated contributions of freshwater ice sheets in predictive sea level rise models [13]. The application of subglacial maps derived from multichannel SAR sounder data in local process studies of glacier dynamics [14], [15] further highlights the continuing scientific utility of these sensors in advancing climate science.

1.1 Problem Statement

Cross-track phase center diversity allows for the application of advanced array processing in SAR sounder image formation. Beamforming over a set of cross-track single look complex SAR images suppresses clutter in the dimension that is perpendicular to (and hence unaffected by) the SAR, enhancing profiling performance of areas with dominating collateral surface clutter and improving sounding performance from high altitude platforms. Multiple cross-track measurements also provide 3-D imaging capability of ice sheet and glacier beds with tomographic image formation. The ice sheet tomography technique, first demonstrated in [16], formulates the multichannel SAR observation model as a direction of arrival (DOA) problem and carries out angle estimation on the SAR pixels using the MUltiple SIgnal Classification algorithm (MUSIC) to resolve scattering interfaces in elevation angle.

Both MUSIC and the Maximum Likelihood Estimator (MLE) [17] are applied in ice sheet tomography. The resolution capability and accuracy of these techniques hinges on how closely the model of the array's response to directional sources approximates the true array response (referred to herein as the *array manifold*) which functionally depends on frequency, platform effects, mutual interaction between sensors, polarization, geometry, and channel-to-channel gain variations. The sensitivities of MUSIC and MLE to manifold modeling errors are well documented in literature [18], [19], [20], [21], [22], [23] and easily demonstrated in simulations. Manifold modeling errors have been suspected as the root cause of large vertical elevation errors observed off nadir and at the swath edges of SAR sounder derived digital elevation models (DEMs) though no evidence was documented in open literature confirming this link prior to the initiation of this dissertation research.

This dissertation formally addresses the manifold calibration problem for SAR ice sounders that rely on angle estimation in tomographic image formation. The methodology, algorithm development, and application are studied and demonstrated for a specific ice depth sounding SAR called the Radar Depth Sounder (RDS), developed and maintained by researchers at the University of Kansas's Center for Remote Sensing of Ice Sheets (CReSIS). The RDS

operates from many different platforms. The work presented here studies the system configured for its operation from NASA's P-3 aircraft; on this platform, the RDS operates with a 15 element cross-track antenna array organized into two wing-integrated subarrays (each comprised of four elements) and one inboard subarray of seven elements that attaches to the bottom of the aircraft. Although the manifold calibration algorithm development is expected to generalize to other versions of the system, some of the error mechanisms are likely specific to this platform. Measured and predicted manifolds presented in this dissertation should be regarded as specific to the P-3 configuration of the RDS while the problem interpretation and methodology are expected to generalize.

1.2 Prior Work

Array manifold calibration is the signal processing step aimed at refining the manifold model applied in array processing to improve beamforming and angle estimation outcomes. The associated literature on array manifold calibration, which spans the fields of array signal processing and antenna theory, shows a lack of consensus on the treatment of electromagnetic phenomenology such as mutual coupling in the manifold calibration problem. Signal processing literature hosts a proliferation of studies that simplify the model of the underlying phenomenology to justify demonstration of specific estimation techniques with contrived simulations. In contrast, the antennas literature tends to focus on well controlled characterizations of the array with pristine measurements captured in electromagnetically isolated environments.

A vast majority of the associated literature in manifold calibration tends to address techniques that are tailored to specific applications and arrays. This happens to be the nature of manifold calibration and our problem proves to be consistent with this trend in the sense that the traditional techniques must be adapted to accommodate RDS manifold calibration. The intention here is thus not to give an exhaustive regurgitation of pathological or obscure signal processing techniques that may or may not apply to our problem. Specific techniques

are cited as appropriate in the body of the dissertation as the mathematical underpinnings of the proposed methodology develop. Instead this dissertation adopts a perspective that distills the body of manifold calibration research evidenced in literature to a generalized parametric and nonparametric taxonomy shown in Figure 1.1. Note that this interpretation shows calibration pursuits leading to maximum likelihood and least squares solutions. Other suboptimal cost functions (like subspace-based objective forms) are possible, depending on the problem, but these are omitted for the sake of simplicity.

Nonparametric manifold calibration refers to the lookup table approaches that aim to measure the array's response to single sources and take one of two forms. The first is referred to as pilot calibration and applies when the calibration source waveform is known, leading to a maximum likelihood estimator of the manifold response vectors. These forms are inapplicable to the SAR sounder problem which interprets reflections from extended surface targets as calibration sources. When the waveform is unknown, the principal component of the array covariance matrix admits an estimate of the orientation of the steering vector in complex P dimensional space. This approach does not provide information about the length of the steering vector. Rather the principal component imparts a unit-norm vector whose entries represent complex offsets from a reference channel and hence cannot provide absolute gain patterns of the elements embedded in the array.

Nonparametric forms are problematic for SAR sounders which lack an adequate number of single source observations over a sufficiently dense angle grid to reconstruct the manifold. Traditionally single source measurements are collected during dedicated calibration flights by measuring specular reflections from non-penetrative extended surface interfaces with a maneuvering platform that rolls through the array's field of view. The coincident roll of the platform, measured from the inertial measurements unit (IMU), is interpreted as the scattering angle of the reflected wave. An example of this technique is documented in [24]. The method is subject to roll restrictions of the aircraft and requires cross-over flights to compensate for unknown terrain slope that can otherwise introduce bias in the lookup table.

It is emphasized that not all seasons have associated calibration flights that are suitable for manifold calibration and alternative techniques for extracting calibration measurements post SAR processing is an important step in calibrating legacy RDS data sets.

The parametric forms rely on an analytic description of the manifold to cast calibration in an estimation framework for determining unknown model parameters such as channel-to-channel gain variation, phase center position uncertainty, and coupling effects. Array shape calibration is easily handled in the parametric framework as the steering vector is immediately written in terms of an unknown geometric offset appended to the sensor position term. Early studies on array shape calibration emerge in literature to address compensating unknown propagation phases in towed array applications, see [25], [26], and [27] for example. Examples of maximum likelihood and eigenstructure solutions to the small scale perturbation problem (where geometric uncertainty is on the order of a tenth of a wavelength) are documented in [28] and [29] respectively. The array shape calibration problem provides a platform for advancing parameter estimation theory and underpins the canonical papers by Rockah and Schultheiss on the derivation of a hybrid Cramér-Rao lower bound for bounding estimator uncertainty when the model is parameterized by both random and deterministic unknowns [30], [31].

The parametric approaches are attractive because they handle calibration with multiple sources simultaneously but they do not offer straightforward expressions that are suitable for representing real arrays which are influenced by mutual coupling and complex platform effects. The associated theory of handling electromagnetic phenomenology in the parametric framework is comparatively less mature and reveals disconnects between signal processing approaches and the perspectives informed by antenna theory. A comprehensive survey of gaps in the representation of electromagnetic fields and effects within parametric calibration literature is found in [32] and [33]. The former study presents a coupled and loaded manifold model which is confirmed in [34]. The derivation is carried out in [35] and requires an assumption of perfectly conducting dipole radiators. The form, which parameterizes the

manifold in terms of the transimpedance parameters of the array and the multichannel microwave load, requires prior knowledge of the complex-valued, open-circuit patterns and may not offer utility beyond the cases of simple free space arrays that are not subject to higher order platform effects. Hence the coupled manifold becomes a function of another manifold which confounds development of signal processing solutions. Many studies obviate the need for modeling the open-circuit manifold by invoking an angle agnostic coupling assumption. This assumption is not expected to be valid in our application.

Parameterization of the SAR sounder manifold in terms of unknown error terms is not straightforward due to the complex kinematic and electromagnetic effects influencing the response of our arrays. We expect the SAR sounder manifold to be influenced by the effects of the irregular ground plane presented by the aircraft's body and, when applicable, the fairing structure housing an ice-sounding array. In our problem, calibration takes place at the output of the SAR processor suggesting that our observations are limited to the systematic errors which are constant over the aperture. It remains unclear how to model the manifold of wing-integrated subarrays that are subject to the array shape deformation from wing flexure and vibration effects documented in [36] and [37]. One significant study is worth mentioning that addresses parametric manifold calibration for wing-integrated arrays through exploitation of non-cooperative targets at unknown angles [38]. In this work, the authors derive a time-dependent model of a flexed and vibrating wing through a Taylor series expansion of the directional response of a vibrating sensor. This work offers a time-dependent model for representing the manifold but additional investigation is needed to understand application of this form in the context of the SAR processor. Understanding how to integrate the many error mechanisms into one model that is representative of SAR sounder manifolds remains an open area of investigation.

Computational tractability commonly challenges the numerical estimation of complex manifold parameters. A geometrically perturbed array of P sensors in two dimensions leads to as many $2P$ unknowns in estimation. When accounting for the mutual coupling between

sensors of a simple array, the P^2 transimpedance parameters of the array must be either estimated or carefully measured experimentally and requires knowledge of the open-circuit manifold in advance. Parameterization of a coupled manifold is likely to impart many unknowns needed to curve fit each individual antenna pattern. Simple examples carried out with a deterministic manifold of a free space array are described in the discussion section of Chapter 6 and indicate that $2P$ coefficients may be needed to curve fit the pattern of a single channel with P potential basis functions. A coupled manifold model with geometric error may lead to as many as $2P + 2P^2$ unknowns, assuming perfect knowledge of the open circuit manifold.

The complexity of the platform and its influence on the array's response limits our knowledge of embedded patterns of individual elements in SAR sounder airborne arrays. The patterns may be predicted with a full wave solver but modeling the platform and structures known to influence the array response is difficult. At present, the study in [24] appears to be the only example in literature that compares measurements to predicted far field gain patterns of the elements in an ice-sounding array. The predictions confirm rippling in the field of regard of the embedded elements but do not specify the phase response of the channels. This array does not operate with a fairing enclosure and leads to a comparatively simpler computational electromagnetic (CEM) modeling problem relative to the RDS P-3 array which is housed within a structure whose components are known to alter the resonance of the antennas [3].

While parametric methods are desirable in the RDS manifold calibration problem space, multiple obstacles must be overcome to apply these approaches. Above all, the array response to directional sources must be known in order to describe the manifold parametrically. When the array response is not known, it must be characterized by first carrying out nonparametric manifold calibration or predicted with a full wave solver. The nonparametric techniques are not immediately applicable in the absence of many single source observations over dense angle grids, spanning the field of view. Pattern prediction with full wave code requires

computational solutions which accurately represent the electromagnetic phenomenology introduced by the irregular ground plane and structural complexity of the fairing housing in the near field of the radiators.

1.3 Dissertation Organization and Scope

This dissertation seeks a more unified interpretation of the array manifold calibration that anchors signal processing methods with applications to both real data and electromagnetic manifolds predicted from a full wave solver. A nonparametric/parametric taxonomy is adopted in approaching the SAR sounder manifold calibration problem. The work reported here elucidates the challenges encountered in applying either form of manifold calibration to our problem and seeks to advance both. Chapter 2 offers the theoretical underpinning needed to contextualize array signal processing in the context of ice sheet imaging. The chapter offers a problem formulation of the multichannel SAR imagery and describes specific array processing techniques applied to these data sets. Parameter estimation theory is discussed that informs the calibration strategies developed in the dissertation. The array manifold is formally defined and a detailed discussion is offered that interprets manifold calibration in the context of SAR sounders.

Chapter 3 describes the data processing methodology that serves as a foundational step in measuring and validating RDS manifolds. The approach capitalizes on the application of the RDS as a SAR to produce large snapshot databases by coregistering RDS imagery to two auxiliary data sets. The databases aid in identification of calibration pixels in the SAR imagery with known arrival angles and helps to avoid subsurface scatterers in calibration. This chapter presents some initial validation of the methodology by comparing sidelobe clutter rejection before and after manifold calibration. The results demonstrate improved suppression of sidelobe sources with a measured manifold and serve to justify the refined manifold calibration work reported in this dissertation.

Chapter 4 presents the derivation of a parametric framework that handles multitarget

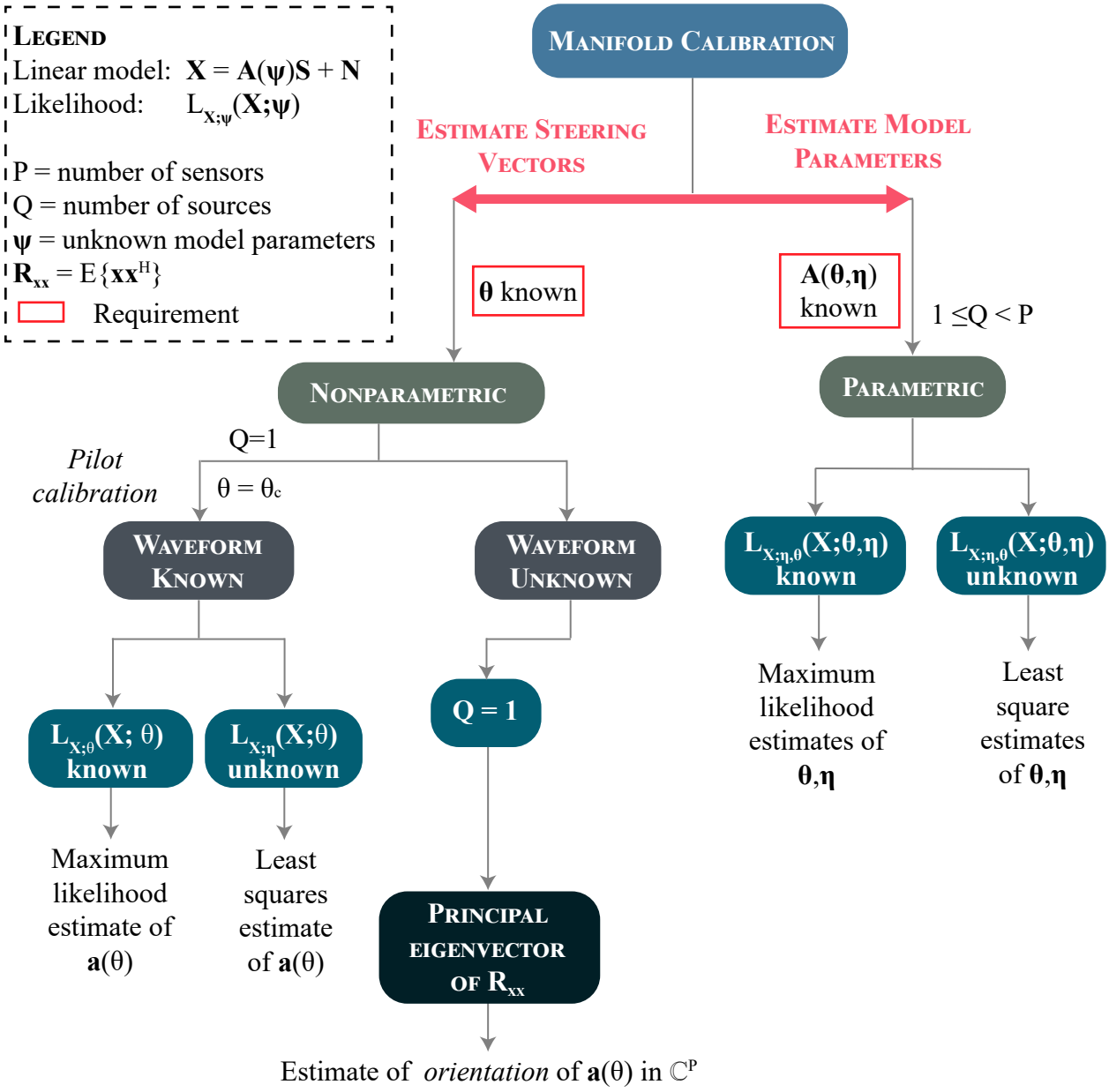

Figure 1.1: Parametric/nonparametric taxonomy of array manifold calibration problems as evidenced in literature.

calibration (shown to be desirable in the SAR sounder manifold calibration problem) and leverages the snapshot database in order to increase the total Fisher information of the observations, leading to more accurate estimates of manifold model parameters. The parametric framework hinges on the derivation of a maximum likelihood estimator of nonlinear manifold parameters from statistically independent observation sets and aggregates observations from many spatially diverse sources to estimate model parameters. The approach casts the estimation problem in a separable Gaussian form composed of many smaller separable Gaussian estimation problems. The resultant estimation framework only requires orientation of the manifold vectors in complex P dimensional space, justifying a unit-norm constraint assumed in the derivation of the principal components based manifold characterization offered in Chapter 5. Performance is verified numerically by exercising the estimator with a geometrically perturbed manifold.

Chapter 5 documents the adaptation of nonparametric methods to measure SAR sounder manifolds. The chapter describes the development of a principal components based nonparametric manifold characterization enabled by a subspace clustering technique that applies partial knowledge of the array response to identify multichannel SAR pixels dominated by single spatial sources. The approach side steps the challenge of acquiring single source snapshots over sufficiently dense elevation angle grids encountered in measuring SAR sounder manifolds. Three RDS P-3 manifolds are measured as offsets from a nominal manifold model. Angle estimation with measured manifolds is demonstrated with observations drawn from the snapshot database. Measured manifolds are shown to reduce angle estimation error on average by a factor of 4.8 in MUSIC.

Chapter 6 studies the potential utility of CEM modeling in the prediction of SAR sounder manifolds. A legacy CEM model of the RDS P-3 inboard subarray is refactored and adapted to investigate the manifold calibration problem. The CEM methodology is described for predicting receive RDS P-3 manifolds. In producing predicted patterns, several CEM solver settings are identified that have the potential to introduce modeling artifacts in computation.

Predictions of the RDS P-3 manifolds are produced with a full Method of Moments (MoM) solver for the full model of the inboard subarray, housed in the fairing and integrated onto the platform. The MoM predictions are compared to the measured manifolds documented in Chapter 5 in angle estimation. When compared against the nominal model, the EM manifold leads to improved angle estimator outcomes over certain angular windows off nadir and on average reduces angle estimation error by a factor of 3 in MUSIC.

Chapter 7 demonstrates the application of nonparametric manifold calibration in tomography. Both quantitative and qualitative evidence is summarized that substantiates the methodology described in Chapter 5 for measuring the RDS manifold. Performance is judged from vertical elevation errors of RDS-derived DEMs of rocky terrain and sea ice in the Canadian Arctic, produced under varying array response models applied in angle estimation. Tomography products generated over 16 frames consistently show error reductions with the application of a measured manifold in 3-D image formation. The dissertation research is summarized in Chapter 8. The major findings and technical outcomes are highlighted. Recommendations and future work are offered as next steps in the SAR sounder manifold calibration problem.

1.4 Summary of Original Research Contributions

The significant outcomes of the dissertation research are summarized upfront and include three major technical achievements, listed here.

1. *The development of a principal components based nonparametric manifold characterization algorithm for multichannel SAR ice sounders, enabled by the application of a subspace alignment measure to identify pixels dominated by one spatial source.* Important outcomes of this research include:

    - Measuring RDS manifolds from three independent data sets,

    - Designing a procedure to validate manifold performance in angle estimation and

tomography,

- Applying measured manifolds in angle estimation, demonstrating that the measured manifolds reduce angle estimation error by a factor of 4.8 on average,
- Applying measured manifolds in 3-D image formation, leading to **reductions in vertical elevation uncertainty of RDS-derived DEMs of surface topography by as much as a factor of 3.9 over the 3 dB swath width**.

2. *The generation of SAR sounder receive manifold predictions with a full Method of Moments solver and complete model of the inboard integrated subarray within its fairing enclosure, attached to the P-3 aircraft.* Original research contributions include:

   - Refactoring of a legacy CEM model to enable prediction of the RDS P-3 receive manifold,
   - Improving model fidelity by more accurately representing structural components in the near field of the radiators,
   - Applying the predicted manifold in angle estimation with real RDS snapshots, demonstrating an **average reduction of angle estimation error by a factor of 3** and providing initial confirmation of the utility of CEM modeling in predicting receive manifolds.

3. *The derivation of a parametric manifold calibration framework based on maximum likelihood estimation of nonlinear manifold parameters common across statistically independent observation subsets. The approach handles multiple targets simultaneously and leverages a snapshot database to form a superset of observations.* The significant technical milestones include:

   - Numerically validating performance by exercising the proposed estimator with controlled simulations of geometrically perturbed manifolds under an assumption of isotropic radiation,

- Providing analytical evidence of the influence of source spatial bandwidth and snapshot support on estimator accuracy of angle dependent nonlinear manifold parameters,
- Identifying challenges observed when applying the technique to a deterministic EM manifold for a simple linear array,
- Establishing methodology needed to validate the parametric framework with deterministic EM manifolds from a full wave solver.

1.4.1 Publication Record

The maturation of this research is captured in a publication record spanning the dissertation horizon. Aspects of the work were disseminated at two technical symposia in 2020 and 2021 which culminated in a larger manuscript submission to a peer reviewed journal in the fall of 2021. The publication record is summarized here:

1. **T. Moore** and J. Paden, "Array Manifold Calibration for Multichannel Radar Ice Sounders," *2020 IEEE International Geoscience and Remote Sensing Symposium (IGARSS 2020)*, pp. 92-95, doi: 10.1109/IGARSS39084.2020.9323719.

2. **T. Moore** and J. Paden, "Nonparametric Array Manifold Calibration for Ice Sheet SAR Tomography," *2021 IEEE International Geoscience and Remote Sensing Symposium (IGARSS 2021)*, pp. 2919-2922, doi: 10.1109/IGARSS47720.2021.9554640.

3. **T. Moore**, J. Paden, C. Leuschen, and F. Rodríguez-Morales, "Nonparametric Array Manifold Calibration for Ice Sheet Tomography," *IEEE Transactions on Geoscience and Remote Sensing*. [Accepted for publication]. Submitted: August 9, 2021. Revised: October 17, 2021. doi: 10.1109/TGRS.2021.3137145.

An additional manuscript submission is planned for the summer of 2022. This paper will address parameterization of the RDS manifold using predicted antenna patterns of the integrated subarrays evaluated with a computational electromagnetics software package.

1.5 Broader Impact

The most substantial impact of this dissertation is that it represents the first formal assessment of manifold calibration for ice penetrating SARs. The technical treatment of manifold calibration in this application reveals complex and challenging engineering problems which warrant well developed signal processing and CEM modeling solutions extending beyond the scope of this dissertation. The research summarized here stands to lead to more involved and robust solutions that can help to bridge gaps in the array manifold calibration literature and lead to important scientific outcomes. Chapter 7 provides both quantitative and qualitative evidence that confirms the manifold calibration methodology and algorithm development presented in this work, indicating that the proposed techniques lead to more accurate estimates of vertical elevation in tomographic DEMs. It is found that the use of the nominal array response model in tomographic image formation leads to biased angle estimates that propagate directly into the RDS-derived DEMs. The application of measured manifolds in angle estimation significantly reduces the mean elevation errors of RDS DEMs and leads to better layer tracking performance. It is shown that *manifold calibration increases the total width of the swath imaged in tomography* by enabling the layer tracker to track the surface for a longer duration in time (corresponding to a broader angular extent across the track) compared to the nominal manifold results. The observed outcomes point to further improvements in basal detection performance when the measured manifold is applied in geometric nulling or generalized sidelobe cancellation in profiling. The measured manifolds presented in this dissertation are immediately available for producing bed maps of the Canadian Arctic with tomography. These maps would support a large effort currently underway (the AtaaMap project) focused on constraining estimates of ice volume in the Canadian Arctic Archipelago to improve predictive sea level rise models.

Chapter 2

Background

2.1 Introduction

The role of researchers at the University of Kansas (KU) in developing ice-penetrating radar traces back to an airborne, Very High Frequency (VHF) system developed by engineers from the Radar Systems and Remote Sensing Laboratory (RSL) in the late 1980s [39], [40], [41]. This early system, called the Coherent Antarctic Radar Depth Sounder (CARDS), used unfocused synthetic aperture radar techniques to detect shallow layering and bottom echoes in Antarctic ice up to 1.2 km thick from a Twin Otter aircraft. This radar was the progenitor of the modern ice-penetrating SARs developed and deployed by CReSIS today. CReSIS's RDS now leverages advanced signal processing techniques to measure ice sheet interiors with very fine detail. This state of the art remote sensing technology results from an inheritance of four decades of hardware optimization and technological refinements to the original ACARDS system and its successors, made possible through significant NASA and National Science Foundation (NSF) investments [42], [43], [44], [45], [46], [8].

Changes made over the last two decades to the depth sounder's transmit and receive arrays have been instrumental in addressing specific engineering challenges in the ice sheet remote sensing problem. Element-level digitization of the cross-track sensors enables the application of tomographic imaging techniques for mapping the ice sheet subsurface in three dimensions. The ice sheet tomography technique, which was first demonstrated for ice bottom imaging on a ground-based system [47], [16] and demonstrated with an airborne system soon after [17], relies on parametric and subspace-based angle estimation techniques

to resolve scattering interfaces beyond the Rayleigh resolution limit in elevation angle θ. These estimators suffer performance degradation when the assumed model of a received array snapshot does not match reality.

The deleterious impacts of poorly constrained array modeling on angle estimation are well documented in literature [48], [23], [49], [20], [18], [19]. The mismatch introduces errors in our elevation angle measurement which is used to map the ice sheet subsurface. Furthermore, array gain uncertainties have been identified as the largest source of error in obtaining a radiometric measurement of the backscattering coefficient from SAR imagery [50]. This suggests that in the absence of an array calibration step in imaging, measuring the basal reflectivity (from which we may infer material properties of the bed) is unlikely. The importance of providing high quality measurements of ice bottom topography and reflectivity to the scientific community justifies the development of a robust manifold calibration method.

This chapter seeks to anchor array manifold calibration in the context of multichannel SAR sounders. The array processing problem formulation of multichannel SAR imagery is defined, relating the snapshot of traditional array signal processing nomenclature to the dominant scattering interfaces in the sounder's SAR pixels. Array signal processing techniques applied in ice sheet imaging are discussed, noting particular nuances inherited by the SAR sounder sensing geometry. A formal definition of the array manifold is presented as it relates to classical array theory. The chapter also provides a high level overview of signal processing strategies for array manifold calibration. This description avoids an application-specific dissection of the literature and adopts a more generalized taxonomy of manifold calibration techniques that naturally structures approaches into nonparametric and parametric forms. The array manifold calibration problem is interpreted through this lens, noting specific challenges in pursuing nonparametric and parametric calibration of SAR sounder manifolds.

2.2 Array Processing Formulation of Multichannel SAR Imagery

We formulate the multichannel SAR imaging problem by first adopting the geometry of Figure 2.1 which illustrates an airborne SAR system used to geocode focused scatterers over an illuminated swath. A local flight coordinate system translates the positions of SAR-focused scattering elements, natively described in a cylindrical geometry, to geodetic coordinates. The Cartesian SAR flight coordinate system (FCS) orients its x axis to point along a mean flight path of a synthesized aperture, z aligns with *up* in an East-North-Up geometry and y completes the right-handed coordinate system. This figure demonstrates pixel areas on a flat interface as they map into a SAR focused image.

The RDS resolves targets in three sequential processing steps. Pulse compression provides resolution in slant range or fast time. Uniformly sampled fast-time gates or slant range gates, when projected onto a flat surface, map to nonuniformly spaced ground range areas as illustrated in 2.1. Here a color gradient is meant to emphasize the fast-time dependence of an echoing patch's area and demonstrate the fast time coincidence of patches to the left and right sides of the track. The extent of a pixel in the cross-track depends on both incidence angle θ and slant-range resolution σ_R as shown. *Slow time* denotes time evolution along the track as the platform traverses the scene. The RDS in general does not squint its beam and the SAR processor focuses scattering interfaces into zero-Doppler planes of thickness σ_x using an f-k migration algorithm described in [51].

Figures 2.2(a) and (b) offer additional intuition to pixel scattering areas in the RDS SAR-focused imagery using a top-down view of fast-time and slow-time pixel scattering areas. Figure 2.2 demonstrates the propagation time gates post pulse compression resulting from a nadir-directed transmit beam as projected onto a flat surface. The RDS is designed to probe the subsurface of freshwater ice and each of its fast-time gates following that which contains the surface reflection corresponds to a range shell that intersects the air-to-ice interface and penetrates into the ice sheet. Prior to SAR image formation, the RDS range bins map to an echoing annulus on the ice surface and a spherical shell at ice depth.

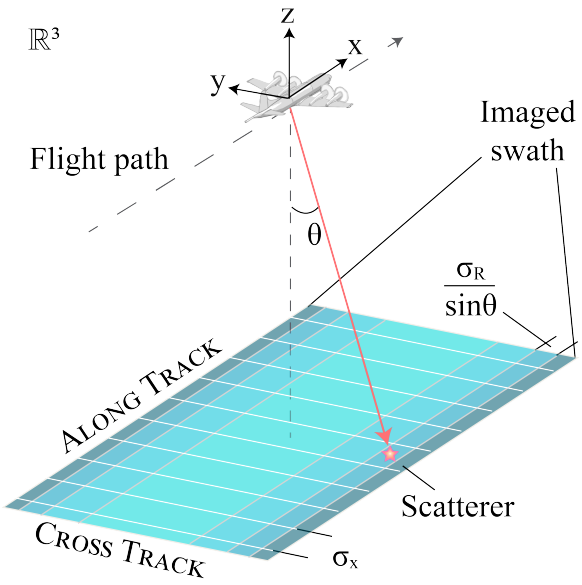

Figure 2.1: Pixel areas projected onto a flat surface after SAR image formation.

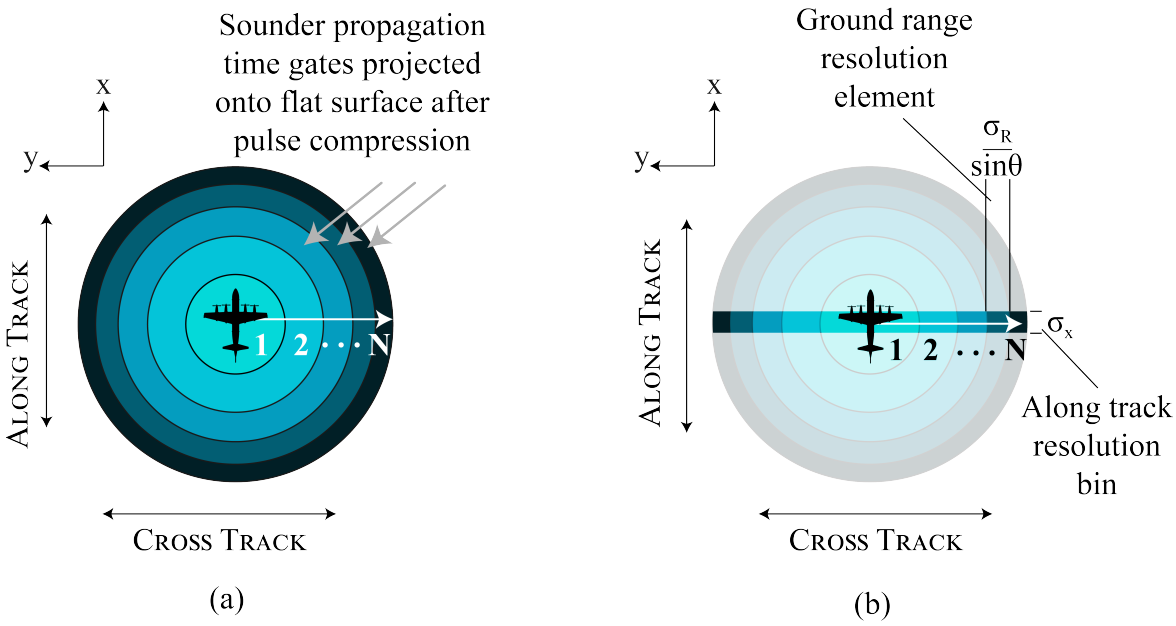

Figure 2.2: Supporting illustrations for formulating the SAR ice sounder problem: (a) a top down view of fast time gates after pulse compression when projected onto a flat interface and (b) a top down view of fast-time gates after pulse compression and SAR focusing to a zero-Doppler plane of thickness σ_x.

Figure 2.3 offers a cross-track and propagation-delay perspective of a zero-Doppler plane. This view demonstrates the common scattering contributions of a pixel containing the echo

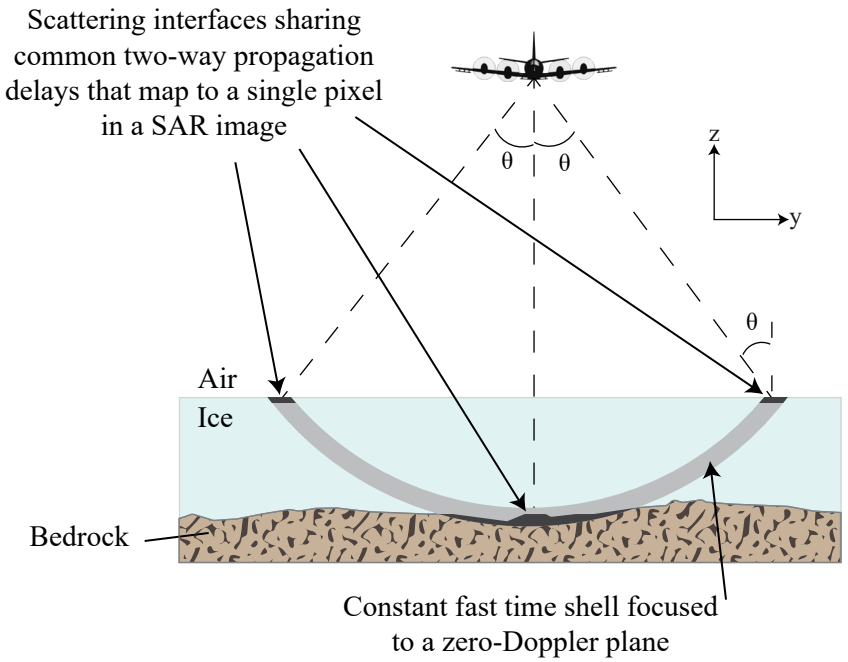

Figure 2.3: Scattering contributions to a pixel in the SAR focused imagery (cross-track plane perspective).

from the ice-to-bedrock interface and serves as the starting point for casting the multichannel SAR imagery as an array processing problem. We adopt the snapshot model from array signal processing literature [52] to describe pixel neighborhoods in a set of P cross-track diverse, SAR-focused images following the nomenclature in [53]. A set of pixels measured at a discrete time index m across P co-registered cross-track phase centers is modeled using the following system of linear equations:

$$\mathbf{x}_m = \mathbf{A}(\mathbf{\Theta})\mathbf{s}_m + \mathbf{n}_m, \tag{2.1}$$

Where

- $\mathbf{x}_m \in \mathbb{C}^{P\times 1}$ is the complex-valued vector containing samples of the received signal measured over P single look complex (SLC) SAR images,

- m is an index referring to a specific pixel in the SAR image,

- Q is the number of scattering interfaces contributing to pixel m,

- $\boldsymbol{\Theta} \in \mathbb{R}^{Q\times 1}$ is a vector containing the arrival angles of the Q scattering interfaces that are coincident in propagation time with the q^{th} entry denoted as $[\boldsymbol{\Theta}]_q = \theta_q$,

- $\mathbf{A}(\boldsymbol{\Theta}) \in \mathbb{C}^{P\times Q}$ performs a linear mapping of the signal subspace to our P dimensional observation space. We define this operator as the matrix of array manifold vectors (or steering vectors) which mathematically model the response of the P cross-track phase centers to the Q scattering interfaces. The notation $[\mathbf{A}(\boldsymbol{\Theta})]_{p,q} = a_p(\theta_q)$ denotes the (p, q) entry of $\mathbf{A}(\boldsymbol{\Theta})$ and refers to the response of phase center p to source q,

- $\mathbf{s}_m \in \mathbb{C}^{Q\times 1}$ is proportional to the complex reflectivities of the Q scattering interfaces scaled by propagation losses and transmit gain in each direction,

- $\mathbf{n}_m \in \mathbb{C}^{P\times 1}$ is a random vector containing samples of a zero-mean, multichannel noise process with covariance $\mathbf{R}_\mathbf{n}$ for SAR pixel m.

Expansion of the singleton dimensions of $\mathbf{x}_m, \mathbf{s}_m$, and $\mathbf{n}_m$ provides a model for a neighborhood M pixels over which the vector $\boldsymbol{\Theta}$ is assumed stationary. The set of M measurements is given by the following form

$$\mathbf{X} = \mathbf{A}(\boldsymbol{\Theta})\mathbf{S} + \mathbf{N}. \tag{2.2}$$

Note that the interpretation of operator $\mathbf{A}(\boldsymbol{\Theta})$ in (2.2) does not change relative to the single snapshot form. The matrices $\mathbf{X} \in \mathbb{C}^{P\times M}$, $\mathbf{N} \in \mathbb{C}^{P\times M}$, and $\mathbf{S} \in \mathbb{C}^{Q\times M}$ contain M stationary observations of the corresponding vector quantities as defined in (2.1).

2.2.1 Stated Assumptions

The following minimum assumptions underlie the manifold calibration work presented throughout the dissertation unless otherwise stated:

A1: The linear model $\mathbf{A}(\boldsymbol{\Theta})\mathbf{s}_m$ is taken to be overdetermined so that the number of spatial sources, Q, is always less than the number of cross-track phase centers P. This ensures

an injective mapping between the signal subspace and its image in our observation space.

A2: The columns of $\mathbf{A}(\boldsymbol{\Theta})$ form a linearly independent set from which we can assert that $\mathbf{A}(\boldsymbol{\Theta})$ has full column rank and hence always admits a left pseudoinverse based on the invertibility of the full-rank $Q \times Q$ matrix $\mathbf{A}^H(\boldsymbol{\Theta})\mathbf{A}(\boldsymbol{\Theta})$.

A3: $\mathbf{N}$ represents a multichannel noise process containing zero-mean random vectors whose complex-valued random entries are independent and uncorrelated both spatially and temporally.

A4: All sources originate from the far field such that the plane wave approximation holds in describing incident signals at the array.

A5: The complex envelope of any signal incident on the array varies slowly with respect to the carrier such that the narrowband criterion holds [52] which enables propagation delays to be modeled as phase shifts evaluated at the carrier f_c.

A6: The array is composed of uniformly polarized elements such that the array response vector is sufficiently modeled by its response in a single polarization state.

Assumptions **A5** and **A6** do not restrict the generality of manifold calibration approaches described in this work but a point is emphasized here to the reader: while the manifold vector $\mathbf{a}(\theta)$ is described at a single frequency and polarization it should be understood that the manifold in general varies with both. The exercise of manifold calibration is one of improving model fidelity and hence the most accurate model of the manifold is one that extends to account for the range of frequencies and polarization states sensed by the array in operation.

2.3 Array Signal Processing in Ice Sheet Imaging

2.3.1 2-D Image Formation

Given a set of P SAR images obtained from multiple cross-track measurements, we use array processing techniques to form both two-dimensional and three-dimensional imagery of the subsurface. Prior to array processing, we will assume that we have performed a channel equalization step to obtain a set of coefficients which, when applied, ensure that the cross-track measurements are corrected in delay up to the feed point of the antenna and relative gain and phase variations are removed at nadir.

We use digital beamforming to generate two-dimensional echograms of a vertical ice profile below the aircraft that are used to estimate overall ice thickness and image internal layering within the ice sheet. During this combining, images are multilooked to reduce speckle. An example of a 2-D echogram is shown in Figure 2.4. This image is a representative result of combining SAR imagery over a set of cross-track measurements. The overall intent of digital beamforming is to improve detection performance and enable estimation of the basal reflectivity σ^0_{basal}.

We use both adaptive and nonadaptive techniques to estimate the signal portion of a pixel as the following average over coherently summed snapshots in a pixel neighborhood

$$\hat{s}(n_t, n_x) = \frac{1}{M} \sum_{m=1}^{M} \mathbf{w}^H \mathbf{x}_m, \tag{2.3}$$

Where the vector $\mathbf{x}_m$ denotes the m^{th} column vector of our pixel neighborhood defined in 2.2. The weight vector $\mathbf{w} \in \mathbb{C}^{P \times 1}$ represents a general beamformer. The specific weights are chosen to satisfy some optimality criterion at the output of the beamformer. Here we describe the two common nonadaptive and adaptive beamformers used in our array processor. We also present a geometric nulling beamformer that aids in identifying mismatch in the depth sounder's array manifold and motivates a refined array calibration methodology in our array

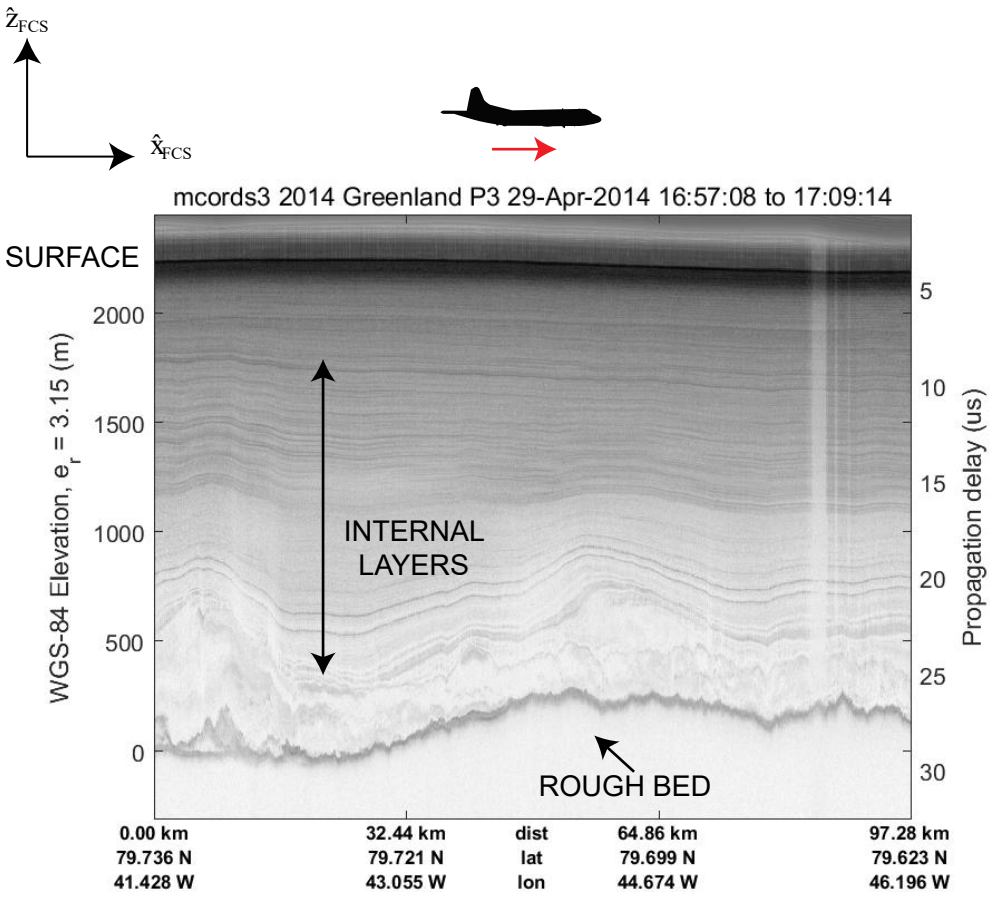

Figure 2.4: Radar Depth Sounder 2-D profiling product (standard method)

processor [54].

2.3.1.1 Standard Combining Method: The Spatial Matched Filter

The standard combining method for forming a two-dimensional vertical profile of the subsurface is the spatial matched filter. The spatial matched filter, sometimes referred to in literature as the the Maximum SNR beamformer [55], [56], is an optimal set of weights which maximize SNR of the estimated source waveform when observed in the presence of spatially uncorrelated noise. The derivation of the weights is carried out in Appendix A and the solution is restated here for a source DOA, θ_t,

$$\mathbf{w}_{MF} = \frac{\mathbf{a}(\theta_t)}{\|\mathbf{a}(\theta_t)\|}. \tag{2.4}$$

From this result we note that the spatial matched filter corresponds to the normalized steering vector for the desired source and does not depend on the data itself.

The matched filter is problematic for the sounder problem if we want to invert the data to obtain an estimate of the backscattering coefficient σ^0 because co-range clutter biases our estimate of power from the ice bottom. We can establish this fact with an informal proof by contradiction. Suppose $\mathbf{x}$ is a snapshot across the multichannel images containing the ice-bottom echo. Assume a typical sounding setup such that $Q = 3$ sources impinge on the array (one from nadir and two from the ice surface). Let θ_t correspond to the nadir DOA (which may be nonzero in an aircraft roll) and let θ_l, θ_r correspond to the bearing angles of the backscatter from the left and right sides of the track at the air-to-ice interface. Assume, for the sake of illustration, that we have perflectly removed the system effects of each channel up to the point of beamforming and let φ represent the complex reflectivity variable (which when squared corresponds to the backscatter from a patch). Let $\mathbf{a}_t, \mathbf{a}_l, \mathbf{a}_r$ represent the steering vectors for the three DOAs $(\theta_t, \theta_l, \theta_r)$ so that we can suppress the angle

argument. The signal model for this setup (assuming observation in zero-mean noise) is

$$\mathbf{x} = \varphi_t \mathbf{a}_t + \varphi_l \mathbf{a}_l + \varphi_r \mathbf{a}_r + \mathbf{n}. \tag{2.5}$$

The estimate of our desired waveform is the matched filter output given by

$$\begin{aligned} \hat{\varphi}_t &= \mathbf{w}_{MF}^H \left(\varphi_t \mathbf{a}_t + \varphi_l \mathbf{a}_l + \varphi_r \mathbf{a}_r + \mathbf{n} \right), \\ &= \frac{\mathbf{a}_t^H}{\sqrt{\mathbf{a}_t^H \mathbf{a}_t}} \left(\varphi_t \mathbf{a}_t + \varphi_l \mathbf{a}_l + \varphi_r \mathbf{a}_r + \mathbf{n} \right), \\ &= \varphi_t \frac{\mathbf{a}_t^H}{\sqrt{\mathbf{a}_t^H \mathbf{a}_t}} \mathbf{a}_t + \varphi_l \frac{\mathbf{a}_t^H}{\sqrt{\mathbf{a}_t^H \mathbf{a}_t}} \mathbf{a}_l + \varphi_r \frac{\mathbf{a}_t^H}{\sqrt{\mathbf{a}_t^H \mathbf{a}_t}} \mathbf{a}_r + \frac{\mathbf{a}_t^H}{\sqrt{\mathbf{a}_t^H \mathbf{a}_t}} \mathbf{n}. \end{aligned} \tag{2.6}$$

We assume the steering vectors to be normalized such that $0 \leq \mathbf{a}_i^H \mathbf{a}_j \leq 1$ where the inner product evaluates to one when $i = j$ and an inner product of zero corresponds to orthogonality. We do this to suppress the normalization factor in the denominator with no loss of generality. Suppose $\hat{\varphi}_t = \mathbf{w}_{MF}^H \mathbf{x}$ is an unbiased estimator of the reflectivity of the basal patch. Then by definition the estimator bias is

$$\varepsilon_{\varphi_t} = E\left\{ \hat{\varphi}_t \right\} - \varphi_t = 0. \tag{2.7}$$

The expected value of the estimator is

$$\begin{aligned} E\left\{ \hat{\varphi}_t \right\} &= E\left\{ \varphi_t \mathbf{a}_t^H \mathbf{a}_t + \varphi_l \mathbf{a}_t^H \mathbf{a}_l + \varphi_r \mathbf{a}_t^H \mathbf{a}_r + \mathbf{a}_t^H \mathbf{n} \right\}, \\ &= E\left\{ \varphi_t \right\} \mathbf{a}_t^H \mathbf{a}_t + E\left\{ \varphi_l \right\} \mathbf{a}_t^H \mathbf{a}_l + E\left\{ \varphi_r \right\} \mathbf{a}_t^H \mathbf{a}_r + \mathbf{a}_t^H E\left\{ \mathbf{n} \right\}, \\ &= E\left\{ \varphi_t \right\} \mathbf{a}_t^H \mathbf{a}_t + E\left\{ \varphi_l \right\} \mathbf{a}_t^H \mathbf{a}_l + E\left\{ \varphi_r \right\} \mathbf{a}_t^H \mathbf{a}_r. \end{aligned} \tag{2.8}$$

Lacking a priori knowledge of the parameters of the scattering distributions, we treat the reflectivities as deterministic but unknown waveforms. Then the expectation in Equation 2.8 becomes

$$E\left\{ \hat{\varphi}_t \right\} = \varphi_t + \varphi_l \mathbf{a}_t^H \mathbf{a}_l + \varphi_r \mathbf{a}_t^H \mathbf{a}_r. \tag{2.9}$$

The inner product of two non-identical steering vectors $\mathbf{a}_i^H \mathbf{a}_j$ is a measure of spatial correlation between the directional sources and although we can assume it to be small when then surface DOAs are large, it is not perfectly zero. From this we state the following

$$E\left\{\hat{\varphi}_t\right\} = \varphi_t + \varphi_l \mathbf{a}_t^H \mathbf{a}_l + \varphi_r \mathbf{a}_t^H \mathbf{a}_r \not\Rightarrow \varphi_t, \tag{2.10}$$

which contradicts the criterion of the estimator being unbiased in Equation 2.7 and we conclude that as posed the converse must be true. Given the pervasive contamination of our measurement with co-range returns from the ice surface, it is desirable to find an unbiased estimator that at least tends towards the desired term asymptotically.

2.3.1.2 Adaptive Combining: Minimum Variance and Distortionless

In contrast to the fixed beamformer described above, adaptive techniques offer an advantage of flexibility in that they change in response to the data and adapt to suppress interference. We use an adaptive beamformer belonging to a family of filters derived under stochastic criteria to obtain a distortionless estimate of the waveform in the direction of interest with minimum variance. Following the convention presented by Van Trees in [55], we categorize the specific implementation of our adaptive beamformer as a *Minimum Power Distortionless Response* (MPDR) filter in contrast to the Minimum Variance Distortionless Response (MVDR) beamformer first derived by Capon [57]. The distinction lies in how we train to obtain the weights. The MPDR beamformer is the solution to following optimization problem

$$\begin{aligned} &\text{minimize:} && \mathbf{w}^H \mathbf{R}_{\mathbf{x}} \mathbf{w} \\ &\text{subject to:} && \mathbf{w}^H \mathbf{a}(\theta_t) = 1. \end{aligned} \tag{2.11}$$

The resultant weights are derived in Appendix A and stated here:

$$\mathbf{w}_{MPDR} = \frac{\mathbf{a}^H(\theta_t)\mathbf{R}_\mathbf{x}^{-1}}{\mathbf{a}^H(\theta_t)\mathbf{R}_\mathbf{x}^{-1}\mathbf{a}(\theta_t)}, \tag{2.12}$$

Where the matrix $\mathbf{R}_\mathbf{x}^{-1}$ denotes a matrix inverse of the observation covariance matrix given by

$$\mathbf{R}_\mathbf{x} = E\left\{\mathbf{x}\mathbf{x}^H\right\}, \tag{2.13}$$

Which in general we estimate over a neighborhood of M pixels as

$$\hat{\mathbf{R}}_\mathbf{x} = \frac{1}{M}\mathbf{X}\mathbf{X}^H. \tag{2.14}$$

The distinction between the MVDR and MPDR filters lies in the covariance matrix used to evaluate the weight vectors. In contrast to Equation 2.12, which we evaluate in terms of the observation covariance matrix $\mathbf{R}_\mathbf{x}$, the MVDR weights rely on knowledge of the interference plus noise covariance, $\mathbf{R}_\mathbf{n}$. Hence MVDR assumes a training period in which the desired signal is absent or when the signal is buried in the interference and noise. This type of signal environment is more indicative of a barrage jamming type of problem where a directional interferer broadcasts stationary broadband noise to cover a signal. In most cases, our problem does not really fit this description. The exception may be the case of sounding at the outlet glaciers where the heavily crevassed surface presents significant clutter and masks the basal echo. Though we explicitly use our observation covariance matrix in computing the weights, the specific beamformer regime is more of an academic construct that enables us to predict performance in different scenarios and which regime we fall into ultimately depends on the signal to interference plus noise (SINR) of the element-level IQ measurements.

The MPDR filter has been used to demonstrate high altitude operation of the depth sounder from a NASA DC-8 aircraft [58] and while it has shown promise for handling the sidelobe clutter problem in ice sheet sounding, it also demonstrates aberrant behavior that

compromises its performance in certain cases. Specifically we have observed self-nulling phenomenology in imagery combined with the MPDR beamformer. Self-nulling refers to the cases when an adaptive beamformer interprets the signal of interest as interference and suppresses it in the combined output of the beamformer. The self-nulling effects increase with increasing source SNR [55]. The problem is a complex one that is actively under investigation for ice sheet sounding (see [59] and references therein). Although a full description of the problem is beyond the scope of this dissertation, some of the pertinent aspects of self-nulling are addressed here as a prelude to the array manifold calibration research outlined for the RDS.

The self-nulling behavior is symptomatic of a mismatch between the terms in Equation 2.12 and may be attributed to two causes [55]:

1. **Steering vector mismatch**: Steering vector mismatch occurs when our model of $\mathbf{a}(\theta_t)$ does not match reality. This can result from pointing error in frequency-wavenumber space (where our assumption of either θ_t or the wavenumber k does not match truth). Mismatch also occurs when the modeled steering vector deviates from truth due to errors in sensor phase, gain, or locations (manifold calibration errors).

2. **Covariance matrix mismatch**: Covariance matrix mismatch refers to the case when our estimate of the data covariance matrix (in the MPDR case) $\hat{\mathbf{R}}_{\mathbf{x}}$ is a poor estimate of the true quantity $\mathbf{R}_{\mathbf{x}}$. Poor estimates may be due to non stationarity of the signal and interference environment or snapshot starvation.

Several sources of potential mismatch characterize the ice sheet remote sensing problem. Poor estimates of the covariance matrix likely play a significant role in the self-nulling observed in depth sounder combined images just by virtue of our sensing geometry. Non-stationarity in fast time of scattering near nadir limits the number of adjacent pixels that can be used for estimating the covariance matrix. The range gates containing basal echoes correspond to a large footprint at the bottom of the ice sheet and the echoing area may be

several hundreds of meters across in 2 km thick ice for example. This large footprint contains many scatterers which appear correlated to the radar. At depth the angular extent of the footprint may be on the order of the half-power beamwidth (HPBW) of the array. Adjacent pixels in fast time may perceive scatterers with significantly different DOAs. The scattering changes rapidly in fast time near vertical incidence and this limits the number of adjacent range gates that we may use for averaging a covariance matrix.

We also know that uncertainties associated with our desired source DOA assumption, θ_t, are inevitable due to natural variation of subglacial topography. We define the DOA of our target as the angle between nadir (aligned with the z axis of the SAR flight coordinate system) and the z axis of the aircraft's body coordinate system. The body coordinate system is the right-handed geometry fixed to the platform through arbitrary Euler rotations while the SAR coordinate system is treated as the non-rotated, inertial frame. The angle θ_t which we use to beamform in the direction of interest is taken to be the roll angle between the level flight coordinate system and the rotated frame of the aircraft body coordinate system in the zero-Doppler plane.

In the ideal geometry shown in Figure 2.5, the propagation vector of the basal scattering aligns with nadir so that the DOA, θ_t is exactly equal to the platform roll angle ψ. This assumes vertical incidence at depth which implies a flat bed with zero cross-track slope. Because vertical incidence at the ice-bottom is an assumption, cross-track slopes present an error to our angle hypothesis. An illustration of the error introduced due to sloped basal topography across the track is shown in Figure 2.6. The angle of the propagation vector is ε_θ. The true direction of the signal of interest is $\theta_t = \psi + \varepsilon_\theta$ while our hypothesis of the target DOA, $\hat{\theta}_t$, is ψ. Geometric perturbations of the array positions present mismatch in a similar way to the DOA uncertainty problem.

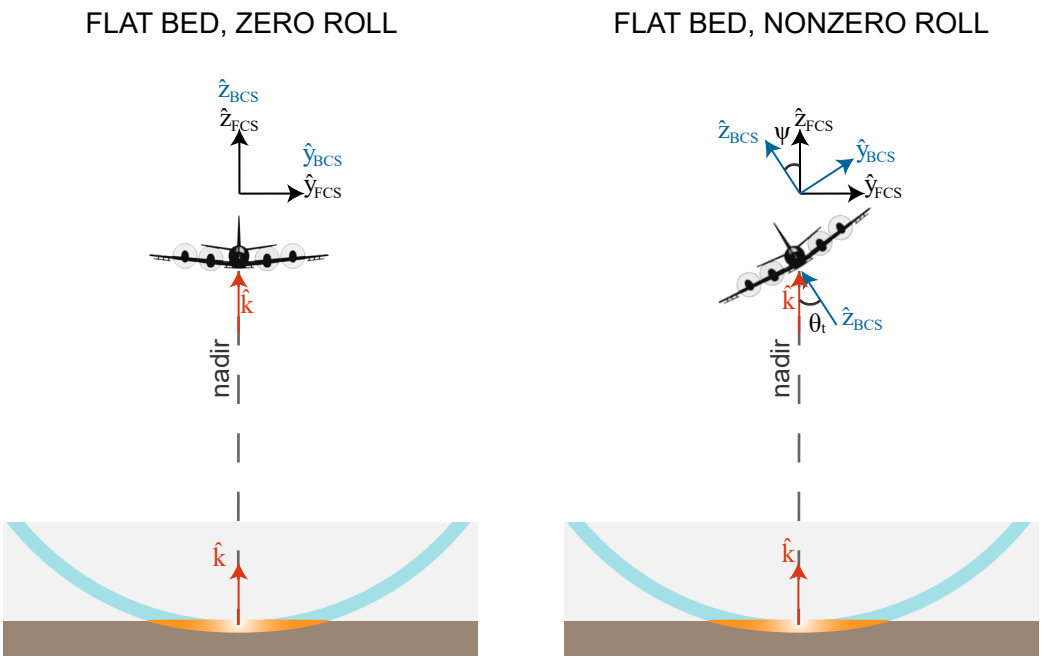

Figure 2.5: Basal echo DOA in zero roll condition (left) and nonzero roll condition (right).

2.3.1.3 Geometric Null Placement

Finally we address the geometric null placement approach for estimating the signal from the direction of interest. In the formulation of the geometric nulling beamformer, we assume prior knowledge of all of the source DOAs, $\mathbf{\Theta} = \left[\theta_t, \theta_1^i, \ldots, \theta_{Q-1}^i\right]$, where θ_q^i is used to denote the q^{th} interferer. The matrix of steering vectors is given by

$$\mathbf{A}(\mathbf{\Theta}) = \left[\mathbf{a}(\theta_t), \mathbf{a}(\theta_1^i), \ldots, \mathbf{a}(\theta_{Q-1}^i)\right]. \tag{2.15}$$

Provided that $\mathbf{A}(\Theta)$ has full column rank and presents an over-determined system, then it admits a left-inverse such that the least-squares estimate of the vector of spatial sources $\mathbf{s}$ is

$$\hat{\mathbf{s}}(\mathbf{x}) = \left(\mathbf{A}^H(\mathbf{\Theta})\mathbf{A}(\mathbf{\Theta})\right)^{-1}\mathbf{A}^H(\mathbf{\Theta})\mathbf{x}. \tag{2.16}$$

The entries in $\hat{\mathbf{s}}$ are given by

$$\hat{\mathbf{s}} = \left[\hat{s}_t, \hat{s}_1^i, \ldots, \hat{s}_{Q-1}^i\right]^T. \tag{2.17}$$

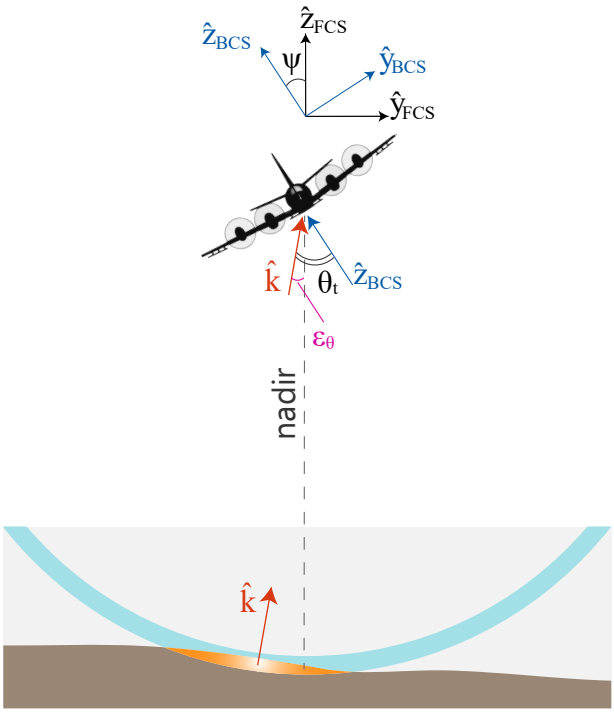

Figure 2.6: Basal echo DOA in nonzero roll condition with cross-track slope.

The least-squares estimate of the target is obtained by using a constraint vector $\mathbf{g}$ whose only nonzero element is the first entry following a convention that the first column of $\mathbf{A}(\boldsymbol{\Theta})$ always corresponds to the target steering vector. The geometric nulling weights are then given by

$$\mathbf{w}_{GEO} = \mathbf{A}(\boldsymbol{\Theta})\left(\mathbf{A}^H(\boldsymbol{\Theta})\mathbf{A}(\boldsymbol{\Theta})\right)^{-1}\mathbf{g}. \tag{2.18}$$

When certain conditions are met, the pseudoinverse solution corresponds to a maximum likelihood estimator of $\mathbf{s}$ which is unbiased assuming the linear model of the array data in Equation 2.1 and Appendix B.2.3. The fact that the output of the beamformer in Equation 2.18 leads to an unbiased estimate of the basal echoes makes it better suited for estimating radiometric quantities from our extended targets. The form above produces nulls in the directions of interferers based on the constraint vector. Null pointing exhibits sensitivity to

manifold mismatch which manifests as a degradation of interference suppression due to the null not pointing exactly where intended in frequency-wavenumber space.

2.3.2 3-D Image Formation

Three-dimensional image formation requires resolution of the unknown elevation angle of the Q scattering interfaces in the (ρ, θ) plane. The Rayleigh resolution of the array in the cross-track dimension, which is extremely coarse compared to the slant-range and along-track dimensions, is given by

$$\sigma_y = \kappa_y \frac{\lambda}{L_y}, \tag{2.19}$$

Where L_y is the of the cross-track aperture and κ_y is a tapering factor. Array processing techniques which compare the phase across multiple cross-track measurements provide estimates of θ that exceed the Rayleigh resolution limit of the physical array under certain conditions. These techniques provide estimates of the elevation angle for basal scattering pixels which can then be converted back into cartesian coordinates.

The exploitation of cross-track measurement diversity to obtain a measurement of θ is well-established in Interferometric SAR (InSAR) literature (see [60] for a more recent survey of the techniques and additional references, see [61] for some of the early InSAR results). The InSAR technique is a special case of array processing that provides the DOA estimate of a single source using $P = 2$ cross-track measurements, obtained by receivers that are spatially offset by a large baseline. The spatially diverse images may be obtained over multiple passes (typical in satellite imaging geometries) or in a single pass (more common with airborne SARs with two receivers).

Tomographic SAR emerges more recently in the record of literature with a realization that cross-track measurements relate to a projection of a surface's two-dimensional reflectivity at a particular DOA [62]. This relationship pointed to the possibility of 3-D image reconstruction based on an important principle in imaging science referred to as the Fourier Slice Theorem.

A majority of the examples of Tomographic SAR use multipass measurements in sidelooking geometries to three-dimensionally reconstruct extended targets [63], [60], [64].

The first examples of SAR Tomography applied to ice-bottom mapping are carried out on a ground based system and rely on the MUltiple SIgnal Classification (MUSIC) algorithm to separate sources in elevation angle θ [16]. The ice sheet tomography technique is demonstrated with an airborne sounder using maximum likelihood estimation of the DOA in [17]. Both cases demonstrate a single pass approach where a cross-track phased array provides the spatially diverse SAR image set for estimating arrival angle. Here we briefly describe the two most commonly used angle estimators for ice sheet tomography before the formal treatment of the array calibration problem.

2.3.2.1 MUltiple SIgnal Classification

The MUSIC algorithm belongs to a class of subspace techniques that exploit a vector space model of the array observations to assert an angle estimator. The early work is generally attributed to [65] but a more comprehensive list of the contributions to the literature of subspace methods can be found in [66] and [67]. The MUSIC estimates of the DOA are obtained by finding the values of θ corresponding to the Q peaks of the following one-dimensional MUSIC pseudospectrum written as

$$S_{music}(\theta) = \frac{1}{\mathbf{a}^H(\theta)\hat{\mathbf{U}}_n\hat{\mathbf{U}}_n\mathbf{a}(\theta)}, \tag{2.20}$$

Where $\hat{\mathbf{U}}_n \in \mathbb{C}^{P\times(P-Q)}$ is an estimate of the set of eigenvectors of $\mathbf{R_x}$ which span the left null space of the true $\mathbf{A}(\mathbf{\Theta})$ and $\mathbf{a}(\theta)$ represents our model of the steering vector evaluated at a specific angle. The MUSIC cost function is derived in detail from the linear model under a set of stated assumptions in Appendix B. The formulation leads to an expansion of the

covariance matrix as a superposition of orthogonal subspaces

$$\mathbf{R_x} = \mathbf{A}(\mathbf{\Theta})\mathbf{R_s}\mathbf{A}^H(\mathbf{\Theta}) + \sigma_n^2 I_p = \underbrace{\mathbf{U}_s\mathbf{\Lambda}_s\mathbf{U}_s^H}_{\text{signal subspace}} + \underbrace{\mathbf{U}_n\mathbf{\Lambda}_n\mathbf{U}_n^H}_{\text{noise subspace}}. \tag{2.21}$$

The MUSIC algorithm assumes that the principal components of $\mathbf{R_x}$ span the signal subspace and that all of the columns of $\mathbf{A}(\mathbf{\Theta})$ are orthogonal to the noise eigenvectors

$$\mathbf{a}^H(\theta_i)\mathbf{u}_i^n = 0, \quad i = 1, \ldots, Q \tag{2.22}$$

Because the denominator of Equation 2.20 is a measurement of orthogonality between an estimate of the noise eigenbasis and our assumed model, the MUSIC spectrum produces sharp peaks when a steering vector under test is orthogonal to the noise. The MUSIC estimates of the DOAs are interpreted as the Q largest peaks of the cost function in 2.20

$$\hat{\mathbf{\Theta}}_{music} = \max_{\mathbf{\Theta}} \left\{ \frac{1}{\mathbf{a}^H(\theta)\hat{\mathbf{U}}_n\hat{\mathbf{U}}_n\mathbf{a}(\theta)} \right\}. \tag{2.23}$$

We see that the MUSIC estimates require the following aspects of a priori knowledge:

1. A priori knowledge of the number of sources Q,
2. Knowledge of the manifold vector set $\{\mathbf{a}(\theta)\}$ for all possible angles in our field of view,
3. Estimate of the covariance matrix.

The MUSIC estimates are those that maximize the orthogonality between our measured noise basis and the model. Because it is not a measurement of power, the MUSIC cost function is referred to as a pseudospectrum. We note here that the beamforming techniques required knowledge of a single steering vector while the DOA estimators requires knowledge of the entire manifold.

2.3.2.2 Maximum Likelihood Estimation

In contrast to the subspace techniques which require our observations to adhere to a vector space description, statistical estimation paradigms formulate the problem based on a model of the probability distribution function of our observation parameterized by a set of unknowns. The Maximum Likelihood (ML) methods are referred to as the classical techniques and regard the unknown parameters as deterministic which is mathematically equivalent to treating an unknown as random with infinite variance.

The MLE for $\mathbf{\Theta}$ is derived in Appendix B.2.3 under a set of stated assumptions following the procedure outline in [1]. It is interesting to note that the assumptions required to formulate the MUSIC estimator are a subset of those required to obtain the MLE. To derive the MLE we treat the Q directional sources as deterministic and unknown variables which we observe in the presence of circularly symmetric independent and identically distributed (IID) noise. This allows us to cast the problem into a general Gaussian estimation model where the array samples represent complex Gaussian random vectors distributed as $\mathbf{x} \sim C(\mathbf{A}(\mathbf{\Theta})\mathbf{s}, \sigma_n^2 I_P)$.

The MLE of the vector of unknown arrival angles is shown in Appendix B.2.3 to be the solution of the following maximization

$$\hat{\mathbf{\Theta}}_{mle} = \max_{\mathbf{\Theta}} \left\{ \text{tr}\left(\mathbf{P}_{\mathbf{A}(\mathbf{\Theta})} \mathbf{R} \right) \right\}. \tag{2.24}$$

We arrive at this form by evaluating the likelihood function in terms of the ML estimates of the noise variance and the sources. The argument of the maximization is called a compressed likelihood [68] which arises for the special class of separable Gaussian estimation problems. Our estimate of the DOAs corresponds to the solution which maximizes a nonlinear multidimensional cost function in $\mathbf{\Theta}$. In contrast to the one-dimensional MUSIC pseudospectrum, the form in 2.24 ensures a global maximum at the solution but poses computational challenges as it requires an exhaustive search of Q dimensions.

We can recast the ML estimator in 2.24 in a different form to gain additional insight into the ML solution. Here we will manipulate the argument of the maximization using the following properties of the trace (written in terms of arbitrary matrix quantities)

$$\mathrm{tr}(\mathbf{C}+\mathbf{D}) = \mathrm{tr}(\mathbf{C}) + \mathrm{tr}(\mathbf{D}), \tag{2.25a}$$

$$\mathrm{tr}(\alpha\mathbf{C}) = \alpha\mathrm{tr}(\mathbf{C}), \tag{2.25b}$$

$$\mathrm{tr}\left(\mathbf{c}\mathbf{d}^H\right) = \mathbf{c}^H\mathbf{d}. \tag{2.25c}$$

We can write the covariance matrix $\mathbf{R}_\mathbf{x}$ in terms of its eigenexpansion as

$$\mathbf{R}_\mathbf{x} = \mathbf{U}\mathbf{\Lambda}\mathbf{U}^H = \sum_{i=1}^{P} \lambda_i \mathbf{u}_i \mathbf{u}_i^H. \tag{2.26}$$

We rewrite the likelihood function in Equation 2.24 in terms of the eigendecomposition of $\mathbf{R}_\mathbf{x}$

$$L(\mathbf{\Theta}) = \mathrm{tr}\left(\mathbf{P}_{\mathbf{A}(\mathbf{\Theta})}\mathbf{R}\right) = \mathrm{tr}\left(\mathbf{P}_{\mathbf{A}(\mathbf{\Theta})}\sum_{i=1}^{P}\lambda_i\mathbf{u}_i\mathbf{u}_i^H\right). \tag{2.27}$$

Pulling the projection operator inside of the summation and using the trace property in 2.25a, we rewrite this form as

$$L(\mathbf{\Theta}) = \sum_{i=1}^{P}\mathrm{tr}\left(\lambda_i\mathbf{P}_{\mathbf{A}(\mathbf{\Theta})}\mathbf{u}_i\mathbf{u}_i^H\right). \tag{2.28}$$

Applying the property in 2.25b we pull the eigenvalue out of the trace operator to obtain

$$L(\mathbf{\Theta}) = \sum_{i=1}^{P}\lambda_i\mathrm{tr}\left(\mathbf{P}_{\mathbf{A}(\mathbf{\Theta})}\mathbf{u}_i\mathbf{u}_i^H\right). \tag{2.29}$$

We use the last trace property in 2.25c to rewrite the the likelihood function as

$$L(\mathbf{\Theta}) = \sum_{i=1}^{P}\lambda_i\mathbf{u}_i^H\mathbf{P}_{\mathbf{A}(\mathbf{\Theta})}^H\mathbf{u}_i. \tag{2.30}$$

The Hermetian symmetry and idempotence of $\mathbf{P}_{\mathbf{A}(\mathbf{\Theta})}$ allow this form to be rewritten as

$$\begin{aligned} L(\mathbf{\Theta}) &= \sum_{i=1}^{P} \lambda_i \mathbf{u}_i^H \mathbf{P}_{\mathbf{A}(\mathbf{\Theta})}^H \mathbf{u}_i, \\ &= \sum_{i=1}^{P} \lambda_i \mathbf{u}_i^H \mathbf{P}_{\mathbf{A}(\mathbf{\Theta})}^H \mathbf{P}_{\mathbf{A}(\mathbf{\Theta})} \mathbf{u}_i, \\ &= \sum_{i=1}^{P} \lambda_i \mathbf{u}_i^H \mathbf{P}_{\mathbf{A}(\mathbf{\Theta})}^H \mathbf{P}_{\mathbf{A}(\mathbf{\Theta})} \mathbf{u}_i, \\ &= \sum_{i=1}^{P} \lambda_i \|\mathbf{P}_{\mathbf{A}(\mathbf{\Theta})} \mathbf{u}_i\|_2^2. \end{aligned} \tag{2.31}$$

Because multiplication of the cost function by a scalar will not change the solution, we can equivalently write the likelihood function in the following form which offers an interesting interpretation

$$L(\mathbf{\Theta}) = \frac{1}{P} \sum_{i=1}^{P} \lambda_i \|\mathbf{P}_{\mathbf{A}(\mathbf{\Theta})} \mathbf{u}_i\|_2^2. \tag{2.32}$$

We see that the MLE of $\mathbf{\Theta}$ is the solution that maximizes the weighted average of the squared Euclidean length of the eigenvectors projected onto the signal subspace. The weighting by the eigenvalues ensures that the principal components of $\mathbf{R}_\mathbf{x}$ have more influence over the estimator than the noise. This result is distinct from the MUSIC cost function which is divorced from specific eigenvalues and maximizes orthogonality between our estimated noise eigenbasis vectors and the model of the steering vectors.

2.3.2.3 MUSIC and MLE Comparison

Ziskind and Wax offer an alternating projection algorithm to efficiently obtain ML estimates of a set of arrival angles in [1]. The authors numerically verify the asymptotic efficiency of the alternating projection algorithm and demonstrate its performance relative to MUSIC in simulation for a sensor array of three elements with half-wavelength spacing assuming two equal power sources from 0° and 20°. Their study reports performance for the following two experiments over a set of Monte Carlo Trials:

1. **Experiment 1:** Two uncorrelated equal power sources with a fixed number of snapshots ($M = 10$) and per sensor SNR sweeping over the interval 10 dB $<$ SNR $<$ 25 dB.

2. **Experiment 2:** Two uncorrelated equal power sources with a fixed combined SNR of 20 dB and snapshots varying over the interval $10 < M < 1000$.

For each experiment, Ziskind and Wax present root mean squared (RMS) errors of the angle estimates of the source at 0°. These results have been recreated in simulation for both sources. Numerical results for the first experiment are presented in Figures 2.7a and 2.7b respectively while the second experiment is summarized in Figures 2.7c and 2.7d. The first experiment corresponds to the limited snapshot case and establishes estimator error as SNR increases. At low SNRs, MLE provides more accurate estimates than MUSIC until SNR reaches 20 dB at which point their performance converges. The second experiment validates the efficiency of MLE and shows that both estimators achieve the Cramér Rao Lower Bound (CRLB) by about 100 snapshots. The CRLB used to generate these plots is developed in Appendix C. The Ziskind and Wax results are reproduced here with a modeled array response that perfectly matches the snapshot model to offer a qualitative verification of the implementation of both angle estimators used in this dissertation.

Both MUSIC and MLE exhibit extreme sensitivity to small deviations between the true and assumed models of the array response to directional sources. This sensitivity has been studied in array processing literature for multiple decades. Friedlander presents sensitivity parameters for studying superresolution degradation of MUSIC in the presence of model mismatch in [21]. In a companion paper published the same year, Friedlander proposes a detailed sensitivity analysis of MLE in [22]. Swindlehurst and Kailath published two companion papers that numerically evaluates the degradation of both MUSIC [23] and MLE [49] estimators due to model mismatch.

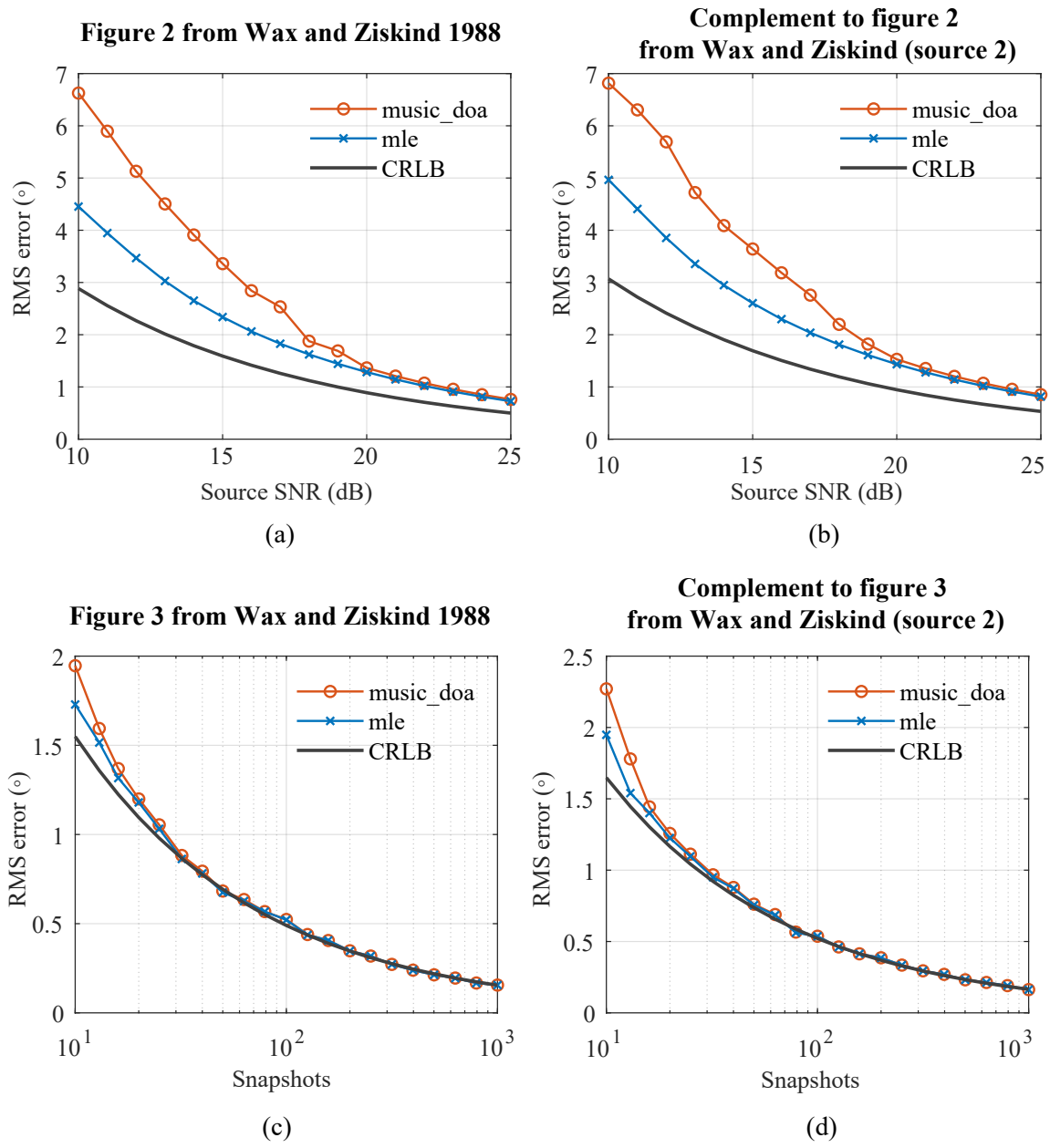

Figure 2.7: Reproduced estimator performance for ideal manifold used to benchmark MUSIC and MLE algorithms. [1].

2.4 The Array Manifold

At this point, the explicit definition of the array manifold is offered. In array signal processing, the *array manifold* refers to the response of a sensor array to spatial sources. The array's transfer function admits dependence on many parameters including frequency, polarization, propagation medium, mutual coupling, multipath, radiator type, sensor positions within the array, and angle of arrival on receive or observation angle on transmit. The manifold vector or steering vector $\mathbf{a}(\boldsymbol{\psi}) \in \mathbb{C}^{P\times 1}$ which mathematically describes the response of an array of P sensors as a function of a real-valued parameter vector $\boldsymbol{\psi} \in \mathbb{R}^{N_\Psi \times 1}$ may be written in the following general form:

$$\mathbf{a}(\boldsymbol{\psi}) = \left[a_1(\boldsymbol{\psi})e^{j\phi_1(\boldsymbol{\psi})} \dots a_P(\boldsymbol{\psi})e^{j\phi_P(\boldsymbol{\psi})}\right]^T. \tag{2.33}$$

The array manifold is then defined over a parameter space Ψ to be the locus of all manifold vectors for all possible values in the space as

$$\mathcal{A} = \{\mathbf{a}(\boldsymbol{\psi}) \ \ \forall \ \ \boldsymbol{\psi} \in \Psi\}. \tag{2.34}$$

The earliest literature on direction of arrival estimation acknowledges this interpretation of the manifold as a parametric function in multidimensional complex space. For the special case where the manifold is a function of one parameter, for example elevation angle, the manifold is interpreted as a curve that snakes through $\mathbb{C}^P$ space. In his doctoral dissertation, Schmidt illustrates this interpretation for an array of three sensors with a notional manifold described by a warped circle in $\mathbb{C}^3$ [2]. This illustration is recreated from [2] and presented in Figure 2.8. Note that in the case where the array response functionally depends on two parameters, say azimuth and elevation angle for instance, the manifold becomes a two-dimensional surface in $\mathbb{C}^P$.

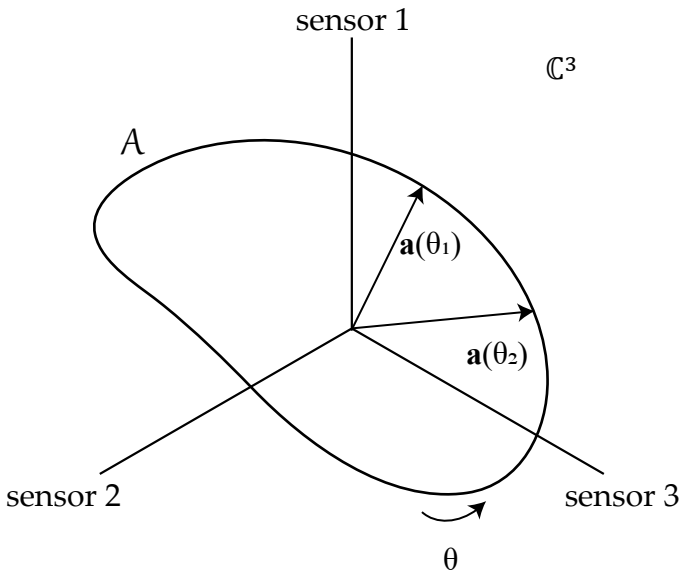

Figure 2.8: Parametric manifold interpretation for a three sensor array, reproduced from [2].

2.4.1 Idealized Array Manifolds and Classical Array Theory

The isotropic manifold is a common surrogate for the true array response vector that emerges in array processing theory [52], [69], [70]. For an array with sensor position vectors defined in a typical spherical geometry where the elevation angle θ is measured off the z axis and an azimuth angle ϕ is measured off the x axis, the isotropic manifold model on receive is given by

$$\mathbf{a}_{\text{isotropic}}(\phi,\theta) = \begin{bmatrix} e^{-jk(x_1 \sin\theta\cos\phi + y_1 \cos\theta\cos\phi + z_1\cos\theta)} \\ \vdots \\ e^{-jk(x_P \sin\theta\cos\phi + y_P \cos\theta\cos\phi + z_P\cos\theta)} \end{bmatrix}. \tag{2.35}$$

Here k is the wavenumber evaluated as $k = n\dfrac{2\pi}{\lambda}$ where λ is the wavelength in the propagation medium and $n = 2$ when the sensor positions refer to monostatic equivalent phase centers, otherwise $n = 1$. We define a unit vector $\hat{\mathbf{k}}$ that points along the direction of propagation and is oriented to be perpendicular to the plane of constant phase of an incident wavefront

as

$$\hat{\mathbf{k}}(\phi,\theta) = \begin{bmatrix} \sin\theta\cos\phi \\ \cos\theta\cos\phi \\ \cos\theta \end{bmatrix} \tag{2.36}$$

The position vector pointing from the origin to sensor p is denoted as $\mathbf{r}_p \in \mathbb{R}^3$ and expressed in the general form $\mathbf{r}_p = [x_p, y_p, z_p]^T$. Then 2.35 is alternatively expressed more compactly as

$$\mathbf{a}_{\text{isotropic}}(\phi,\theta) = \begin{bmatrix} e^{-j\mathbf{k}^T(\phi,\theta)\mathbf{r}_1} \\ \vdots \\ e^{-j\mathbf{k}^T(\phi,\theta)\mathbf{r}_P} \end{bmatrix}. \tag{2.37}$$

The negative sign points the propagation vector towards the origin of the geometry (assumed to be at the center of the array). This convention is consistent with a receiving array. The array response under the isotropic form assumes the directivity of each sensor to be unity over all directions and simply accounts for the inter-element phase variation due to plane wave propagation over the array face.

To interpret the form of the array response vector in Equation 2.35, we turn to classical antenna theory. The radiation pattern is arguably one of the most important properties of an antenna; it describes the angular variation of radiation in the far field over a sphere of constant radius and graphically illustrates an antennas spatial filtering properties. There are two important results from antenna theory related to the radiation pattern that offer insight into our understanding of the isotropic manifold: the radiation integral and the principal of pattern multiplication.

The radiation integral establishes a Fourier transform type of relationship between the current distribution of an antenna and its far field pattern [71]. This quantity determines the pattern factor $f(\theta,\phi)$ which we use to compute the total pattern of a radiator by the principle of pattern multiplication. The pattern multiplication principle states that the total normalized field pattern, $F(\theta,\phi)$, is a product of an element pattern due to an infinitesi-

mally small current element (which comes from the radiation integral) and a pattern factor determined by the spatial distribution of current on the antenna

$$F(\theta, \phi) = g_e(\theta, \phi) f(\theta, \phi). \tag{2.38}$$

For a z-directed line source of length L_z, the elemental pattern of an infinitesimal current element in the distribution can be shown to be $g_e(\theta, \phi) = \sin\theta$ [71]. Assuming a uniform current distribution over the line source, the field pattern evaluates to

$$F(\theta, \phi) = \underbrace{\frac{\sin\left(k \cdot \frac{L}{2}\cos(\theta)\right)}{\left(k \cdot \frac{L}{2}\cos(\theta)\right)}}_{f(\theta,\phi)} \overbrace{\sin\theta}^{g_e(\theta,\phi)}. \tag{2.39}$$

From this form we recognize the pattern factor as a Fourier transform along z of a boxcar weighted current distribution. We also note that the interpretation of the field pattern as a product of Fourier quantities points to a frequency-domain representation of convolution. Given knowledge of the element factor, we can compute the total field pattern for arbitrary tapers by computing the Fourier transform of the excitation function.

The pattern multiplication principle is extended to derive the expression for the field patterns of phased arrays [72]. Assuming that the sensors in the array are similar (which as we will see is not sufficient in array calibration due to mutual coupling effects), the normalized field pattern is a product of the normalized pattern of a single element in the array and the normalized array factor. The array factor takes the place of the radiation integral in the phased array formulation and the spatial integration of currents becomes a discrete summation. The array factor evaluated at a particular angular coordinate in the spherical geometry is evaluated as the following coherent sum of excitations on an array of isotropic radiators

$$AF(\theta, \phi) = \sum_{n=1}^{P} I_n e^{-j\mathbf{k}^T(\theta,\phi)\mathbf{r}_n}. \tag{2.40}$$

The array factor is completely determined by the complex excitation current on each element with a phase shift that captures the propagation offset a sensor relative to the origin of the array face geometry. The excitation I_n represents a current that is appropriately weighted to steer a tapered beam with a maximum value of one to an angular coordinate (θ_0, ϕ_0).

We define $\mathbf{h}(\theta_0, \phi_0) \in \mathbb{C}^{P\times 1}$ as the vector containing excitations needed to steer the pattern to a coordinate (θ_0, ϕ_0) with a particular taper $\mathbf{w} \in \mathbb{C}^{P\times 1}$ as the following Hadamard product between the taper and the steering vector evaluated at the pointing direction

$$\mathbf{h}(\theta_0, \phi_0) = \mathbf{w} \odot \mathbf{a}(\theta_0, \phi_0). \tag{2.41}$$

Then the n^{th} element of $\mathbf{h}$ corresponds to I_n

$$[\mathbf{h}]_n := I_n^* = w_n \cdot [\mathbf{a}(\theta_0, \phi_0)]_n \,. \tag{2.42}$$

Recognizing the term $e^{-j\mathbf{k}^T(\theta,\phi)\mathbf{r}_n}$ as the n^{th} entry of the isotropic steering vector in Equation 2.35, we can evaluate the array factor at any angular coordinate as the following projection of the tapered beamformer onto the isotropic steering vector

$$AF(\theta, \phi) = \mathbf{h}^H(\theta_0, \phi_0)\mathbf{a}_{\text{isotropic}}(\theta, \phi). \tag{2.43}$$

We can see that the isotropic steering vector simply accounts for the relative phase offset (due to propagation) between elements but lacks information about the variation in amplitude gain. Using the principle of pattern multiplication, the total field pattern for an array of similar elements is given by

$$F(\theta, \phi) = g_e(\theta, \phi)AF(\theta, \phi) = g_e(\theta, \phi)\mathbf{h}^H(\theta_0, \phi_0)\mathbf{a}(\theta, \phi). \tag{2.44}$$

To prepare for modified forms of the manifold vectors to follow, we rewrite this expression

as a quadratic form

$$F(\theta, \phi) = \mathbf{h}^H(\theta, \phi)\mathbf{G}(\theta, \phi)\mathbf{a}(\theta, \phi), \tag{2.45}$$

Where $\mathbf{G}(\theta, \phi)$ is a $P \times P$ diagonal matrix that contains the directional voltage gain of each sensor down the main diagonal.

For the array of similar and interacting elements $\mathbf{G}_{\text{isolated}}(\theta, \phi) = \text{diag}\{g_e(\theta, \phi)\}$ where the element pattern, $g_e(\theta, \phi)$, represents the field pattern of a single element measured in isolation. The diagonal form presumes that the elements are isolated and mutual coupling does not exist. The complete array response vector for the isolated manifold is

$$\mathbf{a}_{\text{isolated}}(\theta, \phi) = \mathbf{G}_{\text{isolated}}(\theta, \phi)\mathbf{a}_{\text{isotropic}}(\theta, \phi). \tag{2.46}$$

When the isotropic steering vector is used to represent the manifold in array processing, it implies an array of non-interacting sensors with isotropic gain (unity in all directions). Because we know that isotropic radiators are a theoretical construct used in classical array theory (and not physically realizable), this form is mismatched from reality by definition. The isolated steering vector in Equation 2.46 incorporates the element gain but assumes the sensors to have identical element patterns and ignores coupling. Both forms are problematic because they neglect the electromagnetic interactions between antennas in the array.

2.4.2 The Coupled and Loaded Manifold

The isotropic and isolated manifold vectors are not matched to the true array response because both forms assume the radiators to be non-interacting and similar. The coupling matrix is generally introduced in mutual coupling calibration in order to obtain a more realistic model of the multichannel voltages captured by the ADCs and treats sensors as interacting elements in the context of microwave networks (see [73] for an early example). Figure 2.9 illustrates the corresponding model used to develop the interpretation and definitions relating to the coupled manifold.

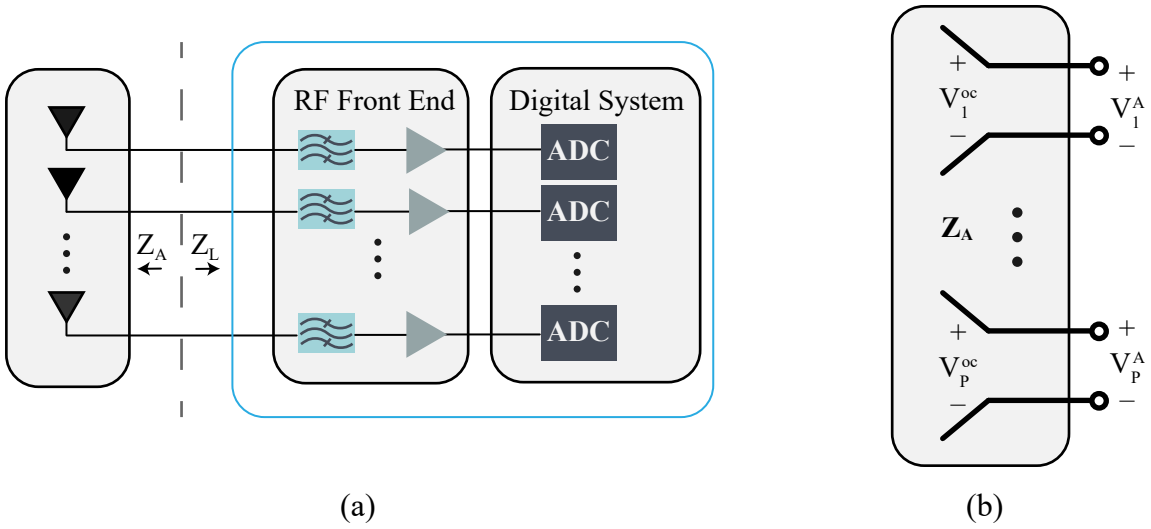

Figure 2.9: Microwave interpretations assumed in the derivation of the coupled and loaded manifold: (a) microwave network model of an array attached to a multiport receive network and (b) the Thévenin representation of the array.

Mutual coupling refers to the electromagnetic interaction between an antenna element and objects in its environment. In phased arrays, the mutual coupling effect changes the distribution of currents on the individual elements in the array (along with the magnitude and phase of the currents) from the individual isolated currents in free space. An isolated antenna element is characterized by an input impedance. Introduction of a neighboring antenna in close proximity changes the impedance properties of both elements which alters the currents flowing on each device. The mutual coupling effect erodes the validity of the pattern multiplication theorem which, as we saw, establishes a model for the array radiation pattern in terms of the isolated pattern of a single element and the isotropic manifold.

In general, analytic forms of the coupled steering vector do not account for reflections from adjacent structures and focus mainly on developing a mathematical definition of coupling from the array mutual impedance matrix, $\mathbf{Z_A} \in \mathbb{C}^{P \times P}$. The mutual impedance matrix is derived by treating the array as a multi-port device to obtain expressions for the transfer

impedance terms and is written in a general form as follows

$$\mathbf{Z_A} = \begin{pmatrix} Z_{11} & Z_{12} & \dots & Z_{1P} \\ Z_{21} & Z_{22} & \dots & Z_{2P} \\ \vdots & \vdots & \ddots & \vdots \\ Z_{P1} & Z_{2P} & \dots & Z_{PP} \end{pmatrix}. \tag{2.47}$$

The diagonal entry, Z_{pp}, is the self-impedance of the p^{th} embedded element and is not to be confused with the input impedance of the element in isolation. The (m, n) entry of the mutual impedance matrix is defined as the ratio of the open-circuit voltage developed at the terminals of antenna m due to a current impressed on the terminals of antenna n

$$Z_{mn} = \left.\frac{V_m}{I_n}\right|_{I_j=0, j\neq n}. \tag{2.48}$$

The voltage developed on the m^{th} port due to the aggregated effect of coupled currents is

$$V_m = Z_{1m}I_1 + Z_{2m}I_2 + \ldots + Z_{Pm}I_P. \tag{2.49}$$

The input impedance at the terminals of the m^{th} embedded element is

$$Z_{in}^m = \frac{V_m}{I_m} = Z_{1m}\frac{I_1}{I_m} + Z_{2m}\frac{I_2}{I_m} + \ldots + Z_{Pm}\frac{I_P}{I_m} \tag{2.50}$$

Under plane-wave excitation, we treat the array as a Thévenin equivalent source with multiport open circuit voltages given by $\mathbf{V_{oc}} \in \mathbb{C}^{P\times 1}$ and a mutual impedance matrix $\mathbf{Z_A}$ [73]. The terminal voltages presented to a load are

$$\mathbf{V_L} = \mathbf{Z_L}\left(\mathbf{Z_L} + \mathbf{Z_A}\right)^{-1}\mathbf{V_{oc}}, \tag{2.51}$$

Where we have used the following relationships

$$\mathbf{V_A} = \mathbf{Z_A I_A} + \mathbf{V_{oc}}, \tag{2.52a}$$

$$\mathbf{V_A} = -\mathbf{Z_L I_A}. \tag{2.52b}$$

The forms in 2.52, originally attributed to [74], summarize a circuit equivalent model of the multichannel voltages captured by an embedded array. These expressions were rederived in [35] using a method of moments formulation and assuming perfectly conducting elements.

The open-circuit voltages relate proportionally to the open-circuit field patterns and model parasitic coupling between sensors. We measure the open-circuit voltage pattern of the n^{th} element in the array, denoted $g_n^{\text{oc}}(\theta, \phi)$, by impressing a current on antenna n with all other antennas open-circuited [75]. We expect the patterns for sensors at the edge of the array to show distinctions relative to the center antennas based on differences in their coupling environments. For a very large array, a majority of the sensors experience similar coupling environments and $g_n^{\text{oc}}(\theta, \phi)$ is approximated as being similar over the elements. In contrast, the open-circuit patterns may exhibit significant differences in a small array and such an approximation may not be valid.

The open-circuit manifold vector is given by

$$\mathbf{a}_{\text{oc}}(\theta, \phi) = \mathbf{G}_{\text{oc}}(\theta, \phi)\mathbf{a}_{\text{isotropic}}(\theta, \phi). \tag{2.53}$$

Which we use to evaluate the manifold of the embedded and loaded array

$$\begin{aligned} \mathbf{a}(\theta, \phi) &= \mathbf{Z_L} \left(\mathbf{Z_L} + \mathbf{Z_A}\right)^{-1} \mathbf{a}_{\text{oc}}(\theta, \phi), \\ &= \underbrace{\mathbf{Z_L} \left(\mathbf{Z_L} + \mathbf{Z_A}\right)^{-1} \mathbf{G}_{\text{oc}}(\theta, \phi)}_{\mathbf{C}(\theta,\phi)} \mathbf{a}_{\text{isotropic}}. \end{aligned} \tag{2.54}$$

This form is cited in recent work by Friedlander in [32] as the proper linear transformation of the isotropic steering vectors that accounts for mutual coupling. This model uses a direction-

dependent coupling matrix which handles the angle-dependent variation of the embedded element patterns. The coupling matrix as defined here is a rank P complex-valued square matrix that provides an isomorphic mapping from an isotropic basis to a coupled basis. Using $\mathbf{a}_{\mathrm{c}}(\theta,\phi)$ to denote the coupled manifold, the model is summarized here in terms of the isotropic steering vector in Equation 2.35 and the mutual impedance matrix in 2.47:

$$\mathbf{a}_{\mathrm{c}}(\theta,\phi) = \mathbf{C}(\theta,\phi)\mathbf{a}_{\mathrm{isotropic}}(\theta,\phi), \tag{2.55a}$$

$$\mathbf{C}(\theta,\phi) = \mathbf{Z_L}\left(\mathbf{Z_L}+\mathbf{Z_A}\right)^{-1}\mathbf{G}_{\mathrm{oc}}(\theta,\phi), \tag{2.55b}$$

$$\mathbf{G}_{\mathrm{oc}}(\theta,\phi) = \mathrm{diag}\left\{g_1^{\mathrm{oc}}(\theta,\phi),\ldots,g_P^{\mathrm{oc}}(\theta,\phi)\right\}, \tag{2.55c}$$

$$\mathbf{Z_L} = \mathrm{diag}\left\{Z_{L1},\ldots,Z_{LP}\right\}. \tag{2.55d}$$

The model above books all of the direction dependence of the coupled manifold into the open circuit gain patterns. The extent to which the coupled form summarized in 2.55 admits parameterization depends on the form of the open-circuit patterns $g_p^{oc}(\theta,\phi),\ 1 \le p \le P$ which account for the radiation properties of an isolated antenna in the array and the mutual interactions between sensors.

A simple example is presented here to demonstrate the distortion of the isolated antenna patterns due to mutual interaction between sensors. The open circuit patterns of a linear array of wideband dipole elements are simulated in Feko [4]. Details on the use of a computational electromagnetics package to study array manifold calibration is deferred to Chapter 6. Predicted patterns from a full-wave solution are shown here to offer the reader intuition to the mutual coupling effect on elements in the array. Figure 2.10 shows cuts through elevation angle of the open circuit gain patterns (on a linear scale) measured for each antenna in the array by driving each element individually with an ideal excitation and with all other elements unloaded. In isolation the radiation pattern follows a cosine function in elevation angle, illustrated by the red dotted curve. Mutual coupling degrades the peak gain relative to the isolated pattern and distorts the patterns in angle. The patterns exhibit symmetry

in elevation angle based on their symmetry in the array.

2.5 Array Manifold Calibration

Array manifold calibration refers to a signal processing step in the array processor designed to improve the representation of the transfer function assumed in angle estimation and beamforming. Approaches described in literature are well-described under a parametric/nonparametric taxonomy. Parametric forms assume prior knowledge of a closed form expression for the manifold model and seek to estimate unknown model parameters. Provided that the manifold admits an analytic form, parametric manifold calibration supports calibration with multiple sources simultaneously. Nonparametric techniques in contrast do not presume knowledge of the array transfer function and instead focus on estimating the array response to single sources over the field of view from measurements. This section offers a high-level survey of array manifold calibration from the parametric/nonparametric perspective and does not address the many application-specific approaches evidenced in literature that bear no value to the problem of calibrating the multichannel SAR sounder. In the discussion that follows, the azimuth angle dependence is dropped from the notation to present mathematic notation that is consistent with the array processing formulation presented at the start of the chapter.

2.5.1 Parametric Calibration

Parametric manifold calibration methods seek estimates of the model parameters of the non-ideal array response in order to characterize deviations of the steering vectors from either idealized or nominal forms. The deviations are attributed to geometric uncertainties, phase and gain imbalances and mutual coupling. In general, the majority of research papers address one subset of the aforementioned mismatch models. Source arrival angles range from completely unknown (blind calibration), to constrained (almost-blind, auto-calibration, or

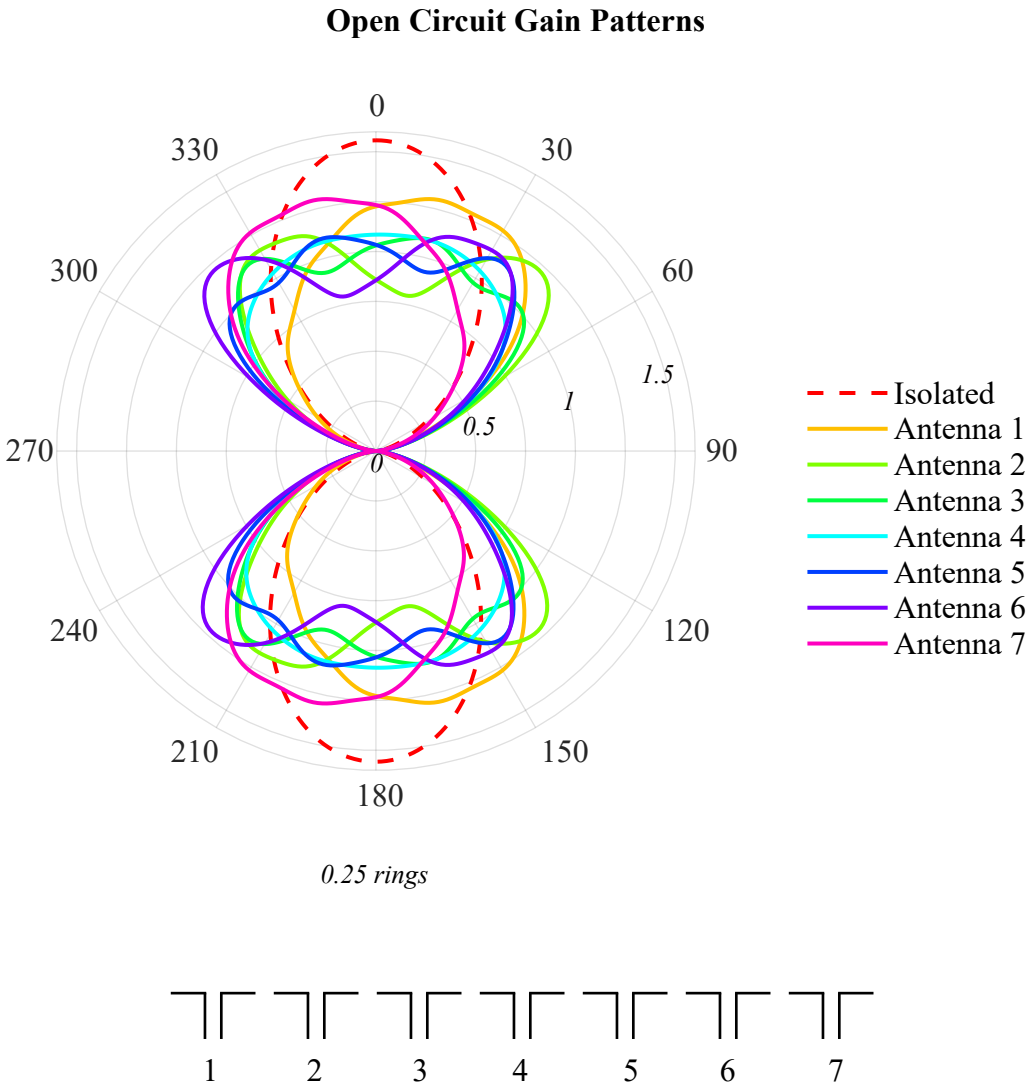

Figure 2.10: Open circuit gain patterns of a linear array of wideband dipoles [3] in free space.

self-calibration) to well-known. When the source DOA is unknown, the calibration problem is formulated as a joint estimation of arrival angle and array parameters.

In parametric calibration, the snapshot model is written in terms of a manifold which is functionally dependent on the usual vector of arrival angles and a set of additional parameters stored in $\boldsymbol{\eta}$

$$\mathbf{X} = \mathbf{A}(\boldsymbol{\Theta}, \boldsymbol{\eta})\mathbf{S} + \mathbf{N}, \tag{2.56}$$

Where we have suppressed the ϕ dependence. Parametric approaches state an analytical form of $\mathbf{A}(\boldsymbol{\Theta}, \boldsymbol{\eta})$ which is used to develop a real-valued cost function in the variable $\boldsymbol{\eta}$ and $\boldsymbol{\Theta}$. When convenient, we may interpret $\mathbf{A}(\boldsymbol{\Theta}, \boldsymbol{\eta})$ to be a linear transformation of a nominal manifold (which may be the isotropic manifold for example or a nominal form from some baseline calibration step). In this case we will use $\mathbf{A_0}(\boldsymbol{\Theta})$ to denote the nominal model. We use the notations $\hat{\boldsymbol{\eta}}$ and $\hat{\boldsymbol{\Theta}}$ to refer to estimates of the true values.

2.5.1.1 Separable Gaussian Problems in Parameter Estimation

When the columns of $\mathbf{N}$ correspond to vectors of independent Gaussian random variables and the parameters of $\mathbf{A}(\boldsymbol{\Theta}, \boldsymbol{\eta})$ as well as the sources are taken to be deterministic, then the model in Equation 2.56 is treated as *separable Gaussian* [76]. In the separable Gaussian estimation problem, the probability density function (pdf) of our observation is parameterized by both linear and nonlinear parameters. Separable problems admit analytic forms for the ML estimates of the linear parameters which can be used to form a compressed likelihood function to solve for the nonlinear parameters [68]. The MLE of the DOAs derived in Appendix B.2.3 is a special case of a separable Gaussian problem that provides exact solutions for the estimators of the linear parameters which we used to obtain a compressed likelihood in terms of the nonlinear parameters (arrival angle).

For the given form in Equation 2.56, we handle the observation vectors (corresponding to the columns of $\mathbf{X}$) as complex Gaussian random vectors, each distributed as $\mathbf{x} \sim$

$C\left(\boldsymbol{\mu}_{\mathbf{x}}(\boldsymbol{\eta}_{\boldsymbol{\mu}}), \mathbf{R}_{\mathbf{x}}(\boldsymbol{\eta}_{\mathbf{c}})\right)$ where the mean is given by

$$\boldsymbol{\mu}_{\mathbf{x}}(\boldsymbol{\eta}_{\boldsymbol{\mu}}) = \mathbf{A}(\boldsymbol{\eta}_{\mathbf{nl}})\overset{\mathbf{s}}{\overbrace{\boldsymbol{\eta}_{\mathbf{l}}}}. \tag{2.57}$$

The total parameter vector for the mean is the composition of nonlinear parameters (which includes $\boldsymbol{\Theta}$ in the joint estimation approaches) and linear parameters

$$\boldsymbol{\eta}_{\boldsymbol{\mu}} = \begin{bmatrix} \boldsymbol{\eta}_{\mathbf{nl}} \\ \boldsymbol{\eta}_{\mathbf{l}} \end{bmatrix}. \tag{2.58}$$

Using $\boldsymbol{\eta}_{\boldsymbol{c}}$ to refer to parameters of the covariance (which would just be the noise variance, σ_n^2, for the IID case), the total parameter vector is the concatenation of the mean and covariance parameters:

$$\boldsymbol{\eta} = \begin{bmatrix} \boldsymbol{\eta}_{\boldsymbol{\mu}} \\ \boldsymbol{\eta}_{\boldsymbol{c}} \end{bmatrix}. \tag{2.59}$$

The compressed likelihood function for the separable Gaussian problem (assuming IID complex Gaussian noise) takes the following form (written in terms of the unknown, nonlinear mean parameters)

$$L(\mathbf{X}; \boldsymbol{\eta}_{\mathbf{nl}}) = \left\| \mathbf{X} - \mathbf{A}(\boldsymbol{\eta}_{\mathbf{nl}}) \left(\mathbf{A}^H(\boldsymbol{\eta}_{\mathbf{nl}}) \mathbf{A}(\boldsymbol{\eta}_{\mathbf{nl}}) \right)^{-1} \mathbf{A}^H(\boldsymbol{\eta}_{\mathbf{nl}}) \mathbf{X} \right\|^2. \tag{2.60}$$

When the likelihood takes this form, the MLE of the nonlinear parameter vector $\boldsymbol{\eta}_{\mathbf{nl}}$ is the solution to the following maximization

$$\hat{\boldsymbol{\eta}}_{\mathbf{nl}} = \max_{\boldsymbol{\eta}_{\mathbf{nl}}} \left\{ \mathrm{tr}\left(\mathbf{P}_{\mathbf{A}(\boldsymbol{\eta}_{\mathbf{nl}})} \mathbf{R}_{\mathbf{x}} \right) \right\}. \tag{2.61}$$

The separable Gaussian form reduces to a nonlinear least squares problem which we solve through a multidimensional search. Blind and autocalibration techniques regard $\boldsymbol{\Theta}$ as an unknown nonlinear parameter contained in $\boldsymbol{\eta}_{\mathbf{nl}}$ while the informed techniques may treat the

DOAs as either known or approximately known. Note that the classical Maximum Likelihood Estimator of the DOA presented in Appendix B.2.3 follows the work of Ziskind and Wax [1] who propose an Alternating Projection optimization based on the compressed log-likelihood form in Equation 2.61.

2.5.1.2 Array Shape Calibration

Interest in parametric array shape calibration appears to emerge in literature to address the problem of angle estimation with towed and flexible arrays. The foundational work on array shape calibration in the blind calibration framework is attributed to a set of papers published by Rockah and Schultheiss in 1987 [30], [31]. In [30], the authors derive a hybrid Cramér-Rao Lower Bound (CRLB) for the blind calibration problem, under an assumption of small scale perturbations generally understood to be less than 0.1λ. The CRLB is used to benchmark estimator performance and provides a theoretical lower bound on the variance of unbiased estimators. The classical form, attributed to Fisher [68], bounds the variance on estimates of deterministic parameters. When the number of unknown parameters is greater than one, the CRLB is obtained from an appropriate entry of the inverse of the Fisher Information Matrix (FIM). The detailed steps for finding the FIM in the seperable Gaussian problem are presented in Appendix C and are discussed in later portions of this work.

The hybrid CRLB of Rockah and Schultheiss bounds estimator accuracy for parameter vectors composed of both random and nonrandom unknowns. Defining $\mathbf{J}_D(\boldsymbol{\eta}_D)$ to be the FIM dependent on a deterministic parameter vector $\boldsymbol{\eta}_D$ and let $\mathbf{J}_R(\boldsymbol{\eta}_R)$ be an information matrix describing the random parameters. The hybrid CRLB is then obtained by inverting the hybrid information matrix given by

$$\mathbf{J}_H(\boldsymbol{\eta}_D, \boldsymbol{\eta}_R) = \mathbf{J}_D(\boldsymbol{\eta}_D) + \mathbf{J}_R(\boldsymbol{\eta}_R). \tag{2.62}$$

In the derivation, Rockah and Schultheiss treat source DOAs as deterministic and assume

geometric perturbations to be random with known Gaussian distributions to describe the uncertainties in each dimension. We see that the random portion of the information plays a similar role to the a priori distribution in the Bayesian information matrix.

The work by Rockah and Schultheiss provides important contributions to array calibration theory and more broadly to the general area of parameter estimation. In [77], Van Trees acknowledges their work as being representative of a class of problems emerging in the field of parameter estimation focused on bounding performance under misspecified models (for a recent tutorial, see [78]). Their work has been significant to the development of small perturbation theory in parametric array calibration because of the important findings in [30] regarding the identifiability problem in blind array shape calibration. Their study establishes specific limitations on the joint estimation of sensor position uncertainties and source bearings. The authors conclude that the DOAs and perturbations can be *unambiguously* estimated provided the following conditions hold:

1. Snapshots are obtained from at least three spatially disjoint angles,

2. The location of one sensor is known,

3. The direction to an adjacent sensor is known,

4. The nominal geometry is not linear.

Weiss and Friedlander present a Maximum Likelihood framework for the array shape calibration problem under small perturbations and with unknown DOAs in [28]. They formulate the problem under an assumption of IID complex Gaussian observation noise and treat source parameters (waveform and arrival angle), noise parameters, and perturbations as deterministic but unknown variables. Although the problem as defined fits the separable Gaussian framework described earlier, Weiss and Friedlander propose an iterative solver to the following cost function J_{cost} based on updating the unknown waveform sequentially with the left pseudoinverse:

$$J_{\text{cost}} = \frac{1}{MP} \sum_{i=1}^{M} \left\| \mathbf{x}_i - \mathbf{A}(\boldsymbol{\eta}_{\mathbf{nl}}) \mathbf{s}_i \right\|^2 . \tag{2.63}$$

Here M is number of snapshots, P is number of sensors, i is a discrete time index, and $\boldsymbol{\eta}_{\mathbf{nl}} = [\boldsymbol{\Theta}, x_1, y_1, \ldots, x_P, y_P]$ is the vector of real nonlinear parameters.

Weiss and Friedlander minimize the cost function in 2.63 with an iterative sequential technique. On a given iteration, an estimate of the DOAs is obtained using alternating projection style minimization (see [1]). This estimate is held fixed to update the estimated geometric perturbations. Under a small perturbation assumption the authors propose a MacLaurin series approximation which enables a closed form solution to the minimization of the perturbations on an arbitrary sensor (written in terms of the ML estimate of the waveform). The closed form solution obviates the requirement of a multidimensional search and allows for an efficient update to the estimates of geometric uncertainties for a given estimate of $\boldsymbol{\Theta}$ (then used to update the DOA estimates and so on). The sequential estimation framework is carried out until satisfaction of some convergence criterion.

A Maximum A Posteriori (MAP) framework for small perturbations is presented by Viberg and Swindlehurst in [79]. In this work, the geometric uncertainties are treated as random variables with known a priori distributions and the vector of source DOAs are taken to be deterministic and unknown. The authors develop a simpler noise subspace fitting technique to ease computation over the optimal MAP estimator, referred to as MAP-NSF. The asymptotic performance of MAP-NSF is established in [79]. Weiss and Friedlander also develop a subspace technique for the small perturbation problem based on a MUSIC like cost function and address the solution identifiability problem that arises in array shape calibration with unknown DOAs in [28].

Flannagan extends the body of array shape calibration to handle large perturbations (where the perturbation scale exceeds 0.1λ) [80], [81] and proposes a more robust autocalibration procedure that evades approximations made under the small perturbation approaches (see [29], [28] for example). Flanagan's procedure, which he refers to as QWF (with Q be-

ing related to a function in the algorithm and WF denoting a weighted fitting) integrates aspects of nonparametric calibration procedures [82], [83] to handle large perturbations with features of the parametric estimation techniques for small perturbations [79], [29] to refine estimates of the parameters all within in an iterative framework. Flannagan treats geometric uncertainties as random variables and numerically verifies the identifiability conditions first presented by Rockah and Schultheiss [30]. His results establish performance of the QWF estimator relative to the small perturbation techniques of Weiss and Friedlander [29] and the MAP-NSF technique of Viberg and Swindlehurst [79].

The large body of work in the area of array shape calibration is largely attributed to the direct extension of the isotropic manifold model to account for geometric uncertainties. The geometrically perturbed manifold vector is modeled with an introduction of error terms in the phase center location of each sensor. The p^{th} entry of a perturbed manifold vector generalizes to the following form:

$$[\mathbf{a}(\theta,\phi)]_p = e^{-jk[(x_p+\Delta x_p)\sin\theta\cos\phi+(y_p+\Delta y_p)\cos\theta\cos\phi+(z_p+\Delta z_p)\cos\theta]}. \tag{2.64}$$

The perturbations $\{\Delta x_i, \Delta y_i, \Delta z_i \in \mathbb{R} \mid 1 \leq i \leq P\}$ may be treated as deterministic or random. When treated as random, the uncertainties are commonly assumed to be zero-mean Gaussian random variables with respective variances $\sigma^2_{xi}, \sigma^2_{yi}, \sigma^2_{zi}$ [80], [81]. Let $\boldsymbol{\eta}_{\mathbf{r}}$ be the real valued parameter vector containing the unknown position offsets for all of the sensors, written in the following general form for the azimuth and elevation dependent manifold

$$\boldsymbol{\eta}_{\mathbf{r}} = \Big[\Delta x_1, \Delta y_1, \Delta z_1, \ldots, \Delta x_P, \Delta y_P, \Delta z_P\Big]^T. \tag{2.65}$$

In this form, the position errors present $3P$ unknowns in the manifold model. When the unknown DOA is constrained to the elevation dimension or when the z components are zero, we restrict our attention to perturbations in x and y and the length of the unknown parameter vector reduces to $2P$. The general array response vector parameterized by the

DOAs and position uncertainties is denoted as $\mathbf{a}(\theta, \phi; \boldsymbol{\eta}_\mathbf{r})$.

The perturbations on the array geometry impart a propagation phase offset on the spatial measurements relative to the ideal geometry. We can model the perturbed vector in terms of a linear transformation on the ideal form by defining the matrix $\mathbf{D}_\mathbf{r}(\theta, \phi; \boldsymbol{\eta}_\mathbf{r})$ to be the diagonal matrix which models the phase shifts of each element based on the additional path lengths in $\boldsymbol{\eta}_\mathbf{r}$. We can then state the following model of the perturbed steering vector as

$$\mathbf{a}(\theta, \phi; \boldsymbol{\eta}_\mathbf{r}) = \mathbf{D}(\theta, \phi; \boldsymbol{\eta}_\mathbf{r}) \mathbf{a}_{\text{isotropic}}(\theta, \phi), \tag{2.66a}$$

$$\mathbf{D}_\mathbf{r}(\theta, \phi; \boldsymbol{\eta}_\mathbf{r}) = \text{diag}\left\{ e^{-j\mathbf{k}^T(\theta,\phi)\Delta\mathbf{r}_1} \dots e^{-j\mathbf{k}^T(\theta,\phi)\Delta\mathbf{r}_P} \right\}, \tag{2.66b}$$

$$\Delta\mathbf{r}_p = \begin{bmatrix} \Delta x_p, & \Delta y_p, & \Delta z_p \end{bmatrix}^T, \tag{2.66c}$$

$$\boldsymbol{\eta}_r = \begin{bmatrix} \Delta\mathbf{r}_1^T, & \dots, & \Delta\mathbf{r}_P^T \end{bmatrix}^T. \tag{2.66d}$$

Recall the common (and essential) assumption of linear independence between the manifold vectors in MUSIC and MLE. We can note that the diagonal matrix $\mathbf{D}_\mathbf{r}(\theta, \phi; \boldsymbol{\eta}_\mathbf{r}) \in \mathbb{C}^{P \times P}$ is a linear transformation that preserves the number of principal components in the covariance matrix. Hence the perturbed manifold preserves the mathematical properties asserted in the derivations of the MUSIC and MLE cost functions. Furthermore because the model parameters group into the set of unknown nonlinear parameters of the manifold, the geometrically perturbed manifold lends itself to a separable Gaussian formulation by which we can obtain a minimum variance and unbiased estimator of $\mathbf{a}(\theta, \phi; \boldsymbol{\eta}_\mathbf{r})$. The practical applicability of this model depends entirely on the sources of manifold uncertainty in a given application and the extent to which one may reasonably attribute a majority of error to phase center uncertainty.

2.5.2 Nonparametric Calibration

Nonparametric manifold calibration approaches do not assume a model description of manifold uncertainty and instead aim to measure the array response to single sources in controlled collections. These techniques are the lookup table approaches that require steering vectors to be measured and stored at many calibration points from sources with known arrival angles. When a calibration signal, $s^c(t)$, is known and the observation noise is zero-mean and IID, the ML estimator of the true manifold vector is estimated from the vectors of discrete samples by regarding the manifold response vector as deterministic and unknown [84]. The MLE is given by:

$$\hat{\mathbf{a}}_{MLE}(\theta) = \frac{1}{M}\sum_{i=1}^{M}\frac{\mathbf{x}_i s_i^{c*}}{|s_i^c|^2}. \tag{2.67}$$

Ideally $\mathbf{x}$ would represent the multichannel voltages across the terminal loads of the direction finding receiver (coupled through the electronics that would be used in practice) and the steering vectors would be estimated at many angles. The estimator in 2.67 is unbiased and can be used to parameterize the manifold, thereby enabling multitarget calibration under the parametric umbrella.

In the case where the waveform is unknown, the principal eigenvector of the measured array covariance matrix can provide an estimate of the orientation of the vector $\mathbf{a}(\theta)$ in $\mathbb{C}^{P\times 1}$ space but requires a constant-norm constraint in the derivation. This result does not account for roll-off of the element pattern and merely estimates a systematic phase offset of each channel relative to a nominal manifold. The principal eigenvector proof is documented in a submitted manuscript (accepted for publication) which documents the nonparametric manifold calibration methodology carried out for this dissertation [53] and discussed further in Chapter 5.

2.6 Assessment of Manifold Calibration for SAR Sounders

The discussion that follows offers a synthesis of the assessed array manifold literature in the context of SAR ice sounders. In all cases, we assume that manifold calibration starts at the output of the SAR processor. This starting point is consistent with the formulation of the linear model in 2.1 and simplifies the manifold calibration problem to one of characterizing the response of the cross-track phase centers through elevation angle. The most accurate manifold is one that characterizes the transfer function of the integrated array. Hence a data-dependent characterization should rely on measurements collected by the array after installation and a modeling approach should have sufficient fidelity to capture the dominant error mechanisms influencing channel to channel deviations from the nominal manifold.

In approaching the manifold calibration problem for ice-penetrating SARs, challenges emerge immediately at the crossroads of the parametric and nonparametric routes as obstacles present themselves along either pathway. The nonparametric classes of manifold calibration refer to the measure and store approaches that do not require prior knowledge of the manifold response model $\mathbf{a}(\theta)$ but do however mandate observations of spatial sources at known arrival angles. The most accurate manifold model may be obtained when single spatial sources with known bearing angles present known waveforms to the installed array. This case, known as pilot calibration, admits an MLE of $\mathbf{a}(\theta)$ that is unbiased and this estimate can be used to develop a parametric manifold model. Pilot calibration sources are not available in airborne ice sounding missions hence this approach is inapplicable to the SAR ice sounder manifold measurement problem.

Lacking access to known pilot sources, SAR sounder manifold characterization instead relies on scattered signal from a diffuse surface to characterize aspects of the array transfer function. When a waveform is unknown, the principal eigenvector of the array covariance estimated from many snapshots of single directional sources provides a measure of a manifold vector's orientation in $\mathbb{C}^{P\times 1}$ space. When data sets from dedicated calibration flights over specular surfaces are not available, single source observations must be extracted by other

means. This poses practical challenges as the sounder, which is well described as an altimeter, rarely captures single sources. Thus the principal eigenvector technique does not appear universally applicable to all data sets either. We pause here to emphasize that the principal eigenvector approach provides an estimate of the orientation of a manifold vector in complex P dimensional space. This measure does not account for rolloff of an element pattern as it is derived assuming a constant magnitude over all θ. The implications of this constraint on angle estimator accuracy remain unclear and justify further investigation to determine the importance of measuring the length of the vector $\mathbf{a}(\theta)$ over the field of view.

Returning to the initial crossroads of the taxonomy in Figure 1.1, we consider the parametric approach. Pursuit of the parametric path is predicated on knowledge of the manifold model. To date, there have been no attempts to develop a parametric description of a SAR ice sounder's array manifold. Development of such a model should be informed by the dominant error mechanisms influencing the array's directional response. We expect mutual coupling and platform effects to significantly alter embedded element patterns from the isolated radiation pattern of one antenna element. Antenna patterns may be predicted with a full-wave solver but obtaining these predictions requires detailed and intensive computational electromagnetic solvers that may not lead to forms which are easily parameterized, as will be shown in Chapter 6. The appeal of a parametric calibration approach is that it handles multitarget calibration which is better suited for the SAR ice sounder problem but the extremely large number of parameters needed to describe the manifold quickly leads to intractable multidimensional optimization problems that are difficult to initialize and risk converging to local extrema when improperly initialized.

2.7 Conclusion

This chapter presents the array processing formulation of multichannel SAR sounder imagery. The primary array signal processing techniques used in 2-D and 3-D image formation are described. Specific considerations in ice sheet imaging are emphasized in the context

of array processing. The array manifold is formally described and related to classical array theory. A generalized overview of signal processing techniques for array manifold calibration is presented that adopts a nonparametric/parametric categorization of approaches. Calibration of SAR sounder manifolds is interpreted through this perspective, noting specific challenges facing either form.

Chapter 3

Instrumentation and Data Processing Methodology

Abstract

Nonparametric manifold calibration requires observations of spatial sources from known arrival angles to characterize the response of array elements in magnitude and phase. In the SAR sounder manifold characterization problem, subsurface scatterers are regarded as undesirable calibration sources because they require an assumption of plane wave velocity in a medium that may lead to error in the interpreted DOA. A data processing architecture is developed to produce snapshot databases of SAR focused multichannel observations tagged with surface incidence angle and target classification by coregistering the complex imagery to two auxiliary data sets. This chapter introduces the instrumentation studied in this dissertation and describes the development of the snapshot database, which enables the application and validation of the nonparametric manifold calibration technique presented in Chapters 5 and 7. This chapter also documents the initial application of the database in measuring the RDS receive manifold. The measured manifold is applied in geometric nulling of sidelobe clutter and demonstrates larger clutter suppression relative to null steering with the nominal manifold model, helping to confirm the methodology outlined in this chapter.

3.1 SAR System and Instrumentation Overview

The research documented in this dissertation relies on multichannel SAR measurements from CReSIS's RDS to demonstrate manifold calibration techniques. The modern RDS, which

advanced over multiple decades of technological developments by KU researchers affiliated with both CReSIS and KU's Radar and Remote Sensing Laboratory [39], [40], [85], [43], [8], operates in the Very High and Ultra High Frequency (VHF and UHF) ranges and surveys freshwater ice of Greenland and Antarctica from multiple platforms including Twin Otter, Basler, P-3, DC-8, C-130H, and Gulfstream aircraft [8], [86]. Table 3.1 summarizes typical RDS parameters [8] for the system flown on NASA's Operation IceBridge campaigns.

Table 3.1: Typical depth sounder operating parameters during Operation IceBridge [8].

Variable	*Value*	*Units*	*Parameter*
f_c	195	MHz	Center frequency
B	30	MHz	Chirp bandwidth
T_{pd}	≤ 30	μs	Pulse duration
PRF	≤ 12	kHz	Pulse repetition frequency
θ_0	0	$^\circ$	Elevation pointing angle
ϕ_0	0	$^\circ$	Azimuth pointing angle (squint)
P_{TX}	≤ 1200	Watts	Peak transmit power
h	500	meters	Platform height above surface

3.1.1 RDS P-3 Antenna Array

The RDS transmit and receive cross-track array varies by platform. The RDS P-3 array, described in [3], is comprised of 15 wideband dipoles, organized into three subarrays: one fuselage mounted transmit/receive subarray of seven elements and two receive-only wing mounted subarrays, each with four elements. The subarrays are embedded in aerodynamic fairing structures which attach to the P-3 hard points, originally intended as weapon stations for Navy tactical missions. The integrated subarrays are shown on their inaugural flight at the NASA Flight Facility in Wallops Island, Virginia in Figure 3.1. The structural and material details of the RDS P-3 fairings are provided in [87] and [6].

Figure 3.1: Installed RDS subarrays on the P-3 aircraft. Image courtesy of Rick Hale, 2011.

We identify each physical antenna with a numerical identifier following the convention illustrated in Figure 3.2. This diagram also specifies the approximate dimensions of each cross-track subaperture, measured sensor to sensor. The nominal sensor positions assumed in this work are reported in Table 3.2 assuming a body coordinate system defined in Figure 3.2. Each sensor's coordinates are expressed as an offset of its feed point relative to that of Antenna 4 in meters in Table 3.2. In this work, Antenna 4 is regarded as the geometric reference of the array coordinate system and the phase reference in the nonparametric calibration described in Chapter 5.

Elevation cuts of the RDS array factors at 195 MHz are plotted in Figure 3.3 for each subarray using the following expression:

$$AF_s(\theta, \theta_0) = \frac{1}{P_s} \sum_{i=1}^{P_s} e^{j\mathbf{r}_i^T[\mathbf{k}(\theta)-\mathbf{k}(\theta_0)]}. \tag{3.1}$$

The argument θ_0 refers to the pointing angle in elevation. Here $s \in \{\text{left, center, right}\}$, hence P_j denotes the number of elements in a subarray of interest. The vector $\mathbf{k}(\theta) \in \mathbb{R}^{2\times 1}$ is the propagation vector and $\mathbf{r}_i \in \mathbb{R}^{2\times 1}$ is the position vector of the i^{th} sensor. The array factors assume the nominal geometry summarized in Table 3.2. The null-to-null width of the center array factor is 35° while the smaller outboard subarrays show a null-to-null beamwidth of 62.5°.

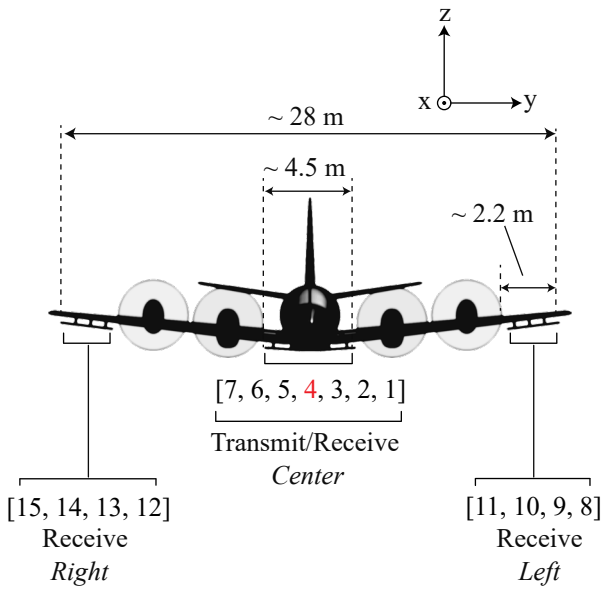

Figure 3.2: RDS P-3 antenna array with numbering convention and approximate subaperture dimensions. The electrical and geometric reference element, Antenna 4, is shown in red. *Left*, *right*, and *center* conventions are defined with respect to the pilot's perspective.

3.1.2 RDS Multibeam Acquisition and Data Sets

The array manifold calibration work carried out for this dissertation leverages data sets collected in a multibeam acquisition mode over minimally penetrative surface targets in the Canadian Arctic Archipelago during NASA's Spring 2014 Operation IceBridge Campaign. In multibeam mode, illustrated in Figure 3.4, the RDS multiplexes elevation-steered transmit beams in slow time from pulse-to-pulse. Figure 3.4 shows illuminated footprints projected onto a flat interface for three beams, generically denoted in the illustration as *left*, *right*, and *center* where the convention of each is defined relative to the pilot's perspective. The pulse repetition intervals are chosen to satisfy quarter wavelength sampling of each subswath in the along-track dimension. The multibeam collects from this field season are obtained at a higher altitude and use slightly different settings than conventional sounding. The settings specific to this mode are summarized in Table 3.3, along with relevant resolution quantities.

CReSIS organizes radar data by days, segments, and frames. In most cases, segments

Table 3.2: Lever arms assumed in the nominal model, defined with respect to the coordinate system of Figure 3.2.

		Position		
Subarray	*Antenna*	x (meters)	y (meters)	z (meters)
center	1	0	2.2504	0.1194
center	2	0	1.4910	0.0737
center	3	0	0.7722	0.0279
center	4	0	0	0
center	5	0	-0.7722	0.0279
center	6	0	-1.4910	0.0737
center	7	0	-2.2504	0.1194
left	8	-0.0356	13.9497	1.5392
left	9	-0.0356	13.2232	1.4503
left	10	-0.0356	12.4765	1.3589
left	11	-0.0356	11.7399	1.2700
right	12	-0.0356	-11.7399	1.2700
right	13	-0.0356	-12.4765	1.3589
right	14	-0.0356	-13.2232	1.4503
right	15	-0.0356	-13.9497	1.5392

correspond to specific science missions and represent uninterrupted collection over which the radar operates with consistent settings. Segments are broken up into approximately 50 km processing frames, favoring frame boundaries on turns so that aircraft banking artifacts appear at the edges of an image. Frames are then identified with a YYYYMMDD_SS_FFF frame identifier where YYYYMMDD is populated based on the year-month-day, while SS and FFF indicate zero-padded segment and frame numbers respectively.

Figure 3.5 illustrates the Canadian Arctic flight lines associated with the multibeam data sets considered in the dissertation which include 20140325_07, 20140401_03, and

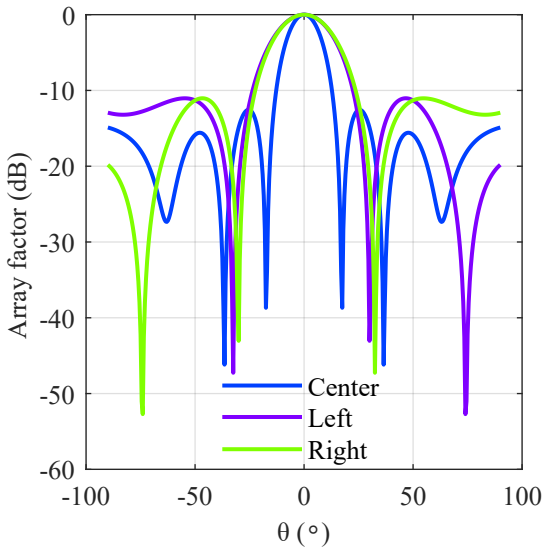

Figure 3.3: Elevation cuts of the RDS P-3 array factors at 195 MHz for the center, left, and right subarrays.

20140506_01 [88]. Manifold corrections are measured from each of these data sets and presented later in Chapter 5. Magnitude and phase corrections are plotted with the same color mapping as that shown in Figure 3.5 for the sake of relating measurements back to these data sets. Note that the three data sets represent data collections from three different days spaced out over the field season and correspond to almost completely non overlapping areas in the Canadian Arctic. The 20140325_07 data set (indicated with the green flight line) is the smallest, containing only four useful frames while the 20140401_03 data set (orange) contributes the largest number of useful frames to calibration but contain radio frequency interference from an onboard navigation system whose emissions coupled into the RDS receivers intermittently during the flight.

On transmit, a Hanning taper is applied across the elements to suppress sidelobes and improve two-way isolation performance. The RDS array factors for the steered transmit beams radiated by the center subarray are evaluated at 195 MHz assuming the nominal sensor positions reported in Table 3.2 and using the following form of the array factor:

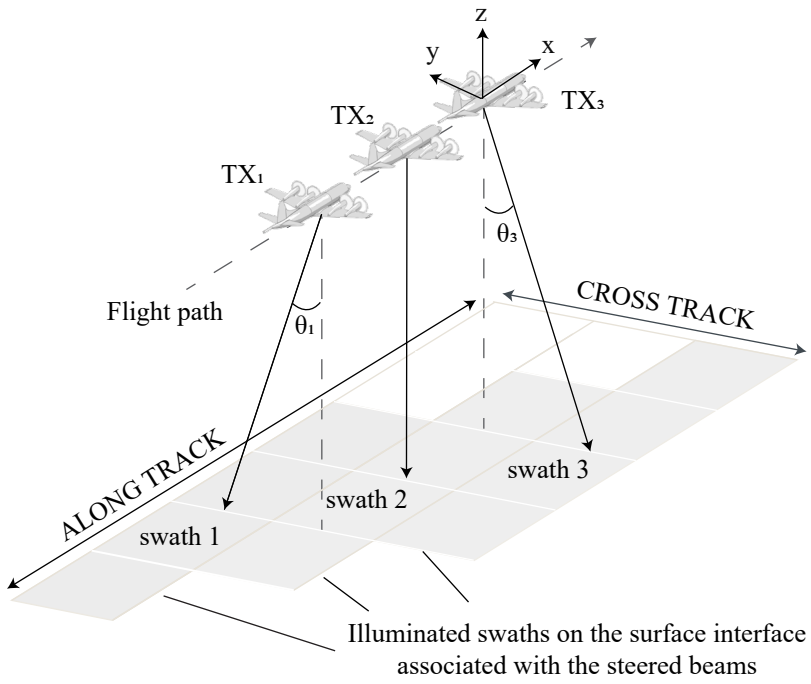

Figure 3.4: Multibeam acquisition showing three consecutive transmit events and corresponding illumination footprints projected onto a flat interface.

Table 3.3: Summary of configuration parameters for the multibeam data sets and resolution quantities.

Variable	*Value*	*Units*	*Parameter*
T_{pd}	3	μs	Pulse duration (swath imaging mode)
PRF	12	kHz	Pulse repetition frequency
θ_0	$[-30, 0, 30]^T$	$^\circ$	TX elevation scan angles
σ_r	~ 6	meters	Slant range resolution, $B = 30$ MHz
σ_x	~ 2.5	meters	Along-track resolution
h	915	meters	Platform height above surface

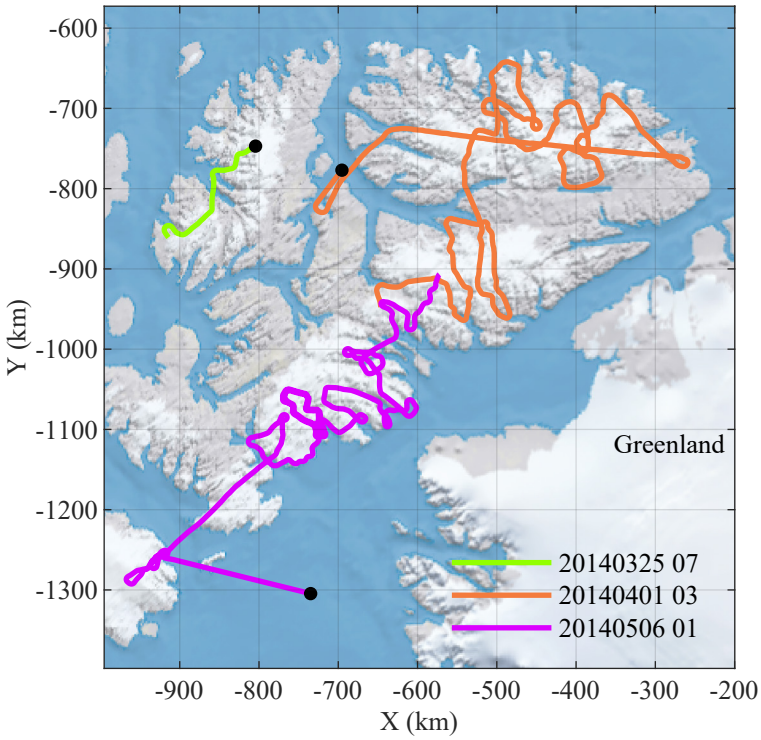

Figure 3.5: 2014 NASA Operation IceBridge flights in the Canadian Arctic Archipelago with RDS multibeam data.

Table 3.4: Frames processed for array calibration.

Day Segment	*Frames*	*Mission*
20140325_07	[2-5]	Axel Heiberg - Eureka
20140401_03	[4-5, 13, 15-16, 34-36, 40-43, 45-46]	North Canada Glaciers
20140506_01	[14-16, 34-36, 40-43, 45, 46]	South Canada Glaciers

$$AF(\theta, \theta_0) = \sum_{i=1}^{P_j} h_i e^{j\mathbf{r}_i^T[\mathbf{k}(\theta)-\mathbf{k}(\theta_0)]}. \tag{3.2}$$

Here h_i is the i^{th} entry of a real valued taper vector $\mathbf{h}$ normalized such that the array factor evaluates to unity at the steering angle θ_0. Array factors assuming uniform and Hanning cross-track illumination tapers are illustrated in Figure 3.6a and Figure 3.6b respectively, showing the broadening of the mainlobe due to the Hanning window.

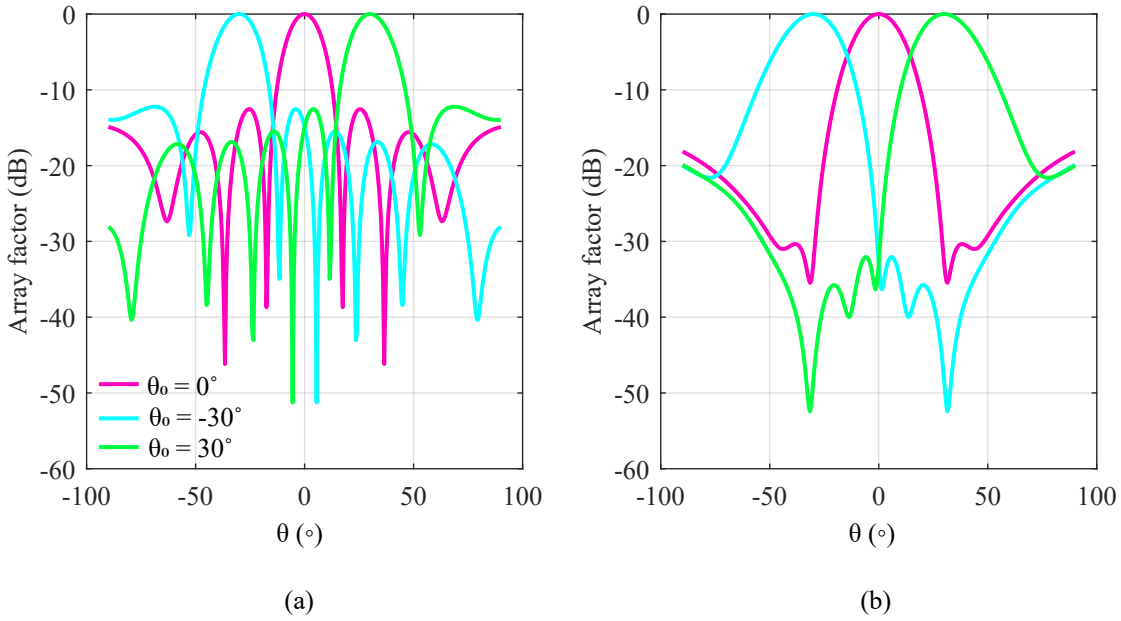

Figure 3.6: Elevation cuts of the RDS P-3 array factors at 195 MHz for the steered transmit beams radiated from the center subarray with (a) uniform taper and (b) Hanning taper.

3.2 Snapshot Database Creation

The summarized dissertation research relies on the creation of snapshot databases containing geocoded observations, tagged with information about the scattering contributions of the measurement. Snapshot database creation is realized through alignment of RDS swaths to two auxiliary data sets in order to identify potential calibration sources in the single look complex SAR imagery. An independent DEM of the surface, when aligned to the SAR coordinate system, provides angles of incidence at the air-to-surface interface for the RDS fast time bins of each synthesized aperture while aligned land classification maps aid in identifying geophysical target types for each directional source. The section that follows describes the auxiliary data sets and processing steps used to assign source DOAs and terrain types in the RDS imagery.

3.2.1 Auxiliary Data Sets

The ArcticDEM project [89], initiated in 2016, is a joint effort between the National Science Foundation and the National Geospatial-Intelligence Agency (NGA) that addresses a broad need for comprehensive, fine-resolution surface elevation models of the Arctic. The ArcticDEM data are derived with stereoscopic processing from optical satellite imagery acquired by the NGA-licensed Digital Globe Satellite Constellation [89] using a surface extraction approach with irregular network-based triangulation described in [90]. Data are available in strip and mosaic tile formats. ArcticDEM strip files contain the overlapping stereopair swaths as collected by the DigitalGlobe constellation along with metadata files describing offsets to filtered ICESat ground control points. Although the strip maps reference ground control points, the strip files are not corrected.

ArcticDEM mosaic files are processed from high quality strip DEMS into blended and feathered 50 km x 50 km tiles, available as 2 m, 10 m, 100 m, 500 m, and 1 km rasters and corrected with filtered ICESat altimetry to improve absolute vertical accuracy. The number of strip files making up a mosaic tile generally ranges from 40 to 60. The metadata accompanying the mosaic tiles specifies a list of input strip map files along with the corresponding vertical and horizontal RMS errors of each strip after ground control. Strip widths and lengths range from 16 to 18 km and 110 to 120 km. The alignment statistics of a single strip which may cover on the order of a 2000 km^2 area of terrain are conveyed with single x, y, z RMS errors. The spatially sparse reporting of mosaic DEM error limits a detailed error propagation analysis of the RDS-derived DEMs produced for this dissertation after calibrating with the ArcticDEM.

The RDS array calibration approach is designed to reject SAR focused pixels containing subsurface scatterers since their locations are unknown. This is achieved with the application of a binary ice mask, aligned to both the ArcticDEM and the RDS trajectory, that indicates the presence or absence of glacial ice. The ice mask is derived from glacier outlines published in a supplementary to the Global Land Ice Measurements from Space (GLIMS) database [91]

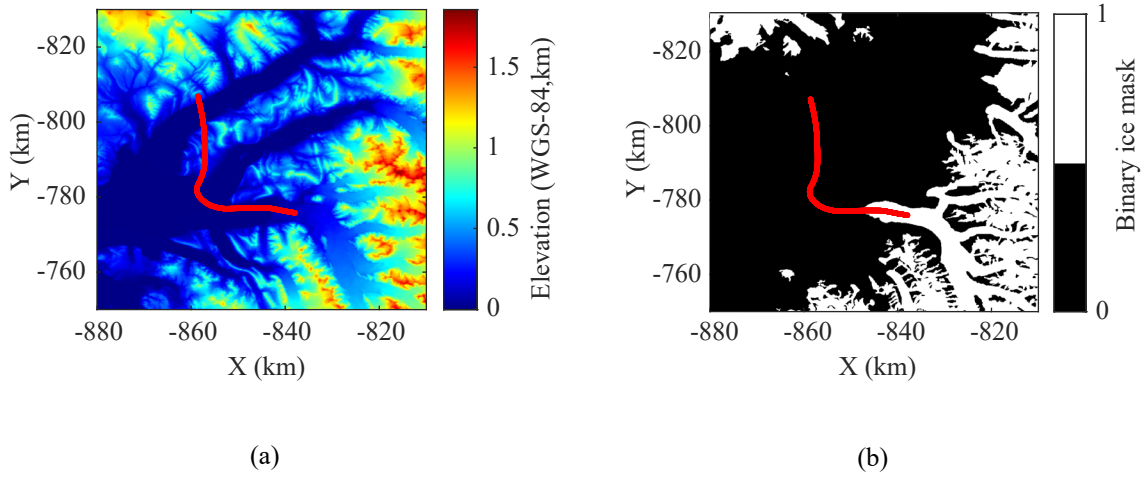

Figure 3.7: Auxiliary data sets used to build a database of calibration pixels, shown aligned to a 2014 IceBridge flight line (red): (a) the ArcticDEM terrain from 10 meter mosaic tiles and (b) binary ice mask.

called the Randolph Glacier Inventory [92]. In the calibration pixel extraction described later, the binary ice mask preserves scatterers from all other extended surface targets including sea ice and rocks.

3.2.2 Signal and Data Processing Tools

Single look complex SAR images are generated with the *f-k* migration algorithm implemented in the CReSIS toolbox for the frames summarized in Table 3.4. Because both freshwater ice surface and subsurface returns are excluded as potential calibration sources, the CReSIS SAR processor is run under a free-space propagation assumption which assigns a relative permittivity field of one in *f-k* migration. All other processing steps preceding the SAR, including coherent noise removal and channel equalization, are unmodified relative to standard processing.

Figure 3.8 outlines some of the custom modifications made to the CReSIS toolbox to enable an array manifold calibration architecture. The modifications hinge on creation of surface data objects that allow pixels to be tagged with the angle of arrival of coincident

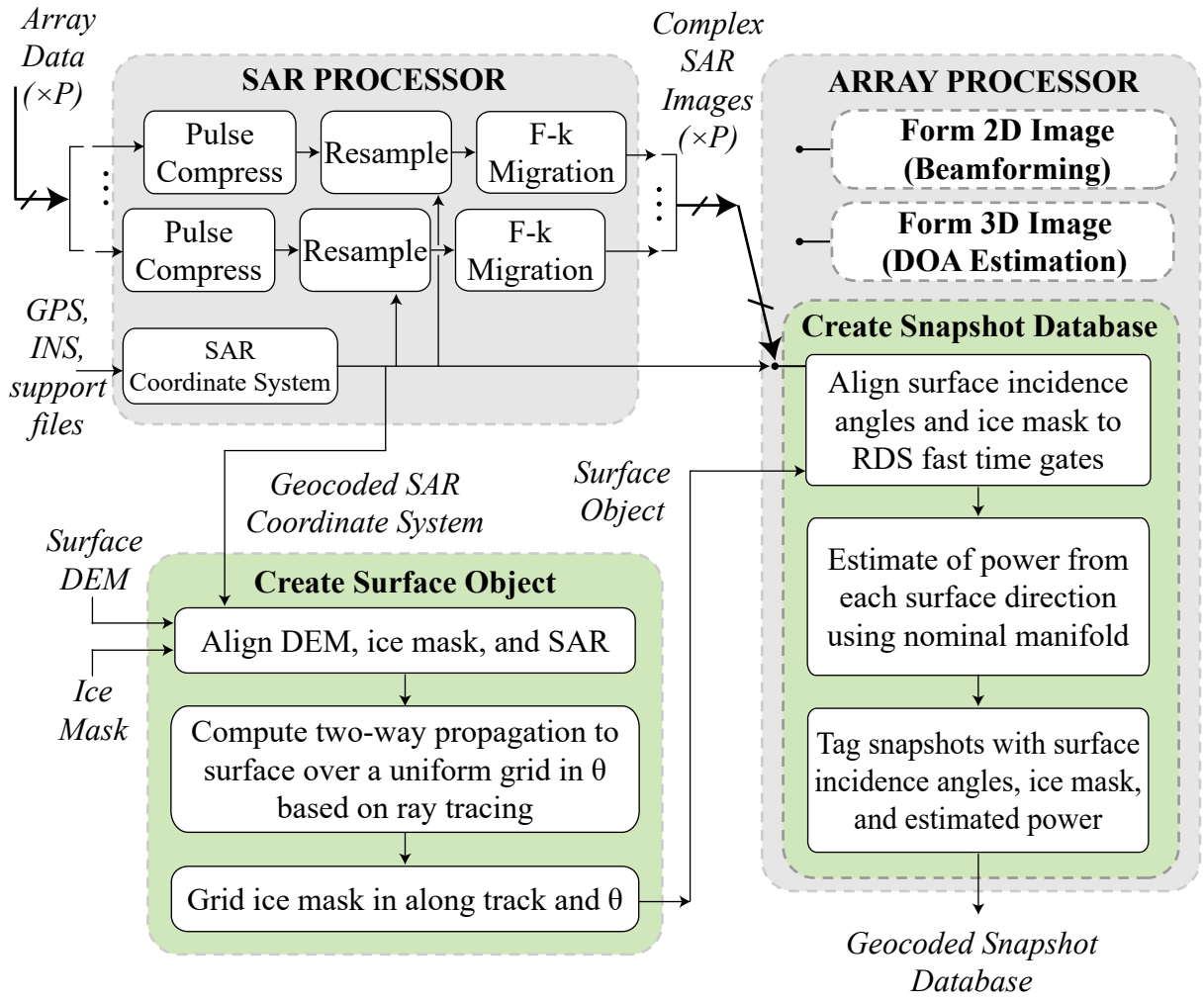

Figure 3.8: New array manifold calibration functionality (green) including surface object and snapshot database creation in the context of the CReSIS signal processing architecture (gray).

scattering interfaces mapped to a propagation delay and along track bin. This step requires the geocoded SAR coordinate system, an independent surface DEM such as the ArcticDEM and a binary ice mask. For each synthesized aperture along the flight path, the two-way propagation delay over a uniform angle grid to the first intersection of a given ray is determined and the ice mask is queried at the intersection point. Surface objects are stored as time delays to the intersection points along rays that are uniformly gridded in along track and angle.

The surface data objects, multichannel SAR imagery, and geocoded SAR coordinate

system are passed to the array processor which is modified to support creation of large snapshot databases. The snapshot database creation aligns the surface data objects to the RDS time gates. This stage outputs geocoded snapshots that are tagged with incidence angle at the surface and the ice mask value of each intersection. Note that an ice mask indication and angle are determined for each coincident scattering interface of a pixel meaning that the snapshot database also assigns number of sources or Q for each pixel in the imagery.

3.3 Preliminary Validation of Methodology with Beamforming Test

The approach outlined in this chapter proposes characterizing the directional response of the RDS by coregistering multichannel single look complex SAR imagery with an independent, fine resolution DEM and extracting calibration measurements from spatial sources with known directions of arrival. The study in [54] documents the earliest validation of the approach, carried out by creating a coarse database of directional sources with a pilot version of the framework in Figure 3.8. The study relies on geometrically steering nulls with the uncalibrated array in an effort to estimate power in a direction of interest. The ratio of directional source powers are used to tag each pixel with an approximate measurement of isolation. Pixels containing sources that exhibit at least 15 dB isolation are regarded as suitable approximations of single-source measurements that may be used to form a steering vector lookup table.

One of the drawbacks of this method for pulling out single source pixels is that it relies on steering a null prior to manifold calibration in order to compute a culling metric. Null steering accuracy depends on our steering vector knowledge and implies some knowledge of the array response vectors prior to calibration. We expect that a culling criterion derived from this SINR measure to correctly identify approximately single source observations in a direction of interest when the array response in the interference direction is known extremely well. But if this were the case over all θ, then the manifold would already be calibrated. It stands to reason that this approach will not work well over all possible angles. The

limitations of the methodology outlined in [54] motivate a more robust metric for culling single source observations in a particular angle bin. A refined approach is developed for this dissertation, outlined in Chapter 5, and is the subject of the study documented in [53].

Despite being processed with a lookup table derived from this initial culling technique, the results that helped to confirm a need for array calibration are presented here to document this milestone along the dissertation trajectory. A study of sea ice sidelobe clutter suppression in nonadaptive beamforming provides initial verification of mismatch between the isotropic model described in Equation 2.35 and truth. Echograms are produced using the nonadaptive geometric nulling beamformer (sometimes referred to as *geonull* beamformer) described in Chapter 2 (Equation 2.18) with isotropic and measured manifolds; weights are chosen to steer the main beam to nadir and nulls in the direction of scattering from the surface, determined by the surface data objects derived from the ArcticDEM. These images are compared to both geonull images created assuming the isotropic steering vector model as well as images formed with the standard combining method. The *ideal* or *nominal* manifold vector takes the isotropic form of Equation 2.35. All results assume free-space propagation ($\varepsilon_r = 1$) when evaluating the wavenumber in the array processor and clutter-rejection performance assessment is restricted to portions of the image that do not contain scattering from a subsurface.

Table 3.5: Measured relative sidelobe clutter at specified cumulative probabilities by beamforming method.

	x (dB)		
$F(x)$	*Geonull Measured*	*Geonull Nominal*	*Standard*
0.25	-161	-156	-153
0.50	-156	-150	-147
0.75	-148	-142	-139
0.95	-131	-127	-124

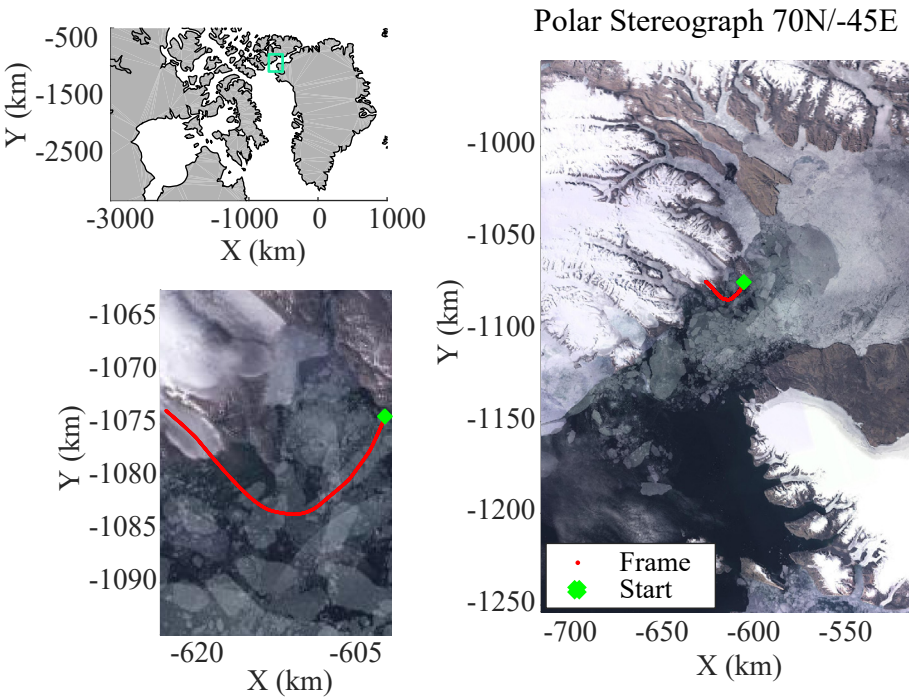

(a)

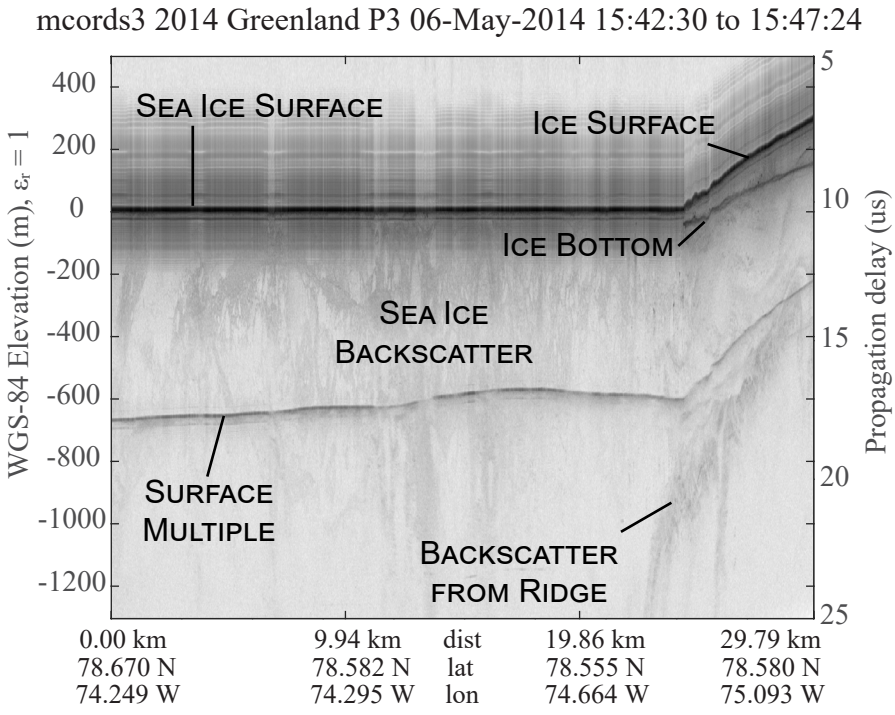

(b)

Figure 3.9: Frame for validating manifold mismatch: (a) map and (b) echogram $\theta_{TX} = 0°$.

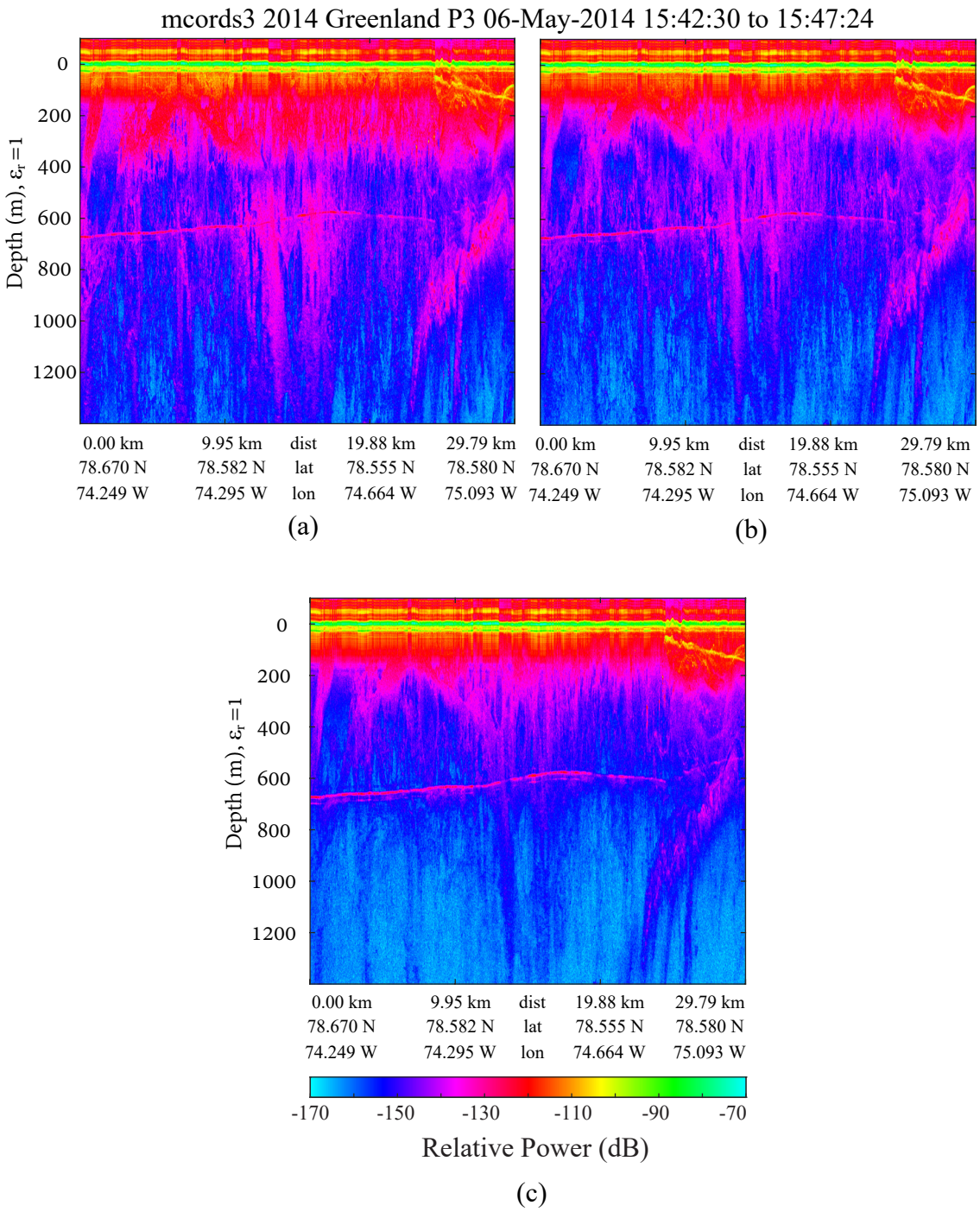

Figure 3.10: Nonadaptive clutter suppression with sidelooking illumination and geometric nulling applied to data from the $\theta_{TX} = 30°$ beam: (a) standard beamforming, (b) geometric nulling with isotropic manifold and (c) geometric nulling with measured manifold.

The following examples demonstrate improved sidelobe clutter suppression of the geonull beamformer with a measured manifold model using data collected over a 25 km extent

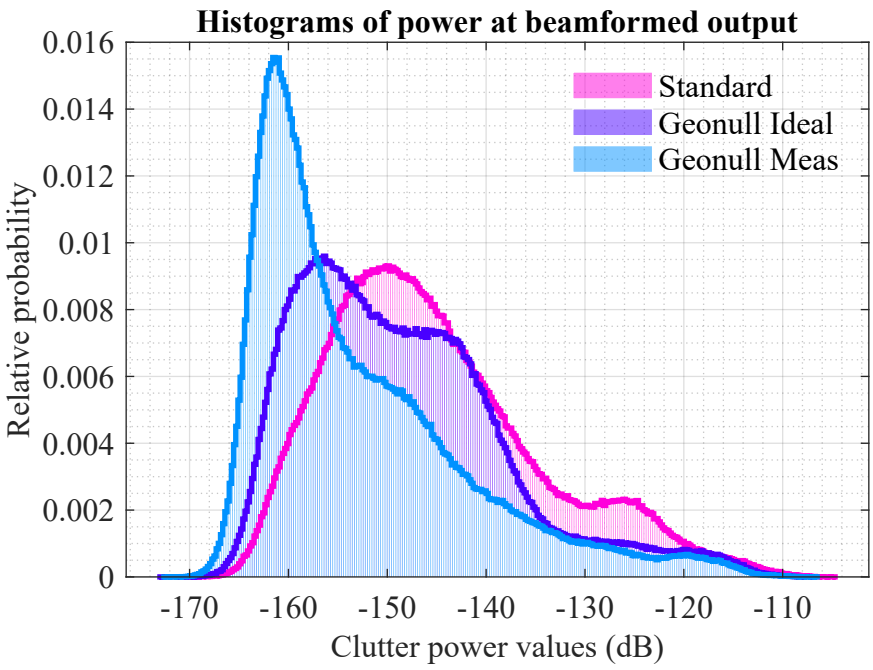

(a)

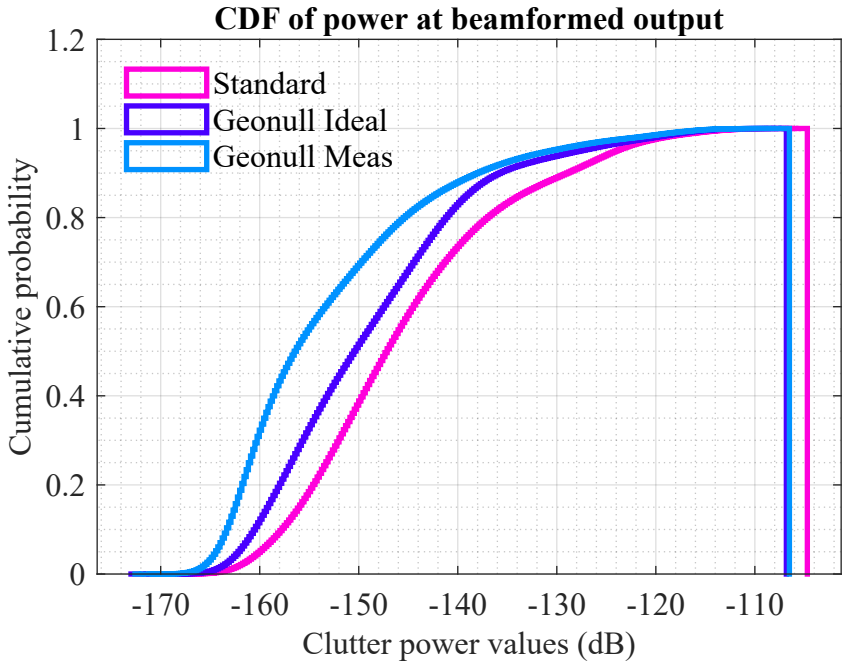

(b)

Figure 3.11: Sidelobe clutter suppression study to justify refined manifold calibration: Histogram (a) and Cumulative Distribution Function (b) views of output powers of standard beamformer, geometric null-steering beamformer with isotropic manifold and geometric null-steering beamformer with measured manifold.

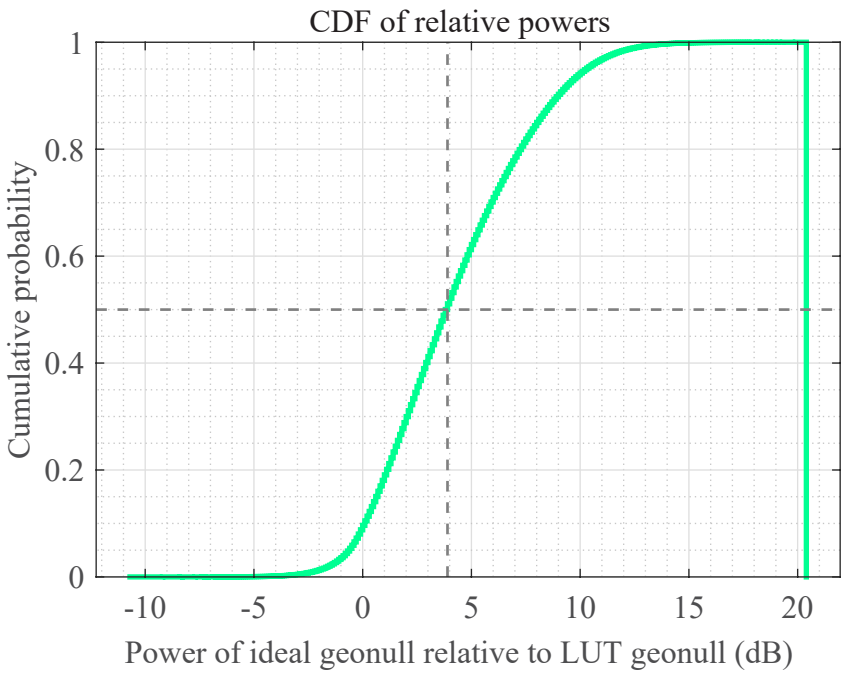

Figure 3.12: CDF of sidelobe clutterpower in geonull with isotropic manifold relative to sidelobe clutter power in geonull with measured manifold.

(approximately) of sea ice from May 6, 2014 in the Canadian Archipelago in swath-imaging mode. Figure 3.9a shows the flight line with the green point indicating the start of the frame. Over the frame, the aircraft banks into a turn before leveling off as it flies over a floating tongue of freshwater ice. Figure 3.9b shows the corresponding echogram from the $\theta_{TX} = 0°$ transmit beam and combined with the standard weights which form a digital beam directed at nadir. The range gates are shown as heights measured with respect to the WGS-84 ellipsoid. The sea ice surface return appears at zero (sea level) and the sidelobes from the surface response dominate the image for approximately 200 meters. With the exception of the surface multiple, the later range gates are dominated by off-nadir clutter from the sea ice until the aircraft flies over the tongue and we see a ridge from exposed rock off to the side of the track as well as the basal echo of the freshwater ice mass.

Clutter rejection is studied using imagery from a sidelooking transmit beam. Figure 3.10 compares the standard combining method in Figure 3.10a to geonull images formed with an isotropic manifold model and measured manifold model in Figures 3.10b and 3.10b)

and measured steering vectors (Figure 3.10) for the transmit beam pointed to the left of the track ($\theta_{TX} = 30°$). The images are shown using an HSV colormap on a common scale. These images are presented as a depth relative to the surface which has the effect of flattening the surface in the imagery. The standard image is formed by pointing a digital beam to nadir. The geonull images result from pointing nulls at the surface clutter angles to the left and right sides of the track while pointing a beam towards nadir. The images show a progressive attenuation of surface clutter from the standard to ideal geonull and ideal geonull to the measured manifold geonull.

Clutter power values in the combined images are plotted as histograms and cumulative probabilites by beamforming method. This type of data visualization, shown in Figure 3.11a and Figure 3.11b, provides a quantitative means for comparing clutter rejection in the results. Provided that we have good knowledge of the surface clutter DOAs a priori, we expect nulling to improve clutter rejection in the combined image over the standard beamforming method. Hence we expect a global decrease in the power of pixels containing scattering from the surface. We also expect larger clutter rejection when using the measured manifold to null sidelobe clutter over the nulling performance with ideal steering vectors. Sidelobe clutter pixels are extracted by first only taking pixels containing sea ice backscatter from range gates of 200 meters or greater. The range gates lying in a small neighborhood around the surface multiple are also removed from the data set to ensure that only sidelobe targets are assessed.

The histograms of the sidelobe clutter power by beamforming method are presented in Figure 3.11a. The y axis denotes frequency of the binned values, given by a ratio of the number of values in a bin to the total number of values. The normalization ensures that the sum of the bin heights is equal to one. This result shows how the geometric null-steering beamformer with the isotropic manifold model concentrates power to lower values relative to the standard result. The null-steering beamformer with the measured manifold concentrates sidelobe clutter to a lower power (relative to the standard result) of approximately -162 dB.

The cumulative distribution functions (CDFs) in Figure 3.11b provide an alternative illustration of the global reduction of power by beamforming method. In the CDFs we see a negative translation along the clutter power axis by beamforming method. As postulated, geonull beamforming with a measured manifold provides the largest attenuation of sidelobe clutter relative to the standard beamformer. Clutter powers are stated at four specified cumulative probabilities in Table 3.5. The CDFs show that 95% of the clutter pixels are less than -131 dB in the LUT-based geonull image. In the ideal geonull result, 95% of the pixels are less than -128 dB. This result indicates that the measured manifold has the potential to recover at least 3 to 4 dB of sensitivity in areas with off-nadir clutter from the surface and may have important implications for sounding challenging areas where basal echo detection is impeded by clutter returns from a crevassed surface.

3.4 Discussion

This chapter outlines critical methodology that enables the manifold calibration work carried out for the dissertation research. Design details are described for the specific ice depth sounding SAR instrumentation and data sets used in applying manifold calibration techniques to real data. The research thus far has been limited to a set of RDS measurements collected from the P-3 aircraft in a multibeam configuration during a 2014 field season on three separate days in the Canadian Arctic Archipelago. The flight lines show almost no geographic overlap and offer three independent sets for testing calibration. The application to real data (presented in Chapter 7) is limited to imagery from the inboard subarray; the techniques have not yet been tested on the wing-mounted subarrays which are subject to distinct slow-time dependent error mechanisms due to vibration, wing flexure, propeller modulation, and changing multipath environments presented by the aircraft's reflective control surfaces that move throughout flight.

The ArcticDEM provides a means to coregister the RDS imagery to an independent 3-D surface model. This model is queried to determine surface intersection angles in the

fast-time gates of the multichannel single look complex SAR images in the creation of a geocoded snapshot database. In manifold calibration, the database becomes the mechanism for harvesting calibration targets at known arrival angles from the RDS SAR focused outputs. Thus far, only pixels with one or two sources are considered in calibration. Pixels containing contributions from three or more sources in elevation are not considered in this work. The database created for this dissertation coregisters the RDS using the ArcticDEM gridded on a 10 meter raster. Results have not been recreated to date with the finer 2 meter gridded spacing to determine if this product improves manifold calibration. It is expected that the model with 2 meter grid spacing would potentially improve the accuracy of a measured manifold and justifies an informal test in practical application of the proposed methodology. We expect the manifold calibration routine developed for this research to improve with the application of additional ground control using the onboard Airborne Topographic Mapper (ATM) lidar instrument flown as part of Operation IceBridge. It is recommended that the surface object creation be modified to read in ArcticDEM metadata when possible and store reported uncertainties of a tile after ground control. This would enable snapshots to be tagged with a notional quality based on the ArcticDEM tile level error and may aide in interpreting calibration performance after generation of RDS-derived DEMs.

3.5 Conclusion

This chapter summarizes the general array manifold calibration methodology carried throughout the dissertation research and provides engineering detail of the specific instrumentation and data sets studied in algorithm development. The snapshot database creation is described as the data processing strategy which enables identification of potential calibration sources in the SAR imagery. The required auxiliary data sets for database creation are specified and include an independent model of the surface and land classification data that align to the RDS swath. Two dimensional beamforming images are presented that serve as initial verification of the snapshot database methodology and confirm mismatch between our nominal

array response model and truth.

Chapter 4

Parametric Manifold Calibration Framework with Spatially Diverse Calibration Sets

Abstract

Traditional methods for measuring *single* directional sources with multichannel SAR sounders rely on capturing specular returns from smooth and flat extended surface targets with a maneuvering aircraft on dedicated calibration flights. These methods are subject to roll restrictions of the host platform and mandate crossover lines to measure unknown terrain slope. Many historic data sets lack measurements from allocated flights needed to characterize the array and motivates the need for alternative signal processing solutions capable of calibrating the array when the number of scattering interfaces exceeds one. Parametric manifold calibration handles multiple targets simultaneously, provided a model of the array's directional transfer function is known. This chapter proposes a parametric manifold calibration framework for SAR sounders whose manifolds may be described analytically with functional dependence on a nonlinear parameter set. A maximum likelihood estimator for deterministic and unknown nonlinear manifold parameters common across disjoint observation sets of spatially diverse sources is derived by casting an estimation problem in a separable Gaussian form composed of many smaller separable Gaussian estimation problems. The derivation is developed for the use case of systematic geometric phase center position errors but the approach generalizes to any arbitrary nonlinear manifold parameters that are constant with respect to the SAR. The technique is numerically demonstrated in simulation

by exercising the estimator with array shape calibration problems. Examples are presented that illustrate the role of calibration source spatial diversity in improving angle estimation performance when the manifold functionally depends on angle of arrival and a set of nonlinear parameters.

4.1 Observation Model Adopted for Parametric Calibration

An array of P sensors oriented in a two-dimensional plane and characterized by geometric uncertainties is used to collect many snapshots in a stationary signal environment where the arrival angles of the far field sources are fixed throughout the collection. We refer to the subset of snapshots as a calibration bin which is characterized by some arbitrary number of sources and snapshots. Suppose the array geometry is offset from a nominal model of the sensor positions and we wish to estimates these geometric offsets. We treat the geometric uncertainties as nonlinear parameters of the manifold which are common to all calibration sets while other parameters are not necessarily similar between observation sets.

Let $\boldsymbol{\eta}_{\mathbf{r}}$ denote the real-valued parameter vector comprised of geometric uncertainties that we wish to estimate from a collection of N_b subsets. Let M_j denote the number of snapshots in the j^{th} subset where $1 \leq j \leq N_b$, with N_b denoting the total set of calibration bins. The subsets are disjoint in time and we assume that the source DOAs of each subset are generally distinct so that as we collect calibration bins, we are able to increase the Fisher information in the accumulated subsets. Note that *bin* is used to refer to a subset of calibration data. Each bin is characterized by some number of sources, Q_j, which we require to be non-zero and less than the number of sensors so that our system of equations is overdetermined.

The narrowband model of the array data in the j^{th} calibration bin is stated as:

$$\mathbf{x}_j(t_{m_j}) = \sum_{q_j=1}^{Q_j} \mathbf{a}(\theta_{q_j}, \boldsymbol{\eta}_{\mathbf{r}}) s_{q_j}(t_m) + \mathbf{n}_j(t_{m_j}) = \mathbf{A}(\boldsymbol{\eta}_j^{nl})\mathbf{s}_j(t_{m_j}) + \mathbf{n}_j(t_{m_j}), \tag{4.1a}$$

$$\mathbf{A}(\boldsymbol{\eta}_j^{nl}) = \left[\mathbf{a}_1(\boldsymbol{\eta}_j^{nl}) \ldots \mathbf{a}_{Q_j}(\boldsymbol{\eta}_j^{nl})\right], \tag{4.1b}$$

$$\mathbf{a}_{q_j}(\boldsymbol{\eta}_j^{nl}) = \left[a_1(\theta_{q_j}) e^{-j\mathbf{k}^T(\theta_{q_j})\mathbf{r}_1(\boldsymbol{\eta}_{\mathbf{r}_1})}, \ldots, a_P(\theta_{q_j}) e^{-j\mathbf{k}^T(\theta_{q_j})\mathbf{r}_P(\boldsymbol{\eta}_{\mathbf{r}_P})} \right]^T, \tag{4.1c}$$

$$\mathbf{s}_j(t_{m_j}) = \left[s_{1_i}(t_{m_j}), \ldots, s_{Q_j}(t_{m_j}) \right]^T, \tag{4.1d}$$

$$\mathbf{n}_j(t_{m_j}) = \left[n_1(t_{m_j}), \ldots, n_P(t_{m_j}) \right]^T. \tag{4.1e}$$

The parameter vector that contains the nonlinear parameters of the manifold in the j^{th} set of calibration data which includes the geometric perturbations on the elements and the vector of arrival angles (when taken to be unknown) is:

$$\boldsymbol{\eta}_j^{nl} = \left[\boldsymbol{\Theta}_j^T, \quad \boldsymbol{\eta}_{\mathbf{r}}^T \right]^T \tag{4.2}$$

Where $\boldsymbol{\Theta}_j \in \mathbb{R}^{Q_j \times 1}$ contains the Q_j arrival angles in the j^{th} set of snapshots. The vector $\boldsymbol{\eta}_{\mathbf{r}} \in \mathbb{R}^{2P \times 1}$ contains the geometric uncertainties of each sensor in each dimension

$$\boldsymbol{\eta}_{\mathbf{r}} = \left[\boldsymbol{\eta}_{\mathbf{r}_1}^T, \quad \ldots, \quad \boldsymbol{\eta}_{\mathbf{r}_P}^T \right]^T. \tag{4.3}$$

The two-element vector $\boldsymbol{\eta}_{\mathbf{r}_p}$ contains the geometric uncertainties of sensor p in the y-z plane

$$\boldsymbol{\eta}_{\mathbf{r}_p} = \left[\Delta y_p, \Delta z_p \right]^T, \tag{4.4}$$

So that the notation $\mathbf{r}_p(\boldsymbol{\eta}_{\mathbf{r}_p})$ represents a true position of sensor p, determined by the nominal position (which we know from a lidar survey and CAD description of the array) plus geometric offsets in each dimension

$$\mathbf{r}_p(\boldsymbol{\eta}_{\mathbf{r}_p}) = \mathbf{r}_p^0 + \boldsymbol{\eta}_{\mathbf{r}_p}. \tag{4.5}$$

The matrix of M_j snapshots for bin j is written as

$$\mathbf{X}_j = \mathbf{A}(\boldsymbol{\eta}_j^{nl})\mathbf{S}_j + \mathbf{N}_j, \tag{4.6a}$$

$$\mathbf{A}(\boldsymbol{\eta}_j^{nl}) \in \mathbb{C}^{P\times Q_i} = \left\{\mathbf{a}(\theta_{q_j}, \boldsymbol{\eta}_\mathbf{r}), \quad 1 \le q_i \le Q_j\right\}, \tag{4.6b}$$

$$\mathbf{S}_j \in \mathbb{C}^{Q_j\times M_j} = \left\{\mathbf{s}_j(t_{m_j}), \quad 1 \le m_j \le M_j\right\}, \tag{4.6c}$$

$$\mathbf{N}_j \in \mathbb{C}^{P\times M_j} = \left\{\mathbf{n}_j(t_{m_j}), \quad 1 \le m_j \le M_j\right\}. \tag{4.6d}$$

Finally we state a set of assumptions that we require for each set of snapshots here.

A1 : The linear model is overdetermined, hence $Q_j < P \quad \forall \quad 1 \le j \le N_b$.

A2 : The columns of $\mathbf{A}(\boldsymbol{\eta}_j^{nl})$ are linearly independent.

A4 : The noise process $\mathbf{N}_j$ is an ergodic and stationary complex Gaussian random process of zero mean and covariance $\sigma_{n_j}^2\mathcal{I}_P$.

A5 : Within a bin, each snapshot contains complex Gaussian observation noise. The noise snapshots contain IID complex Gaussian random variables such that $\mathbf{n}_j(t_{m_j}) \sim \mathcal{C}(\mathbf{0}, \mathbf{R}_{\mathbf{n}_j})$. We assume that $\mathbf{R}_{\mathbf{n}_j} = E\left\{\mathbf{n}_j\mathbf{n}_j^H\right\} = \sigma_{n_j}^2 I_P$.

A6 : Noise snapshots are statistically independent, $p(\mathbf{n}_j(t_{m_i}), \mathbf{n}_j(t_{m_j})) = p(\mathbf{n}_j(t_{m_i}))p(\mathbf{n}_j(t_{m_j}))$.

A7 : The measurements between calibration sets are statistically independent, $p(\mathbf{X}_i, \mathbf{X}_j) = p(\mathbf{X}_i)p(\mathbf{X}_j)$.

A8 : Sources are treated as deterministic but unknown.

A9 : The number of sources in the j^{th} bin, Q_j, is known.

A10 : Geometric uncertainties are modeled as deterministic but unknown.

As the problem is formulated, we treat sensor position uncertainties and DOAs as the nonlinear parameters of the manifold but the solution generalizes to any nonlinear parameters upon which the mean of an array snapshot functionally depends in a nonlinear way.

4.2 Derivation of an Estimator of Nonlinear Manifold Parameters

We introduce the following lemma to support the derivation of the nonlinear parameters of the manifold:

Lemma 4.2.1. *Let* $\mathbf{x}$ *be a multivariate complex Gaussian observation vector distributed as* $\mathbf{x} \sim \mathcal{C}\left(\mathbf{A}(\boldsymbol{\gamma}_{nl})\boldsymbol{\gamma}_l, \mathbf{R}_{\mathbf{n}}\right)$*, where* $\boldsymbol{\gamma}_{nl}$ *and* $\boldsymbol{\gamma}_l$ *denote the deterministic and unknown real nonlinear and linear parameters of the mean. The maximum likelihood estimator of the nonlinear parameter vector* $\boldsymbol{\gamma}_{nl}$ *is one that maximizes the following compressed likelihood function*

$$L(\boldsymbol{\gamma}_{nl}) = tr\Big(\mathbf{P}_{\mathbf{A}(\boldsymbol{\gamma}_{nl})}\mathbf{R}_{\mathbf{x}}\Big) \tag{4.7}$$

Where

$$\mathbf{P}_{\mathbf{A}(\boldsymbol{\gamma}_{nl})} = \mathbf{A}(\boldsymbol{\gamma}_{nl})\left(\mathbf{A}(\boldsymbol{\gamma}_{nl})^H\mathbf{A}(\boldsymbol{\gamma}_{nl})\right)^{-1}\mathbf{A}(\boldsymbol{\gamma}_{nl})^H,$$
$$\mathbf{R}_{\mathbf{x}} = E\left\{\mathbf{x}\mathbf{x}^H\right\}.$$

Lemma 4.2.1 results from the formulation of the problem under separable Gaussian estimation theory [68] which was introduced in Chapter 2. Lemma 4.2.1, which was proven in Appendix B inadvertently through the derivation of the DOA MLE, is a powerful fact that asserts that a maximum likelihood estimator of any arbitrary, nonlinear parameters of the observation mean can always be determined by maximizing the form in 4.7. We generalize this fact to the array manifold calibration problem with the following corollary.

Corollary 4.2.1.1. *Let* $\mathbf{x}$ *denote a snapshot of deterministic and unknown directional sources described as a linear combination of manifold vectors in observation noise:* $\mathbf{x} = \mathbf{A}(\boldsymbol{\Theta}, \boldsymbol{\eta}_{nl})\mathbf{s} + \mathbf{n}$*. Assuming a separable Gaussian formulation, then* $\mathbf{x} \sim \mathcal{C}\left(\mathbf{A}(\boldsymbol{\Theta}, \boldsymbol{\eta}_{nl})\mathbf{s}, \mathbf{R}_{\mathbf{n}}\right)$*. If* $\boldsymbol{\eta}_{nl}$ *represents nonlinear and nonrandom parameters of the manifold, then a maximum likelihood*

estimator of this parameter vector is obtained by maximization of the compressed likelihood:

$$L(\boldsymbol{\Theta}, \boldsymbol{\eta}_{nl}) = tr\Big(\mathbf{P}_{\mathbf{A}(\boldsymbol{\Theta},\boldsymbol{\eta}_{nl})}\mathbf{R}_{\mathbf{x}}\Big). \tag{4.8}$$

We now state the following theorem which contends that the nonlinear parameters can be estimated from disjoint sets of observations provided that the parameters are common to all sets and the sets are statistically independent. The resultant estimator is one that maximizes over a sum of compressed likelihoods where the compressed likelihood of a given set is as defined in Lemma 4.2.1.

Theorem 4.2.2. *Suppose we have N_b disjoint calibration bins. Let $\mathbf{X}_j$ denote the snapshot set of the j^{th} bin which we treat as having a separable Gaussian form $\mathbf{X}_j \sim \mathcal{C}(\mathbf{A}_j(\boldsymbol{\eta}_{nl})\mathbf{S}_j, \mathbf{R}_{\mathbf{n}_j})$. Here $\mathbf{A}_j(\boldsymbol{\eta}_{nl}) = \mathbf{A}(\boldsymbol{\Theta}_j, \boldsymbol{\eta}_{nl})$. Assuming statistical independence across the bins, the maximum likelihood estimate of the common nonlinear parameter vector is the solution which maximizes the sum of the compressed likelihoods of each bin:*

$$\hat{\boldsymbol{\eta}}_{nl} = \max_{\boldsymbol{\eta}_{nl}} \left\{ \sum_{j=1}^{N_b} L_j(\boldsymbol{\Theta}_j, \boldsymbol{\eta}_{nl}) \right\}$$

Proof. We seek a likelihood function $L_T(\boldsymbol{\eta}_T; \mathbf{X}_T)$ which we may maximize to obtain an estimator for the nonlinear parameters of the manifold that are common across calibration bins. The approach recognizes that the total set of calibration measurements (obtained by aggregating N_b bins) can be decomposed into N_b separable Gaussian estimation problems. The distribution of a snapshot in the j^{th} bin is described as $\mathbf{x}_j \sim C(\mathbf{A}(\boldsymbol{\eta}_j^{nl})\mathbf{s}_j, \mathbf{R}_{\mathbf{n}_j})$. The vector $\boldsymbol{\eta}_j^{nl} = [\boldsymbol{\Theta}_j, \boldsymbol{\eta}_{\mathbf{r}}]^T$ contains the nonlinear parameters of the snapshot mean in bin j.

Because the observations admit a separable Gaussian form, we can always derive a compressed likelihood function that provides a maximum likelihood estimate of the nonlinear parameters [68]. This procedure was detailed in Appendix B.2.3 when deriving the MLE of the DOA. The steps include finding the MLE of the noise variance and substituting that

estimator into the likelihood function to eliminate the unknown noise power, σ_n^2. Then the MLE of the source waveform is found to be the pseudoinverse of the observations. This solution is back-substituted into the likelihood function to obtain the compressed form which solves for the nonlinear parameters of the manifold.

The compressed likelihood of the j^{th} set is written as

$$L_j(\boldsymbol{\eta}_j; \mathbf{X}_j) = -\sum_{m_i=1}^{M_j} \left\| \mathbf{P}^{\perp}_{\mathbf{A}(\boldsymbol{\eta}_j^{nl})} \mathbf{x}_j(t_{m_i}) \right\|^2 \tag{4.9}$$

Where $\mathbf{P}^{\perp}_{\mathbf{A}(\boldsymbol{\eta}_j^{nl})}$ is the $P \times P$ perpendicular projection which projects a vector to a subspace that is orthogonal to the subspace spanned by the columns of $\mathbf{A}(\boldsymbol{\eta}_j^{nl})$. The projection matrix and its orthogonal projector are defined as

$$\mathbf{P}_{\mathbf{A}(\boldsymbol{\eta}_j^{nl})} = \mathbf{A}(\boldsymbol{\eta}_j^{nl}) \left(\mathbf{A}^H(\boldsymbol{\eta}_j^{nl}) \mathbf{A}(\boldsymbol{\eta}_j^{nl}) \right)^{-1} \mathbf{A}^H(\boldsymbol{\eta}_j^{nl}), \tag{4.10a}$$

$$\mathbf{P}^{\perp}_{\mathbf{A}(\boldsymbol{\eta}_j^{nl})} = \mathcal{I}_P - \mathbf{P}_{\mathbf{A}(\boldsymbol{\eta}_j^{nl})}. \tag{4.10b}$$

The ML estimate of the nonlinear parameters in the j^{th} set of measurements is the solution to the following multidimensional optimization

$$\hat{\boldsymbol{\eta}}_j^{nl} = \min_{\boldsymbol{\eta}_j} \left\{ \sum_{m_i=1}^{M_j} \left\| \mathbf{P}^{\perp}_{\mathbf{A}(\boldsymbol{\eta}_j^{nl})} \mathbf{x}_j(t_{m_i}) \right\|^2 \right\}. \tag{4.11}$$

Hence the MLE of the nonlinear parameter vector is the solution which minimizes the energy in the orthogonal subspace. In Appendix B.2.3, we showed that the form in Equation 4.11 can be written as a maximization of the trace of the projected covariance matrix:

$$\hat{\boldsymbol{\eta}}_j^{nl} = \max_{\boldsymbol{\eta}_j^{nl}} \left\{ \mathrm{tr} \left(\mathbf{P}_{\mathbf{A}(\boldsymbol{\eta}_j^{nl})} \mathbf{R}_{\mathbf{x}_j} \right) \right\}. \tag{4.12}$$

This form is consistent with the assertion of Lemma 4.2.1. To define an estimator which uses information from multiple measurement sets, we first define an aggregated parameter

vector $\boldsymbol{\eta}_T$. Based on the problem formulation, we treat $\boldsymbol{\eta}_{\mathbf{r}}$ as being a common parameter vector among all of the sets and define a total parameter vector as

$$\boldsymbol{\eta}_T = \left[\boldsymbol{\eta}_{\mathbf{r}}^T, \quad \boldsymbol{\Theta}_1^T, \ldots, \boldsymbol{\Theta}_{N_b}^T, \quad \mathbf{s}_{11}, \ldots, \mathbf{s}_{1Q_1}, \quad \ldots \quad \mathbf{s}_{N_b 1}, \ldots, \mathbf{s}_{N_b Q_{N_b}}, \quad \sigma_{n_1}^2, \quad \ldots \quad , \sigma_{n_{N_b}}^2\right]^T.$$

The vector $\mathbf{s}_{ij} \in \mathbb{C}^{1\times M_j}$ denotes the discrete representation of the i^{th} source in the j^{th} bin and corresponds to the i^{th} row of $\mathbf{S}_j$. The density function of the aggregated calibration bins is the joint density of all of the observations parameterized by $\boldsymbol{\eta}_T$ and written as $p(\mathbf{X}_1, \ldots, \mathbf{X}_{N_b}; \boldsymbol{\eta}_T)$. Under an assumption of statistical independence between the noise snapshots within and between calibration bins, we write the parameterized density as the following product

$$\begin{aligned} & p(\mathbf{X}_1, \ldots, \mathbf{X}_{N_b}; \boldsymbol{\eta}_T) \\ & \quad = p(\mathbf{X}_1; \boldsymbol{\eta}_{\mathbf{r}}, \boldsymbol{\Theta}_1, \mathbf{S}_1, \sigma_{n_1}^2) p(\mathbf{X}_2; \boldsymbol{\eta}_{\mathbf{r}}, \boldsymbol{\Theta}_2, \mathbf{S}_2, \sigma_{n_2}^2) \ldots p(\mathbf{X}_{N_b}; \boldsymbol{\eta}_{\mathbf{r}}, \boldsymbol{\Theta}_{N_b}, \mathbf{S}_{N_b}, \sigma_{n_{N_b}}^2) \\ & \quad = \prod_{j=1}^{N_b} p(\mathbf{X}_j; \boldsymbol{\eta}_{\mathbf{r}}, \boldsymbol{\Theta}_j, \mathbf{S}_j, \sigma_{n_j}^2). \end{aligned} \tag{4.13}$$

Where the probability density of the measurements in the j^{th} set is given by

$$p(\mathbf{X}_j; \boldsymbol{\eta}_{\mathbf{r}}, \mathbf{S}_j, \sigma_{n_j}^2) = \prod_{m_i=1}^{M_j} \frac{1}{\pi^P} \frac{1}{\sigma_{n_j}^{2P}} \exp\left[-\frac{1}{\sigma_{n_j}^2} \left\|\mathbf{x}_j(t_{m_i}) - \mathbf{A}(\boldsymbol{\Theta}_j, \boldsymbol{\eta}_{\mathbf{r}}) \mathbf{s}_j(t_{m_i})\right\|^2\right]. \tag{4.14}$$

The likelihood function of the total set of unknown parameters is written as

$$\begin{aligned} L_T(\boldsymbol{\eta}_T) &= L_T(\boldsymbol{\eta}_{\mathbf{r}}, \boldsymbol{\Theta}_1, \ldots, \boldsymbol{\Theta}_{N_b}, \mathbf{S}_1, \ldots, \mathbf{S}_{N_b}, \sigma_{n_1}^2, \ldots, \sigma_{n_{N_b}}^2; \mathbf{X}_1, \ldots, \mathbf{X}_{N_b}), \\ &= \ln\left[\prod_{j=1}^{N_b} p(\mathbf{X}_j; \boldsymbol{\eta}_{\mathbf{r}}, \boldsymbol{\Theta}_j, \mathbf{S}_j, \sigma_{n_j}^2)\right], \\ &= \sum_{j=1}^{N_b} \ln p(\mathbf{X}_j; \boldsymbol{\eta}_{\mathbf{r}}, \boldsymbol{\Theta}_j, \mathbf{S}_j, \sigma_{n_j}^2), \\ &= \sum_{j=1}^{N_b} L_j(\boldsymbol{\eta}_{\mathbf{r}}, \boldsymbol{\Theta}_j, \mathbf{S}_j, \sigma_{n_j}^2; \mathbf{X}_j). \end{aligned} \tag{4.15}$$

We see that the total likelihood of the parameter vector $\boldsymbol{\eta}_T$ is the sum of the individual likelihoods. Ultimately we seek to estimate the perturbations in $\boldsymbol{\eta}_{\mathbf{r}}$ using all of the calibration bins. When the angles are unknown, the estimator of $\boldsymbol{\eta}_{\mathbf{r}}$ is coupled to $\{\boldsymbol{\Theta}_j\}$, for $1 \leq j \leq N_b$. To solve for an estimator of the nonlinear parameters, we must eliminate dependence of the likelihood on the unknown nuisance parameters $\mathbf{S}_1, \ldots, \mathbf{S}_{N_b}, \sigma_{n_1}^2, \ldots, \sigma_{n_{N_b}}^2$. Recognizing that

$$\frac{\partial}{\partial \sigma_i^2} L_j(\boldsymbol{\eta}_{\mathbf{r}}, \boldsymbol{\Theta}_j, \mathbf{S}_j, \sigma_{n_j}^2; \mathbf{X}_j) = 0, \qquad \text{for } i \neq j \tag{4.16a}$$

$$\frac{\partial}{\partial \mathbf{S}_i} L_j(\boldsymbol{\eta}_{\mathbf{r}}, \boldsymbol{\Theta}_j, \mathbf{S}_j, \sigma_{n_j}^2; \mathbf{X}_j) = 0, \qquad \text{for } i \neq j \tag{4.16b}$$

We can substitute the ML estimates for $\left\{\mathbf{S}_j, \sigma_{n_j}^2\right\}$ to create a compressed likelihood for each set. We denote the compressed likelihood of the j^{th} set as

$$L_j(\boldsymbol{\eta}_{\mathbf{r}}, \boldsymbol{\Theta}_j; \mathbf{X}_j) = L_j(\boldsymbol{\eta}_{\mathbf{r}}, \boldsymbol{\Theta}_j, \mathbf{S}_j, \sigma_{n_j}^2; \mathbf{X}_j)\Big|_{\sigma_{n_j}^2 = \hat{\sigma}_{n_j}^2, \mathbf{S}_j = \hat{\mathbf{S}}_j} \tag{4.17}$$

Where the estimates refer to maximum likelihood estimates. The steps for obtaining ML estimates of each unknown were detailed in Appendix B.2.3. The procedure here is identical

and leads to the following estimators

$$\hat{\sigma}^2_{n_j} = \frac{1}{M_j P} \sum_{i=1}^{M_j} \left\| \mathbf{x}_j(t_i) - \mathbf{A}^H(\boldsymbol{\eta}_\mathbf{r}, \boldsymbol{\Theta}_j)\mathbf{s}_j(t_i) \right\|^2, \tag{4.18a}$$

$$\hat{\mathbf{S}}_j = \left(\mathbf{A}^H(\boldsymbol{\eta}_\mathbf{r}, \boldsymbol{\Theta}_j)\mathbf{A}(\boldsymbol{\eta}_\mathbf{r}, \boldsymbol{\Theta}_j) \right)^{-1} \mathbf{A}^H(\boldsymbol{\eta}_\mathbf{r}, \boldsymbol{\Theta}_j)\mathbf{X}_j. \tag{4.18b}$$

We substitute these forms into Equation 4.17 to obtain the compressed likelihood of the j^{th} bin

$$L_j(\boldsymbol{\eta}_\mathbf{r}, \boldsymbol{\Theta}_j; \mathbf{X}_j) = \mathrm{tr}\left(\mathbf{P}_{\mathbf{A}(\boldsymbol{\eta}_\mathbf{r}, \boldsymbol{\Theta}_j)} \mathbf{R}_{\mathbf{x}_j} \right). \tag{4.19}$$

The total likelihood with eliminated nuisance parameters is given by

$$\begin{aligned} L_T(\boldsymbol{\eta}_\mathbf{r}, \boldsymbol{\Theta}_1, \ldots, \boldsymbol{\Theta}_{N_b}; \mathbf{X}_1, \ldots, \mathbf{X}_{N_b}) &= \sum_{j=1}^{N_b} L_j(\boldsymbol{\eta}_\mathbf{r}, \boldsymbol{\Theta}_j; \mathbf{X}_j), \\ &= \sum_{j=1}^{N_b} \mathrm{tr}\left(\mathbf{P}_{\mathbf{A}(\boldsymbol{\eta}_\mathbf{r}, \boldsymbol{\Theta}_j)} \mathbf{R}_{\mathbf{x}_j} \right). \end{aligned} \tag{4.20}$$

We state the final form of the MLE of the nonlinear parameters as the solution to the following maximization

$$\boxed{\left[\hat{\boldsymbol{\eta}}_\mathbf{r}, \hat{\boldsymbol{\Theta}}_1, \ldots, \hat{\boldsymbol{\Theta}}_{N_b} \right] = \max_{\boldsymbol{\eta}_\mathbf{r}, \boldsymbol{\Theta}_1, \ldots, \boldsymbol{\Theta}_{N_b}} \left\{ L_T(\boldsymbol{\eta}_\mathbf{r}, \boldsymbol{\Theta}_1, \ldots, \boldsymbol{\Theta}_{N_b}; \mathbf{X}_1, \ldots, \mathbf{X}_{N_b}) \right\}} \tag{4.21}$$

$$\boxed{= \max_{\boldsymbol{\eta}_\mathbf{r}, \boldsymbol{\Theta}_1, \ldots, \boldsymbol{\Theta}_{N_b}} \left\{ \sum_{j=1}^{N_b} \mathrm{tr}\left(\mathbf{P}_{\mathbf{A}(\boldsymbol{\eta}_\mathbf{r}, \boldsymbol{\Theta}_j)} \mathbf{R}_{\mathbf{x}_j} \right) \right\}.} \tag{4.22}$$

□

In the case of unknown arrival angles and perturbation of P sensor positions in two dimensions, the solution requires a multidimensional search of $2P+Q_1+\cdots+Q_{N_b}$ dimensions. When the arrival angles are perfectly known, the dimensionality of the search space reduces to the length of the nonlinear parameter vector (taken to be $2P$ when we limit consideration

to unknown geometric perturbations in two dimensions). Note that this result generalizes to arbitrary nonlinear parameters of the manifold model.

The estimator summarized in Equation 4.22 indicates that the θ dependent length of the manifold vectors is arbitrary with respect to the maximization due to the underlying normalization of the model enforced by the projection operator, suggesting that only the orientation of a manifold vector in $\mathbb{C}^P$ is required to implement the estimator form as derived. The estimator projects the observations onto each of the N_b column spaces where the j^{th} column space is specified as

$$\mathrm{C}(\mathbf{A}(\boldsymbol{\eta}_{\mathbf{r}}, \boldsymbol{\Theta}_j)) = \mathrm{span}\left\{\mathbf{a}(\boldsymbol{\eta}_{\mathbf{r}}, \theta_{1_j}) \ldots \mathbf{a}(\boldsymbol{\eta}_{\mathbf{r}}, \theta_{Q_j})\right\}. \tag{4.23}$$

Multiplication of the q_j manifold vector by a *real*, nontrivial scalar $\beta_{q_j} \in \mathbb{R}$ dilates or shrinks $\mathbf{a}(\boldsymbol{\eta}_{\mathbf{r}}, \theta_{q_j})$ but does not change the destination subspace of the projection operator. We can alternatively write the image of the linear transformation summarized by the projection operator as

$$\mathrm{span}\left\{\beta_{1_j}\mathbf{a}(\boldsymbol{\eta}_{\mathbf{r}}, \theta_{1_j}) \ldots \beta_{Q_j}\mathbf{a}(\boldsymbol{\eta}_{\mathbf{r}}, \theta_{Q_j})\right\}, \beta_{q_j} \in \mathbb{R} \text{ and } \beta_{q_j} > 0. \tag{4.24}$$

Equation 4.24 allows us to conclude two important facts:

1. The estimator of nonlinear manifold parameters derived in this chapter and summarized in Equation 4.22 cannot lead to absolute calibration of element patterns because the θ dependent length of the manifold vectors is lost,
2. **The principal components characterization of the manifold which only provides the *orientation* of a manifold vector in $\mathbb{C}^P$ space is sufficient for the application of the estimator proposed in Equation 4.22**.

Item 2 justifies a unit-norm constraint invoked in the derivation of the principal components based manifold characterization described in Chapter 5.

4.3 Fisher Information for the Parametric Framework

The statistical independence of calibration bins enables the total Fisher information matrix to be written as the sum of N_b information matrices

$$\mathbf{J}_T(\boldsymbol{\eta}_\mathbf{r}, \boldsymbol{\Theta}_1, \ldots \boldsymbol{\Theta}_{N_b}) = \sum_{j=1}^{N_b} \mathbf{J}_j(\boldsymbol{\eta}_\mathbf{r}, \boldsymbol{\Theta}_j). \tag{4.25}$$

This form shows explicit dependence on N_b suggesting that the estimator accuracy increases with an increasing number of calibration bins, provided that the Fisher information in an individual bin is nonzero. We can note that the m, n entry of the Fisher information matrix under the separable complex Gaussian formulation adopted in this chapter is given by Bang's formula [93], originally presented in Equation C.12 of Appendix C, and restated here for the j^{th} bin as:

$$\begin{aligned}[\mathbf{J}_j(\boldsymbol{\eta})]_{m,n} = \operatorname{tr}\left[\mathbf{R}_{\mathbf{n}_j}^{-1}(\boldsymbol{\eta})\frac{\partial \mathbf{R}_{\mathbf{n}_j}(\boldsymbol{\eta})}{\partial \eta_m}\mathbf{R}_{\mathbf{n}_j}^{-1}(\boldsymbol{\eta})\frac{\partial \mathbf{R}_{\mathbf{n}_j}(\boldsymbol{\eta})}{\partial \eta_n}\right] + \ldots \\ 2Re\left[\frac{\partial \boldsymbol{\mu}_{\mathbf{x}_j}^H(\boldsymbol{\eta})}{\partial \eta_m}\mathbf{R}_{\mathbf{n}_j}^{-1}(\boldsymbol{\eta})\frac{\partial \boldsymbol{\mu}_{\mathbf{x}_j}(\boldsymbol{\eta})}{\partial \eta_n}\right].\end{aligned} \tag{4.26}$$

In the form above we use the following substitutions

$$\boldsymbol{\mu}_{\mathbf{x}_j}(\boldsymbol{\eta}_j^{nl}, \boldsymbol{\eta}_j^l) = A(\boldsymbol{\Theta}_j, \boldsymbol{\eta}_\mathbf{r})\boldsymbol{\eta}_j^l, \tag{4.27a}$$

$$\mathbf{R}_{\mathbf{n}_j} = \sigma_{n_j}^2 \mathcal{I}_P, \tag{4.27b}$$

$$\boldsymbol{\eta}_j^{nl} = \left[\boldsymbol{\eta}_\mathbf{r}^T, \boldsymbol{\Theta}_j^T\right]^T, \tag{4.27c}$$

And use $\boldsymbol{\eta}_j^l$ to emphasize the interpretation of the unknown waveforms as linear parameters of the mean. Recognizing that the gradient of the covariance term with respect to geometric uncertainties on phase center positions is zero (and also holds for any arbitrary nonlinear manifold parameters under the separable Gaussian formulation outlined in this chapter), we

can write the $N_{nl} \times N_{nl}$ Fisher information matrix associated with the unknown nonlinear parameters of the mean as

$$\mathbf{J}_j(\boldsymbol{\eta}_j^{nl}) = \frac{2}{\sigma_{n_j}^2} Re\left\{ \left(\nabla_{\boldsymbol{\eta}_j^{nl}} \left[(\boldsymbol{\eta}_j^{l})^H \mathbf{A}^H(\boldsymbol{\eta}_j^{nl}) \right] \right) \left(\nabla_{\boldsymbol{\eta}_j^{nl}} \left[(\boldsymbol{\eta}_j^{l})^H \mathbf{A}^H(\boldsymbol{\eta}_j^{nl}) \right] \right)^H \right\}. \tag{4.28}$$

Note that this form is a subblock of the total FIM for bin j. The u, v entry of this matrix is written as

$$\left[\mathbf{J}_j(\boldsymbol{\eta}_j^{nl})\right]_{u,v} = \frac{2}{\sigma_{n_j}^2} Re\left[\frac{\partial \boldsymbol{\mu}_{\mathbf{x}_j}^H(\boldsymbol{\eta}_j^{nl}, \boldsymbol{\eta}_j^{l})}{\partial \eta_u} \frac{\partial \boldsymbol{\mu}_{\mathbf{x}_j}(\boldsymbol{\eta}_j^{nl}, \boldsymbol{\eta}_j^{l})}{\partial \eta_v} \right]. \tag{4.29}$$

The general variable η_i here refers to the i^{th} entry of $\boldsymbol{\eta}_j^{nl}$. Assuming a practical form of the noise covariance that does not lead to a singularity, we can conclude that the Fisher information associated with the m^{th} unknown parameter is nonzero provided the gradient vector is nonzero.

In the numerical examples presented further in this chapter, we exercise the estimator in Equation 4.22 using array shape perturbations of an array oriented in a y-z plane. The manifold model is assumed to be the isotropic steering vector with unknown errors on the phase center positions. The general expression for the errors on phase center p is given by $\Delta\mathbf{r}_p = [\Delta y_p, \Delta z_p]^T$. Suppose the spatial sources are uncorrelated, meaning that $E\{s_i^* s_j\} = 0$ for $i \neq j$, and assume that the angle of arrival is measured off the z axis. The form in Equation 4.29 leads to the following expressions for the Fisher information associated with

the errors on the p^{th} element, under an assumption of uncorrelated sources:

$$J(\Delta y_p) = \sum_{i=1}^{Q_j} \frac{2}{\sigma_{n_j}^2} E\left\{s_i^* s_i\right\} \left[k^2 \sin^2\theta_i\right] = \sum_{i=1}^{Q_j} \frac{2P_i}{\sigma_{n_j}^2} k_y^2(\theta_i) = \sum_{i=1}^{Q_j} 2 \cdot \mathrm{SNR}_i \cdot k_y^2(\theta_i), \tag{4.30a}$$

$$J(\Delta z_p) = \sum_{i=1}^{Q_j} \frac{2}{\sigma_{n_j}^2} E\left\{s_i^* s_i\right\} \left[k^2 \cos^2\theta_i\right] = \sum_{i=1}^{Q_j} \frac{2P_i}{\sigma_{n_j}^2} k_z^2(\theta_i) = \sum_{i=1}^{Q_j} 2 \cdot \mathrm{SNR}_i \cdot k_z^2(\theta_i). \tag{4.30b}$$

Here k is the wavenumber and $k_y(\theta_i), k_z(\theta_i)$ refer to the spatial frequency components in the y and z dimensions respectively for a plane wave with arrival angle θ_i. The forms above are meant to offer intuition into the estimator performance that is demonstrated in the next section when the model perturbations are purely represented with geometric errors. We may first notice that the Fisher information associated with the unknown error parameters is proportional to source SNR, showing that the information in a measurement from a spatial source increases linearly with the associated SNR. Recall that the lower bound on estimator error shares an inverse proportionality with the Fisher information. The expressions above confirm an intuition that high SNR observations lead to more accurate estimates of unknown parameters. In the limiting cases (provided that $k_y(\theta_i), k_z(\theta_i) > 0$) , $J(\Delta y_p), J(\Delta z_p) \to \infty$ when $\sigma_{n_j}^2 \to 0$ or when $P_i \to \infty$ and the associated estimator error *decreases*.

We can also note that the Fisher information for the errors in a particular dimension goes to zero when the corresponding spatial frequency component of that dimension goes to zero. The y component of the spatial frequency is zero at vertical incidence, indicating that snapshots from $\theta = 0^\circ$ sources do not contain Fisher information associated with the errors along the y axis. In other words as $\theta \to 0^\circ$, $J(\Delta y_p) \to 0$. Similarly we can observe that the Fisher information associated with Δz_p goes to zero as $|\theta| \to 90^\circ$ indicating that snapshots collected from sources far off nadir cannot discriminate errors along the z axis. The forms of the Fisher information for the errors in y and z suggest that snapshots obtained near nadir improve estimates of errors in the z dimension and snapshots obtained at the large incidence

angles improve estimates of the errors along the y axis.

4.4 Simulated Performance in Parametric Manifold Calibration

The proposed estimator of nonlinear manifold parameters is demonstrated numerically with a set of simulated scenarios designed in MATLAB [94]. The examples offer insight into the estimation framework and demonstrate the restoration of arrival angle estimator accuracy when we evaluate the model of a perturbed manifold in terms of the maximum likelihood estimates of the nonlinear parameters admitted by Equation 4.22. The scenarios parallel those presented in Chapter 2 for validating the implementation of the MUSIC and MLE estimators. The experiments both assume two equal power spatial sources and evaluate estimator performance with varying source SNR and snapshot support.

4.4.1 Array Shape Perturbation of the Nominal Manifold

In contrast to the results presented in Figure 2.7 from Chapter 2, this example assumes an array of 7 elements with *nominal* sensor positions defined by the RDS lever arms presented in Table 3.2. The *nominal manifold* hence refers to the isotropic manifold response vector in Equation 2.35 evaluated in terms of the *nominal* sensor geometry. The nominal manifold is geometrically perturbed in the y-z plane in simulation by imposing systematic position errors on the nominal geometry as

$$\mathbf{r}_p = \mathbf{r}_p^0 + \Delta\mathbf{r}_p. \tag{4.31}$$

The geometric quantities are illustrated in Figure 4.1 with position vectors referencing a phase center in the array as the origin. The terms in this expression are defined as follows:

- $\mathbf{r}_p \in \mathbb{R}^{2\times 1}$ denotes the *actual* position vector pointing from the reference phase center to phase center p,

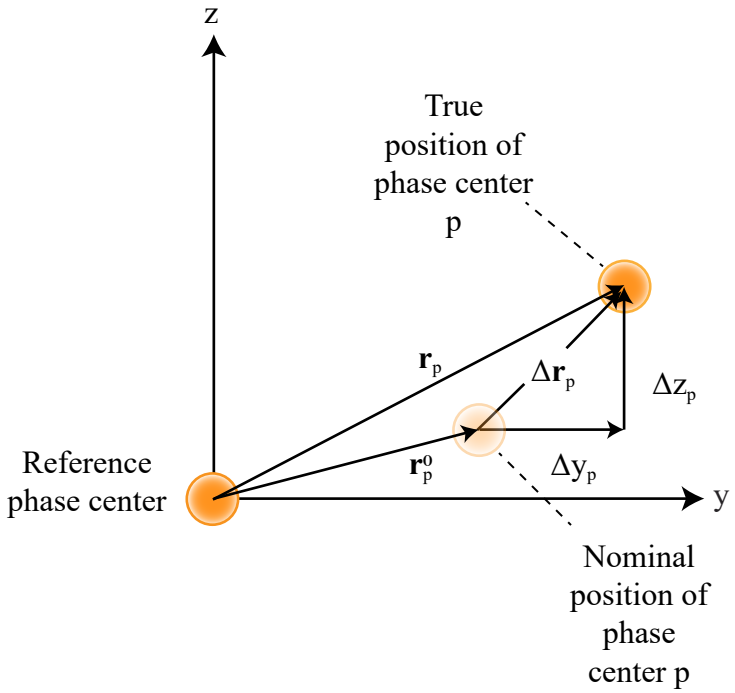

Figure 4.1: Geometrically perturbed manifold conventions.

- $\mathbf{r}_p^0 \in \mathbb{R}^{2\times 1}$ denotes the nominal position vector pointing from the reference to phase center p based on our model of the array geometry,
- $\Delta\mathbf{r}_p \in \mathbb{R}^{2\times 1}$ is the unknown geometric error vector given by $\Delta\mathbf{r}_p = [\Delta y_p, \Delta z_p]^T$.

The RDS phase center positions are perturbed in simulation by adding a geometric error to each position vector. While the position errors are modeled as samples from a Gaussian distribution, they are always assumed to be deterministic with respect to the estimation problem. Position errors in y and z are treated as independent and identically distributed as $\Delta y_p \sim \mathcal{N}(0, \sigma^2)$ and $\Delta z_p \sim \mathcal{N}(0, \sigma^2)$ for an arbitrary phase center. Hence errors are IID in both dimensions and from phase center to phase center. The length of an error vector $\Delta\mathbf{r}_p$ given by $dr_p = \sqrt{y_p^2 + z_p^2}$ is a Rayleigh distributed random variable [95] whose expected

value is written in terms of the variance of the geometric error in either dimension as

$$E\left\{dr_p\right\} = \sqrt{\frac{\pi\sigma^2}{2}}. \tag{4.32}$$

In array shape calibration literature, small scale and large scale perturbations appear to lack a common definition (see [80] for example). The following definitions of small and large scale are adopted in this dissertation:

Definition 1 (Small scale)**.** *In the small scale perturbation regime, the average Euclidean length of the* ***monostatic equivalent phase center*** *position error vector is less than* 0.05λ

$$E\left\{dr_p\right\} \leq 0.05\lambda, \tag{4.33}$$

Which corresponds to the following bound on σ

$$\sigma \leq 0.04\lambda. \tag{4.34}$$

Definition 2 (Large scale)**.** *In the large scale perturbation regime, the average Euclidean length of the* ***monostatic equivalent phase center*** *position error vector is greater than* 0.05λ

$$E\left\{dr_p\right\} > 0.05\lambda, \tag{4.35}$$

Which corresponds to the following bound on σ

$$\sigma > 0.04\lambda. \tag{4.36}$$

The definitions above which assume IID geometric errors across the phase centers can be used to determine the variance of the error distribution in y and z in simulation. Note that in demonstrating the estimator of nonlinear manifold parameters, both small and large scale perturbations are tested. The standard deviation of position errors in either dimension is

written in terms of variable α, introduced to denote a perturbation scale, as $\sigma = \alpha\lambda$. In the simulations that follow, the boundary of the small scale perturbation region is tested using a perturbation scale of $\alpha = 0.035$ to perturb the monostatic equivalent phase center geometry. The estimator is also tested under large scale perturbations assuming a perturbation scale of $\alpha = 0.07$ (well within the large scale regime by Definition 2).

The benefit of demonstrating estimator performance in the array shape calibration case is that the perturbed manifold model is immediately available in closed form. The p^{th} entry of a manifold vector is modeled as

$$\Big[\mathbf{a}(\theta, \boldsymbol{\eta}_{\mathbf{r}})\Big]_p = e^{-\jmath \mathbf{k}^T(\theta)\left(\mathbf{r}_p^0 + \boldsymbol{\Delta}\mathbf{r}_p\right)}. \tag{4.37}$$

The perturbed manifold assumes isotropic radiation of the constituent elements in the array and thereby ignores mutual coupling and all other electromagnetic phenomenology. A point is emphasized here to the reader: the geometric perturbation model in Equation 4.37 is a simple analytic function that serves as an algorithm-development convenience; the form enables a methodology for exercising the estimator of nonlinear manifold parameters derived in Equation 4.22. The geometrically perturbed manifold is not meant to be completely representative of a real array manifold which is subject to many influencing factors including mutual coupling and platform effects.

4.4.2 Synthesis of Calibration Bins

The proposed approach outlined in this chapter aggregates many diverse calibration bins to estimate nonlinear manifold parameters. The total Fisher information increases as more and more spatially diverse sources are presented to the estimator. We expect estimator accuracy to improve as the spatial diversity of sources expands in the calibration sets. To demonstrate increased estimator accuracy with more spatially diverse sources, two calibration sets are tested (denoted A and B). Set A uses a single calibration bin (i.e. $N_b = 1$) to estimate position

Table 4.1: Calibration bin setup in simulations.

		Source Specification in j^{th} Calibration Bin			
	N_b	M_j	Q_j	$\theta_{q_j}(^\circ)$	$\mathrm{SNR}_{q_j}(dB)$
Set					
A	1	100	$Q_j \sim \mathcal{Z}[1,2]$	$\theta_{q_j} \sim \mathcal{U}[-20,20]$	$\mathrm{SNR}_{q_j} \sim \mathcal{U}[10,30]$
B	100	100	$Q_j \sim \mathcal{Z}[1,2]$	$\theta_{q_j} \sim \mathcal{U}[-85,85]$	$\mathrm{SNR}_{q_j} \sim \mathcal{U}[10,30]$
				$1 \leq q_j \leq Q_j$	

errors and restricts the angular range of calibration sources to $\pm 20^\circ$ while Set B increases the spatial bandwidth of the observations, using many calibration bins ($N_b = 100$) originating from a much larger field of view $\pm 85^\circ$. We expect the estimated unknown geometric error to be less accurate when the calibration data span a limited part of the spatial frequency spectrum. We hence anticipate that by increasing the amount of spatial bandwidth spanned by the calibration sets, we will obtain better estimates of the geometric perturbations which in turn will lead to more accurate estimates of arrival angle.

Table 4.1 specifies the simulated sources in each calibration set. Note that the script $\mathcal{Z}$ notation is used to indicate a random integer uniformly distributed over an interval. Recall that we use Q to denote number of sources and M to denote number of snapshots. As shown here, the number of sources in any calibration bin is limited to at most two. The DOA of the q^{th} source is drawn from a uniform distribution whose interval is fixed with respect to the particular set. Per source SNR similarly varies over a uniform distribution and allows a large range of relative powers to be tested.

4.4.3 Estimation of Perturbation Parameters

The optimization problem in 4.22 is cast as a minimization by expressing the objective function in terms of an orthogonal projection and searching for a minimum using MATLAB's built in constrained minimization function in the Optimization Toolbox [94]. The manifold

perturbations are initialized to zero. The algorithm constrains the search by restricting perturbations to a user-defined interval in y and z about the nominal position of each phase center. The solver perturbs the position errors in an iterative search over $2(P-1)$ dimensions for the global minimum. In the simulated results presented here, the position of the reference phase center is taken to be *known* (hence not perturbed).

Examples of the estimated unknown errors are plotted for the manifold model subject to small scale perturbations ($\alpha = 0.035$) and large scale perturbations ($\alpha = 0.07$) are presented for one tested instantiation of geometric error in Figures 4.2 and 4.3 respectively. The plots are given as errors in the array geometry (as opposed to monostatic equivalent phase centers) but the perturbation scales refer to the phase center geometry. Geometric errors are estimated with both sets of calibration data (see Table 4.1). The nominal geometry is denoted with a gray x marker and perturbed positions (corresponding to truth) are plotted with yellow circles. Estimates from Set A and Set B are plotted in green and blue respectively. The cross hairs on each plotted set of estimates indicate the 95% confidence interval of geometric errors estimated over 100 Monte Carlo trials. Each trial creates a new set of random calibration measurements. In other words Set A and Set B change with each trial, providing new estimates of a particular perturbation state.

Comparison of estimates from the small scale scenario in Figure 4.2 and the large scale scenario in Figure 4.3 suggests that the estimates improve (become less biased) when the observations provide more information to the estimator in 4.22. The outcomes do not provide sufficient evidence to interpret whether the increased accuracy is attributable to the fact that Set B has a larger number of calibration bins or if it produces more accurate estimates because it allows sources over a larger field of view. An attempt to understand these two influencing factors on the estimator's performance is developed further below. In the small scale case shown in Figure 4.2, the Set B estimates appear unbiased, showing the center of the blue cross hairs falling over truth (in yellow). The cross hairs are barely observable in the figure due to the tightening of the estimator error about average estimated values.

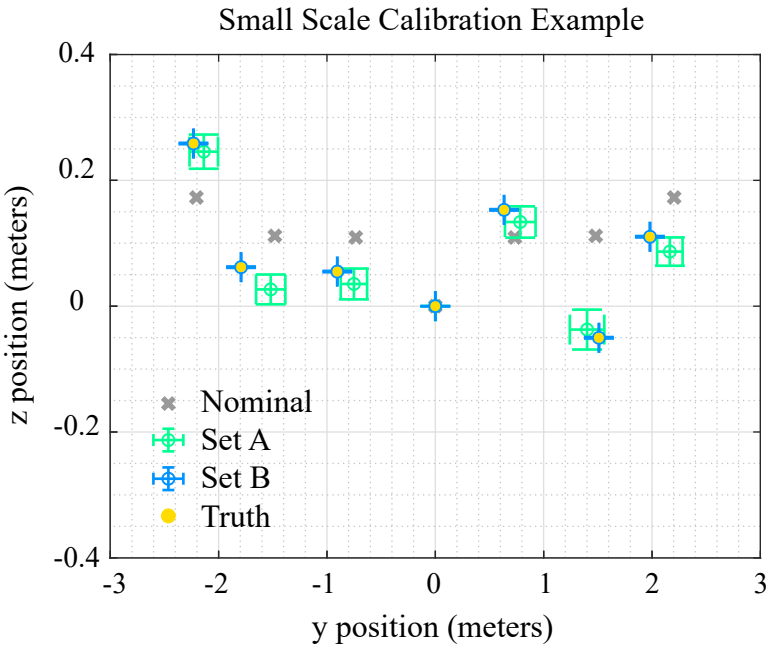

Figure 4.2: Estimated sensor position errors in a small scale scenario for observation sets with reduced Fisher information (Set A) and increased Fisher information (Set B) in parameter estimation. Cross hairs indicate 95% confidence intervals of 100 Monte Carlo trials.

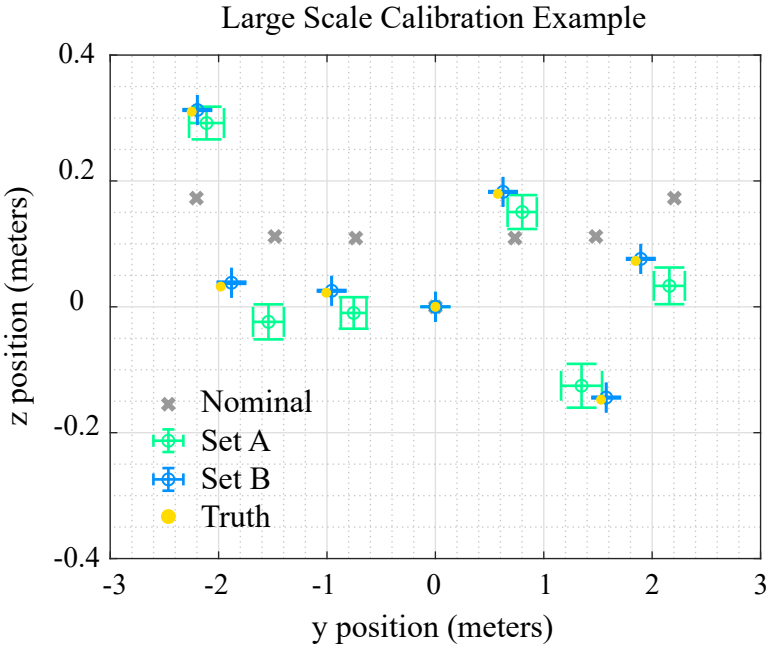

Figure 4.3: Estimated sensor position errors in a large scale scenario for observation sets with reduced Fisher information (Set A) and increased Fisher information (Set B) in parameter estimation. Cross hairs indicate 95% confidence intervals of 100 Monte Carlo trials.

In the large scale case, the estimates derived with observations spanning a larger spatial bandwidth demonstrate improved accuracy but maintain some residual bias, albeit small, after correction of the nominal geometry to the estimated perturbed state.

4.4.4 Angle Estimation Improvement with Parametric Calibration

The estimated perturbed manifold parameters are applied in angle estimation to demonstrate performance restoration in the classic examples produced in Chapter 2 for the ideal manifold. The results presented here limit consideration to the MLE. Experiments 1 and 2 (described in Chapter 2) are carried out assuming the nominal RDS phase centers derived from the geometry reported in Table 3.2 subject to small scale (on the order of 0.025λ) and large scale (on the order of 0.05λ) errors as outlined in the previous section. The description of these experiments is restated below.

1. **Experiment 1:** Two uncorrelated equal power sources $\left(\boldsymbol{\Theta} = [-7^\circ, 12^\circ]^T\right)$ with a fixed number of snapshots ($M = 50$) and per sensor SNR sweeping over the interval 10 dB $<$ SNR $<$ 25 dB.
2. **Experiment 2:** Two uncorrelated equal power sources $\left(\boldsymbol{\Theta} = [-7^\circ, 12^\circ]^T\right)$ with a fixed combined SNR of 20 dB and snapshots varying over the interval $10 < M < 1000$.

The signal environment contains two equal power mainbeam sources at -7° and 12°, referred to as Source 1 and Source 2. Sources are modeled as narrowband and centered at the RDS carrier frequency of 195 MHz.

Maximum likelihood DOA estimation accuracy is numerically evaluated over 500 Monte Carlo trials per tested snapshot or SNR value for the two sources assuming the following manifold models in angle estimation:

1. **True**: True sensor geometry is known and the estimator manifold model perfectly matches truth (corresponds to perfect calibration),
2. **Nominal**: Estimator manifold model assumes the nominal geometry (corresponds to the uncalibrated case),

3. **Cal Set A**: Estimator manifold model assumes geometric perturbations and evaluates the array response in terms of estimated positions obtained with Set A,
4. **Cal Set B**: Estimator manifold model assumes geometric perturbations and evaluates the array response in terms of estimated positions obtained with Set B.

Figures 4.4 and 4.5 present simulated MLE performance for Source 2 ($\theta = 12°$) resulting from Experiment 1 and 2 respectively. Each figure illustrates outcomes when compensating for small scale geometric perturbations in subfigure (a) and large scale perturbations in subfigure (b). The estimates of the Source 2 DOA are marginally worse when calibrating with Set A. Source 1 DOA estimates are omitted here as they admit similar conclusions on a smaller scale. In both the small and large scale perturbation scenarios, the ideal performance (where geometry is perfectly known) shows that the MLE accuracy improves with increasing SNR (Figure 4.4) and converges to the CRLB with high values of SNR. The uncalibrated curves (resulting from the use of nominal geometry in angle estimation) verify degradation in estimator accuracy however we note that both perturbation scenarios show slight improvement in estimator performance with increasing SNR until about 17 dB when the RMSE levels off to a constant value. The error converges to approximately 1.65° at 25 dB for the small scale perturbation case. In the large scale case, the error appears to be bound to 2.8° in the high SNR regime.

Both scenarios verify improved angle estimator performance with more accurate estimates of geometric error. Recall that even in the small scale perturbation scenario, the estimated geometric errors are biased (see Figure 4.2). The observed angle estimator performance admits bias when biased estimates of positions are assumed in the MLE algorithm. Results for both scenarios (small and large scale perturbations) evidence bias in their angle estimates in the highest SNR case when a biased model of geometry (estimated with Set A) is used in angle estimation. This bias is reduced with improved calibration. The unbiased estimates of geometry (estimated with Set B) appear to restore the classic performance of the MLE under matched models (i.e. ideal) in both small and large scale scenarios and we find that the

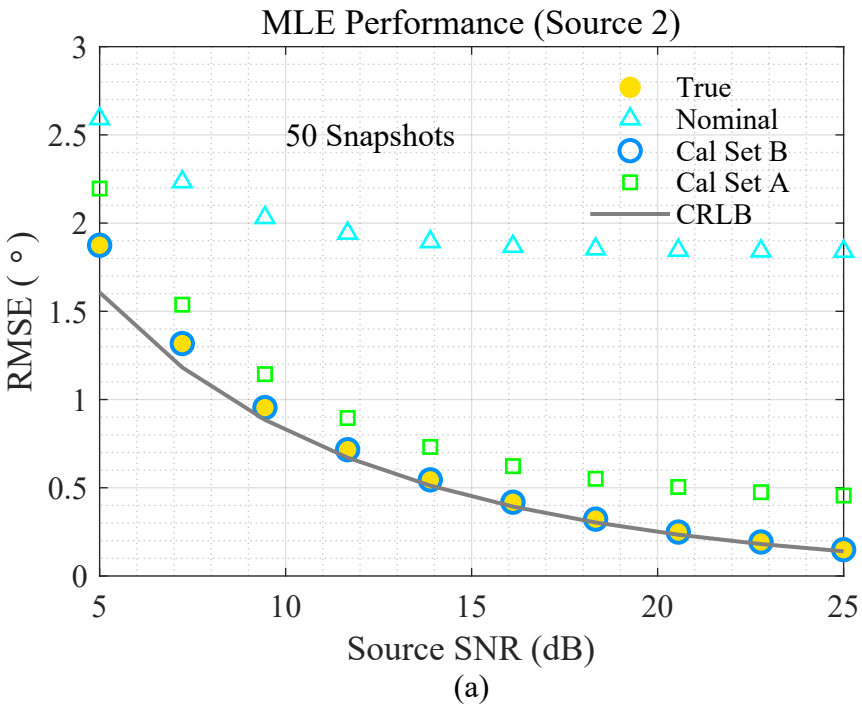

(a)

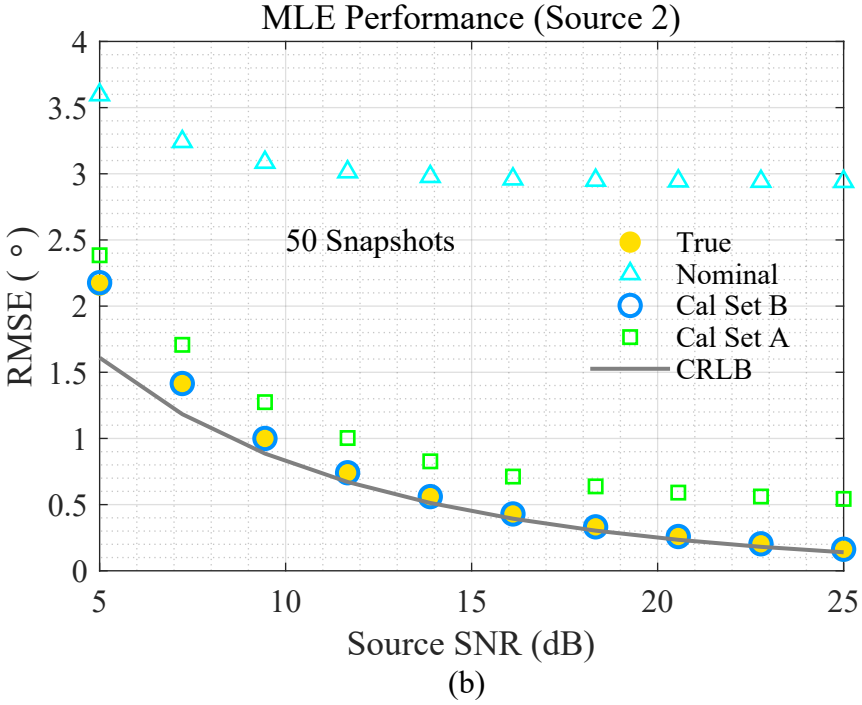

(b)

Figure 4.4: Experiment 1 outcomes for Source 2: (a) RMS perturbation of nominal phase center geometry of 0.035λ (small scale), (b) RMS perturbation of nominal phase center geometry of 0.070λ (large scale).

Table 4.2: Estimated error distribution parameters with 95% confidence intervals for $\theta = 12^\circ$ source with 12 dB per element SNR and 1,000 snapshots.

		Estimated Error Distribution Parameters	
Perturbation	*Manifold Model*	$\hat{\mu}_\theta(^\circ) \pm m$	$\hat{\sigma}_\theta(^\circ) \pm s$
0.035λ	true	0.0039 ± 0.0126	0.1432 ± 0.0089
0.035λ	nominal	1.8215 ± 0.5218	0.2476 ± 0.0154
0.035λ	Set A	0.2125 ± 0.0355	0.4039 ± 0.0251
0.035λ	Set B	-0.0053 ± 0.0131	0.1432 ± 0.0093
0.070λ	true	0.0035 ± 0.0128	0.1457 ± 0.0091
0.070λ	nominal	2.9428 ± 0.0294	0.3340 ± 0.0208
0.070λ	Set A	0.2085 ± 0.0441	0.5021 ± 0.0313
0.070λ	Set B	0.0569 ± 0.0134	0.1524 ± 0.0095

calibrated model closely approaches the CRLB for this particular instantiation of perturbed geometry.

To offer intuition to the DOA estimation performance curves under varying manifold models, a Gaussian distribution is fit to the errors $\hat{\theta} - \theta$ for the case of $M = 1,000$ snapshots and 12 dB per element SNR over the 500 Monte Carlo trials. The maximum likelihood estimated distribution parameters are reported by manifold model in Table 4.2 along with the 95% confidence intervals of the estimates for the small and large scale perturbation cases considered for these examples. The estimates are used to produce plots of the fitted distributions for the small and large scale cases in Figures 4.6a and 4.6b. The histograms of the errors measured from the simulated data are well-described by a Gaussian distribution as we would expect but the binned error plots are omitted from these results to ease readability of the figure which is only offered as an illustration.

For this particular instantiation of perturbed geometry, the DOA estimation performance in the *ideal* manifold case (where the array processor maintains perfect knowledge of the array manifold in angle estimation) is not altered with the larger perturbation scale. The effect

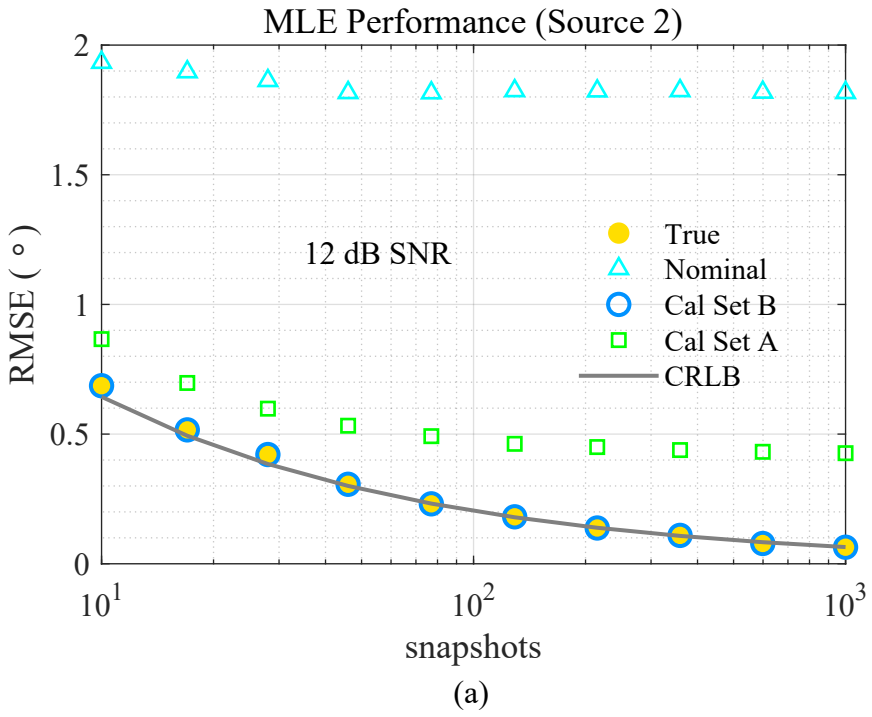

Figure 4.5: Experiment 2 outcomes for Source 2: (a) RMS perturbation of nominal phase center geometry of 0.035λ (small scale), (b) RMS perturbation of nominal phase center geometry of 0.070λ (large scale).

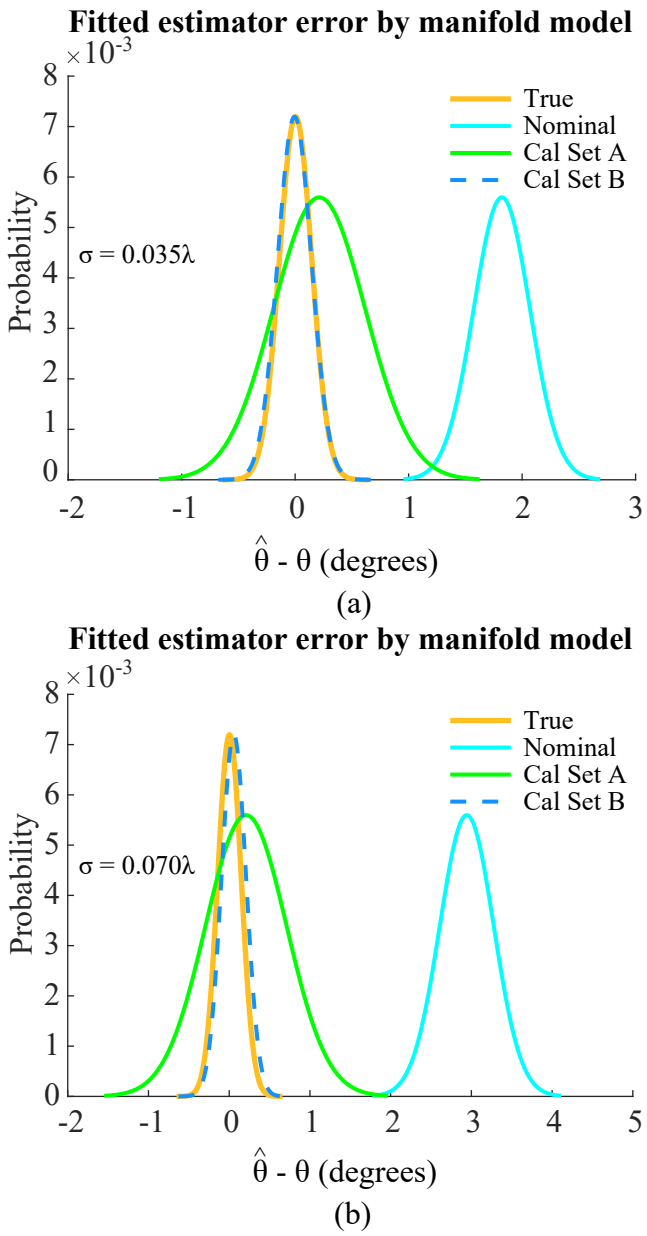

Figure 4.6: Fitted Gaussian distributions to simulated DOA errors estimated with various manifold models in high SNR, high snapshot regime: (a) $\sigma = 0.035\lambda$ (small scale), (b) 0.070λ (large scale).

of assuming the *nominal* manifold (where the nominal phase center positions determine the array response) leads to biased estimates of angle that are larger in the large scale perturbation case. The estimator accuracy improves when estimates of the geometric perturbations are incorporated into the manifold. We can note that the estimated position errors derived from Calibration Set A (where position uncertainties are estimated from one array covari-

ance matrix) reduce the bias of the DOA estimates relative to the uncalibrated case but the variance increases. The manifold model that most closely approximates the performance of the ideal case is realized by Calibration Set B which reduces both bias and variance of the estimator errors.

4.4.5 Summarizing Thoughts on Simulated Outcomes

The simulated results outlined above recreate some of the well-known estimator performance curves in direction of arrival literature [1] in the context of manifold mismatch. The experiments outlined in the original study aim to contrast super resolution performance of MUSIC and MLE. The estimator error distributions under various manifold models presented in Figure 4.6 illustrates the fundamental problem of manifold calibration; even for the best case signal environment where a directional source with high SNR and large sample support presents to the array, a poorly matched manifold model leads to biased estimates of angle with larger uncertainty in angle estimation. We point out that the estimator performance in Figures 4.4 and 4.5 results from a simulation of one perturbed state in order to compare measured estimator accuracy to the CRLB.

There is practical interest in studying manifold calibration over many states of position errors and in assessing the average influence of the number of calibration bins as well as the spatial bandwidth of calibration sources on the proposed estimator of nonlinear model parameters derived earlier in the chapter and summarized in Equation 4.22. This motivates an alternative simulation type to study the influence of training data characteristics on angle estimation outcomes. The section that follows offers simulator results from experiments designed to demonstrate the influence of spatial bandwidth and number of calibration bins on overall angle estimator accuracy over many perturbation states.

4.5 Influence of Training Data Characteristics on Single Source DOA Estimation

The remainder of this chapter establishes DOA estimator performance over many realizations of small scale perturbation states. Estimator accuracy is numerically evaluated with a single high SNR source that presents a stationary signal environment to the array over many snapshots at each point in the field of view. Each simulation varies characteristics of the calibration data set used to estimate the nonlinear manifold parameters and tests a given value over 100 Monte Carlo trials. The perturbation state changes on each Monte Carlo trial and hence each measured error curve summarizes 100 different instantiations of randomized position errors (generated with small scale perturbations). The source parameters assumed in angle estimation include 12.5 per element SNR and 100 snapshots.

Angle estimation performance curves are evaluated with two additional experiments, denoted Experiment 3 and Experiment 4, designed to study angle estimation under various conditions of the training data. Both simulations rely on small scale array shape perturbations to simulate mismatch between the modeled manifold and truth. Again we reiterate that the array shape perturbation model is a convenience that allows us to exercise the parametric calibration technique proposed in this chapter. The experiments are summarized below.

1. **Experiment 3**: The angular interval over which calibration sources are selected is increased from 1° to 180° to verify sensitivity of the angle estimator to spatial bandwidth of the calibration sources.
2. **Experiment 4**: The number of calibration bins is increased from 3 to 100 to verify the influence of N_b on DOA estimator accuracy.

The tested values of each characteristic of the training data are described in further detail below.

4.5.1 Synthesis of Calibration Bins

Experiment 3 investigates the influence of the spatial bandwidth of calibration sources by increasing the angular interval over which calibration sources are selected. This angular interval is always defined about $\theta = 0°$. In the case where a calibration bin contains two sources, a minimum source separation of $10°$ is enforced. When the angular extent $\Delta\theta$ is smaller than the minimum separation, only one source is allowed in each bin. The number of snapshots used to estimate the covariance matrix is held to a constant value of 100 throughout all simulations described in this chapter. When testing the influence of $\Delta\theta$, the number of bins is assigned to $N_b = 100$. The calibration source parameters used to establish the influence of spatial bandwidth on DOA estimator accuracy are summarized in Table 4.3.

Experiment 4 examines the role of the number of calibration bins on DOA accuracy. Recall that N_b determines the number of covariance matrices passed to the optimization problem derived in Equation 4.22. In this experiment, we assume a large interval for selecting arrival angles of calibration sources. All other parameters remain fixed relative to the previous test with the exception of N_b which takes discrete values that vary between 3 and 100 calibration bins. The specifications of the sources in the calibration bins are summarized in Table 4.4.

4.5.2 Angle Estimation Performance Curves

Each simulation tests a characteristic (N_b or $\Delta\theta$) of the training data used to estimate the nonlinear manifold parameters. One tested characteristic is carried out over 100 realizations of perturbed geometry. The estimated manifold parameters of each realization are used by the MLE algorithm in angle estimation. The estimated nonlinear parameters of the manifold are tested against 181 source arrival angles uniformly spaced over $-90° \leq \theta \leq 90°$. The directional sources impinge one at a time on the array so that $Q = 1$ at all times in testing. Every tested training data characteristic leads to one θ dependent performance curve obtained by averaging across the 100 realizations corresponding to different random

Table 4.3: Calibration bin setup in Experiment 3 (scenario for testing spatial bandwidth influence on DOA accuracy).

		Source Specification in j^{th} Calibration Bin			
N_b	$\Delta\theta(^\circ)$	M_j	Q_j	$\theta_{q_j}(^\circ)$	SNR_{q_j} (dB)
100	1	100	$Q_j \sim \mathcal{Z}[1,2]$	$\theta_{q_j} \sim \mathcal{U}[-0.5, 0.5]$	$\text{SNR}_{q_j} \sim \mathcal{U}[10,30]$
100	4	100	$Q_j \sim \mathcal{Z}[1,2]$	$\theta_{q_j} \sim \mathcal{U}[-2, 2]$	$\text{SNR}_{q_j} \sim \mathcal{U}[10,30]$
100	10	100	$Q_j \sim \mathcal{Z}[1,2]$	$\theta_{q_j} \sim \mathcal{U}[-5, 5]$	$\text{SNR}_{q_j} \sim \mathcal{U}[10,30]$
100	16	100	$Q_j \sim \mathcal{Z}[1,2]$	$\theta_{q_j} \sim \mathcal{U}[-8, 8]$	$\text{SNR}_{q_j} \sim \mathcal{U}[10,30]$
100	30	100	$Q_j \sim \mathcal{Z}[1,2]$	$\theta_{q_j} \sim \mathcal{U}[-15, 15]$	$\text{SNR}_{q_j} \sim \mathcal{U}[10,30]$
100	50	100	$Q_j \sim \mathcal{Z}[1,2]$	$\theta_{q_j} \sim \mathcal{U}[-25, 25]$	$\text{SNR}_{q_j} \sim \mathcal{U}[10,30]$
100	180	100	$Q_j \sim \mathcal{Z}[1,2]$	$\theta_{q_j} \sim \mathcal{U}[-90, 90]$	$\text{SNR}_{q_j} \sim \mathcal{U}[10,30]$
				$1 \leq q_j \leq Q_j$	

Table 4.4: Calibration bin setup in Experiment 4 (scenario for testing impact of number of calibration bins on DOA accuracy).

		Source Specification in j^{th} Calibration Bin			
N_b	$\Delta\theta(^\circ)$	M_j	Q_j	$\theta_{q_j}(^\circ)$	SNR_{q_j} (dB)
3	170	100	$Q_j \sim \mathcal{Z}[1,2]$	$\theta_{q_j} \sim \mathcal{U}[-85, 85]$	$\text{SNR}_{q_j} \sim \mathcal{U}[10,30]$
5	170	100	$Q_j \sim \mathcal{Z}[1,2]$	$\theta_{q_j} \sim \mathcal{U}[-85, 85]$	$\text{SNR}_{q_j} \sim \mathcal{U}[10,30]$
10	170	100	$Q_j \sim \mathcal{Z}[1,2]$	$\theta_{q_j} \sim \mathcal{U}[-85, 85]$	$\text{SNR}_{q_j} \sim \mathcal{U}[10,30]$
50	170	100	$Q_j \sim \mathcal{Z}[1,2]$	$\theta_{q_j} \sim \mathcal{U}[-85, 85]$	$\text{SNR}_{q_j} \sim \mathcal{U}[10,30]$
100	170	100	$Q_j \sim \mathcal{Z}[1,2]$	$\theta_{q_j} \sim \mathcal{U}[-85, 85]$	$\text{SNR}_{q_j} \sim \mathcal{U}[10,30]$
				$1 \leq q_j \leq Q_j$	

position error states.

Because the sensor position vectors are randomized with respect to the Monte Carlo trials, the estimator performance technically should not be compared to the classic CRLB; rather the use of the Hybrid CRLB [30] which handles both deterministic and random model parameters is better suited for this problem. The implementation here is complicated because not only are the perturbation states random but calibration source DOAs and number of sources in the training data are also randomized; the HCRLB is hence not immediately available. Instead angle estimator performance curves are plotted against an average estimator accuracy curve resulting from the use of the ideal manifold in MLE. Recall that in these simulations ideal implies perfect knowledge of geometric uncertainty and therefore perfect knowledge of the manifold. Thus the variation of training data characteristics has no bearing on the ideal performance curves and the perfectly matched case represents the best possible performance in angle estimation for a given set of test data. For each test of training data characteristics, the ideal curves are presented but show no sensitivity to the varying parameters. The ideal RMSE curves are only provided to the reader as justification of creating one average ideal curve for benchmarking angle estimator accuracy as a function of varying training data attributes.

4.5.3 Impact of Calibration Source Spatial Bandwidth

Single source angle estimator performance is summarized in Figures 4.7 and 4.8 for a set of values which determine the angle interval over which calibration sources are selected for estimating manifold perturbation parameters. Bias and RMSE are reported for seven tested values of $\Delta\theta$ which determine the allowable angular interval about $\theta = 0^\circ$ for selecting calibration sources in training. Figures 4.7a and 4.7c report bias and RMSE in angle estimation when the true position offsets of each sensor are used in angle estimation while Figures 4.7b and 4.7d summarize the performance with estimated geometric uncertainty. The bias and RMSE curves resulting from the matched or ideal manifold case provide verification that

the variation of training data characteristics does not alter angle estimation performance when the manifold parameters are perfectly known. The ideal RMSE curves in Figure 4.7c approach the limit (with increasing Monte Carlo trials) of achievable accuracy on average with the given nominal conformal RDS geometry which realizes the smallest error near nadir. The RMSE increases as the test source moves off of $\theta = 0^\circ$ with the largest errors realized at the edges of the field of view but not exceeding 0.027°.

Figures 4.7b and 4.7d illustrate angle estimation accuracy with increasing spatial bandwidth in the training set. A detailed view of these results is offered in Figure 4.8. The performance curves confirm the predicted influence of spatial bandwidth on estimator accuracy that propagates error into angle estimation. We observe convergence in RMSE over all values of $\Delta\theta$ at $\theta = 0^\circ$ due to the experiment setup that increases the angular extent of calibration sources in training about nadir. We would expect the convergence point to move if we moved the interval off nadir. In all cases, the RMSE at $\theta = 0^\circ$ is on the order of tenths of a degree and increases as the test source moves off nadir. The largest errors of approximately 19° are realized for test sources approaching $\pm 90^\circ$ and when training snapshots are drawn over the smallest angular interval ($\Delta\theta = 1^\circ$). A small increase in $\Delta\theta$ from 1° to 4° significantly impacts the errors at the edges reducing the largest errors to approximately 2.5°.

4.5.4 Impact of the Number of Calibration Bins

DOA estimator performance with single sources is depicted in Figure 4.9 when the test values of N_b cited in Table 4.4 are used to develop the training data. Similar to the previous example, the DOA estimator bias and RMSE are reported in Figures 4.9a and 4.9b respectively to serve as a reference of DOA estimation performance when the manifold is perfectly known. The DOA estimator performance curves in Figures 4.9b and 4.9d report bias and RMSE when the manifold model is evaluated in terms of the perturbed geometry estimated in calibration. The largest errors correspond to the case where the training data has the smallest

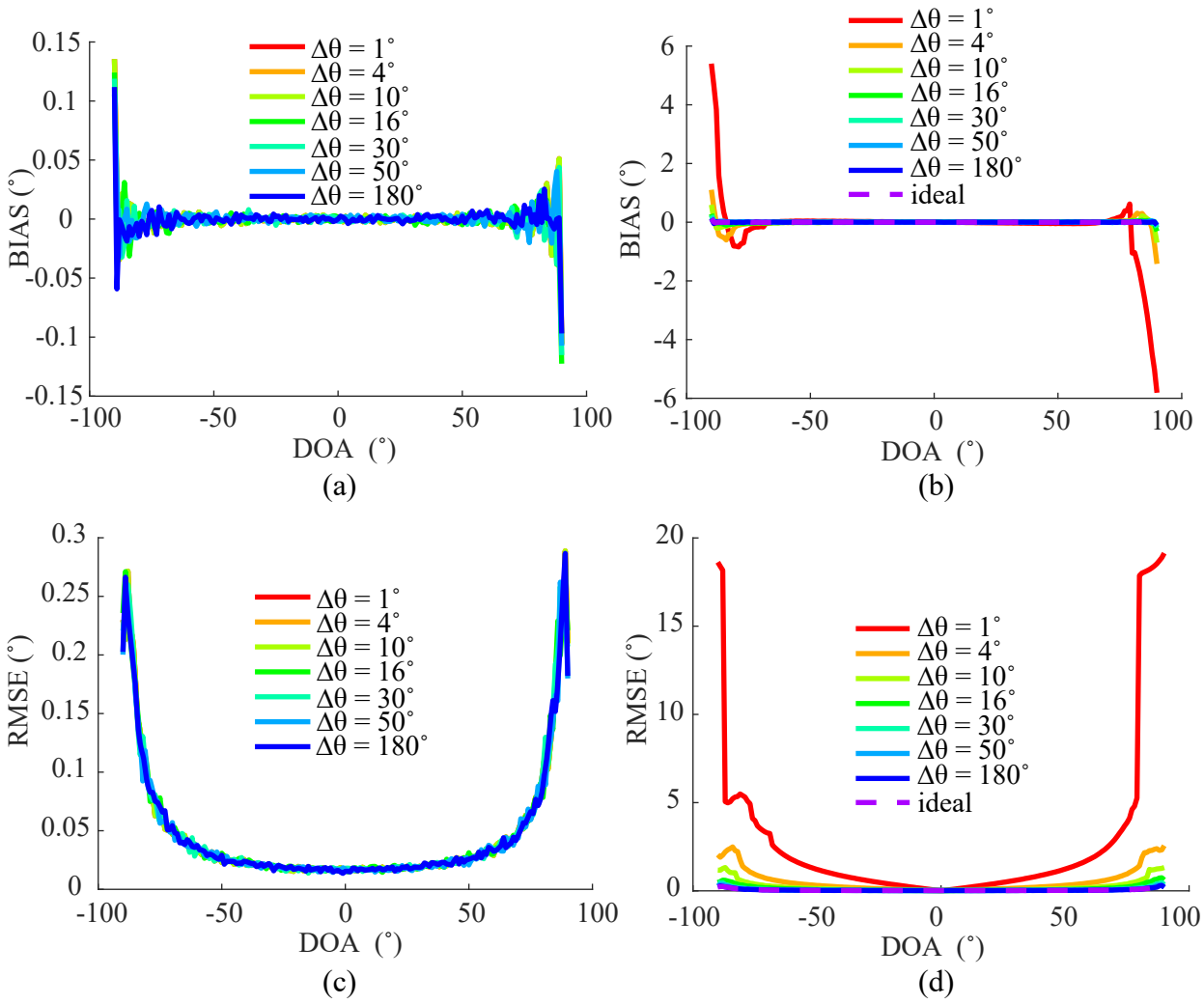

Figure 4.7: Average single source DOA estimator performance for varying degrees of calibration source spatial bandwidth tested over 100 realizations of small scale geometric perturbations: (a) estimator bias with ideal (matched) manifold, (b) estimator bias with calibrated manifold, (c) estimator RMSE with ideal (matched) manifold, (d) estimator RMSE with calibrated manifold.

number of bins in optimization. Unlike the performance curves observed when varying $\Delta\theta$, here the RMSE curves tend to follow a similar shape and the vertex moves closer to zero as N_b increases. While the error curves also demonstrate increasing uncertainty as angle increases, the largest errors realized over this experiment are also much smaller compared to the previous simulation. Here the largest error observed is slightly above 1.2° for a test source at -84°.

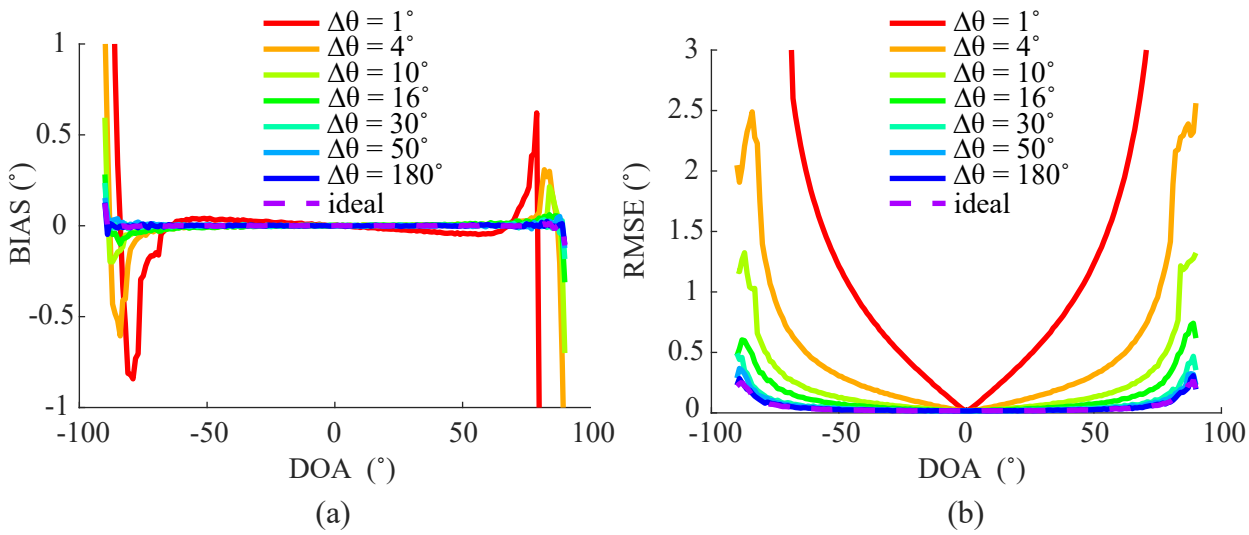

Figure 4.8: Detailed view of DOA estimator performance with calibrated manifold: (a) estimator bias, (b) estimator RMSE.

4.5.5 Summarizing Thoughts on Simulated Outcomes

Experiments 3 and 4 demonstrate the influence of training data attributes on angle estimator accuracy over 100 realizations of random geometric errors (classified as small scale). The generalized form of the Fisher Information Matrix offered in Equation 4.25 expresses the total Fisher information as a summation of the information in each calibration bin. The role of N_b is made explicit in this expression as a discrete summation over number of bins. The role of $\Delta\theta$ is rationalized for the case of geometric perturbations in Equations 4.30a and 4.30b. Experiment 3 provides numerical validation of an improvement in angle estimator performance with increasing spatial bandwidth of the calibration sources realized over 100 instantiations of random position error states. Experiment 4 confirms angle estimation performance improvements with an increasing number of calibration bins.

A comparison of the outcomes of the two experiments suggests that in the case of perturbing the nominal RDS manifold (whose positions are determined from the lever arms of the P-3 inboard subarray cited in Table 3.2) on a small scale, $\Delta\theta$ is a more significant driver of angle estimation performance than N_b. Experiment 3 demonstrates the largest reduction in error (approximately 19°) with the additional Fisher information garnered from increased

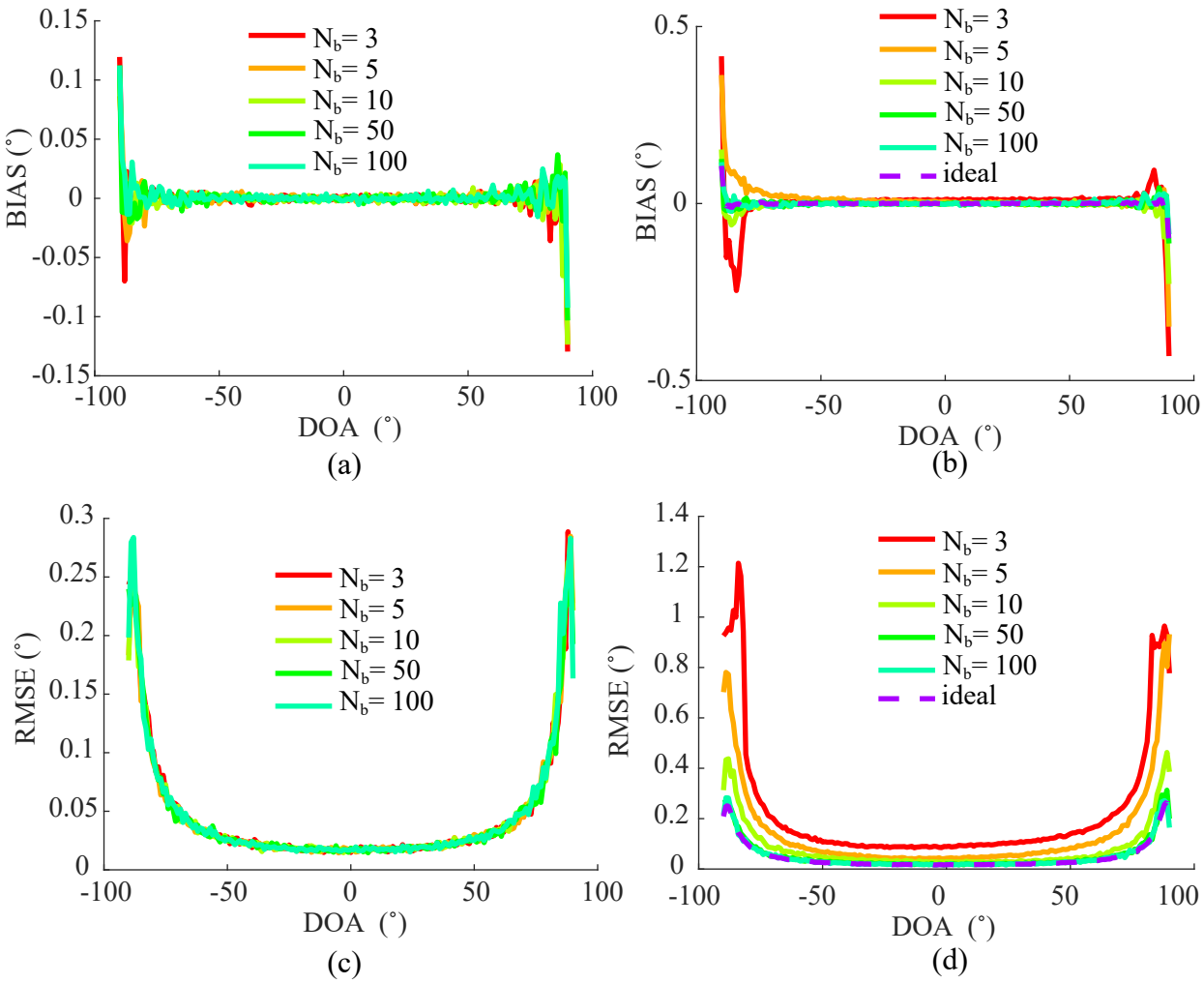

Figure 4.9: Average single source DOA estimator performance for varying number of calibration bins tested over 100 realizations of small scale geometric perturbations: (a) estimator bias with ideal (matched) manifold, (b) estimator bias with calibrated manifold, (c) estimator RMSE with ideal (matched) manifold, (d) estimator RMSE with calibrated manifold.

spatial bandwidth in training. Experiment 4 also demonstrates a reduction in angle estimator error as N_b grows to 100 but the total reduction was much smaller (approximately 1°).

4.6 Discussion

This chapter derives a maximum likelihood estimator of nonlinear manifold parameters that are common across statistically independent subsets of spatially diverse observations. The

estimator requires an analytic description of the manifold with functional dependence on source arrival angle and unknown parameters (such as geometric error or arrival angle when unknown) and guarantees a maximum likelihood estimate of model parameters under a separable Gaussian problem formulation. The estimator is numerically exercised in array shape calibration with four simulated experiments that assume geometric perturbations of a nominal manifold (consistent with the RDS center subarray's nominal geometry). The array shape calibration problem is a mathematical convenience because it admits a model of the error in closed form that is easily simulated in computation. The reliance on these examples does not mean to suggest that the dominant source of error is attributed to phase center position uncertainty. Multiple error mechanisms determine the RDS P-3 manifold in reality; their study is complex and requires the use of computational electromagnetic solvers to develop an understanding of the driving sources of error impacting the integrated arrays. An initial attempt to understand platform effects in the context of array manifold calibration is addressed further in Chapter 6.

The array shape calibration problem is used to study angle estimation performance before and after calibration. Experiments 1 and 2 suggest that biased estimates of phase center positions propagate directly into angle estimation and lead to biased estimates of the DOA. Experiments 3 and 4 numerically verify the influence of spatial bandwidth of calibration sources and the number of calibration sets on improving DOA estimation outcomes. This is demonstrated with sets of DOA estimator error curves realized by testing estimated model parameters in angle estimation of single sources over the field of view. The simulations presented in this chapter estimate the nonlinear manifold parameters (modeled as position errors) assuming perfect knowledge of arrival angle in training. This simplifies the simulation by reducing the search dimension in optimization. We could also cast a joint estimation problem that simultaneously searches for calibration source angle and geometric error.

Chapter 3 describes a methodology for characterizing the manifold at the output of the SAR processor by reorganizing pixels in the image into calibration bins with known direc-

tional sources. Application of the parametric techniques described here assume the model of the manifold is slow-time agnostic. This assumption may be ill-suited in describing the SAR focused images associated with the wing elements. The parametric form is desirable because it provides an estimator of model parameters using observations containing more than one spatial source. This is in contrast to the nonparametric forms that require measurements of single spatial sources over the field of view.

The largest challenge in applying this approach in practice is determining an analytic form of $\mathbf{A}(\boldsymbol{\eta}_{\mathbf{r}}; \boldsymbol{\Theta})$ that sufficiently describes the phenomenology influencing the array response while still offering a tractable optimization problem. A deterministic model of the array response vectors may be predicted with a full wave solver or estimated from a lookup table of single source steering vector measurements. Unique challenges face either path in determining a parametric manifold model. The former leads to a large CEM problem due to the scale of the platform and complexity of the fairing structure housing the array. The latter faces a starvation of true single source observations that must be handled with additional signal processing.

4.7 Conclusion

This chapter outlines a parametric manifold calibration framework that leverages a snapshot database to aggregate subsets of independent observations from a large snapshot superset for estimating common nonlinear manifold parameters. Estimator implementation is predicated on knowledge of the manifold model; specifically a closed form expression for the manifold with functional dependence on angle and some unknown nonlinear parameters is understood ahead of time. Analytic evidence is offered to support an argument that the estimator does not depend on the elevation-angle dependent length of the manifold vectors; such an argument justifies a unit-norm constraint asserted in the derivation of a principal components based characterization proposed in Chapter 5. The estimator is applied in a simple simulation to the array shape perturbation problem. Numerical evidence is presented indicating

that the total Fisher information in the superset increases both when the number of bins over a fixed angular interval increases and when the angular diversity of calibration sources increases. The estimation of unknown nonlinear manifold parameters reduces mismatch in the modeled manifold and leads to more accurate angle estimates. The proposed framework handles multiple spatial sources simultaneously and easily expands to a joint estimation problem where angle is only approximately known. The parametric methodology represents a significant milestone along a broader research trajectory focused on implementing a practical multitarget calibration strategy for the SAR sounder.

Chapter 5

Nonparametric Manifold Calibration with Subspace Clustering and Snapshot Editing

Abstract

Nonparametric manifold calibration techniques characterize an array's directional response by measuring snapshots from single spatial sources with known arrival angles over dense calibration grids. In cases where the source waveform is unknown, the principal component of the array covariance matrix provides a unit norm estimate of the steering vector. Though germane to the multichannel SAR sounder problem where scatterers serve as calibration targets (and hence the waveform is unknown), the principal component form of nonparametric calibration inherits specific challenges from the sounder's sensing geometry that complicates the immediate application of this method. Specifically, many data sets lack enough single source measurements over the field of view while the number of two-source measurements are more abundant. Two-source observations are undesirable in the nonparametric calibration problem because they lead to biased estimates of manifold vectors that ultimately degrade angle estimation performance. This chapter proposes and successfully demonstrates an adaptation of the principal components form of nonparametric calibration for the SAR sounder problem. The methodology adopts a support measure based on the generalized likelihood ratio test (GLRT) that is predicted to be more robust to array calibration errors and that helps to extract approximately single source calibration pixels in the multichannel imagery. Approximately single source calibration bins are assembled by editing

two-source observations based on a GLRT measure, enabling measurement of RDS manifolds from three independent calibration sets. The measured manifolds demonstrate significant improvements in angle estimation relative to the nominal manifold model, indicating a potential to reduce vertical elevation errors of RDS-derived DEMs in tomography.

5.1 Introduction

Chapter 4 develops a parametric framework that leverages a large maximum likelihood estimator of nonlinear manifold parameters across statistically independent sets of calibration bins. Application of this estimator is desirable because it handles calibration with multiple targets simultaneously and generalizes to the case where calibration source angles are only approximately known. The latter is a powerful property as it offers potential immunity to registration errors imparted by the ArcticDEM; the surface intersection angles can serve as well-informed initialization points of the unknown $\boldsymbol{\Theta}$ parameters in solving the optimization problem of Equation 4.22. Of course leveraging this framework requires knowledge of the parametric model $\mathbf{A}(\boldsymbol{\Theta}, \boldsymbol{\eta}_{nl})$, which accounts for platform effects influencing the array in operation.

Nonparametric manifold calibration enables measurement of the array response and is thus a necessary *first step* in the development of a parametric model of $\mathbf{a}(\theta)$ that enables the implementation of the large estimator framework of Chapter 4. Nonparametric forms require single source observations collected over dense calibration grids. Historic techniques for capturing single source observations with the SAR sounder rely on measuring reflections from the surfaces of smooth and non-penetrative extended surface targets with a maneuvering platform to rotate through the elevation angle θ, interpreting roll as the arrival angle. This approach is subject to an aircraft's roll restrictions and prone to errors introduced when nonzero cross-track slopes are neglected. Dedicated calibration flights are not always realizable in the field and many seasons lack the benefit of collections of this kind.

The techniques outlined in this chapter present alternatives for calibrating RDS data sets after the SAR processor, provided that the imagery aligns with an independent surface elevation model like the ArcticDEM. It is emphasized here that both approaches would ideally be leveraged when possible to obtain the most accurate representation of the manifold. Manifold calibration after the SAR cannot account for slow-time dependent perturbations over the aperture such as phase variation imparted by moving control surfaces or wing vibrations. Characterization of these effects from the data will likely mandate a calibration algorithm that precedes the SAR. The collection of specular surface reflections are expected to be essential in measuring slow-time dependent manifold perturbations in these cases.

The remainder of this chapter is organized as follows. The principal eigenvector estimate of the steering vector is derived from the compressed likelihood function for the single source case in Section 5.2. Section 5.3 approaches nonparametric calibration from the perspective of the SAR sounder problem, offering an observation model and processing architecture to edit poor quality calibration snapshots based on a subspace clustering measure prior to eigen-decomposition. Section 5.4 demonstrates the application of the proposed nonparametric calibration framework in measuring manifolds from three independent data sets. The measured manifolds are tested in angle estimation against the nominal model and demonstrate a large reduction in estimator error realized with a measured manifold. Discussion is offered in Section 5.5 prior to conclusion of the chapter.

5.2 Principal Components Based Manifold Characterization

Nonparametric manifold calibration via principal components offers a means of characterizing the array response when pilot calibration (where the source waveform is known) is not available or practical. A derivation is offered here to justify the estimation of the orientation of the vector $\mathbf{a}(\theta) \in \mathbb{C}^{P\times 1}$ in complex P dimensional space using the principal component of the array covariance matrix resulting from a single directional source. The derivation follows one that is outlined in the appendix of a recently submitted manuscript that summarizes this

aspect of the dissertation research [53]. The nonparametric methods assume the availability of single source observations. In the SAR sounder problem, single source snapshots are not necessarily available over all angles of interest. This assumption is addressed in Section 5.3 and offers justification for the relaxation of the single source requirement in certain cases.

The derivation that follows requires the following assumptions in addition to the common assumptions laid out at the beginning of Chapter 2:

A1 : Number of sources, Q, is one,

A2 : Source arrival angle, θ, is known.

We assume the linear model of Equation 2.1 to describe the m^{th} snapshot, restated here:

$$\mathbf{x}_m = \mathbf{a}(\theta)s_m + \mathbf{n}_m. \tag{5.1}$$

The vector $\mathbf{x}_m$ is taken to be an observation in a set of M such measurements, denoted with the matrix $\mathbf{X} \in \mathbb{C}^{P\times M}$. A separable Gaussian form is assumed such that $\mathbf{x}_m \sim \mathcal{C}\left(\mathbf{a}(\theta)s_m, \mathbf{R}_\mathbf{x}\right)$ holds, leading to a compressed likelihood function that is parameterized by the unknown manifold vector for a given set of measurements [68]:

$$L(\mathbf{a}(\theta); \mathbf{X}) = \mathrm{tr}\Big(\mathbf{P}_{\mathbf{a}(\theta)}\mathbf{R}_\mathbf{x}\Big). \tag{5.2}$$

Obtaining a nontrivial estimate of $\mathbf{a}(\theta)$ from this form requires the use of a constraint. We constrain the problem by forcing the length of the manifold vector to be a constant (in this case one). This leads to the following constrained optimization which can be solved using a Lagrange multiplier:

$$\text{maximize:} \quad \mathrm{tr}\Big(\mathbf{P}_{\mathbf{a}(\theta)}\mathbf{R}_\mathbf{x}\Big) \tag{5.3a}$$

$$\text{subject to:} \quad \mathbf{a}^H(\theta)\mathbf{a}(\theta) = 1. \tag{5.3b}$$

An important remark is noted here. Because the constraint in Equation 5.3b removes the directional dependence of the manifold vector magnitude, the solution to the maximization cannot recover the angular magnitude variation, $\|\mathbf{a}(\theta)\|_2$. This is not expected to have any influence over the estimator derived in Chapter 4 to estimate the nonlinear manifold parameters, based on its use of a projection operator to evaluate the cost of a particular solution. This rationale suggests that the estimated manifold unit vectors are sufficient for implementing the framework as outlined in Chapter 4. The assumption should be revisited if the parametric form is formulated in a different manner.

Equation 5.2 is rewritten in terms of the definition of the projection matrix as

$$L(\mathbf{a}(\theta);\mathbf{X}) = \mathrm{tr}\Big(\mathbf{a}(\theta)\left(\mathbf{a}(\theta)^H\mathbf{a}(\theta)\right)^{-1}\mathbf{a}(\theta)^H\mathbf{R}_\mathbf{x}\Big). \tag{5.4}$$

In this form we recognize that $\mathbf{a}(\theta)^H\mathbf{a}(\theta)$ is unity based on the constraint and rewrite the previous expression as

$$L(\mathbf{a}(\theta);\mathbf{X}) = \mathrm{tr}\Big(\mathbf{a}(\theta)\mathbf{a}(\theta)^H\mathbf{R}_\mathbf{x}\Big). \tag{5.5}$$

The (i,j) entry of the $P \times P$ Hermitian matrix $\mathbf{R}_\mathbf{x} \in \mathbb{C}^{P\times P}$ is defined as

$$r_{i,j} = [\mathbf{R}_\mathbf{x}]_{i,j} := E\left\{x_i x_j^*\right\}. \tag{5.6}$$

The term $\mathbf{r}_i$ is introduced to represent the i^{th} column vector of $\mathbf{R}_\mathbf{x}$. The argument of the trace operator in Equation 5.5 is rewritten in the form that follows (where the θ argument

of the manifold vector is suppressed to simplify the equations):

$$\mathbf{a}\mathbf{a}^H\mathbf{R}_\mathbf{x} = \begin{pmatrix} a_1\mathbf{a}^H\mathbf{r}_1 & a_1\mathbf{a}^H\mathbf{r}_2 & \dots & a_1\mathbf{a}^H\mathbf{r}_P \\ a_2\mathbf{a}^H\mathbf{r}_1 & a_2\mathbf{a}^H\mathbf{r}_2 & \dots & a_2\mathbf{a}^H\mathbf{r}_P \\ \vdots & \vdots & \ddots & \vdots \\ a_P\mathbf{a}^H\mathbf{r}_1 & a_P\mathbf{a}^H\mathbf{r}_2 & \dots & a_P\mathbf{a}^H\mathbf{r}_P \end{pmatrix}. \tag{5.7}$$

Here we have adopted the general notation a_i to indicate the i^{th} entry of the manifold vector. Equation 5.5 is equivalent to the following sum of diagonal entries of Equation 5.7

$$L(\mathbf{a};\mathbf{X}) = a_1\mathbf{a}^H\mathbf{r}_1 + \cdots + a_P\mathbf{a}^H\mathbf{r}_P \tag{5.8}$$

Which offers a compact representation as the following discrete summation over P:

$$L(\mathbf{a};\mathbf{X}) = \sum_{i=1}^{P} a_i\mathbf{a}^H\mathbf{r}_i. \tag{5.9}$$

Moving $\mathbf{a}$ outside of the summation leads to the following linear combination of the columns of the covariance:

$$L(\mathbf{a};\mathbf{X}) = \mathbf{a}^H\sum_{i=1}^{P} a_i\mathbf{r}_i. \tag{5.10}$$

The expression above is equivalent to the following quadratic form:

$$L(\mathbf{a};\mathbf{X}) = \mathbf{a}^H\mathbf{R}_\mathbf{x}\mathbf{a}. \tag{5.11}$$

We use this form and introduce the real Lagrange multiplier λ to state the following real-valued cost function subject to the constraint as:

$$J(\mathbf{a},\mathbf{a}^H) = \mathbf{a}^H\mathbf{R}_\mathbf{x}\mathbf{a} + \lambda\left(\mathbf{a}^H\mathbf{a} - 1\right), \tag{5.12}$$

The gradient of the cost function taken with respect to $\mathbf{a}^H$ is

$$\frac{\partial J(\mathbf{a}, \mathbf{a}^H)}{\partial \mathbf{a}^H} = \mathbf{R_x a} + \lambda \mathbf{a}, \tag{5.13}$$

Setting this result to zero, admits the classic eigenvector equation (where I_P refers to the $P \times P$ identity matrix)

$$(\mathbf{R_x} + \lambda I_P)\, \mathbf{a} = \mathbf{0}, \tag{5.14}$$

Confirming that the array manifold vector of the calibration source is an eigenvector of the data covariance matrix.

Introducing σ_s^2 to denote the average power of the calibration source in Equation 5.1, the spectral factorization of $\mathbf{R_x}$ is written as

$$\mathbf{R_x} = \sigma_s^2 \mathbf{a}\mathbf{a}^H + \sigma_n^2 I_P. \tag{5.15}$$

The expression above makes use of the assumption that $\mathbf{n}_m \in \mathbb{C}^{P \times 1}$ represents a complex Gaussian random vector such that $\mathbf{n}_m \sim C(\mathbf{0}, \sigma_n^2 I_P)$. Because the observation covariance matrix is taken to be positive definite and Hermitian, we can conclude that the P eigenvalues of $\mathbf{R_x}$ are real and positive and can be written in descending order as $\lambda_1, \ldots, \lambda_P$ with λ_1 corresponding to the maximum eigenvalue. The corresponding eigenvectors form an orthonormal basis $[\mathbf{u}_1, \ldots, \mathbf{u}_P]$ that spans $\mathbb{C}^{P \times 1}$.

We can substitute the spectral factorization of $\mathbf{R_x}$ into the eigenvector equation as follows:

$$\left(\sigma_s^2 \mathbf{a}\mathbf{a}^H + \sigma_n^2 I_P\right) \mathbf{a} = \lambda \mathbf{a}. \tag{5.16}$$

Factoring the $\mathbf{a}$ inside the parentheses and recalling that the manifold vector was defined to be unit norm, we have

$$\left(\sigma_s^2 + \sigma_n^2\right) \mathbf{a} = \lambda \mathbf{a}. \tag{5.17}$$

When the power of the incident source exceeds the observation noise of the array, then the eigenvalue of $\mathbf{a}$ is considered the dominant eigenvalue and the corresponding eigenvector is referred to as the principal component. This vector is parallel to the true manifold vector in $\mathbb{C}^{P\times 1}$. Note that the underlying phase reference is unknown. Hence the principal component obtained in eigendecomposition of an array covariance matrix is phase referenced to a channel in the array by normalizing all of the elements to $e^{j\phi_{ref}(\theta)}$ where $\phi_{ref}(\theta)$ refers to the phase of the entry of the principal eigenvector $\mathbf{u}_s$ corresponding to the reference element:

$$\phi_{ref}(\theta) = \angle\left[\mathbf{u}_s\right]_{ref}. \tag{5.18}$$

5.3 Nonparametric Methodology for SAR Sounders

Recall that the parametric framework developed in Chapter 4 is desirable because it accommodates calibration with multiple targets simultaneously and natively handles joint estimation of manifold parameters and angle. The application of the parametric approach is predicated on an analytic description of the array manifold with functional dependence on deterministic model parameters. In the absence of a parametric model of the complex gain patterns of the embedded elements, we must first determine the single source steering vectors over the field of view either through a deterministic model (discussed in Chapter 6) or measurements. In our problem, the pilot calibration method of estimating the steering vectors is inapplicable; this leaves the principal components approach as the only viable option for measuring SAR sounder manifolds and motivates a requirement to cull the single source observations that are suitable for measuring the array response vectors over $\pm 90°$.

The challenge we face in applying the principal components flavor of nonparametric calibration is that we lack a sufficient number of single source observations over a calibration grid. Recall that the methodology proposed in Chapter 3 allows us to tag each SAR pixel with the angles of incidence at the surface which immediately provides knowledge of the number of scattering sources Q in a pixel. To illustrate the nature of the calibration observations

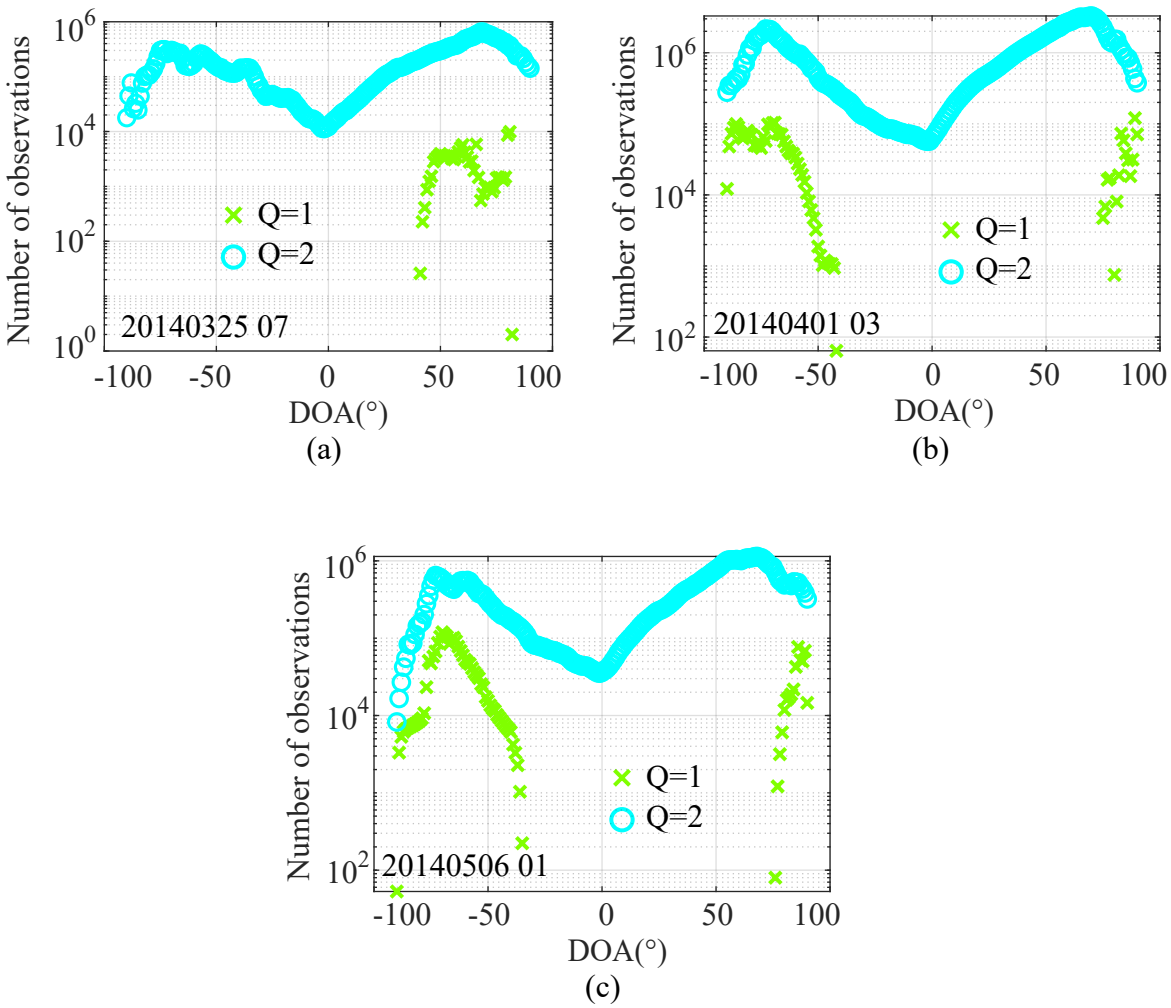

Figure 5.1: Number of single and two source pixels in 1° DOA bins by calibration data set: (a) 20140325 07, (b) 20140401 03, (c) 20140506 01.

available in our data sets, the number of single and two source pixels per 1° DOA bin are plotted in Figure 5.1 for each of the calibration data sets analyzed for this dissertation. All of the data sets suggest that the concentration of single source pixels in 1° bins appear far off nadir while the number of two source pixels span the entire field of view, $-90° \leq \theta \leq 90°$. This underlines the problem with directly applying the principal component method of nonparametric calibration for measuring the RDS manifold.

The RDS measures single sources either when it captures the specular return of a flat interface or when a coincident source is shadowed by the terrain. In most cases, we observe two sources at a time which justifies the need for multitarget calibration. Yet multitarget

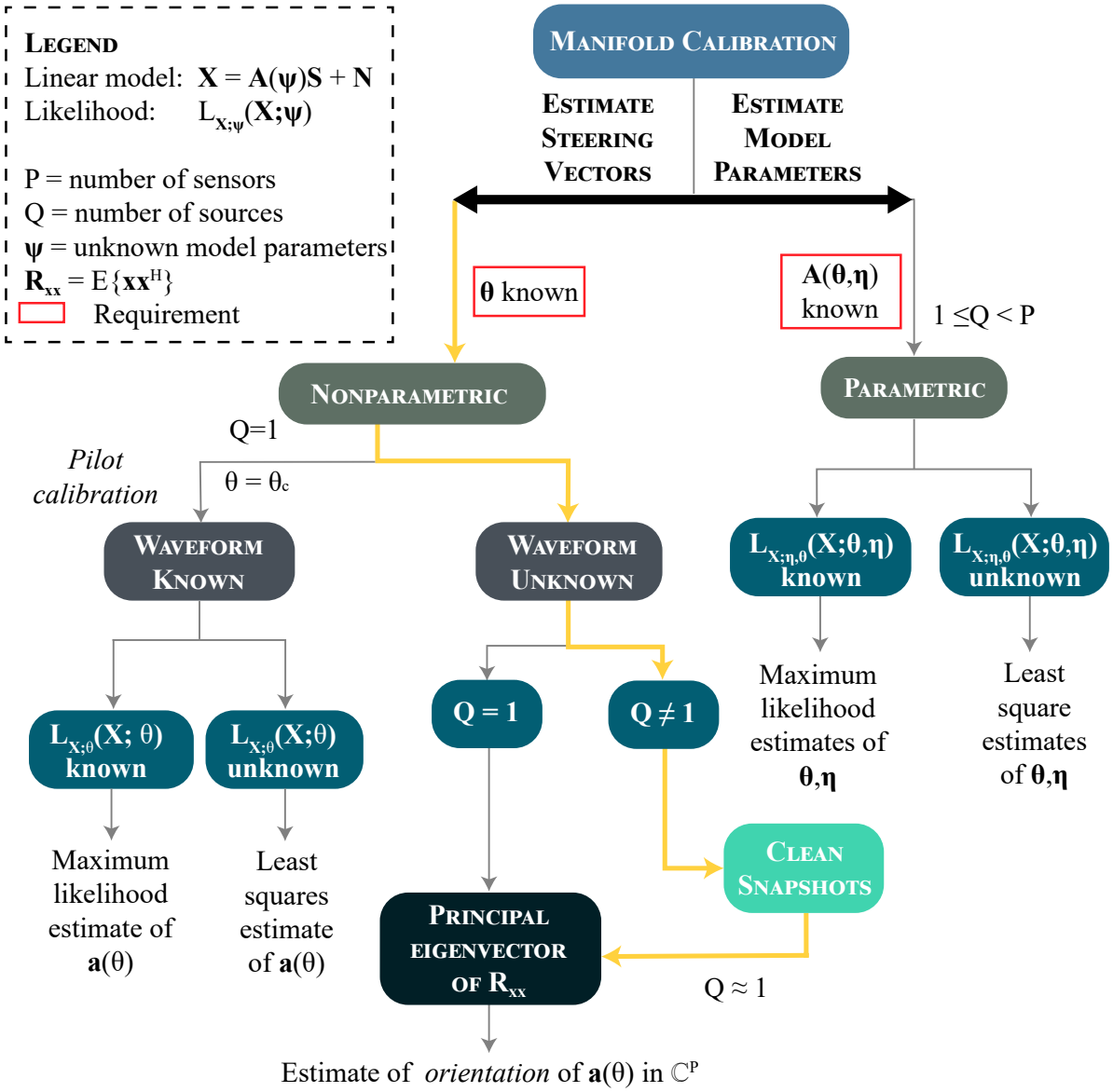

Figure 5.2: Classic parametric/nonparametric manifold calibration taxonomy with modified nonparametric route to enable manifold measurements with SAR sounders.

calibration mandates a manifold model which must be predicted from a full-wave solver or measured from data. The possible solutions for calibrating the RDS manifold face circular challenges and the application of a classic approach per the taxonomy offered in Figure 1.1 is not immediately straightforward. Pursuing the measured manifold characterization with the principal components method means that we need some way of culling those measurements that sufficiently *approximate* single source observations before eigendecomposition of the

array covariance matrix in a calibration bin.

To facilitate extraction of calibration targets from the single look complex SAR imagery, the classic manifold calibration routes outlined in the taxonomy of Figure 1.1 which assume single source observations are modified for our problem by introducing a culling or cleaning step based on subspace clustering prior to estimating single source manifold vectors. The nonparametric/parametric manifold calibration taxonomy originally offered in Chapter 1 is hence altered to show a proposed nonparametric approach tailored to the RDS data sets. The updated taxonomy is presented in Figure 5.2 with a yellow route indicating the path reflected in this dissertation. The cleaning step is an editing approach that clusters measurements in a calibration bin and throws away observations that indicate a dominance of subspace interference.

5.3.1 Adopted Observation Model for Nonparametric Calibration

We relax the single source observation requirement imposed in the nonparametric regime to allow for an additional spatial source within a calibration bin. We limit Q to be at most two in our implementation of nonparametric calibration and bin observations based on a calibration angle of interest. This section describes the model of the measurement sets obtained by binning observations in the snapshot database. The matrix of M_n complex-valued, length P observation vectors (which may be single source or two source measurements) in the n^{th} calibration bin are denoted using the variable $\mathbf{X}_n \in \mathbb{C}^{P \times M_n}$. This matrix may be written as the following concatenation of the $Q = 1$ and $Q = 2$ measurement matrices as follows:

$$\mathbf{X}_n = [\mathbf{X}_{n1} \mid \mathbf{X}_{n2}] \tag{5.19}$$

Where

- $\mathbf{X}_{n1} \in \mathbb{C}^{P \times M_{n1}}$ refers to the M_{n1} observations for which $Q = 1$ in bin n,

- $\mathbf{X}_{n2} \in \mathbb{C}^{P \times M_{n2}}$ refers to the M_{n2} observations for which $Q = 2$ in bin n.

The total number of snapshots in bin n is then the sum of the single source and two source snapshots $M_n = M_{n1} + M_{n2}$.

Following the linear model summarized in Equation 4.6, the single source observations take the following form:

$$\mathbf{X}_{n1} = \mathbf{a}(\theta_n^c)\mathbf{S}_n^c + \mathbf{N}_{n1}. \tag{5.20}$$

Here the c superscript emphasizes that θ_n^c refers to the calibration angle of interest in bin n.

To develop a description of $\mathbf{X}_{n2}$, the variable $\mathbf{\Theta}_{n2} \in \mathbb{R}^{2\times M_{n2}}$ is introduced to denote the $2 \times M_{n2}$ matrix of spatial sources per observation in the $Q = 2$ subset, determined in the surface data object creation (by querying an independent surface DEM). Let m_{n2}, defined as an integer over the interval $1 \leq m_{n2} \leq M_{n2}$, index the observations in this set. The m_{n2} column vector of the $\mathbf{\Theta}_{n2}$ matrix is denoted as $\boldsymbol{\theta}_{m_{n2}}$ and takes the following general form

$$\boldsymbol{\theta}_{m_{n2}} = \left[\theta_n^c, \theta_{m_{n2}}^i\right]^T, \tag{5.21}$$

Where an i superscript intends to emphasize that the source from $\theta_{m_{n2}}^i$ is regarded as subspace interference with respect to the calibration angle θ_n^c. The m_{n2} column of $\mathbf{X}_{n2}$ is modeled as the following linear combination of a calibration source and interference observed in multichannel noise

$$\mathbf{x}_{m_{n2}} = \mathbf{a}(\theta_n^c)s_n^c + \mathbf{a}(\theta_{m_{n2}}^i)s_{m_{n2}}^i + \mathbf{n}_{m_{n2}}. \tag{5.22}$$

Some remarks are stated regarding measurements in the n^{th} calibration bin:

1. The DOAs of each measurement are known a priori based on the creation of snapshot databases as described in Chapter 3. This allows us to restrict measurements based on the angular separation of the calibration source and coincident interferer. To ensure sufficient isolation between the signal of interest and the interference, only measurements whose coincident interferer are more than a beamwidth away are allowed in a calibration bin.

2. Each calibration bin is made up of aggregated observations drawn from disjoint pixel neighborhoods in the imagery. The snapshots are highly correlated because they each contain the coherent scattering contribution from a common spatial source corresponding to θ_n^c, however the set of observations is statistically nonstationary. The observations within a bin exhibit large variation over the set based on differences in illuminating power, terrain scattering properties, and propagation losses for example from one snapshot to the next.

3. The image of the signal subspace in our observation space for the case of $Q = 1$ is well-described as a line through the origin in C^P that is parallel to the true array response vector $\mathbf{a}(\theta_n^c)$.

4. In the case of $Q = 2$, the image of the signal plus interference subspace in our observation space can be geometrically interpreted as a set of up to M_{n2} intersecting planes in C^P through a common line that is parallel to $\mathbf{a}(\theta_n^c)$.

5.3.2 Principal Eigenvector Calibration with Low Rank Interference

Because the majority of observations in the snapshot database correspond to $Q = 2$ cases, the typical assumption of $Q = 1$ in the derivation of a single source steering vector estimator is relaxed in this work to allow $Q = 2$ measurements in a calibration bin provided that the calibration source dominates the measurement. While we prefer single source snapshots with high SNR for measuring the manifold, we allow $Q = 2$ snapshots provided that they have sufficient isolation or signal to interference ratio (SIR) such that the following is a reasonable approximation:

$$\mathbf{x}_{m_{n2}} \approx \mathbf{a}(\theta_n^c) s_n^c + \mathbf{n}_{m_{n2}}. \tag{5.23}$$

In the analysis that follows, SIR or isolation is defined as the ratio of power from the desired spatial source to the power of the subspace interference.

Table 5.1: Calibration bin setup for testing DOA estimator accuracy with manifold measured when calibration source is measured in the presence of subspace interference.

		Source Specification in j^{th} Calibration Bin			
N_b	$\Delta\theta_c$	M_j	Q_j	SNR_j (dB)	INR_j (dB)
181	$-90° \leq \theta_c \leq 90°$	1,000	2	55	50
181	$-90° \leq \theta_c \leq 90°$	1,000	2	55	45
181	$-90° \leq \theta_c \leq 90°$	1,000	2	55	40
181	$-90° \leq \theta_c \leq 90°$	1,000	2	55	35
181	$-90° \leq \theta_c \leq 90°$	1,000	2	55	30
181	$-90° \leq \theta_c \leq 90°$	1,000	2	55	25
181	$-90° \leq \theta_c \leq 90°$	1,000	2	55	20
181	$-90° \leq \theta_c \leq 90°$	1,000	2	55	15
181	$-90° \leq \theta_c \leq 90°$	1,000	2	55	10
181	$-90° \leq \theta_c \leq 90°$	1,000	2	55	5

A simple simulated example is offered to justify this approach. The example that follows demonstrates maximum likelihood angle estimator performance with a measured manifold determined in a nonparametric calibration step from binned snapshots each containing two sources. Subspace interference is injected into each calibration bin. The calibration source SNR is fixed throughout the simulation to 55 dB and the thermal noise floor is set to unity with no loss of generality. The interference to noise ratio (INR) is swept over the interval 5 dB $\leq$ INR (dB) $\leq$ 55 dB. At the high end of tested isolation values, the interference is 5 dB higher than the noise floor and on the low end the interference is 5 dB below the level of the calibration source. The angle of the interfering signal is drawn from a uniform distribution for every calibration bin but the angle is not allowed within one beamwidth of the calibration source. The interference angle is fixed within a calibration bin so that one calibration bin is corrupted with one subspace interferer at a time. Each bin uses 1,000 snapshots to estimate the covariance matrix for determining the principal eigenvector. The

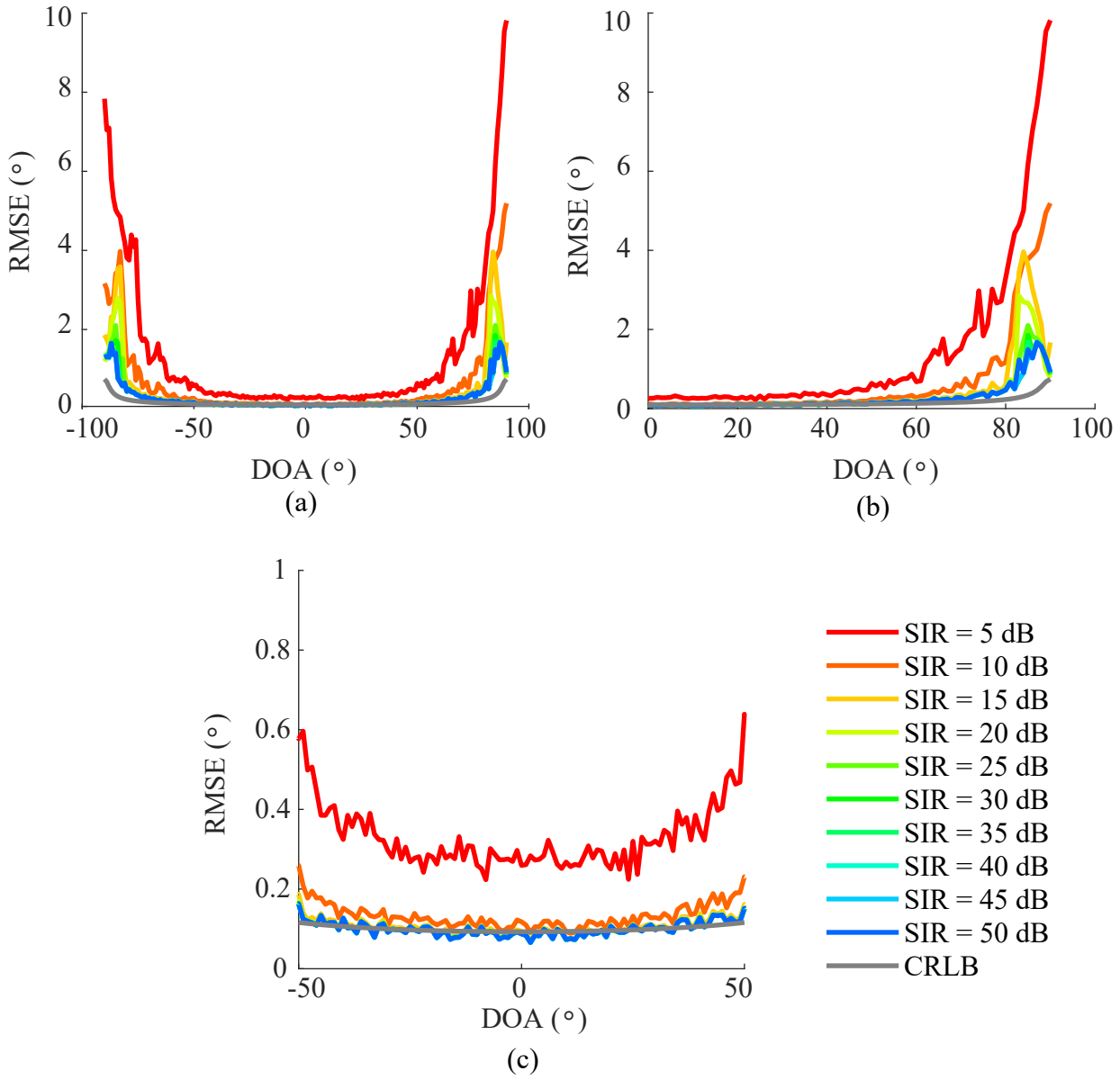

Figure 5.3: Simulated maximum likelihood DOA estimator performance using a manifold measured in the presence of low rank subspace interference over varying levels of signal to interference ratio (SIR): (a) RMSE over $\pm 90°$, (b) Detailed view for $0° \leq \theta \leq 90°$, (c) Detailed view for $|\theta| \leq 50°$.

specification of spatial sources in the calibration bins are summarized in Table 5.1.

Angle estimator performance for a pristine (nonperturbed) array whose geometry is consistent with that of the RDS center P-3 subarray is evaluated over 100 Monte Carlo trials. Each trial leads to a slightly different realization of the calibration bins used to create a measured manifold for angle estimation. In other words, each value of θ_c is tested against

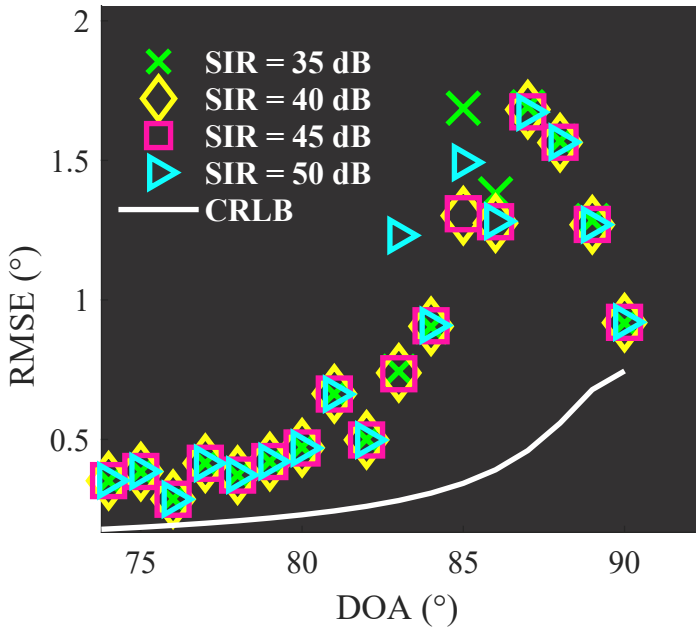

Figure 5.4: Detail at the edge of the field of view showing simulated MLE DOA performance when using measured manifolds obtained with high signal to interference (SIR) calibration sources. Results suggest a SIR limit beyond which angle estimation does not significantly improve for the given calibration bin size tested (corresponding to 1,000 snapshots per calibration bin).

100 different interference angles for a tested SIR level. The measured manifold is then used in maximum likelihood angle estimation of a single high SNR directional, source swept over an angle grid. The test DOAs are chosen to center directly on the calibration grid. The use of a nonperturbed array facilitates comparison of measured estimator performance to the classic CRLB.

The simulated angle estimator performance with a manifold measured via principal components in the presence of low-rank interference is demonstrated for varying levels of calibration to interference source isolation in Figure 5.3. The full field of view is offered in Figure 5.3a while 5.3b and 5.3c present detailed views of one side of the angle range and the center of the field of view respectively. The worst performance (or highest RMSE) is observed when the interference power takes the highest tested value (corresponding to the lowest tested isolation). The results support a trend of increasing accuracy with increasing isolation; as the power of the interference decreases with respect to the calibration source power, the estima-

tor error approaches the lower bound. The RMSE curves corresponding to SINR values that exceed 10 dB are nearly indistinguishable over the interval of $-50^\circ \leq \theta \leq 50^\circ$. Differences realized in estimator accuracy become more apparent as θ moves out to the edges of the field of view, especially as $|\theta| \geq 80^\circ$. Increasing values of SIR beyond 15 dB show significant improvement at the edges. The 5 dB increase from 15 dB isolation to 20 dB isolation shows as much as a 1° reduction in error for example at 84°.

This simulated example presented here models angle estimation outcomes using a manifold measured in the presence of spatial interference and offers evidence that justifies our relaxation of the $Q = 1$ assumption as proposed in this dissertation and the associated manuscript [53]. While the quality of nonparametric manifold calibration through principal components does degrade when the calibration bins are corrupted by spatial interference, the degradation (as quantified by carrying the measured manifold through angle estimation) *decreases* as the interference power decreases with respect to that of the calibration source. The results in Figure 5.3 reinforce the rationale of modifying the traditional nonparametric methodology for the SAR sounder problem as illustrated in the revised taxonomy of Figure 5.2. The degradation observed in lower isolation scenarios and at the edges of the field of view is attributed to the interference manifold vector $\mathbf{a}(\theta_i)$ biasing the estimate of a given $\mathbf{a}(\theta_c)$. The extent to which a biased measurement of the manifold can be used to develop a manifold model for application of the parametric framework outlined in Chapter 4 remains unclear. The desire to ultimately determine an $\mathbf{A}(\theta, \boldsymbol{\eta})$ is restated here to remind the reader of the importance of working towards a calibration strategy that handles multiple targets simultaneously.

Finally we may note that while this example supports the merit of pursuing nonparametric manifold calibration when $Q = 2$, the numerical results of this particular experiment do not appear to confirm a convergence to the CRLB in the high SIR limit. To illustrate this observation, a detailed view of the RMSE curves for 35 dB $\leq$ SIR is presented in Figure 5.4. The results of the four tested isolation levels completely align over the intervals

$72^\circ \leq \theta \leq 82^\circ$ and $87^\circ \leq \theta \leq 90^\circ$. The small variation in RMSEs observed in the 35 dB and 50 dB curves between $83^\circ \leq \theta \leq 86^\circ$ is expected to converge to the values shown by the 40 dB and 45 dB curves with additional Monte Carlo runs. The behavior demonstrated here seems to suggest a high isolation limit on the calibration sources beyond which DOA estimator accuracy does not improve. The experiment as designed is insufficient to contradict the efficiency of the MLE with the manifold measured in the presence of low rank interference. The observations here are interpreted as a bound *given the number of snapshots used in each calibration bin*. Though not tested, it is expected that a measured manifold from high SNR calibration sources that are sufficiently isolated from spatial interference and which provide a larger number of snapshots in each bin would improve performance at the edges of the field of view relative to results demonstrated here.

5.3.3 Subspace-Based Snapshot Editing

The results demonstrated in Figure 5.3 show that nonparametric techniques may still be leveraged in cases where $Q = 2$ and the resulting angle estimation performance improves as a function of increasing isolation. This motivates the implementation of techniques for identifying high SINR observations in the snapshot database. The problem at hand is interpreted as a subspace detection problem where the objective is to identify a signal from a direction of interest in the presence of low rank subspace interference. Identifying high quality calibration snapshots in the presence of subspace interference is compounded by the fact that the array is not well calibrated at the start of calibration processing. The reader is asked to recall the experimental evidence presented at the close of Chapter 3 that we interpret as justification for refined manifold calibration. Specifically a geometric nulling beamformer is applied in 2-D image formation with a coarsely measured manifold and compared to that of the nominal manifold model. The measured manifold demonstrates greater clutter suppression over the nominal model (defined based on Equation 2.35). We interpret the improved clutter mitigation as confirmation that the measured manifold is better matched to truth

than the nominal model.

The initial approach for culling calibration measurements (see both [54] and [9]) in a bin derives an estimate of calibration source power to interference source power using the pseudoinverse based on a measurement's source DOAs $\mathbf{\Theta}_m = [\theta_c, \theta_i]^T$ stored in the snapshot database and the nominal manifold model. The pseudoinverse is stated here in terms of the nominal manifold matrix $\tilde{\mathbf{A}}(\mathbf{\Theta}_m)$ as:

$$\left[\hat{s}_m^c, \hat{s}_m^i\right]^T = \left(\tilde{\mathbf{A}}^H(\mathbf{\Theta}_m)\,\tilde{\mathbf{A}}(\mathbf{\Theta}_m)\right)^{-1}\tilde{\mathbf{A}}^H(\mathbf{\Theta}_m)\,\mathbf{x}_m. \tag{5.24}$$

The pseudoinverse solution of the i^{th} source preserves the component of s_i that is orthogonal to all $1 \leq q \leq Q$ where $i \neq q$. This is realized by an underlying null steering for all sources for $q \neq i$. This estimator degrades when the manifold vectors admit correlation and requires knowledge of the array response in both the calibration and interference directions. The estimates in Equation 5.24 are used to assign an estimate of isolation for each of the two-source observations in the database as the ratio of $\hat{s}_m^c$ to $\hat{s}_m^i$. This is compared to a 15 dB threshold to extract pixels for characterizing the manifold. The approach is limited in that it requires knowledge of Q manifold vectors and leads to a heuristic threshold which is not robust.

Subspace signal detection in the presence of subspace interference and noise is developed in [96] for several variations of problems which admit matched subspace detectors [97] through the derivation of their respective generalized likelihood ratio tests (GLRT). The GLRT refers to a class of detectors that substitute maximum likelihood estimates of unknown nuissance parameters to solve binary hypothesis testing problems. The authors of [96] derive a detector to test for a subspace signal from a direction of interest in the presence of interference by formulating the following binary detection problem for unknown source power and noise power (presented in a nomenclature that is consistent with this dissertation):

$\mathbf{H_0}$: $\mathbf{x}_m \sim \mathcal{C}(\mathbf{a}_i s_m^i, \sigma_n^2 I_P)$,

$\mathbf{H_1}$: $\mathbf{x}_m \sim \mathcal{C}\left(\mathbf{a}_c s_m^c + \mathbf{a}_i s_m^i, \sigma_n^2 I_P\right)$.

Under the null hypothesis, the observation $\mathbf{x}_m$ is modeled as interference, treated as a deterministic and unknown signal from arrival angle θ_i. The likelihood function under hypothesis j is written as

$$L_j(\mathbf{x}_m; \mathbf{H}_j) = L_j(\mathbf{x}; \hat{\boldsymbol{\eta}}_j) \tag{5.25}$$

Where $\hat{\boldsymbol{\eta}}_j$ refers to the maximum likelihood estimates of the unknown nuissance parameter vector under hypothesis j, denoted as $\boldsymbol{\eta}_j$. The nussaince parameters under the null and alternative hypotheses are

$$\boldsymbol{\eta}_0 = \left[\mathrm{Re}\left(s_m^i\right), \mathrm{Im}\left(s_m^i\right), \sigma_n^2\right]^T \tag{5.26}$$

$$\boldsymbol{\eta}_1 = \left[\mathrm{Re}\left(s_m^i\right), \mathrm{Im}\left(s_m^i\right), \mathrm{Re}\left(s_m^c\right), \mathrm{Im}\left(s_m^c\right), \sigma_n^2\right]^T. \tag{5.27}$$

Note that the authors of [97] and [96] technically assume a real observation vector with no specificity of a model (hence the model is not taken to be complex). The theoretical underpinnings of the matched subspace detector (MSD) are extended to develop a class of matched direction detectors formulated for the complex form of the linear model in studies such as [98] and [99]. The generalized likelihood ratio for the matched direction detector leads to

$$\frac{L_1(\mathbf{x}_m; \mathbf{H}_1)}{L_0(\mathbf{x}_m; \mathbf{H}_0)} = \frac{\mathbf{x}_m^H \mathbf{P}_{\mathbf{a}_i}^{\perp} \mathbf{x}_m}{\mathbf{x}_m^H \left(\mathbf{P}_{\mathbf{a}_i}^{\perp} \mathbf{P}_{\mathbf{G}}^{\perp} \mathbf{P}_{\mathbf{a}_i}^{\perp}\right) \mathbf{x}_m} \tag{5.28}$$

Where $\mathbf{G}$ is introduced as the subspace spanned by the component of $\mathbf{a}_c$ that is orthogonal to $\mathbf{a}_i$ given by $\mathbf{G} = \mathbf{P}_{\mathbf{a}_i}^{\perp} \mathbf{a}_c$. The numerator of Equation 5.28 represents the energy in the component of the observation that is orthogonal to the modeled interference subspace, $\mathbf{P}_{\mathbf{a}_i}^{\perp} \mathbf{x}_m$. In detection, this quantity is then compared to the residual energy of this signal when aligned to the portion of $\mathbf{a}_c$ that is orthogonal to $\mathbf{a}_i$. The form has the potential to be problematic for our case where the array is not calibrated in advance and we can not assume that $\mathbf{a}_i$ is not perfectly known ahead of time. We expect small perturbations in both $\mathbf{a}_i$ and $\mathbf{a}_c$ to

have undesirable and unpredictable effects on the statistic. It is interesting to note that one study exists in literature that addresses steering vector uncertainty in the matched direction detector problem [98] but the problem is formulated to assume that the interference steering vector is perfectly known a priori. This assumption leads to perfect interference suppression when computing a statistic to detect the signal of interest aligned with $\mathbf{a}_c$.

In this dissertation, we treat the array as being partially calibrated based on our approximate knowledge of the nominal sensor position vectors. The validity of this assumption depends on the dominant error mechanisms which determine the θ dependent phase responses of each channel in the array. It is emphasized here that this is an open area of investigation. Chapter 6 aims to initiate a more detailed study of the influencing factors on channel to channel phase variation over the manifold using a deterministic electromagnetic model. Let $\phi_p(\theta)$ denote the angle-dependent phase response of the p^{th} phase center. This term can be described as a sum of the propagation phase and some unknown portion as

$$\phi_p(\theta) = \tilde{\phi}_p(\theta) + \phi_p^e(\theta), \tag{5.29}$$

Where $\tilde{\phi}_p(\theta)$ describes propagation from the origin of the array face to sensor p based on the nominal model (as determined by a CAD representation of the array and a lidar survey). The culling approach implemented in the dissertation assumes $\tilde{\phi}_p(\theta) >> \phi_p^e(\theta)$ with the acknowledgment that the validity of such an assumption has not yet been proven.

Following methodology described in [100] for editing observations in a surveillance radar's signal processor prior to monopulse estimation, the approach implemented here tests for three possibilities:

$\mathbf{H_0}$: $\mathbf{x}_m \sim \mathcal{C}\left(\mathbf{0}, \sigma_n^2 I_P\right)$,

$\mathbf{H_1}$: $\mathbf{x}_m \sim \mathcal{C}\left(\mathbf{a}(\theta_1)s_m^1, \sigma_n^2 I_P\right)$ where $\theta_1 = \theta_c$,

$\mathbf{H_2}$: $\mathbf{x}_m \sim \mathcal{C}\left(\mathbf{a}(\theta_2)s_m^2, \sigma_n^2 I_P\right)$ where $\theta_2 = \theta_i$.

The culling algorithm compares a measurement's energy when projected onto one of the tested subspaces to the remaining $P-1$ dimensions using the following measure:

$$T_j(\mathbf{x}) = \frac{\mathbf{x}^H \mathbf{P}_{\tilde{\mathbf{a}}(\theta_\mathbf{j})} \mathbf{x}}{\mathbf{x}^H \mathbf{P}^{\perp}_{\tilde{\mathbf{a}}(\theta_\mathbf{j})} \mathbf{x}} \quad j \in \{1,2\}\,, \tag{5.30}$$

Where the projection matrices are evaluated in terms of the nominal manifold, indicated with a tilde. Following the complex extension for the GLRT in [101], a threshold is fixed for a certain probability of false alarm by regarding Equation 5.30 as a ratio of independent random variables and interpreting the probability of false alarm as

$$P_{FAj} = Q_{\chi^2_{2q_j}}(\gamma_j), \quad j \in \{1,2\}\,. \tag{5.31}$$

An observation is extracted for calibration when it satisfies the following rule:

$$\frac{\mathbf{x}^H \mathbf{P}_{\tilde{\mathbf{a}}(\theta_\mathbf{c})} \mathbf{x}}{\mathbf{x}^H \mathbf{P}^{\perp}_{\tilde{\mathbf{a}}(\theta_\mathbf{c})} \mathbf{x}} - \frac{\mathbf{x}^H \mathbf{P}_{\tilde{\mathbf{a}}(\theta_\mathbf{i})} \mathbf{x}}{\mathbf{x}^H \mathbf{P}^{\perp}_{\tilde{\mathbf{a}}(\theta_\mathbf{i})} \mathbf{x}} > \gamma_1 - \gamma_2 \quad \text{and} \quad \frac{\mathbf{x}^H \mathbf{P}_{\tilde{\mathbf{a}}(\theta_\mathbf{c})} \mathbf{x}}{\mathbf{x}^H \mathbf{P}^{\perp}_{\tilde{\mathbf{a}}(\theta_\mathbf{c})} \mathbf{x}} > \gamma_1. \tag{5.32}$$

It is emphasized that here $T_j(\mathbf{x})$ is interpreted as a notional measure of *quality* rather than a *likelihood*. The culling technique is expected to help edit the low SINR observations which reduce angle estimation performance as illustrated in the simulated example of Figure 5.3. This technique is expected to be more robust to manifold perturbations than the pseudoinverse approach that is implemented in [54] which relies on null-steering accuracy to identify approximately single source measurements in a calibration bin.

The use of the GLRT-based quality measured is justified with a simple simulated example. In simulation the nominal RDS geometry is perturbed with small scale position errors to create mismatch between the presumed model of the array response and truth. Here the phase center positions are perturbed over 50 Monte Carlo trials using an RMS position uncertainty of $\sigma = 0.035\lambda$, satisfying the small-scale definition discussed in Chapter 4. For each perturbed manifold state, a set of two-source calibration bins are generated. Each cal-

ibration bin contains 1,000 $Q = 2$ observations. The interference source power is nominally held 10 dB below the level of the calibration source. The pseudoinverse and GLRT measures are applied to cull calibration measurements from the set following the processing architecture that has been proposed for the dissertation and implemented in the CReSIS toolbox. The edited snapshot set is then used to measure the manifold via the principal component method.

Measured manifolds are tested in maximum likelihood estimation using a high SNR test source and 1,000 snapshots in covariance matrix estimation. The average angle estimation performance with nonparametric calibration using subspace clustering over 50 Monte Carlo trials is reported in Figure 5.5. Note that the randomization of geometric errors over the runs precludes a comparison to the classic CRLB, hence a lower bound is omitted from this result. The result suggests that for this particular setup, the specified thresholds $\gamma_1 = \gamma_2 = 10$ applied to the GLRT-based measure lead to improved angle estimator performance. We emphasize here that *this result alone does not provide sufficient evidence to conclude that the proposed measure is more robust than the pseudoinverse based rule which relies on null steering accuracy to estimate a measure.* Different culling rules lead to different numbers of snapshots that go onto covariance matrix estimation in calibration. This presents challenges in comparing the performance of different culling strategies since the number of snapshots influences the accuracy of the steering vector estimated in a bin. It is difficult to directly attribute angle estimator outcomes to the specific definition of the measure used in culling due to this coupling between culling rules and number of measurements remaining in a clean set for estimating the covariance matrix.

The proposed implementation of nonparametric manifold calibration for the RDS is exercised in simulation with the GLRT measure for culling calibration snapshots. The canonical MLE performance examples, originally published in [1] and recreated in Chapter 2, are again carried out here with a perturbed array to study the nonparametric calibration performance. These examples assume one instantiation of a perturbed manifold enabling comparison to

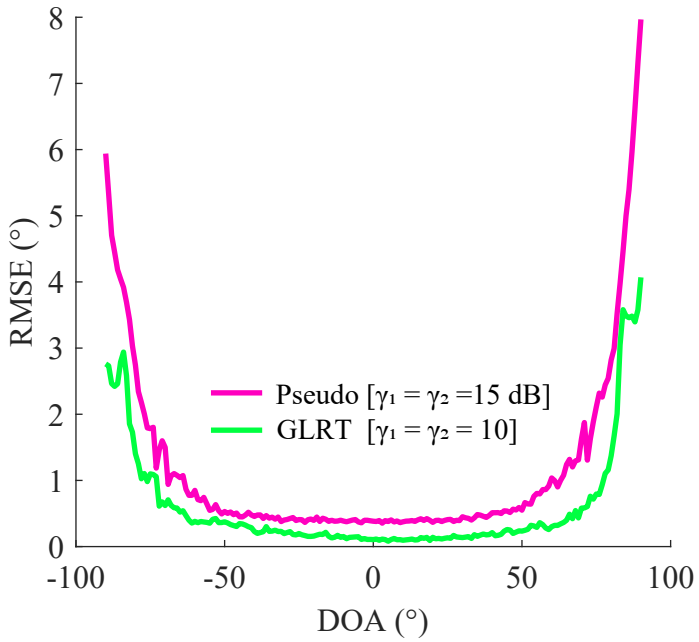

Figure 5.5: Simulated maximum likelihood angle estimator performance with nonparametric manifold characterization based on the proposed subspace clustering and editing prior to eigendecomposition in a calibration bin. Manifold mismatch is created using phase center geometric errors with a perturbation scale of 0.035λ.

the classic CRLB. The perturbation scale on the phase center geometry is set at $\sigma = 0.035\lambda$. In this example the power of the spatial sources is randomized over an interval varying from the thermal noise level (set to unity) up to 20 dB per channel. Each calibration bin contains 10,000 snapshots before culling. The thresholds are set as $\gamma_1 = \gamma_2 = 10$.

The measured lookup table is tested in maximum likelihood angle estimation assuming two sources at 0° and 30° whose parameters vary within two experiments. Each source parameter value (of SNR in Experiment 1 and source snapshots in Experiment 2) is tested over 100 Monte Carlo trials. The experiments are defined as follows:

1. **Experiment 1**: Two equal power, uncorrelated sources with a fixed number of snapshots $M = 50$ and per sensor source SNR sweeping over the interval 10 dB $\leq$ SNR $\leq$ 40 dB.

2. **Experiment 2**: Two equal power, uncorrelated sources with a combined SNR of 20 dB and snapshots varying over the interval $10 \leq M \leq 10,000$.

Estimator performance observed in Experiments 1 and 2 are reported in Figures 5.6a and

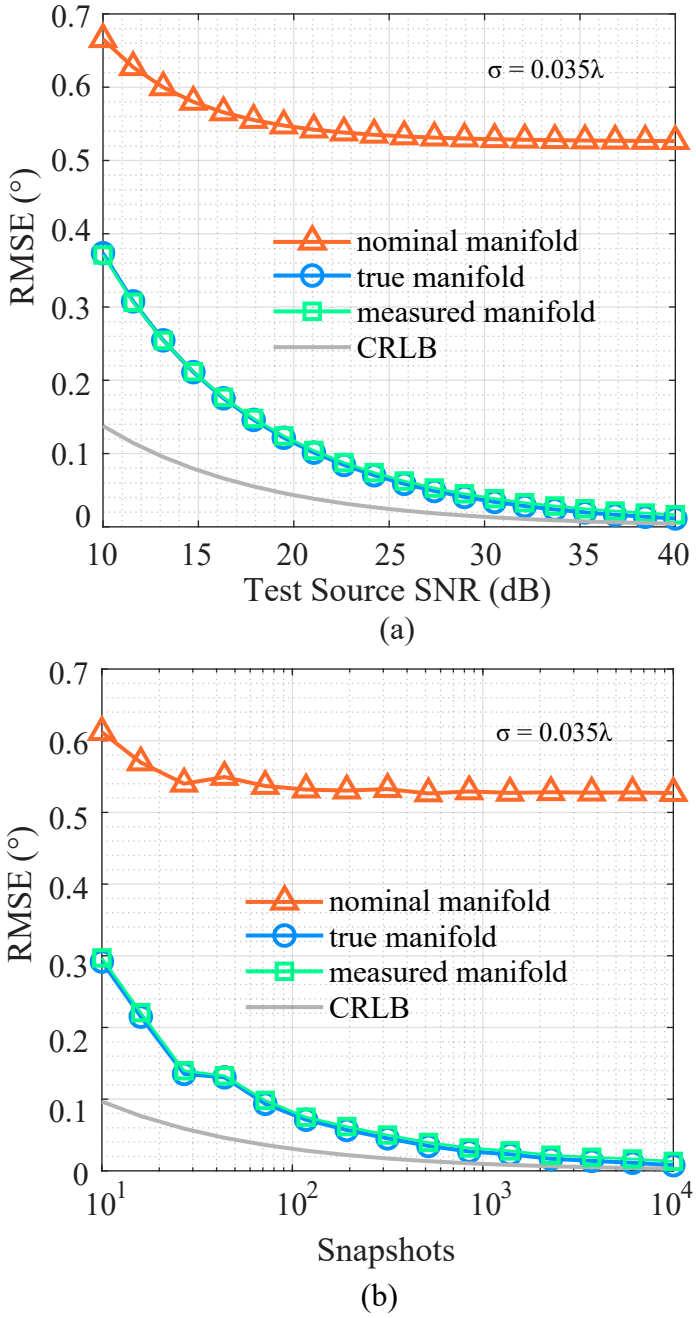

Figure 5.6: Simulated maximum likelihood angle estimator performance with nonparametric manifold characterization based on the proposed subspace clustering and editing with GLRT-based rule prior to eigendecomposition in a calibration bin. Threshold values assumed in editing: $\gamma_1 = \gamma_2 = 10$. Manifold mismatch is created using phase center geometric errors with a perturbation scale of $\sigma = 0.035\lambda$.

5.6b as measured RMS error on the angle estimate of the $\theta = 30°$ source for three manifold models. The following three manifolds are tested in simulation:

- **Nominal manifold**: Assumes the isotropic steering vector evaluated in terms of the *nominal phase center positions* in MLE and does not account for geometric error (corresponds to uncalibrated case).

- **True manifold**: Assumes perfect knowledge of phase center positions when evaluating the steering vectors in MLE (corresponds to perfect calibration case).

- **Measured manifold**: Applies the manifold measured with the proposed methodology when evaluating the steering vectors in MLE (corresponds to calibration with proposed methodology).

In both experiments, the nominal manifold (which corresponds to the uncalibrated case) leads to the largest angle estimator uncertainties that improve slightly with increasing source SNR in Experiment 1 and with increasing snapshots in Experiment 2 but level off after convergence to an error bound that is approximately 0.5° higher than the CRLB. The measured manifold reduces the overall estimator error and closely tracks the true manifold result in both experiments. Close examination of the RMSE values shows differences between the true and measured manifold results at the high SNR edge of Experiment 1 and the high snapshot edge of Experiment 2. Although small (on the order of hundredths of a degree), the numerical results suggest that the angles estimated with the measured manifold exhibit bias. The effect increases slightly as the perturbation scale increases. It is expected that this small bias would reduce by increasing the number of snapshots in each calibration bin which increases the likelihood of harvesting more high SINR results in training.

5.4 Application of Nonparametric Methodology to RDS Datasets

The CReSIS toolbox is modified with custom manifold calibration processing modules to support nonparametric calibration by the principal eigenvector technique with single dominant source culling. These updates will become publicly available in a future release of the toolbox. A high level overview of the calibration processing flow is illustrated in Figure

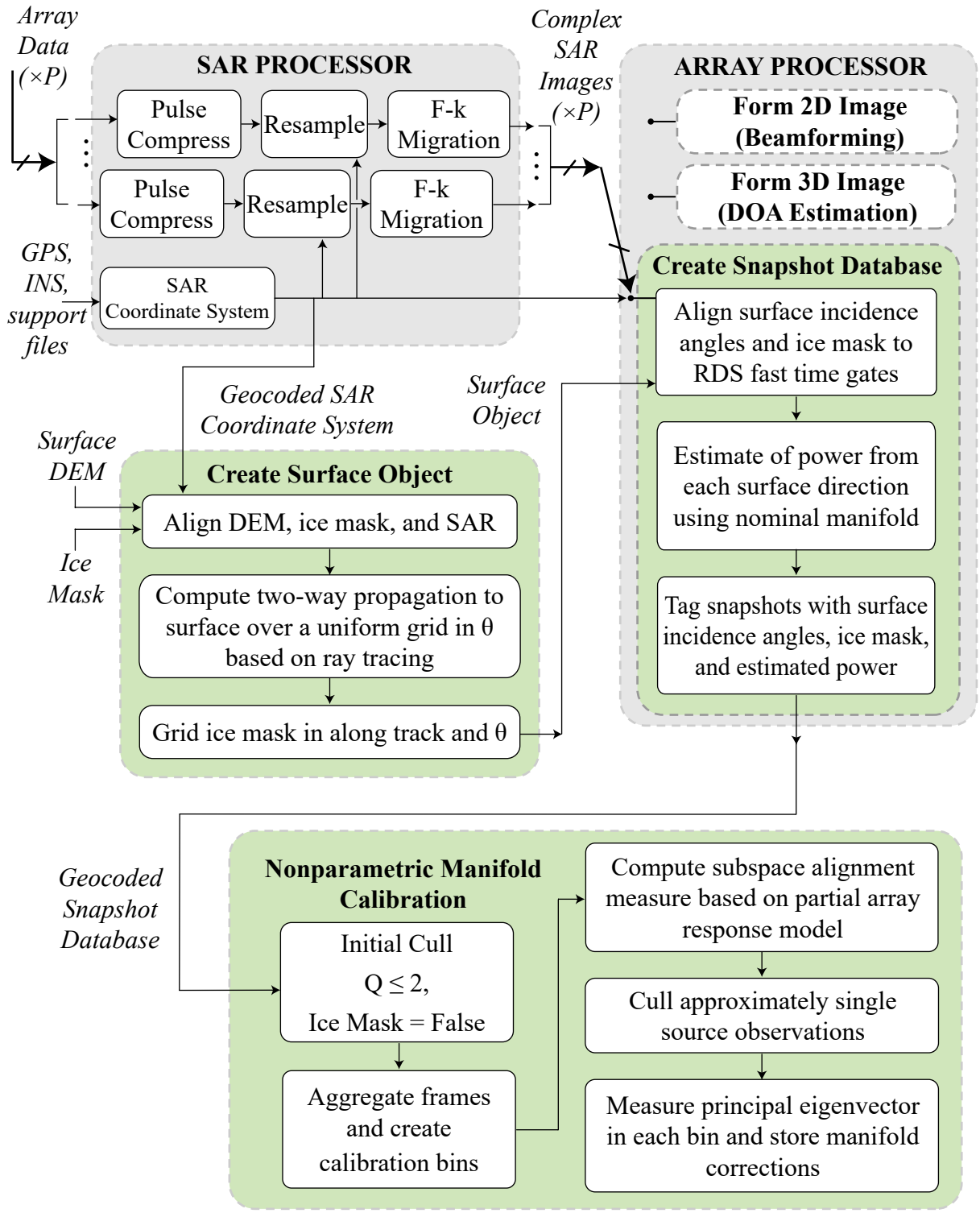

Figure 5.7: New manifold calibration processing architecture (green) including surface object creation, snapshot database creation and nonparametric manifold calibration shown within existing CReSIS signal processing architecture (gray).

Table 5.2: Frames processed in nonparametric manifold calibration.

Day Segment	*Frame List*	*Mission*
20140325_07	[2-5]	Axel Heiberg - Eureka
20140401_03	[4-5, 13, 15-16, 34-36, 40-43, 45-46]	North Canada Glaciers
20140506_01	[14-16, 34-36, 40-43, 45, 46]	South Canada Glaciers

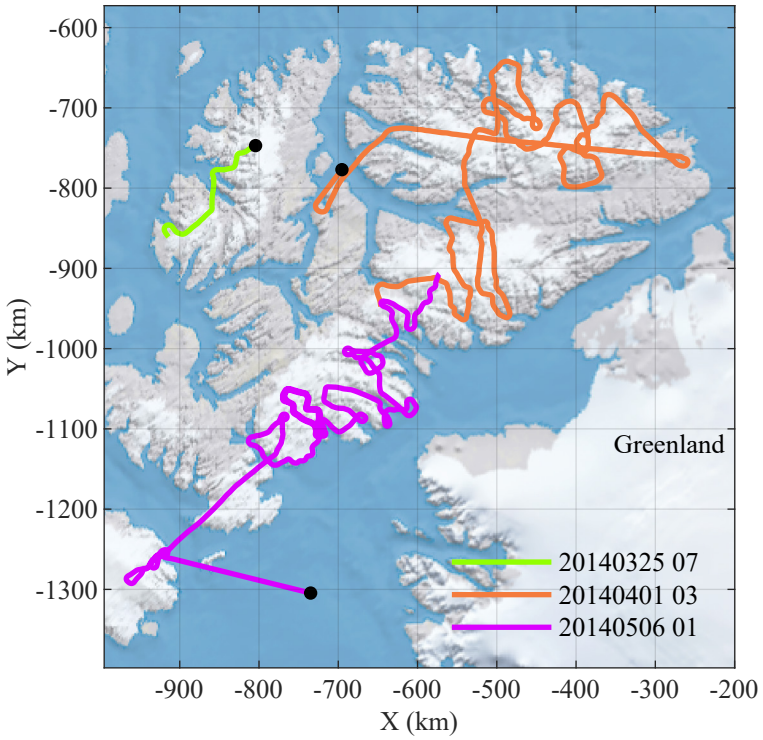

Figure 5.8: 2014 Operation Icebridge Canadian Arctic flight lines indicating the data sets considered in measuring RDS manifolds with the nonparametric approach described in this chapter.

5.7 in the context of the CReSIS SAR and array processors showing the surface object and snapshot database creation described in Chapter 3. The nonparametric manifold calibration routine reads in the geocoded snapshots and culls the single source and two source measurements corresponding to non-penetrative media (sea ice, rock or ocean). The resulting measurements are then aggregated across frames and sorted into 1° angle bins by looping over a DOA grid and querying the database to return all measurements falling within ±0.5°

of a bin center. The measurements are phase shifted to the bin center based on the nominal manifold model. This has the effect of slightly defocusing the second source but the effect is assumed to be marginal.

The binned measurements are edited by comparing the measure of subspace alignment proposed in Equation 5.32 to a parameterized threshold field which is currently derived from a user-defined P_{FA} type of parameter. Again, the point is reemphasized that the measure described by Equation 5.32 is not interpreted as a likelihood so this parameter does not relate to a false alarm probability in the traditional sense. The tuning of the threshold is not yet entirely understood. Threshold selection is carried out by testing a small set of thresholds by hand. This is discussed further below.

The code supports independent thresholding for both the $Q = 1$ and $Q = 2$ snapshots. The algorithms for culling calibration-grade observations from the single source and two source measurements are detailed in Algorithm 1 and Algorithm 2 respectively, provided in Appendix D. The pseudocode describes the bin-level selection of measurements that are interpreted as approximately single source observations. Note that Algorithm 2 requires the definition of a minimum source separation between the calibration and interference sources. When unspecified, this defaults to an angular extent that is equivalent to a beamwidth as computed from the array factor. Additionally any snapshots which indicate the second source impinging on a backlobe are thrown out of the set. Hence the interference angles are strictly limited to the interval $|\theta_i| \leq \pm 90°$.

The cleaned observation set is then used to estimate the covariance matrix for carrying out the eigendecomposition and storing of the eigenvector that maps to the principal eigenvalue. The cleaned set is stored with the resulting manifold. The snapshots in these sets are geocoded and tagged with metadata including aircraft inertial measurements, radar transmit pointing, and originating frame for example to support analysis of a measured manifold. Additional support functions are implemented to coarsely assess the quality of a measured manifold prior to its application in array processing.

The methodology proposed in this chapter for carrying out nonparametric manifold calibration in the presence of low-rank interference is tested on multichannel RDS SAR imagery from the center subarray on the P-3 aircraft. Three independent datasets collected in the Canadian Arctic during the 2014 Operation IceBridge mission are considered for calibration. The three days of interest are also specified in Figure 3.5 as part of the methodology description in Chapter 3 along with the corresponding frames associated with each data set (see Table 3.4). The map and table are presented again in this chapter as a convenience to the reader in Figure 5.8 and Table 5.2 respectively. A manifold is measured for each of the three days indicated on the map which include 20140325_07, 20140401_03, and 20140506_01. Table 5.2 specifies the input frames of each manifold result.

5.4.1 Observations Captured in Algorithm Development

The final measured manifolds presented in this chapter implement the GLRT-based quality measure for editing snapshots as it is expected to be more robust to null-steering errors imparted in the pseudoinverse-based metric. Simulations and assessments of measurements suggest that the threshold influences a complex trade space that is not fully understood. The final threshold values assigned in manifold calibration are $\gamma_1 = 8.99$ and $\gamma_2 = 16.2$. Multiple values are tested by hand to understand the influence of culling on manifold quality. A subset of observations are presented here to offer intuition into the role of the clustering and editing rule on direction of arrival outcomes.

Figure 5.9 offers histograms of measured phase corrections in the $\theta_c = 65^\circ$ calibration bin from the 20140506_01 data set that are interpreted as being representative of cases when the implementation of the GLRT-based rule leads to better estimates of the array response to a give source direction. Note that the histograms are scaled so that the area under each curve sums to one. The channels are phase referenced to Antenna 4 and the propagation phase of each channel is removed based on the nominal model. Phase correction distributions are shown for three cases:

1. **No editing**: No culling of snapshots in the calibration bin.

2. **Pseudo**: Culling based on a measure of SIR, interpreted with estimates of directional source power obtained by application of the pseudoinverse in Equation 5.24.

3. **GLRT**: Culling based on the proposed GLRT measure in Equation 5.32.

In this particular example, the distribution of phase offsets from the nominal model on each channel show the tightest clustering around a mean value when the GLRT based measure is used to extract calibration snapshots. Some of the distributions appear to broaden under the pseudoinverse-based culling. Antenna 7 for example shows a fattening of phase corrections when compared to the case where no editing is applied to the set. This is interpreted as a possible example of degradation under the pseudoinverse rule that would potentially reduce the accuracy of the measured manifold response in this bin.

The eigenspectrum of the covariance matrix estimated from a calibration set offers additional insight into the effect of snapshot culling on angle estimation outcomes. Eigencontrast, defined as the ratio of the first and second eigenvalues when organized in descending order, is hypothesized to increase when the snapshot set more closely approximates a single source set. Figure 5.10 shows an example drawn from the $\theta_c = 45°$ bin of the 20140506_01 set where the eigenspectra of the covariance matrices estimated under the same three possible culling rules is shown in 5.10a and the corresponding MUSIC pseudospectra are plotted in 5.10b. The eigenspectrum of the covariance matrix estimated with the pseudoinverse rule shows approximately 18 dB between the maximum eigenvalue and the second largest eigenvalue while the corresponding GLRT result indicates an eigencontrast that is 10 dB larger, corresponding to 28 dB of separation between the first and second eigenvalues.

A consideration of the MUSIC spectra computed for each case indicates contamination in the calibration set culled under the pseudoinverse rule (evidenced by a second principal peak in the pseudospectrum on the opposite side of nadir). The result obtained with no snapshot editing shows a dominant peak at nadir. Note that the calibration angle is indicated here

and all three sets produce peaks that align with θ_c in this particular example. The MUSIC curve is computed using the nominal steering vectors and while we expect a peak in the neighborhood of θ_c, the location varies depending on both the accuracy of the ArcticDEM and the fact that the nominal manifold is used to compute the spectrum.

An increase in the eigencontrast is expected to lead to more accurate angle estimation outcomes however the use of eigencontrast as a predictor of angle estimator performance remains somewhat unclear. Figure 5.11 reports the 90% range of eigencontrasts per 1° angle bin (along with the mean and median values) for different editing rules. The GLRT rules admit narrower spreads at the large arrival angles. This may indicate improved angle estimator outcomes at the edges of the field of view when using manifolds measured from the GLRT-culled sets though we lack sufficient evidence at this stage to draw this conclusion.

We expect the number of culled snapshots per angle bin to cluster in θ based on the transmit pointing angle. Figure 5.12 illustrates cleaned snapshot counts in 1° DOA bins, broken out by transmit beam for the 20140506_01 data set. Here 5.12a, 5.12b, and 5.12c correspond to pointing angles 30°, 0°, and −30°. The scanned beams cover approximately a ±47° extent within the 3 dB beamwidth on transmit. Note that the pointing angle is measured off array boresight which only aligns with $\theta = 0°$ in a zero roll condition. We expect that when a culling method is performing well, it will favor high energy measurements concentrated over an angular window that agrees with the direction of illumination. The cleaned snapshot counts follow similar trends across the tested culling rules and all seem to show comparable clustering patterns based on transmit pointing angle within the 3 dB window of ±47°.

Differences become apparent at the large DOA angles outside of this window. The pseudoinverse measure appears to produce the largest number of sidelobe detections in the $\theta_{TX} = 0°$ returns. This may be attributable to the predicted null-steering degradation suffered by this measure. The sidelooking beams demonstrate cases where the culling appears to breakdown and returns from the $\theta_{TX} = 30°$ beam for example correlate to echoes over the

$-85^\circ \leq \theta \leq -65^\circ$ window. It is unclear if this is attributable to a breakdown in the culling measures or an indicator of unaccounted for electromagnetic phenomenology in pointing the beam to these angles.

A final note is made to point out that the increased threshold of the GLRT shows negligible changes from $\gamma_2 = 8.99$ to $\gamma_2 = 16.24$. However the highest value of γ_2 tested shows suppression of measurements in the $-85^\circ \leq \theta \leq -65^\circ$ window in both sidelooking beams. The suppression of observations in this window in both sidelooking beams is possibly associated with RFI due to an onboard navigation system installed to support the previous Antarctic mission. The emissions of this system were observed in the starboard subarray and showed falloff in intensity with increasing distance from the fuselage. This hypothesis was not tested here but RFI and multipath are pointed out as plausible explanations for the rejection of these measurements in culling.

5.4.2 Measured RDS Manifolds from Three Independent Data Sets

Three measured manifolds are produced for the three independent data sets specified in Table 5.2. The GLRT culling is adopted to avoid the potential contamination problem sometimes encountered in the pseudoinverse-based editing. The single source threshold is assigned at $\gamma_1 = 8.99$. The threshold for extracting measurements from the $Q = 2$ subsets in each bin is hand selected from a set of manifolds measured with three different values of γ_2 based on measured angle estimation performance that tests a given manifold against cleaned snapshots from a different day. Figure 5.13 demonstrates a representative result intended to compare threshold performance. This result reports the RMSE of angles estimated with MUSIC using the 20140506_01 measured manifold against the cleaned 20140401_03 and 20140325_07 data sets.

The measured MUSIC performance shows a slight decrease in the RMS error by approximately 0.5° between the $\gamma_2 = 8.99$ and $\gamma_2 = 29.25$ curves. The highest threshold admits degradation over the $-70^\circ \leq \theta \leq -50^\circ$ window. Detail of the measured error in this region

is provided in the bottom of Figure 5.13. From the detailed view we observe as much as 5° of uncertainty suffered by increasing the threshold to $\gamma_2 = 29.25$. The increased error in this interval is consistent with expected degradation due to the reduced number of calibration samples in this region, as shown in Figure 5.12. In an effort to avoid large errors at the edges of the swath, the 16.24 threshold is selected for demonstrating nonparametric calibration in generating RDS-derived DEMs. This manifold is interpreted as the one that gives up a marginal amount of accuracy near nadir to avoid large uncertainties in the $-70° \leq \theta \leq -50°$ window.

The final values of $\gamma_1 = 8.99$ and $\gamma_2 = 29.25$ are specified in snapshot editing and used to produce a set of manifolds for each of the calibration sets. A 20140506_01 manifold is also measured using the 15 dB threshold applied to the pseudoinverse-derived measure. This measured manifold is tested against binned snapshots from 20140325_07 and 20140401_03 in angle estimation and compared to the result obtained under the GLRT editing rule using the MUSIC algorithm. Measured bias and RMSE of angle estimates in each bin are reported in Figures 5.14 and 5.15 in degrees respectively. The figures offer detailed views of the interval $-60° \leq \theta \leq 60°$. The bias curves show comparable performance over the 3 dB swath width of $\pm 47°$. The pseudoinverse result exhibits slightly higher error over $65° \leq \theta \leq 75°$ and $-62° \leq \theta \leq -52°$. The comparison in angle estimation outcomes between the GLRT and pseudoinverse culling is provided here for the sake of completeness; comparison of the bias and RMSE of angle estimates show minor differences in performance. The remainder of the chapter presents results obtained under a GLRT measure in snapshot editing.

Measured manifolds for each of the three days are presented in Figures 5.16-5.18 as antenna pairs based on the approximate even-symmetry of elements across the center of the array. Each manifold is phase referenced to Antenna 4 and reported as a correction with respect to the nominal model as a magnitude and phase residual. A thumbnail of the P-3 with array numbering is included with each pair to indicate the physical orientation of the antennas reported in a figure. Figure 5.16 reports measured responses of the outermost elements

corresponding to Antennas 1 and 7. Advances in the figures correspond to advancements along the array moving in the inboard direction toward the reference channel. Patterns show symmetry between pairs that is consistent with our prediction of approximately symmetric coupling environments. Symmetry in the patterns is most easily observed in comparing the magnitude corrections between antenna pairs. Antennas 1 and 7 for example share similarity in their nulls with Antenna 1 consistently showing nulls at -46° and -61° across all three data sets while mirror images are observable in Antenna 7 at 46° and 61°. Results for the most part agree across the days. The largest variation in phase is observed on Antenna 2 near $\theta = 36^\circ$ where the phase measurements differ by approximately 18°.

The three manifolds are applied in MUSIC DOA estimation and compared to the nominal manifold result. Note that the nominal manifold is representative of the current model implemented in the array processor. The implementation of MUSIC in these tests is consistent with the algorithm used in the CReSIS toolbox. Our implementation of MUSIC casts the MUSIC cost function as a minimization in order to leverage MATLAB's constrained minimization search to numerically evaluate the peaks of the pseudospectrum as defined in Equation B.20. In assessing angle estimator accuracy, the number of sources is set to one. Each manifold is tested against independent edited calibration bins to avoid testing with the training data. For example the 20140325_07 manifold is tested only against binned measurements from 20140506_01 and 20140401_03.

The test data are broken into processing chunks of 100 snapshots within each calibration bin. Each chunk provides an estimate of the array covariance matrix that is used to carry out angle estimation with both a measured manifold and the nominal manifold. The RMS error and bias on an angle estimate in a given calibration bin are evaluated over the number

of chunks as follows, N_{chunks} as

$$\text{RMSE}(\theta_c) = \sqrt{\frac{1}{N_{chunks}} \sum_{i=1}^{N_{chunks}} \left(\hat{\theta}_i - \theta_c\right)^2} \tag{5.33a}$$

$$\text{BIAS}(\theta_c) = \frac{1}{N_{chunks}} \sum_{i=1}^{N_{chunks}} \left(\hat{\theta}_i - \theta_c\right). \tag{5.33b}$$

Note that truth, θ_c, is taken to be the incidence angle determined with the ArcticDEM. A nominal result is generated for each measured manifold tested in angle estimation. The three nominal curves are extremely similar. To ease readability of the figure, the three nominal outcomes are averaged together into one RMSE curve or bias curve that is representative of performance in the *uncalibrated* case (and equivalent to our existing angle estimation performance to date).

The measured bias and RMSE are summarized in Figures 5.19 and 5.20 respectively. Both results include a detailed view of $-60° \leq \theta \leq 60°$ in addition to the full field of view. The nominal model and measured manifolds appear to admit comparable bias performance over the $-10° \leq \theta \leq 30°$ interval. The bias in this region is contained within $\pm 1°$. The estimated bias curve of the nominal case shows large increases in the bias prior to manifold calibration that grow as the elevation angle moves off nadir while the measured manifold results are mostly bound within $\pm 1°$ out to $\pm 60°$. The increased bias further off nadir observed in the nominal result is consistent with historic observations of large elevation errors at the edges of RDS-derived DEMs produced with tomographic image formation. The RMSE curves show errors contained within $2°$ when angle estimation is implemented with the measured manifold. All cases show increased error at the edges of the field of view. We expect angle accuracy to gracefully degrade as θ approaches $\pm 90°$ in accordance with the CRLB even in ideal scenarios. The measured bias and RMSE results help to confirm the approach outlined in this chapter and indicate that the measured manifold has the potential to improve both null steering accuracy in ice thickness profiling and angle estimation in tomographic image

formation.

An average error reduction factor is evaluated over θ as the following ratio of uncertainties:

$$\text{Error Reduction}(\theta) = \frac{\text{RMSE}_{\text{nom}}(\theta)}{\text{RMSE}_{\text{meas}}(\theta)}. \tag{5.34}$$

Here RMSE_{nom} refers to the error measured with the application of the nominal array response model and $\text{RMSE}_{\text{meas}}$ is an average error for the three measured manifold results. We may interpret angular sectors where the error reduction values that are less than one as regions of degradation (where the measured manifold model does not outperform the nominal). The reduction in angle estimator error is reported in Figure 5.21 in orange. The portions of the curve that dip below one are overlaid in black. The regions of diminished performance correspond to $\theta = 5°$, $18° \leq \theta \leq 20°$, and $25° \leq \theta \leq 34°$. The smallest value of error reduction reported in the sectors of degraded performance is 0.74 (and the average value of error reduction over all degraded values in 0.86). The average of the error reduction values that evaluate to one or higher is found to be 4.8.

5.4.3 Combined Manifolds

The measured manifolds are combined across the three data sets. These results are plotted to demonstrate the spread of measured corrections over the three data sets in Figures 5.22 - 5.24. Each plot illustrates the interquartile range of phase and magnitude corrections as a shaded region and determined from an empirical cumulative distribution function of the steering vectors in each calibration bin. The mean and median values are also reported as dotted and solid lines respectively.

To aid in the interpretation of the spread of magnitude and phase corrections as a function of angle, detrended spreads are produced by removing the mean from the interquartile range. The 90% spread is added to this plot as well. The intent is to convey the spread of 50% and 90% of the corrections about their mean values. The spread of the estimated magnitude and

phase corrections are presented in Figures 5.25 and 5.26. Again these results are organized as pairs based on the symmetry of antennas within the array. The spreads for the most outboard pair (Antennas 1 and 7) appear at the top of the figure and the most inboard pair (Antennas 3 and 5) appear at the bottom.

In most cases we find that 90% of the magnitude corrections fall within about a 2 dB envelope of their mean values in any bin but some exceptions to this observation are noted here. The responses of Antennas 1 and 7 demonstrate increased magnitude spreads over the intervals of $-90^\circ \leq \theta \leq -60^\circ$ and $50^\circ \leq \theta \leq 90^\circ$ respectively. The increased uncertainty in these areas may be due to shadowing experienced by these elements at the large DOAs based on the conformal geometry of the array that fits the contour of the aircraft belly. We expect Antenna 1 to experience shadowing at the large negative DOAs while Antenna 7 is expected to suffer shadowing at the large positive DOAs. Antennas 6 and 5 similarly demonstrate increased spread at the large positive DOAs but the degree of uncertainty appears to reduce as the channels move more inboard. Most antennas demonstrate a 4 dB window of uncertainty about the mean values over the angular window corresponding to the 3 dB beamwidths of the transmitted beams, covering $\pm 47^\circ$. The phase spreads reveal similar trends. Antennas 2-6 show that 90% of the phases fall within approximately 20° of their respective mean values in a given bin over $\pm 47^\circ$. Antenna 1 shows the largest spread of uncertainties among all the channels. The spread of the measured phases over the interquartile ranges of all channels are contained well within $\pm 10^\circ$ over the 3 dB illumination window.

5.5 Discussion

Nonparametric manifold calibration assumes the availability of single source observations in estimating the directional response of the array. Collecting enough single source measurements over a sufficiently dense angle grid is problematic for the multichannel SAR sounder whose sensing geometry is more amenable to providing two-source measurements on a cal-

ibration grid. The historic approach for capturing $Q = 1$ snapshots relies on calibration flights over an extremely smooth and non-penetrative surface interface with a maneuvering platform. This technique is subject to the roll restrictions of the aircraft and requires planned calibration flights over specific terrain.

This chapter reformulates the nonparametric manifold calibration problem in the context of the multichannel SAR sounder problem space. The observation model is described as a superposition of a signal of interest measured in low-rank subspace interference and noise. This description exploits our prior knowledge of the scattering contributions in each pixel, amassed through the creation of large surface object databases as described in Chapter 3 which allow us to isolate pixels by model order. Numerical evidence indicates that the $Q = 1$ assumption may be allowed to relax provided the power of the calibration source is sufficiently large relative to the interference. We demonstrate the validity of the proposed relaxation in simulation by creating calibration bins over a uniform angle grid, injecting interference into each bin, measuring the manifold via principal components and carrying out angle estimation over many Monte Carlo trials. Note that each bin only includes one spatial interferer so that the number of sources never exceeds two in simulation. The simulated RMS error shows that estimator accuracy improves with increasing isolation up to a point but performance appears bounded for SIRs exceeding approximately 35 dB. We expect that the CRLB could be achieved by increasing the number of snapshots in each bin and making grid spacing arbitrarily small but this has yet to be confirmed.

Initial efforts to apply nonparametric manifold to the RDS documented in [54] and [9] reveal a need to identify calibration pixels in the imagery dominated by single sources. Initially a heuristic threshold of 15 dB was applied to an estimated ratio of spatial source powers. This measure relies on a pseudoinverse, carried out prior to array calibration using the nominal steering vectors. To avoid reliance on the null steering accuracy underpinning the pseudoinverse measure, a generalized likelihood ratio type of measure is adopted that compares energy along a direction of interest to the remaining $P - 1$ dimensions. This

measure is also evaluated using the nominal manifold but does not require simultaneous knowledge of both interference and desired source steering vectors. This measure is expected to be slightly more robust to calibration errors, provided they are sufficiently small. Lacking knowledge of the dominant error mechanisms impacting the RDS array's performance, it is difficult to assess the validity of this assumption. The GLRT technique applied in this chapter uses a hand-selected threshold. Further investigation is needed to understand how this parameter impacts angle estimation outcomes.

The introduction of an error reduction metric provides insight into the comprehensive improvement in angle estimator accuracy over a majority of calibration bins. Though not plotted here, it should be noted that a comparison of the error reduction curves corresponding to manifolds estimated under the GLRT and pseudoinverse rules for editing shows larger extents of degradation within the 3 dB illuminated swath. Specifically the manifold measured with the pseudoinverse clustering leads to diminished error reduction values at $\theta = -34°$, $-7° \leq \theta \leq -1°$, and $13° \leq \theta \leq 35°$. Further investigation has not been carried out to explain the diminished error reduction (under either editing rule) observed within angular regions that fall in the neighborhoods of the off-nadir transmit pointing angles. Degradation in these areas likely indicates windows of poor isolation where a clustering metric breaks down. The error reduction measure does not inform the hand-selected threshold parameters applied in producing the final measured manifold results; in the future, consideration of this factor is recommended in comparing manifolds measured under various editing rules.

The limitations of the editing technique are attributed to its reliance on a manifold-dependent measure for conditioning the $Q = 2$ observations of the sounder calibration sets into approximations of $Q = 1$ sets. This assumes the array is partially calibrated prior to determining the measure and reduces the total number of snapshots in each bin. The description of the observations in a calibration bin developed in Section 5.3 offers a geometric interpretation that may admit an alternative estimator for $\mathbf{a}(\theta_c)$. Each calibration bin can be further binned by interference angle θ_i. Letting $\theta_i^{(k)}$ refer to the k^{th} interference subset, we

can note that the set of N_k manifold vectors in that bin, $\left\{\mathbf{a}(\theta_c), \mathbf{a}\left(\theta_i^{(k)}\right)\right\}$, spans a subspace S_k described as a plane in $\mathbb{C}^P$. This interpretation suggests that the calibration bins admit a geometric description as a set of K planes intersecting along a line in $\mathbb{C}^P$ that is parallel to the true manifold vector of interest allowing us to assert the following:

$$\mathbf{a}(\theta_c) \in S_1 \bigcap S_2 \bigcap \cdots \bigcap S_K. \tag{5.35}$$

This interpretation may lead to a cost function that uses the coincident sources to solve for the best $\mathbf{a}(\theta_c)$ rather than attempting to suppress them by editing. An algorithm that exploits the interpretation of the steering vector in Equation 5.35 is predicted to provide more accurate estimates by leveraging the information available in the $Q = 2$ snapshots rather than suppressing these measurements.

The manifolds measured for this chapter demonstrate significant improvements in angle estimator performance when tested on the approximately single source snapshots. The comparison of angle estimator performance by manifold model helps to confirm large errors that have been observed at the edges of the swath in tomography using the nominal model. The assessment suggests that these errors are dominated by an angle dependent bias that increases as the elevation angle moves further off nadir. The use of the measured manifold removes the bias leading to a large reduction in error over the RDS swath. We expect the measured manifolds to reduce errors in RDS-derived DEMS which will lead to more accurate estimates of ice volume. We also expect the measured manifold to improve the null steering accuracy of the geonull beamformer. The large improvements demonstrated in this chapter justify thorough testing of the measured manifold in improving sensitivity over challenging sounding targets like the marine terminating outlet glaciers in Greenland.

The manifolds measured in this chapter show large variations in θ which suggest that the angle-agnostic forms of coupling commonly evidenced in mutual coupling literature will not likely hold for our problem. We expect these patterns to lead to complex paramet-

ric descriptions with many unknown parameters. Attempts to fit the measurements to a model described by a summation of complex exponential functions indicate the optimization problem is poorly initialized and poorly understood. Further study is needed to understand initialization and number of terms required to model each pattern. The parameterization of measured RDS manifolds is addressed further in the Discussion section of Chapter 6.

5.6 Conclusion

This chapter presents a principal components based nonparametric calibration algorithm for the characterization of SAR sounder manifolds, enabled by a subspace clustering technique for extracting pixels that are dominated by single sources. The approach relaxes the single source requirement generally assumed in nonparametric calibration. Numerical evidence was presented showing that such a relaxation may be reasonable provided that the power of the calibration source is much higher than that of a coincident interferer. A GLRT measure is adopted based on partial knowledge of the array response to identify calibration pixels in the multichannel SAR imagery. The measure enables clustering of approximately single source calibration and interference measurements in a bin and edits observations prior to eigendecomposition. Manifolds are measured from three independent data sets and tested in angle estimation. Application of the measured manifolds in direction of arrival confirms improved performance over the nominal manifold model for a majority of the field of regard. On average, the measured manifold models reduce angle estimation uncertainty by a factor of 4.8. The improved angle estimation performance indicates that the application of the measured manifolds in the 3-D image formation step of tomography will lead to reductions in the vertical elevation errors of RDS-derived DEMs, resulting in more accurate estimates of freshwater ice volume.

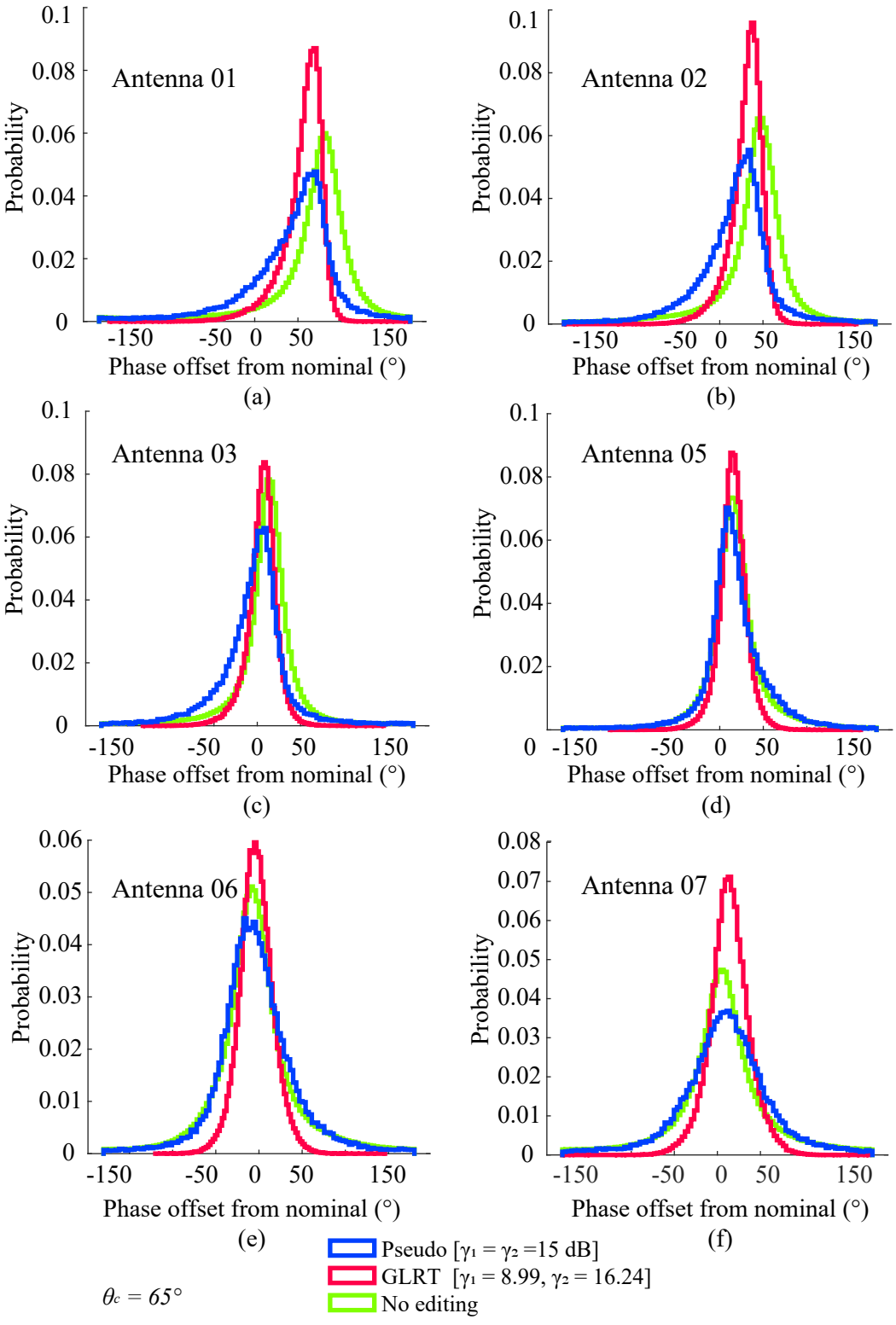

Figure 5.9: Distribution of residual phases measured in the $\theta_c = 65°$ calibration bin of the 20140506_01 data set under different culling rules, referenced to Antenna 4 and with propagation phase removed based on nominal model.

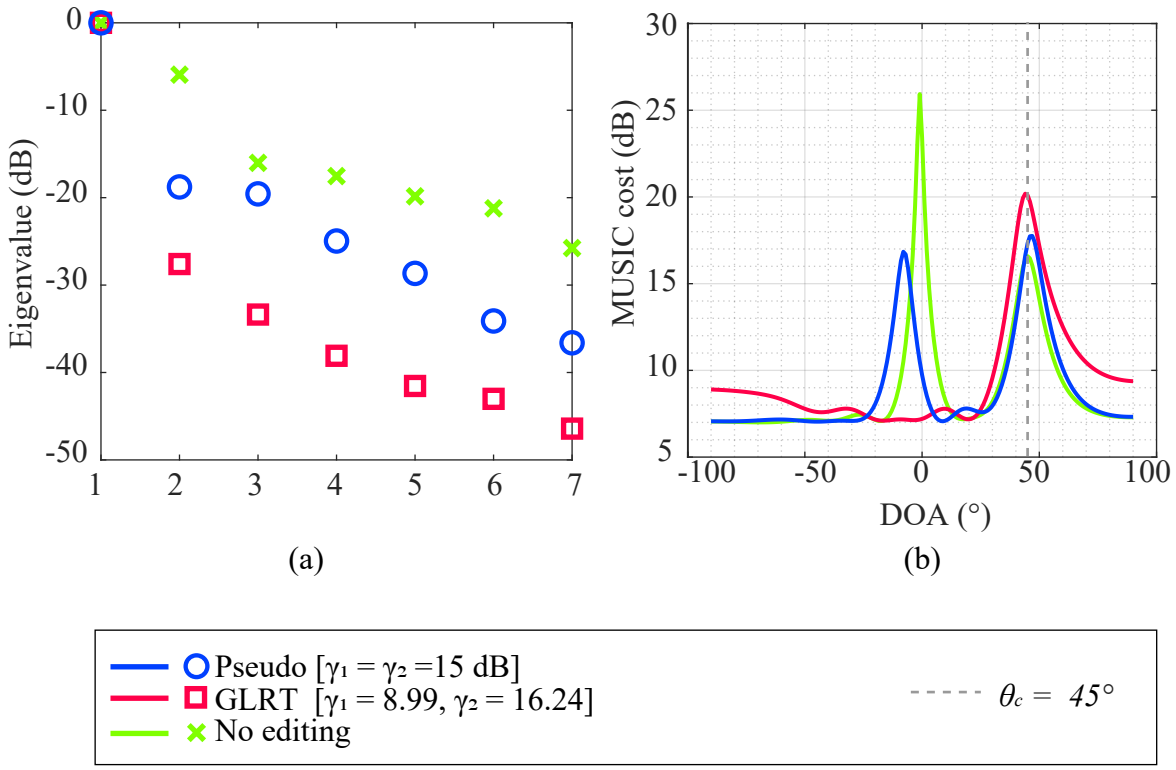

Figure 5.10: Representative example showing (a) increased contrast between first and second eigenvalues under GLRT based culling in the $\theta_c = 45°$ bin of the 20140506_01 calibration set and (b) corresponding MUSIC pseudospectra computed with the nominal model, indicating contamination in the set obtained with the pseudoinverse measure.

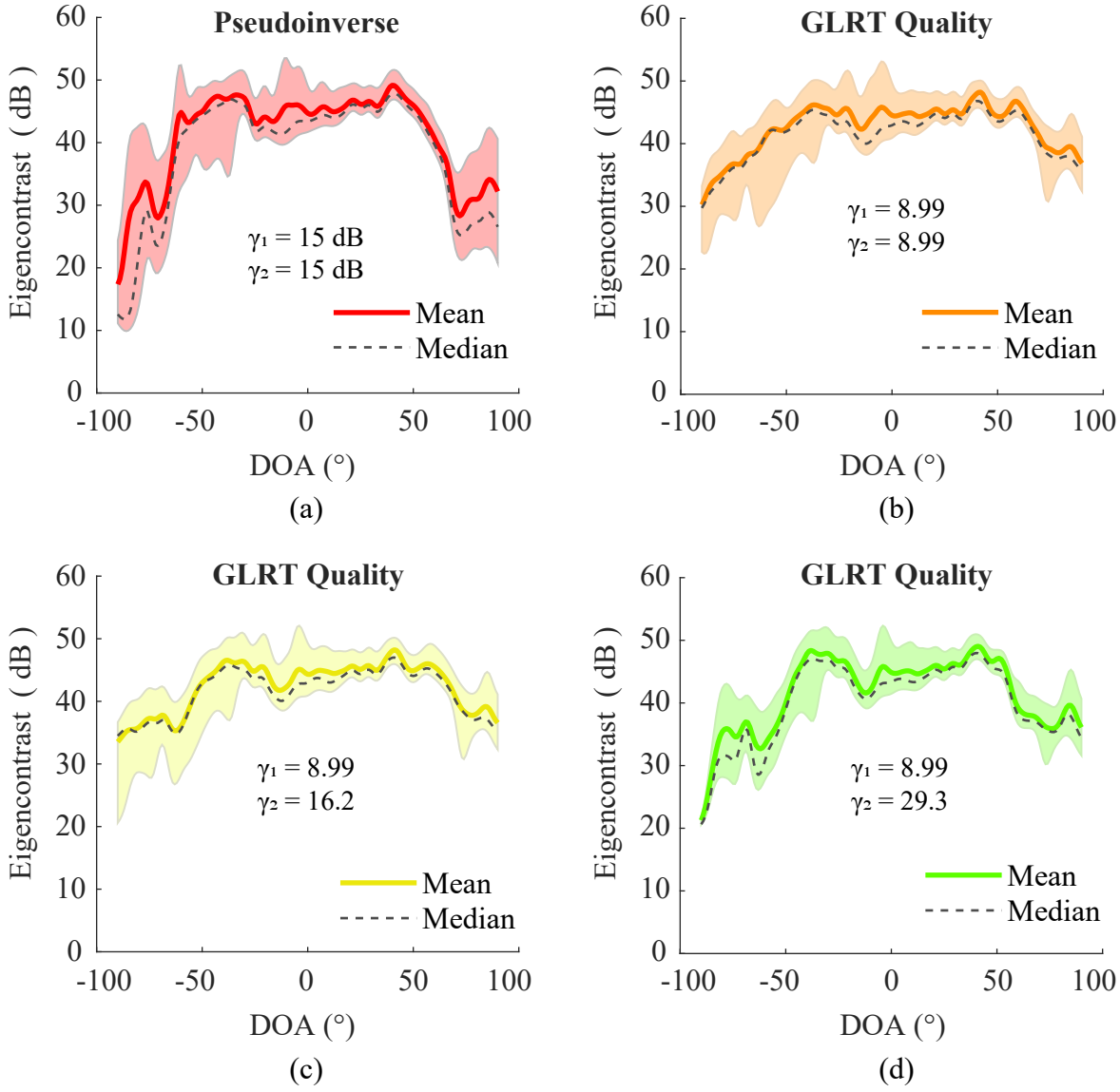

Figure 5.11: 90% range of eigencontrast values (on dB scale) per calibration bin for the 20140506 01 data set for various clustering rules and threshold combinations: (a) ratio of the pseudoinverse-based estimates of directional source power to interference and noise power with $\gamma_1 = \gamma_2 = 15$ dB, (b)-(d) GLRT-based quality with $\gamma_1 = 8.99$ in all cases and $\gamma_2 = 8.99$, $\gamma_2 = 15.2$, and $\gamma_2 = 29.3$ in (b), (c), and (d) respectively. Mean and median eigencontrasts are indicated with solid and and dotted lines. Eigencontrast is defined as the ratio of the first to second eigenvalues when listed in descending order.

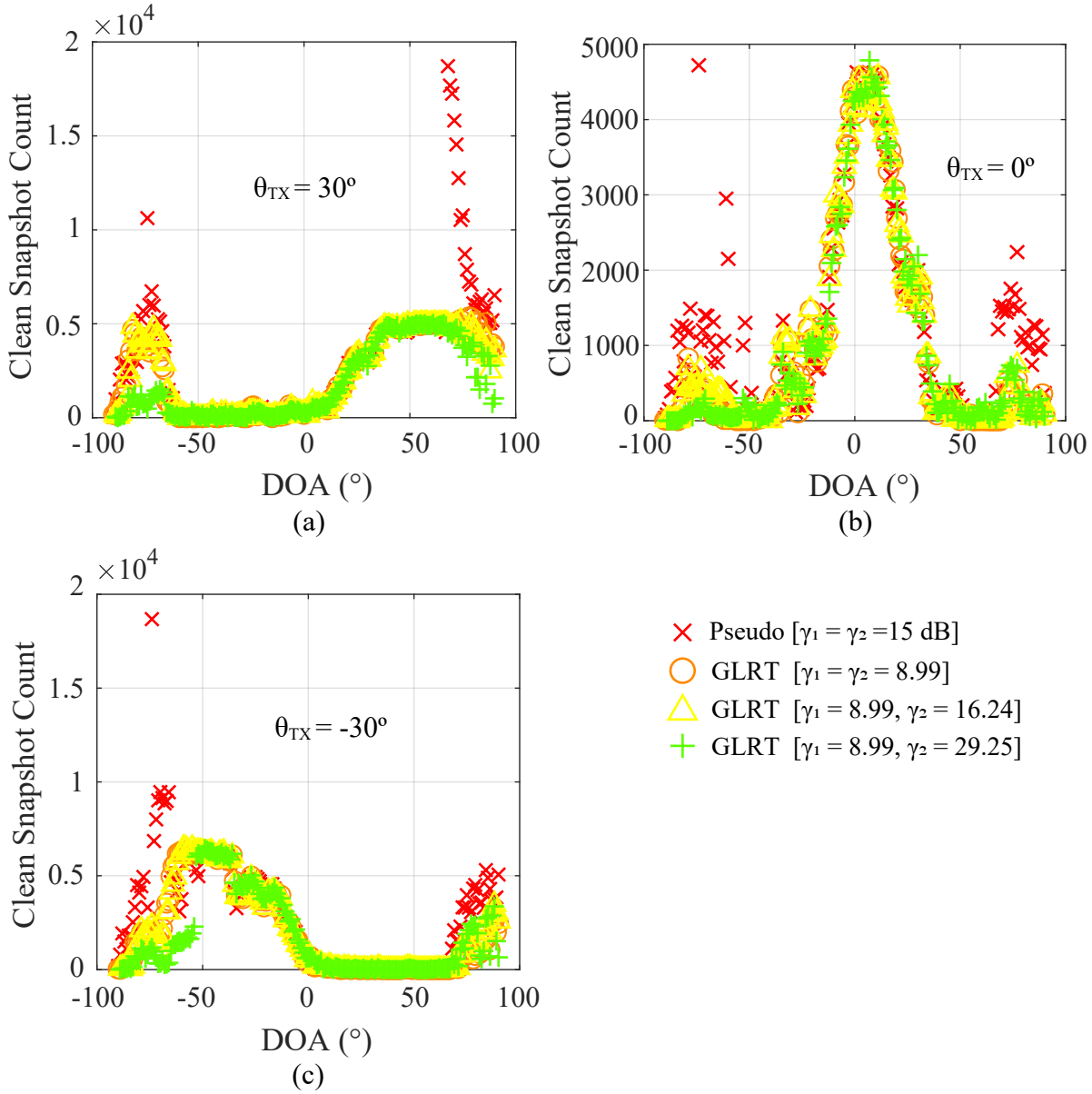

Figure 5.12: Clean snapshot count in 1° angle bins for 20140506_01 calibration set, broken out by transmit pointing direction for multiple culling methods.

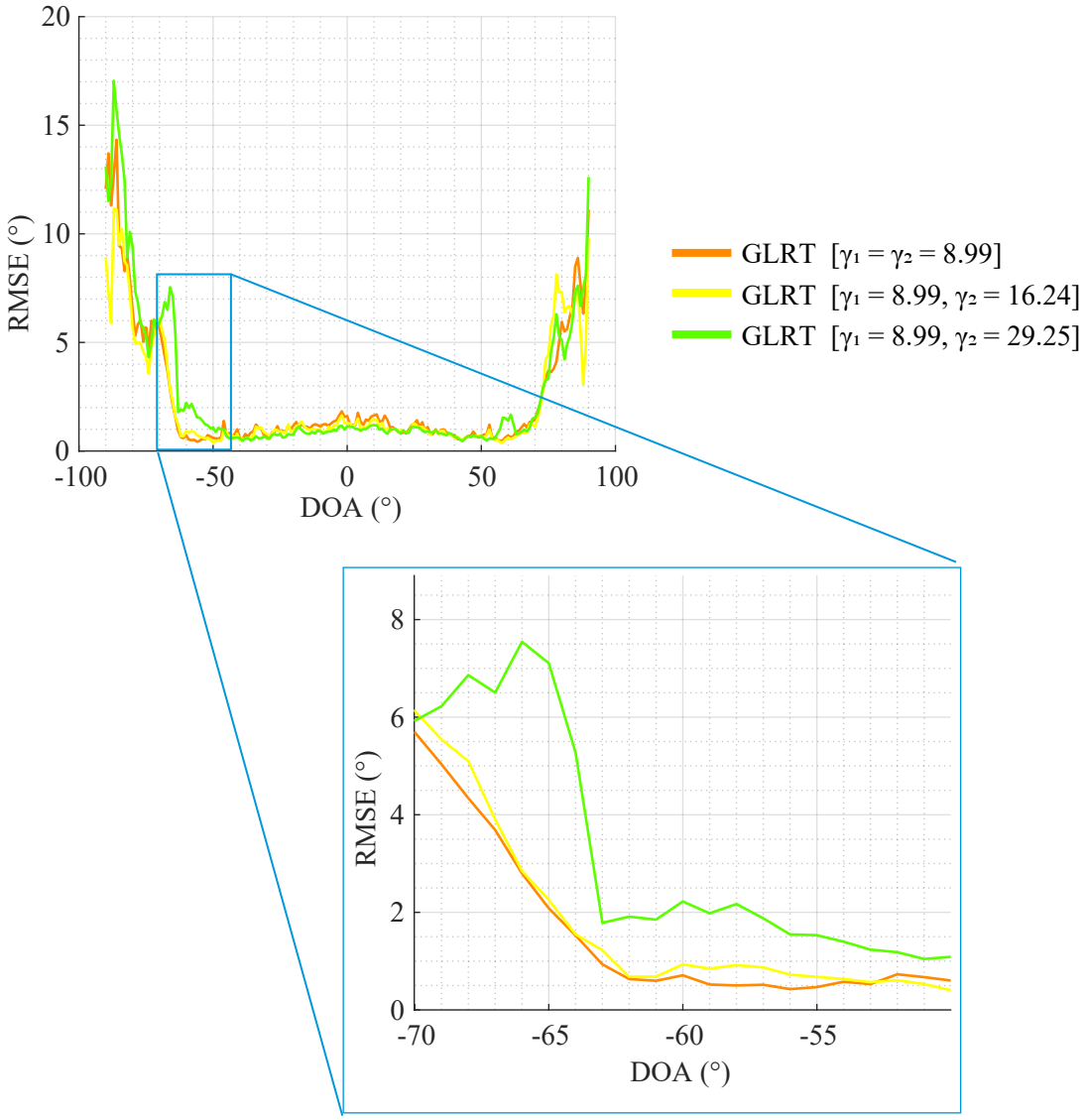

Figure 5.13: MUSIC angle estimation performance with manifolds measured from 20140506_01 calibration set under three thresholds, tested against 20140325_07 and 20140401_03 data sets.

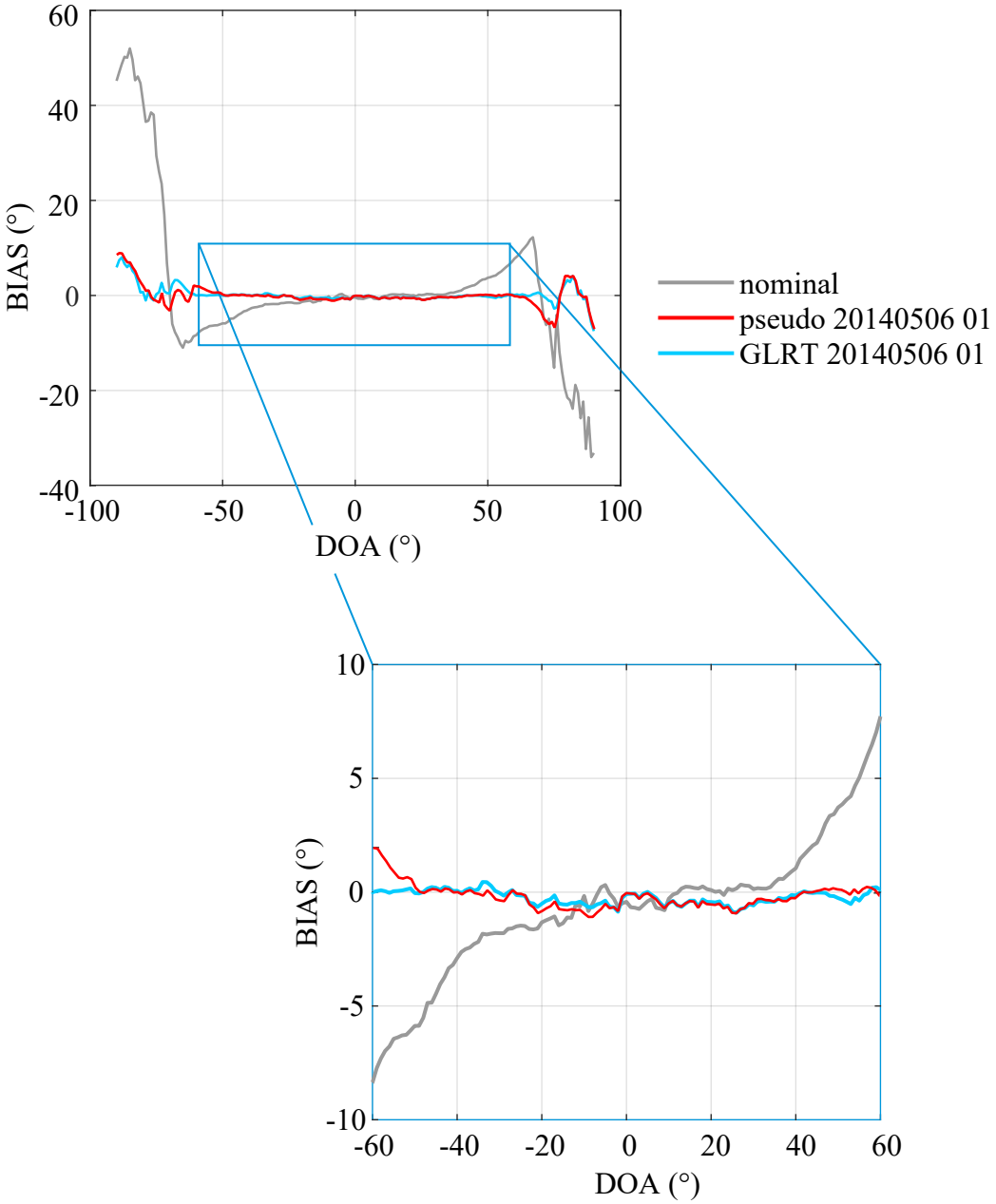

Figure 5.14: MUSIC angle estimation performance with manifolds measured from 20140506_01 calibration with GLRT and pseudoinverse measures in snapshot editing (tested against 20140325_07 and 20140401_03 data sets). Performance is reported in this figure as a bias of estimated arrival angles in degrees.

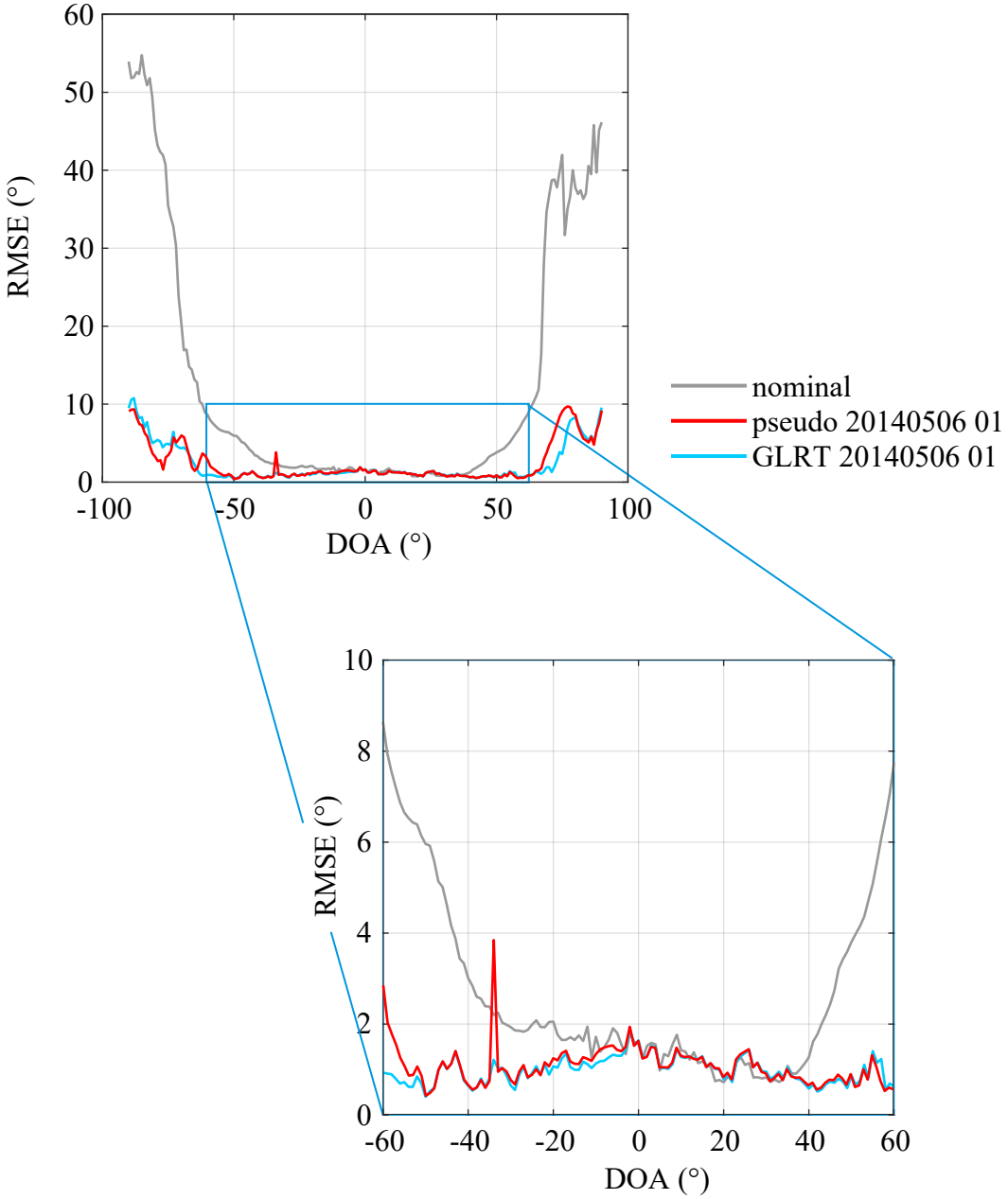

Figure 5.15: MUSIC angle estimation performance with manifolds measured from 20140506_01 calibration with GLRT and pseudoinverse measures in snapshot editing (tested against 20140325_07 and 20140401_03 data sets). Performance is reported in this figure as the root mean squared error of estimated arrival angles in degrees.

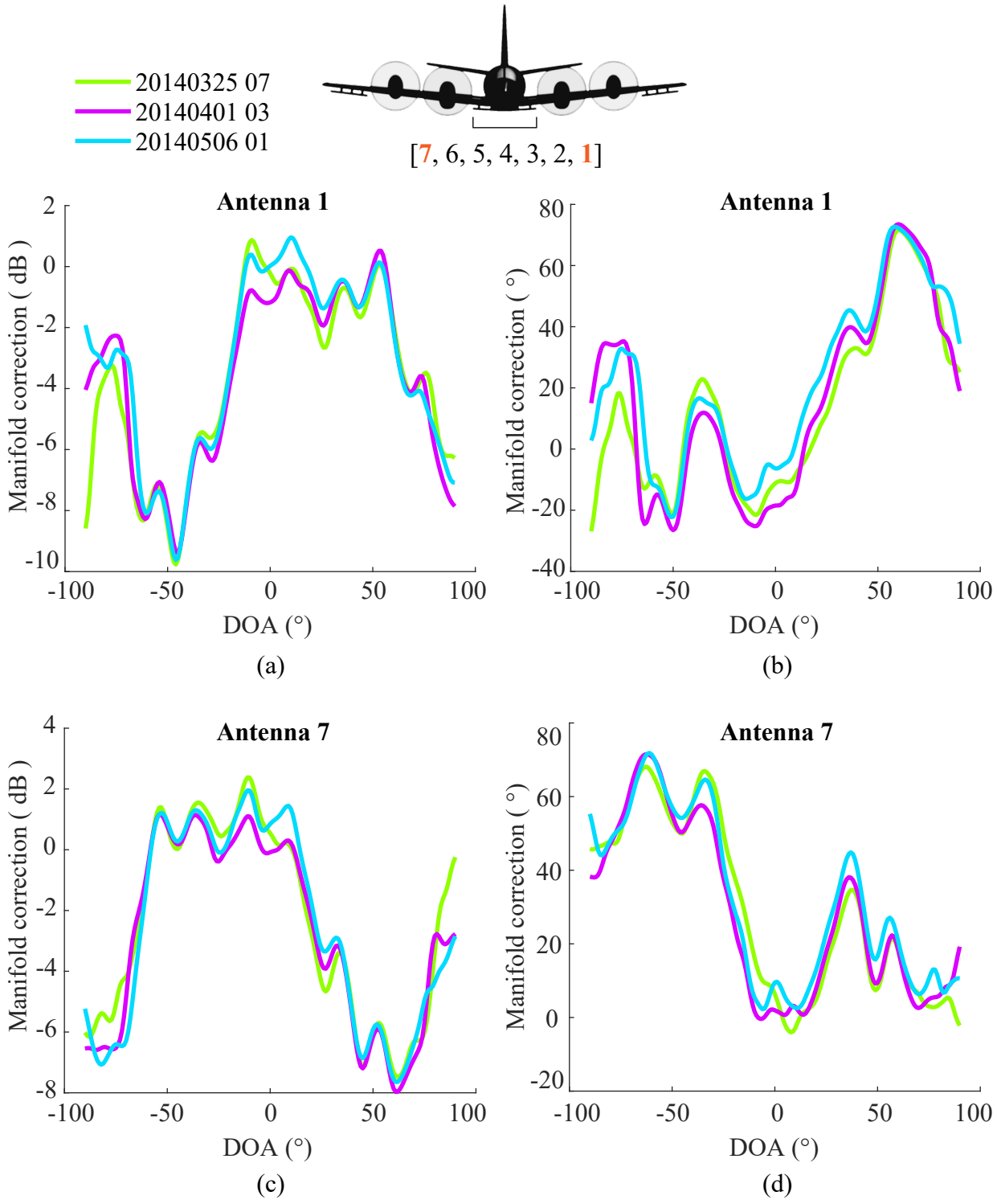

Figure 5.16: Measured manifold corrections for Antenna 1 [(a),(b)] and 7 [(c),(d)] of the RDS center P-3 subarray from three independent calibration sets collected during 2014 NASA Operation IceBridge Mission. Manifolds shown as a correction relative to the isotropic steering vector assuming our nominal model of geometry and reported as magnitude in dB in (a) and (c) and phase in degrees in (b) and (d).

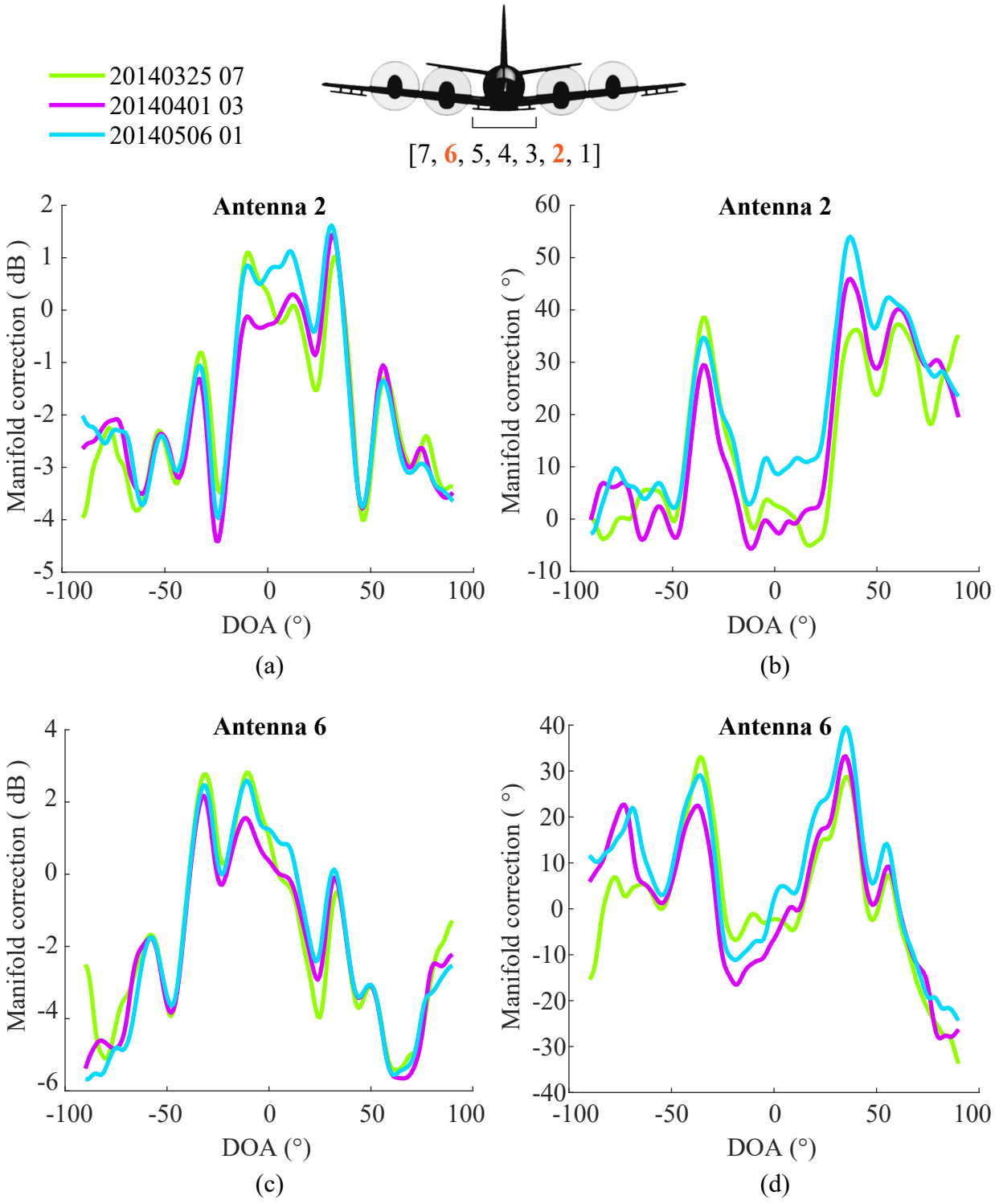

Figure 5.17: Measured manifold corrections for Antenna 2 [(a),(b)] and 6 [(c),(d)] of the RDS center P-3 subarray from three independent calibration sets collected during 2014 NASA Operation IceBridge Mission. Manifolds shown as a correction relative to the isotropic steering vector assuming our nominal model of geometry and reported as magnitude in dB in (a) and (c) and phase in degrees in (b) and (d).

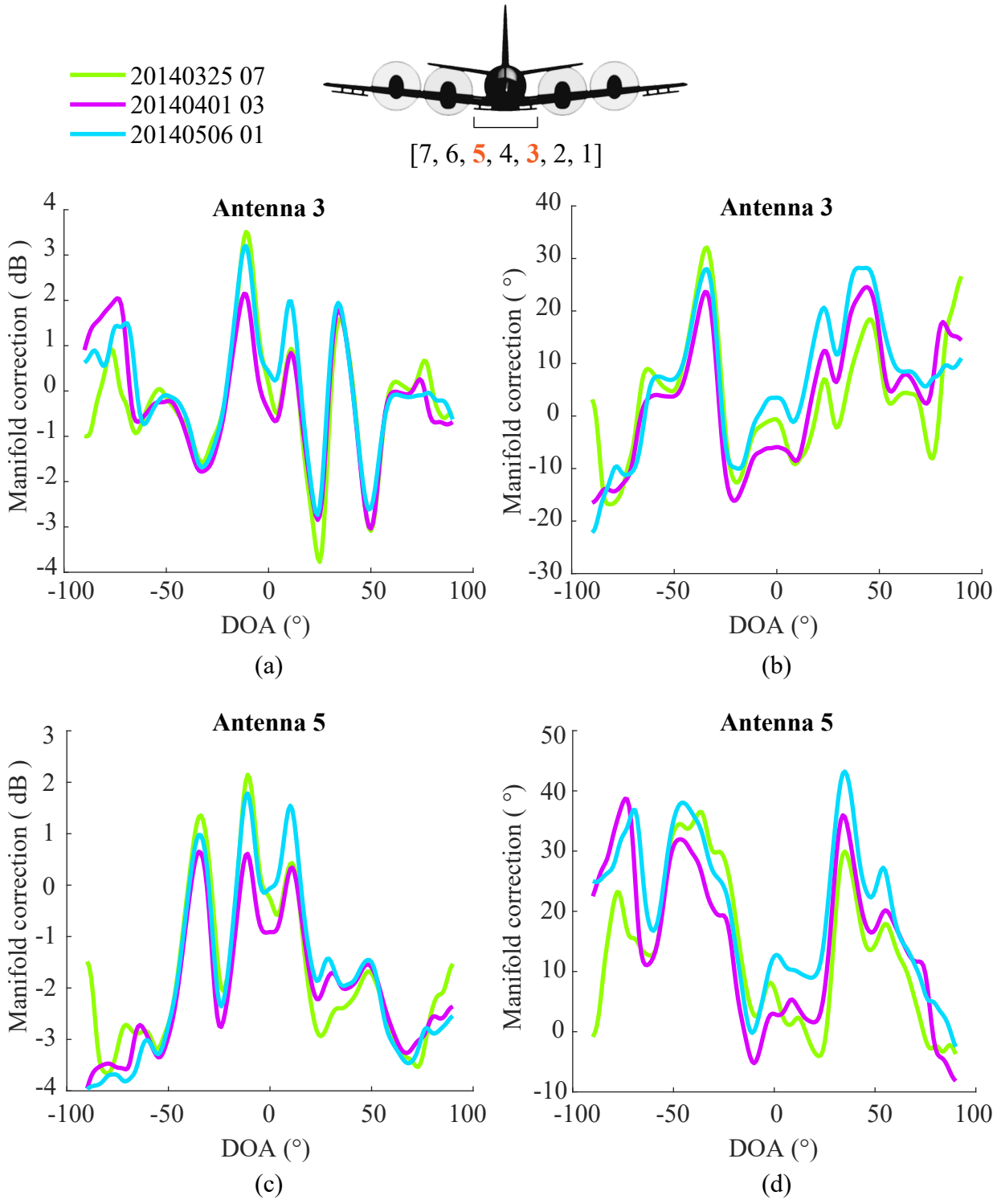

Figure 5.18: Measured manifold corrections for Antenna 3 [(a),(b)] and 5 [(c),(d)] of the RDS center P-3 subarray from three independent calibration sets collected during 2014 NASA Operation IceBridge Mission. Manifolds shown as a correction relative to the isotropic steering vector assuming our nominal model of geometry and reported as magnitude in dB in (a) and (c) and phase in degrees in (b) and (d).

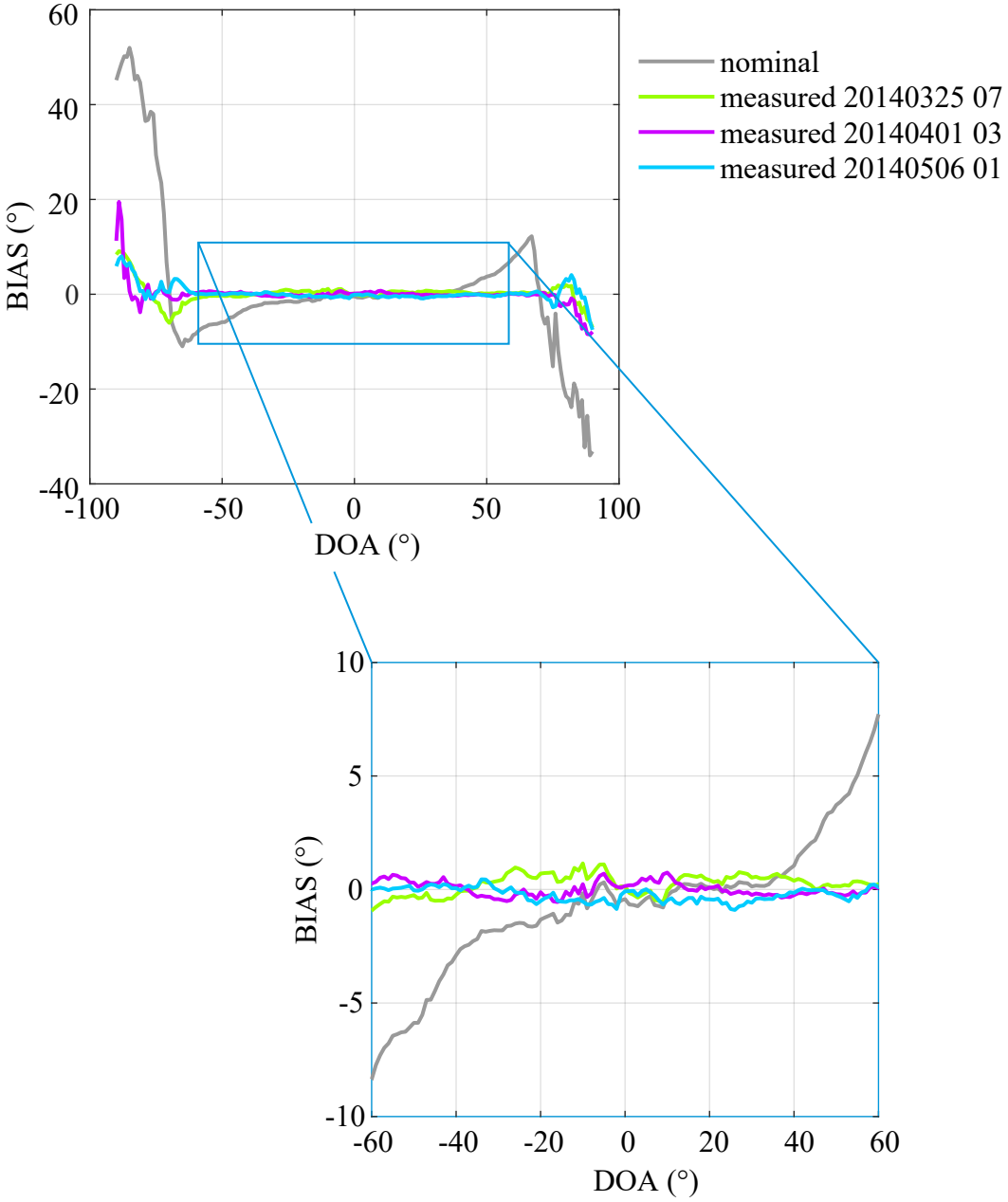

Figure 5.19: Measured MUSIC DOA performance (reported here as estimator bias) comparing angle estimates from four potential manifold models and demonstrating improvements realized with manifold calibration. The nominal curve denotes to the isotropic steering vector result in terms of our existing model of phase center geometry. Measured manifolds refer to results of the nonparametric manifold calibration methodology proposed in this dissertation and summarized in Figures 5.16 - 5.18.

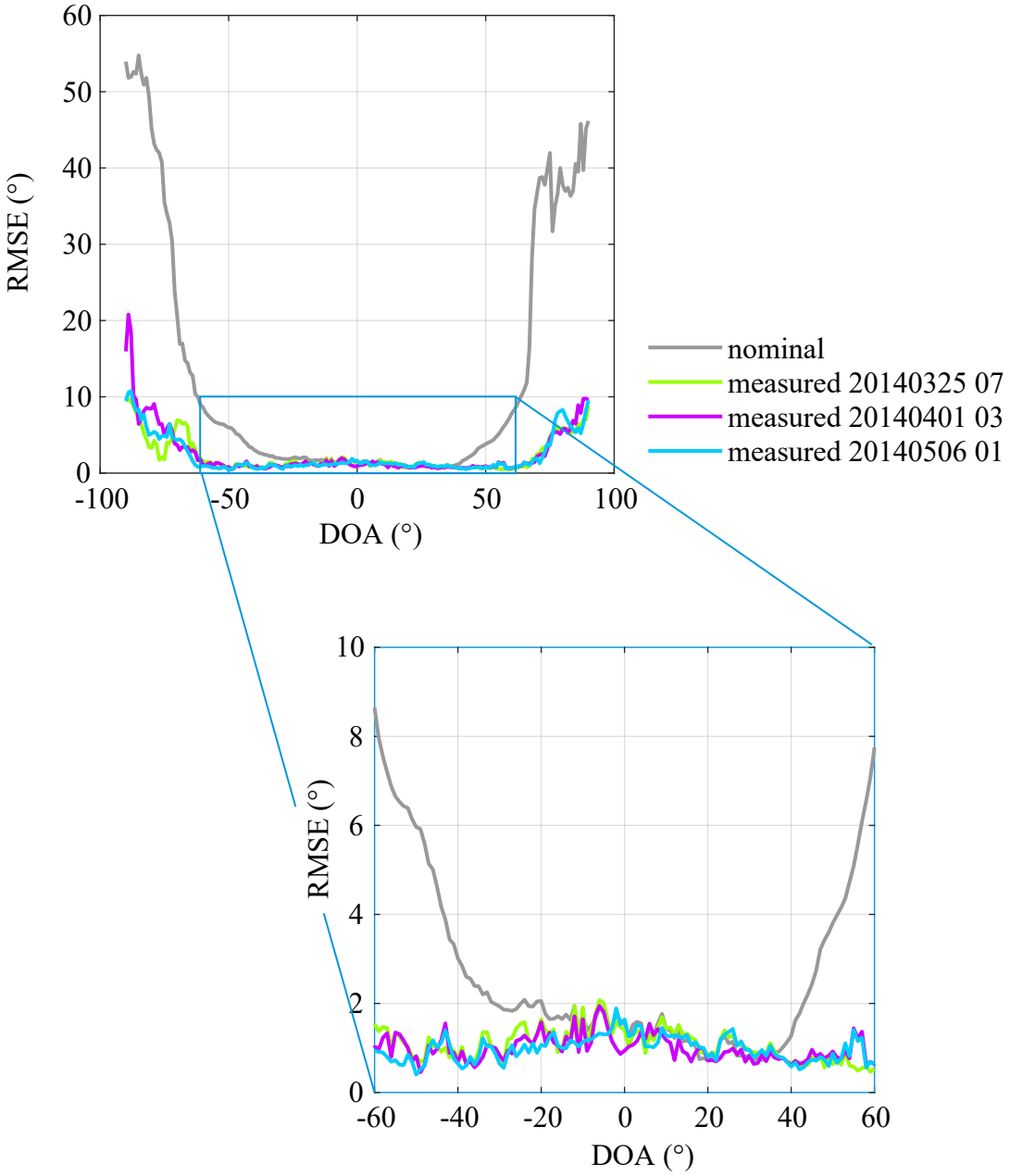

Figure 5.20: Measured MUSIC DOA performance (reported here as estimator error) comparing angle estimates from four potential manifold models and demonstrating improvements realized with manifold calibration. The nominal curve denotes the isotropic steering vector result, evaluated in terms of our existing model of phase center geometry. Measured manifolds refer to results of the nonparametric manifold calibration methodology proposed in this dissertation and summarized in Figures 5.16 - 5.18.

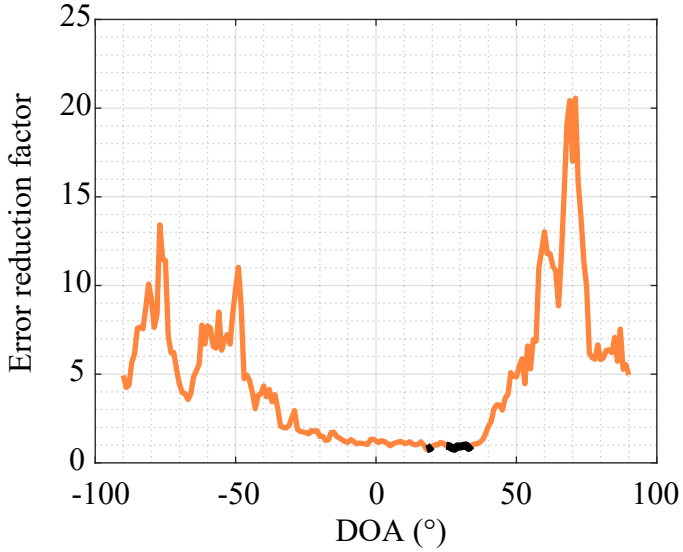

Figure 5.21: Average RMS error reduction demonstrated with measured manifolds, defined as the average ratio of RMS angle estimation error of the nominal model to the RMS error observed with a measured manifold. The black portions indicate where this ratio is less than one and hence interpreted as a localized degradation (where the measured manifold does not outperform the nominal in angle estimation).

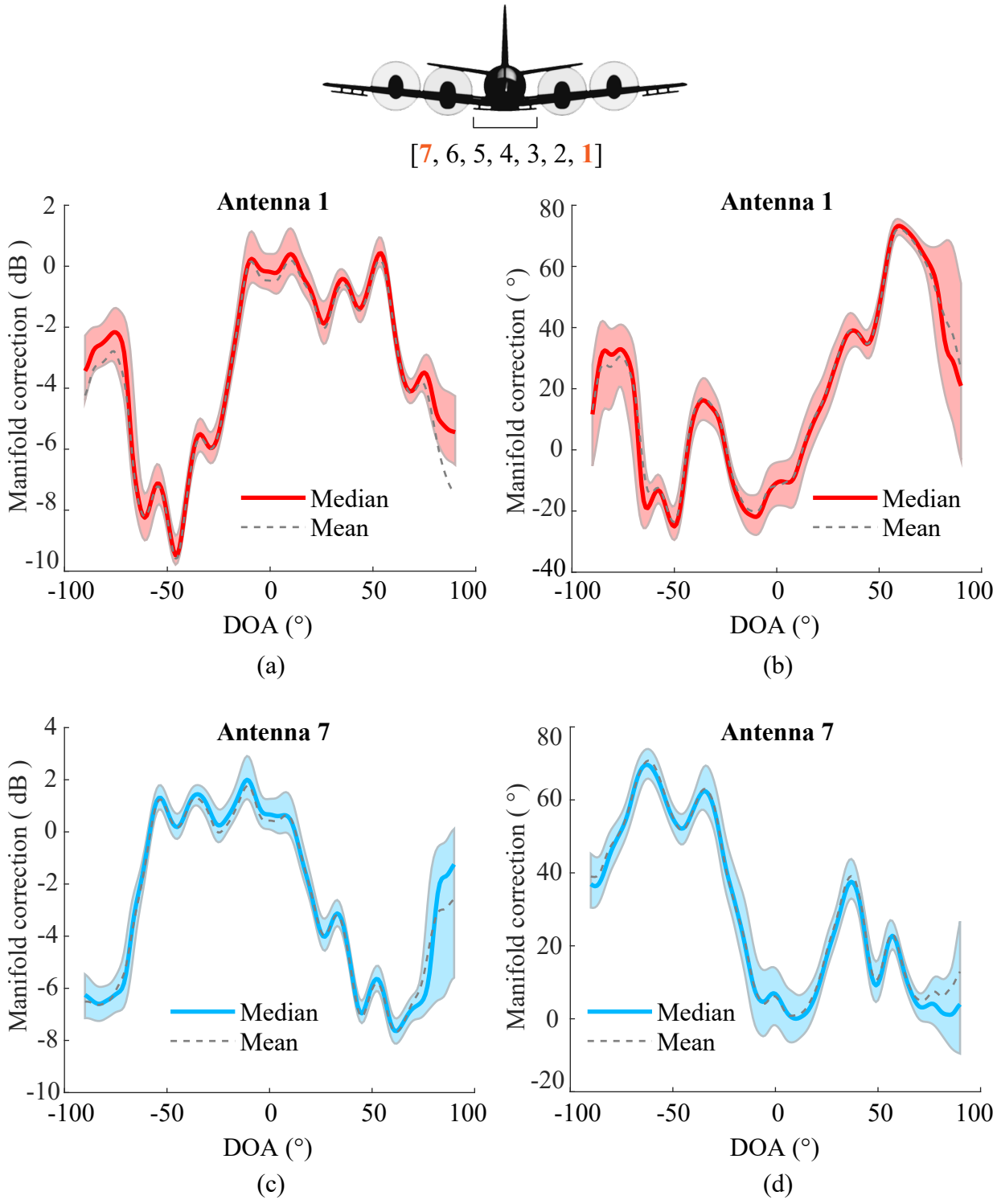

Figure 5.22: Measured manifold offsets relative to nominal model for the RDS P-3 center subarray calibration data collected during the 2014 NASA IceBridge campaign. Responses of antennas 1 and 7 are presented as pairs based on approximate symmetry of antennas within the array. Interquartile ranges (shaded) shown with median and mean steering vectors as: (a), (c) magnitude (dB) and (b), (d) phase (°).

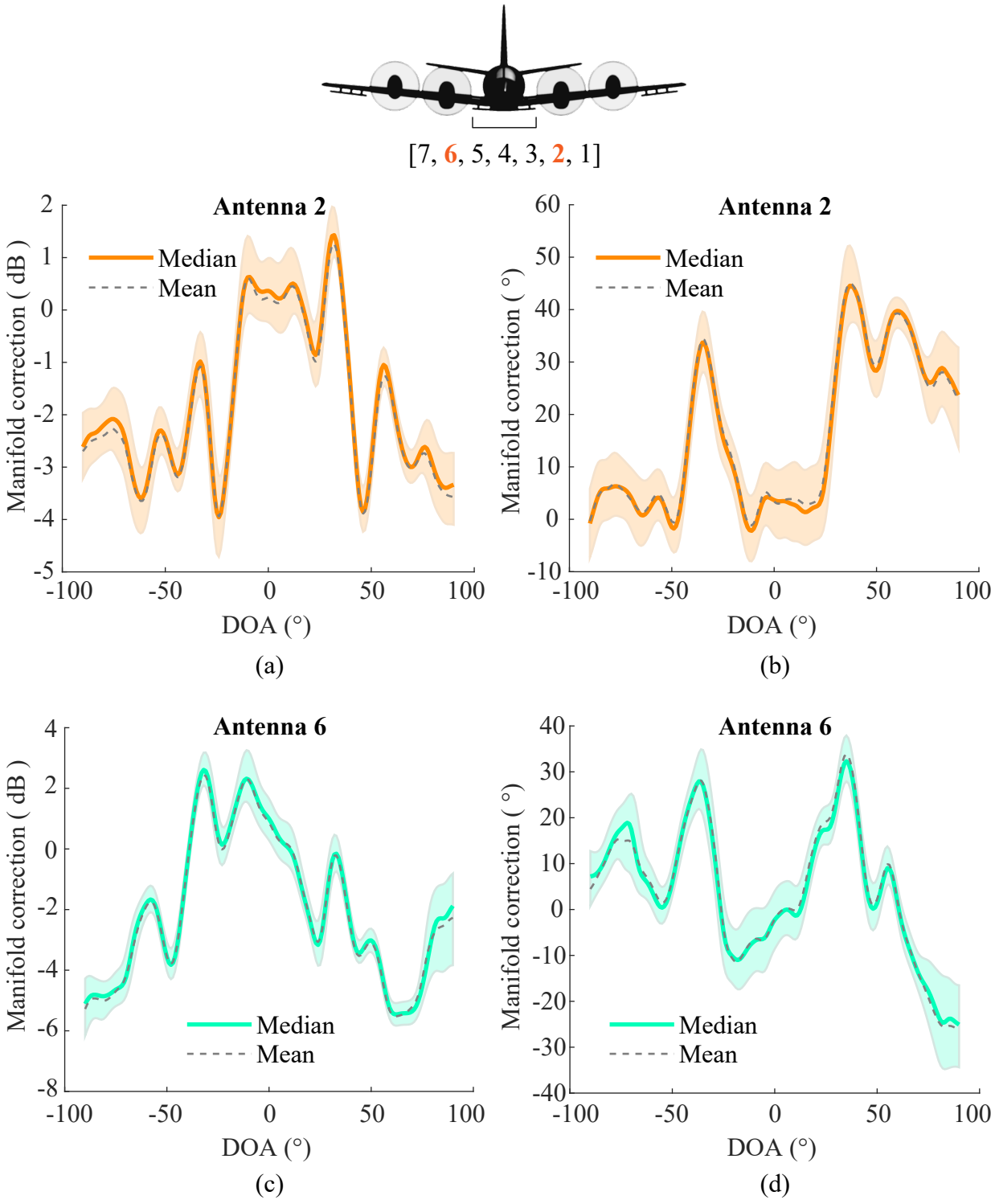

Figure 5.23: Measured manifold offsets relative to nominal model for the RDS P-3 center subarray calibration data collected during the 2014 NASA IceBridge campaign. Responses of Antennas 2 and 6 are presented as pairs based on approximate symmetry of antennas within the array. Interquartile ranges (shaded) shown with median and mean steering vectors as: (a), (c) magnitude (dB) and (b), (d) phase (°).

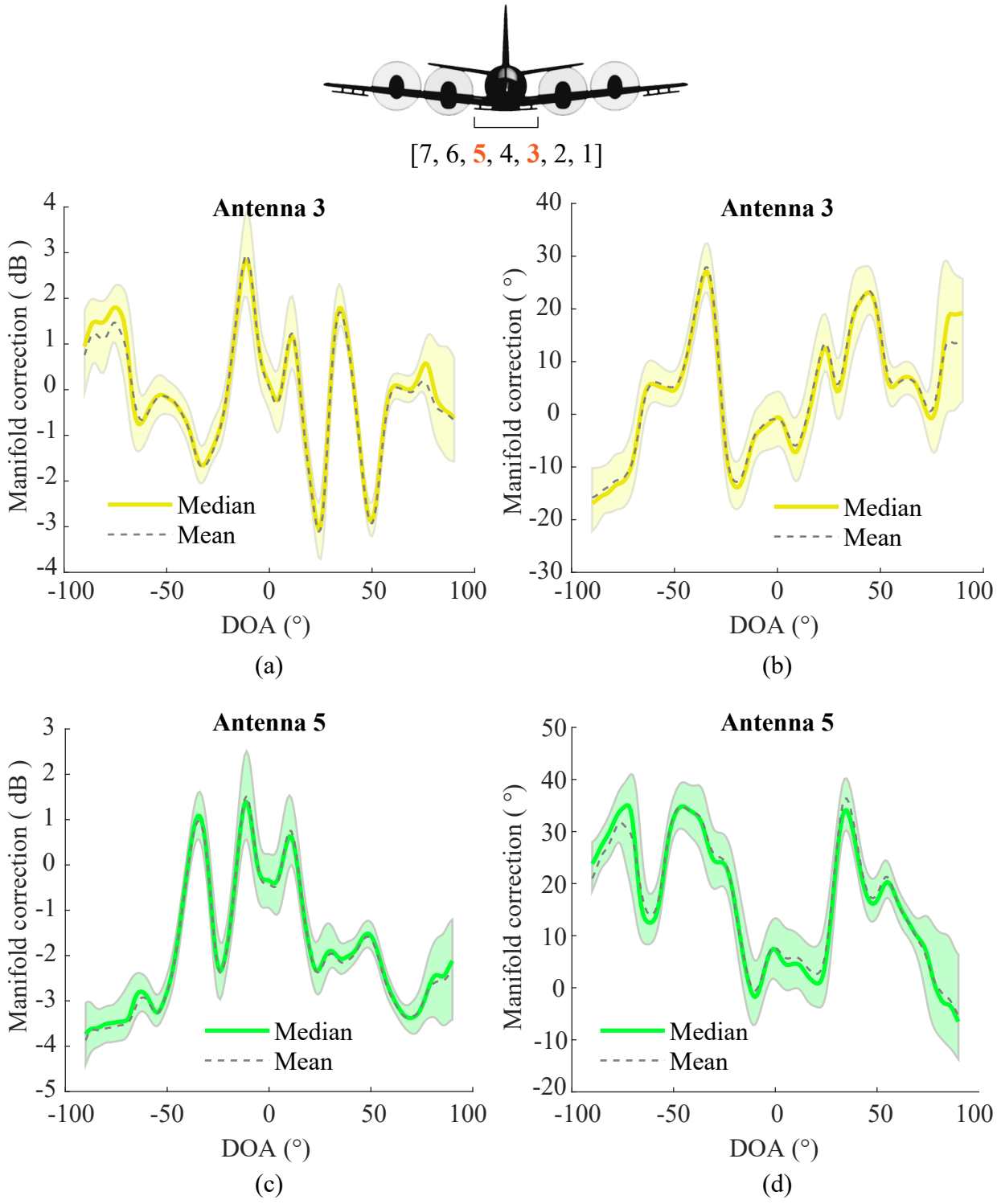

Figure 5.24: Measured manifold offsets relative to nominal model for the RDS P-3 center subarray calibration data collected during the 2014 NASA IceBridge campaign. Responses of antennas 3 and 5 are presented as pairs based on approximate symmetry of antennas within the array. Interquartile ranges (shaded) shown with median and mean steering vectors as: (a), (c) magnitude (dB) and (b), (d) phase (°).

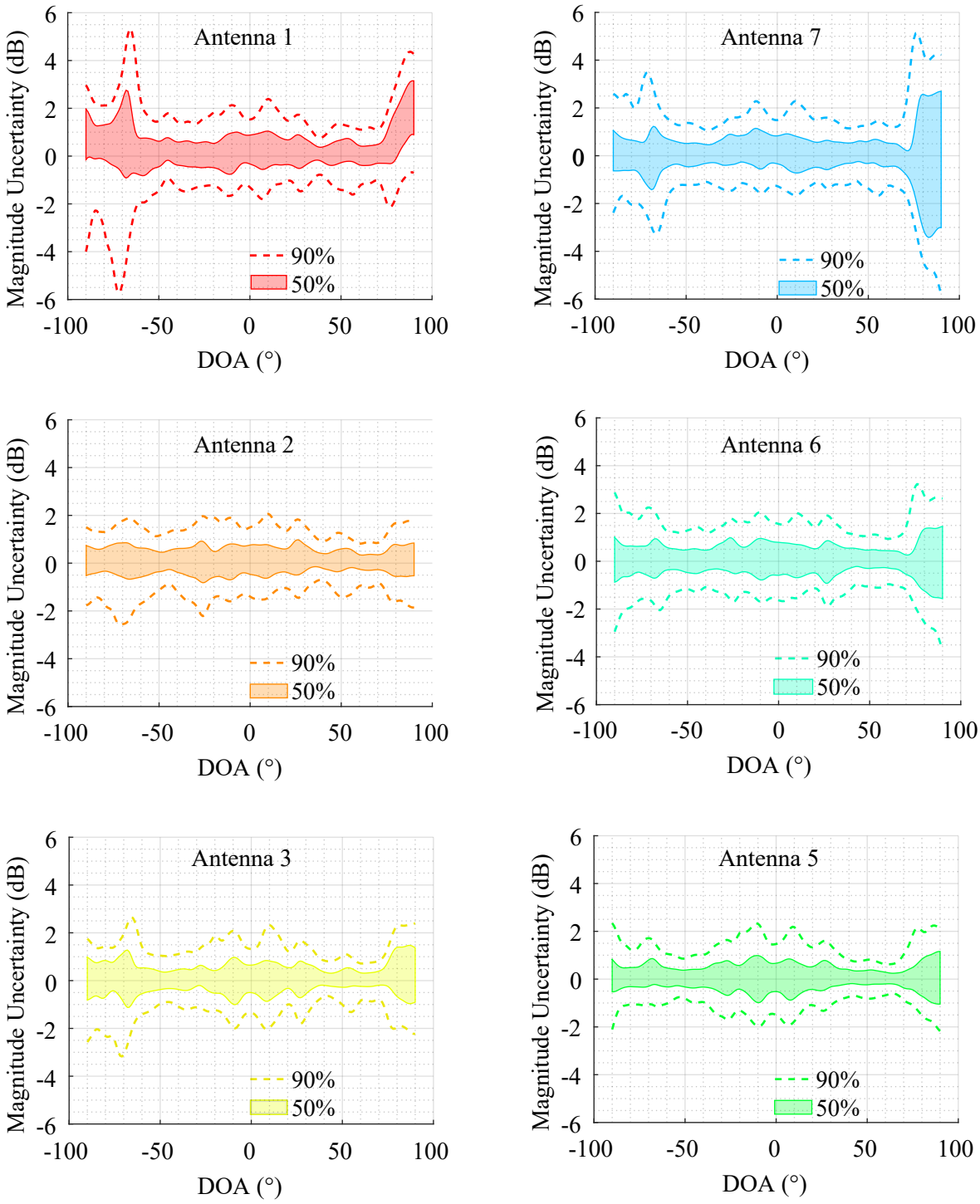

Figure 5.25: Measured spread of combined manifold's magnitude corrections per antenna, showing 90% and 50% spreads in each calibration bin.

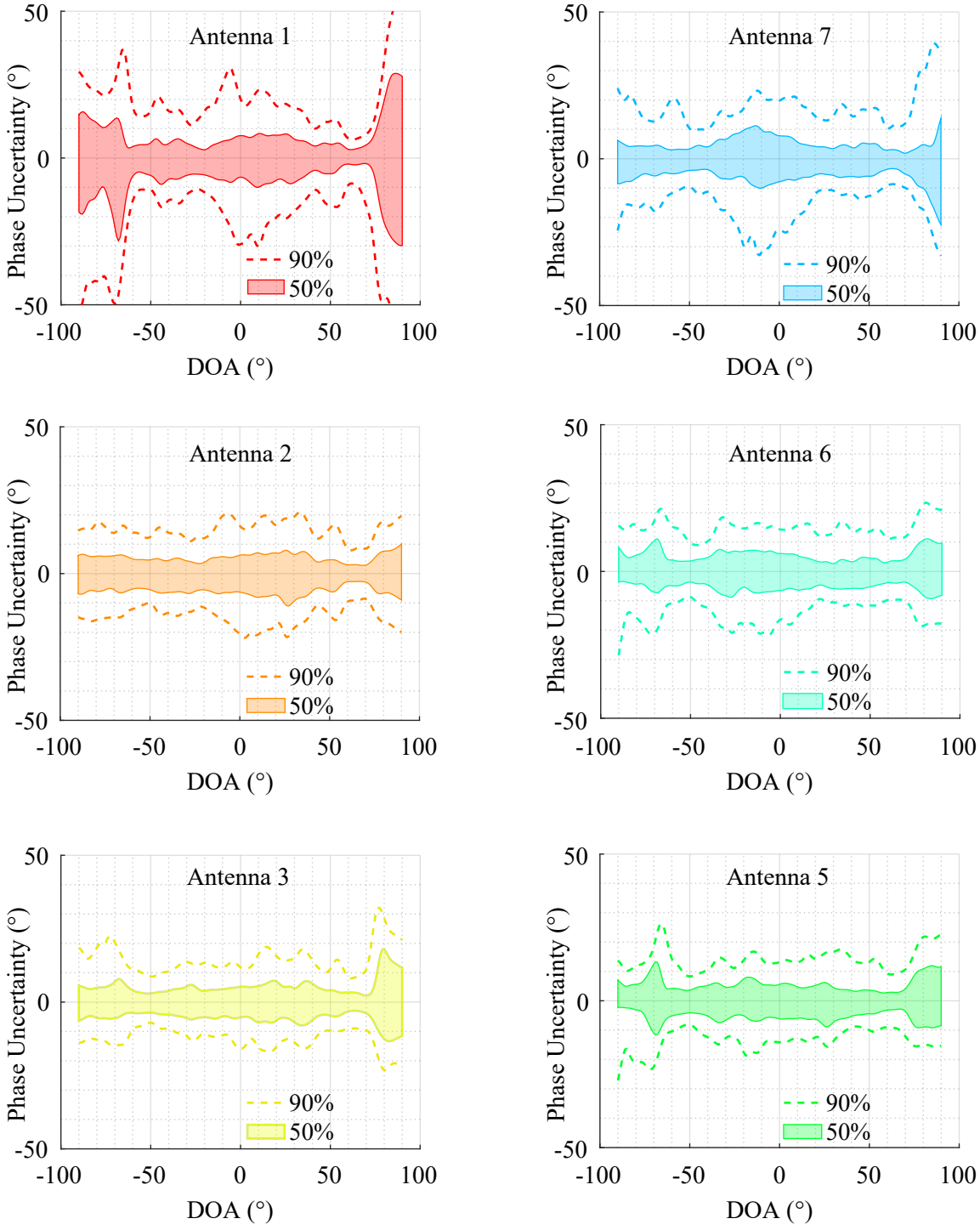

Figure 5.26: Measured spread of combined manifold's phase corrections per antenna, showing 90% and 50% spreads in each calibration bin.

Chapter 6

Deterministic Manifold Modeling with a Full Wave Solver

Abstract

Parametric manifold calibration techniques handle multiple spatial sources simultaneously and pose attractive solutions in the SAR sounder problem space. The parametric approaches assume prior knowledge of a manifold model which may be measured from data or predicted in simulation. Predicting the manifolds of practical sounder airborne arrays requires a high fidelity, full wave solution that accurately accounts for the electromagnetic phenomenology (mutual coupling, multipath, and other platform effects) determining the complex response of the individual elements in their operational environment. To fully understand the error mechanisms determining the RDS array response and to support parametric algorithm benchmarking, a legacy computational electromagnetics (CEM) model of the RDS inboard subarray on the P-3 is refactored for studying manifold calibration as a part of this dissertation. This chapter documents the refactoring of this model and offers some initial predictions of RDS receive manifolds under varying degrees of complexity (from free space to fully integrated on the aircraft with a fairing enclosure). A full method of moments solution for the RDS P-3 receive manifold is presented that realizes tractability with a coarse surface mesh on the platform. Application of this manifold in angle estimation with real sounder observations reduces angle estimator error on average by a factor of 3. The improved angle estimator performance helps confirm the value of CEM predictions in manifold calibration. While the development and validation of this model is still in the early

stages of refinement, the predicted manifolds are expected to offer important utility in parametric manifold calibration algorithm development.

6.1 Introduction

A lack of mensurated embedded element patterns for the RDS P-3 array limits both the application of parametric calibration techniques in the array processor capable of supporting multitarget calibration as well as the interpretation of a manifold measured from data. As a part of the dissertation research, a legacy HFSS model of the RDS P-3 subarrays developed at CReSIS during the initial array design and optimization stages [7], [3], [6] is customized for simulating the embedded patterns with Feko [4], a commercial off-the-shelf CEM software package from Altair. To date, the legacy model has not successfully confirmed the embedded gain patterns of RDS P-3 subarrays. Discrepancies between observations and predictions are attributed to limitations in both the generation of CEM tools and computational resources available at the time the model was developed. Predictive capacity of modeled manifolds is expected to improve with the availability of CEM software that supports hybrid solvers which simultaneously handle both the differential form and integral forms of Maxwell's equations in one model and that offer advanced meshing techniques to capture electrically small features that are known to alter the resonance of the antennas against electrically large structures. Predicting receive RDS P-3 manifolds with a full wave solver is a complex modeling problem, driven by the structural intricacies of the fairing enclosures; results offered in this chapter should be regarded as tertiary predictions that warrant further investigation.

This chapter documents the refactoring of the legacy RDS P-3 inboard subarray model and its integration into Feko. The antenna model of the RDS wideband dipole elements is described including its feeding, balancing and basic performance validation. The fairing structure is discussed in detail, describing material properties and component dimensions. CEM methodology is offered which outlines the approach for scaling the computational size of the model (required to carry out simulations given the computational resources available)

and potential limitations imposed in scaling the problem are discussed. Predicted receive manifolds are presented to illustrate deviations from a nominal manifold with varying degrees of platform complexity.

6.2 CEM Model Development of Inboard Subarray

In the section that follows, the porting and refactoring of the legacy HFSS model in Feko is documented. Antenna feeding and validation are described. We document modifications meant to increase the representation of structural detail in the near field of the radiators. Specific modifications include representing the layered dielectric substrate structure of the fairing's bottom skin with embedded conductive structural components.

6.2.1 RDS Wideband Antenna Element Model

The wideband dipole element design of the RDS antennas making up the P-3 subarrays optimizes return loss and operating bandwidth of the elements when embedded in the fairing structure and an individual element is designed to have a 50 Ω input impedance [3]. The final design supports operation of the subarrays over the 160-240 MHz frequency range with a minimum return loss of 10 dB. The planar antenna elements have two layers of copper on opposite sides (top and bottom) of a 69 mil FR-4 substrate, modified from their original bow-tie design to reduce mutual coupling with triangular notches at the copper edges [3]. A Feko [4] model of the RDS P-3 antenna element is illustrated in Figure 6.1, showing the top conductor layer with modified edges (copper) lying on the dielectric substrate (in blue).

This figure specifies the geometry assumed in the Feko model. Script angle variables are used here to emphasize a distinction between those assumed in the array processor. The Feko coordinate system measures elevation angle, ϑ, with respect to zenith (aligned to *up* in an East-North-Up coordinate system). We measure angle of arrival, θ, with respect to nadir (aligned to *down* in a North-East-Down coordinate system) in tomography. Results

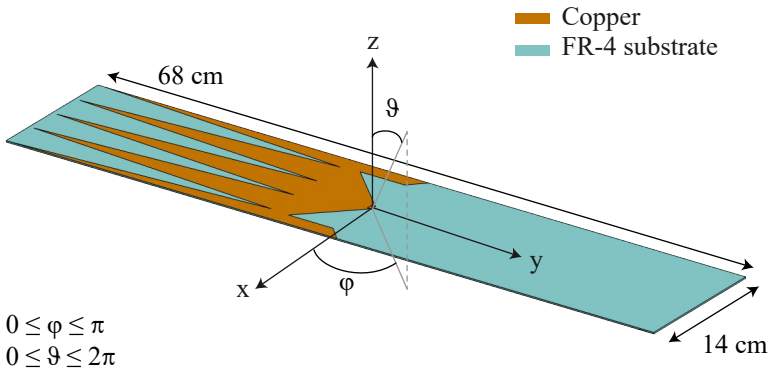

Figure 6.1: RDS wideband dipole model developed in Feko [4] showing top copper layer on 69 mil FR-4 substrate.

presented further in this chapter plot gains and manifolds with respect to our angle of arrival, θ. These plots cover the angular range of $-90° \leq \theta \leq 90°$ when reporting results within the field of regard. Patterns plotted over the range $-180° \leq \theta \leq 180°$ include antenna field quantities in the backlobe region where $|\theta| > 90°$

A center-fed dipole antenna is said to be balanced when the current distributions in the arms of the dipole are of equal magnitude and opposite direction. Symmetrical element designs are inherently balanced by their physical symmetry. Balanced and unbalanced geometry is illustrated for a wire dipole shown in Figure 6.2. The balanced configuration in 6.2a ensures equal magnitude currents in the arms of the dipole while the asymmetry in 6.2b alters the impedance of the element leading to an asymmetric current distribution in the arms. While parallel wires provide inherently balanced feeds for a balanced element such as the wire dipole, a coaxial cable leads to unbalanced current distributions when currents flow on the outside of the outer conductor which may cause the cable to radiate. The balun is a device designed to transform the balanced antenna impedance to the unbalanced impedance of the coax in order to suppress current flow out the outside of the outer conductor.

The feed design of the P-3 array, described in [3], involves ferrite transmission line transformers created from twisted-pair magnet wire looped through the interior of binocular ferrite core to suppress current propagation on the outside of the outer conductor. Ferrite beads spaced along the coaxial cables that route from the interior of the cabin out to the arrays

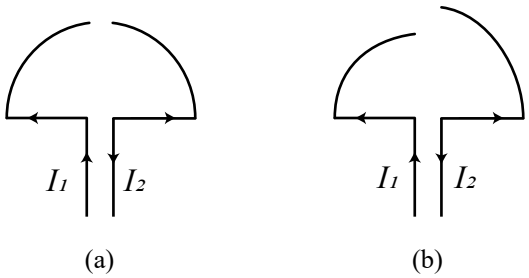

Figure 6.2: Illustration of (a) balanced and (b) unbalanced operation of a wire dipole, recreated from [5].

serve as common mode current chokes that suppress parasitic currents leading to unintentional radiation of the feed cables. These components add complexity to the Feko model considered beyond the scope of this dissertation. Hence the model which generates results presented in this chapter regards the antenna ports as the plane of reference and does not handle the microwave network attached to the array.

The legacy HFSS model of the antenna includes a via passing through the FR-4 substrate and electrically connecting the top and bottom conductors as shown in Figure 6.3. The box is slightly offset from the center of the element and creates a small asymmetry in the surface current distribution when the antenna is excited without the balun. The HFSS excitation port, also indicated in Figure 6.3, is a rectangular face that points to an input source file, presumably measured experimentally. For the purpose of this study, both the via and the excitation aperture are removed to restore structural symmetry, thereby balancing the current distribution in the Feko model. The antenna faces are modified slightly to allow a small overlap at the center of the geometry to accommodate a conductive face for installation of an ideal edge port. In the Feko model, the antenna is fed with a voltage source at the very center of the element where the top and bottom patches overlap in the z dimension. The modified feed point is shown in Figure 6.4. The balanced instantaneous current distribution is illustrated in Figure 6.5 to visually demonstrate symmetry across the top and bottom conductors. The dielectric is suppressed from the figure to show both faces simultaneously.

The modeled RDS antenna is benchmarked in Feko prior to simulating the element in

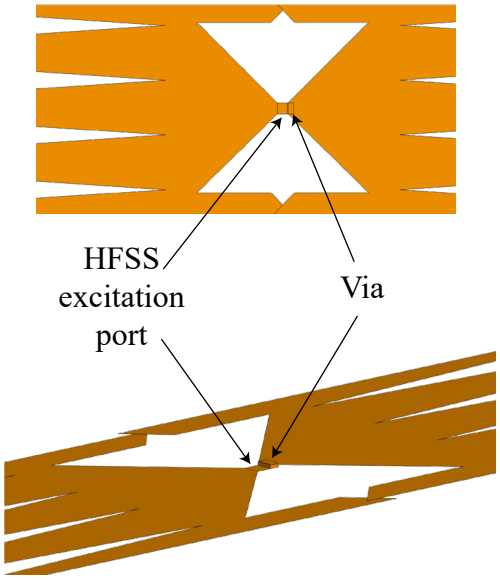

Figure 6.3: Structural components of the legacy HFSS model altered for this study.

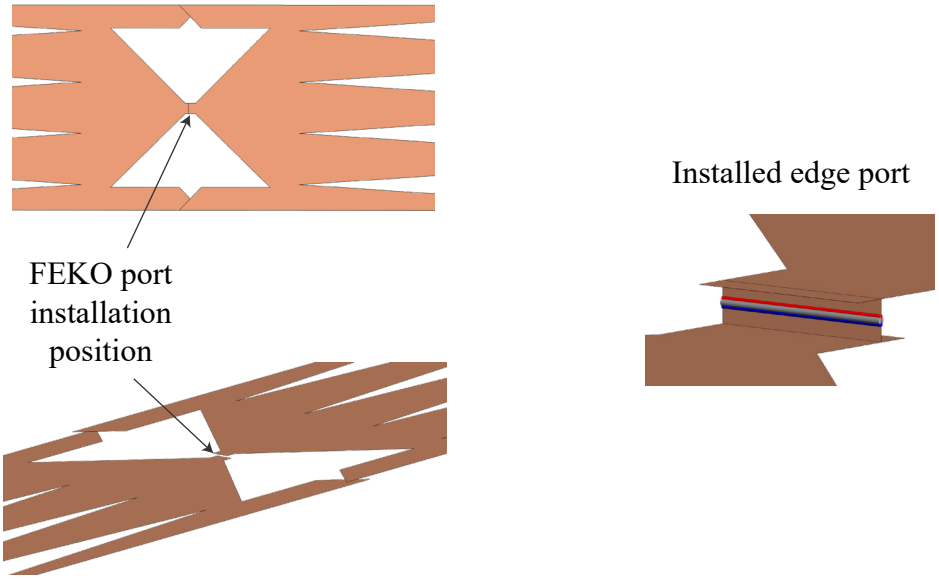

Figure 6.4: Modified feed site and installed edge port in the Feko model.

the context of an array. The following antenna performance parameters are reported here: frequency-dependent return loss and mismatch efficiency referenced to 50 Ω, antenna input impedance and polarization properties. The purpose of reviewing the performance metrics of the modeled antenna element is to identify a reasonable operating frequency for the Feko based studies that follow.

Scattering parameters of the antenna over the 150 to 300 MHz frequency range are

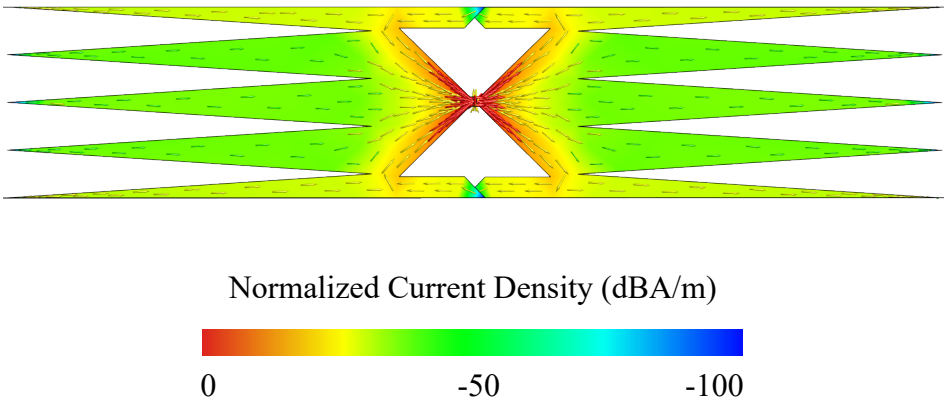

Figure 6.5: Normalized instantaneous surface current density in top and bottom conductors of an RDS antenna with a 195 MHz excitation. The dielectric substrate is suppressed in the figure to show symmetry between conductive faces.

measured from the modeled antenna using the S-Parameter configuration in Feko with a 50 Ω reference impedance. The simulation creates a Touchstone file that can be used to create an S-parameter object with MATLAB's RF toolbox [94]. The measured S_{11} is interpreted as the voltage reflection coefficient, Γ, that is used to compute the return loss and mismatch efficiency as

$$\mathrm{RL(dB)} = -20\log_{10}(\Gamma), \tag{6.1}$$

and

$$q = 1 - |\Gamma|^2. \tag{6.2}$$

The input impedance of the isolated element, Z_A, is computed using the following relationship between the reflection coefficient, the reference impedance, Z_0, and Z_A

$$\Gamma = \frac{Z_0 - Z_A^*}{Z_0 + Z_A}. \tag{6.3}$$

Return loss, mismatch efficiency and input impedance are plotted as a function of frequency in Figure 6.6. The Feko implementation of the RDS wideband dipole achieves at least 13 dB return loss in isolation over the RDS band of 180 to 210 MHz, thereby satisfying

the specified minimum value of 10 dB cited in [3]. We can expect this metric to alter when the antenna is embedded in the array due to platform effects such as capacitive loading of aluminum doublers in the fairing structure described in [3]. Matching efficiency, derived from Γ using Equation 6.2, exceeds 95% over the band. We note from Figure 6.6(c) that over the frequency range of interest, the antenna is slightly inductive. This can be offset with a matching circuit that introduces capacitance in feeding the element or terminating in a perfectly matched load on receive.

The three-dimensional far field gain pattern is shown in Figure 6.7(a) at 195 MHz overlaid on the element showing a typical dipole shaped pattern. A cut through the pattern in elevation is shown in Figure 6.7 as a polar plot divided in 10 dBi rings. The pattern realizes a peak gain of approximately 1.9 dBi at 195 MHz, which suggests that at this frequency the RDS antenna lies between the characteristics of a short wave and half-wavelength dipole [102]. The peak gain, G_0, and peak directivity, D_0 are measured in Feko as a function of frequency over the 150 to 300 MHz band and used to determine the radiation efficiency of the antenna based on the following relationship

$$G_0 = e_r D_0. \tag{6.4}$$

The radiation efficiency e_r is plotted in Figure 6.8(a) while peak gain and directivity are shown in (b).

6.2.2 Constitutive Parameters of Materials in Feko Model

The components of the integrated array model are handled as one of the four types of materials: perfect electric conductor, aluminum, S-2 glass, FR-4 epoxy, and Rohacell 71 IG foam. The constitutive parameters of the conductive materials and dielectric materials are summarized in Table 6.1 and Table 6.2 respectively. Both tables categorize the components of the Feko model by material type and offer references for the cited values. Note that conductive materials are defined using Feko libraries only thus Table 6.1 does not offer

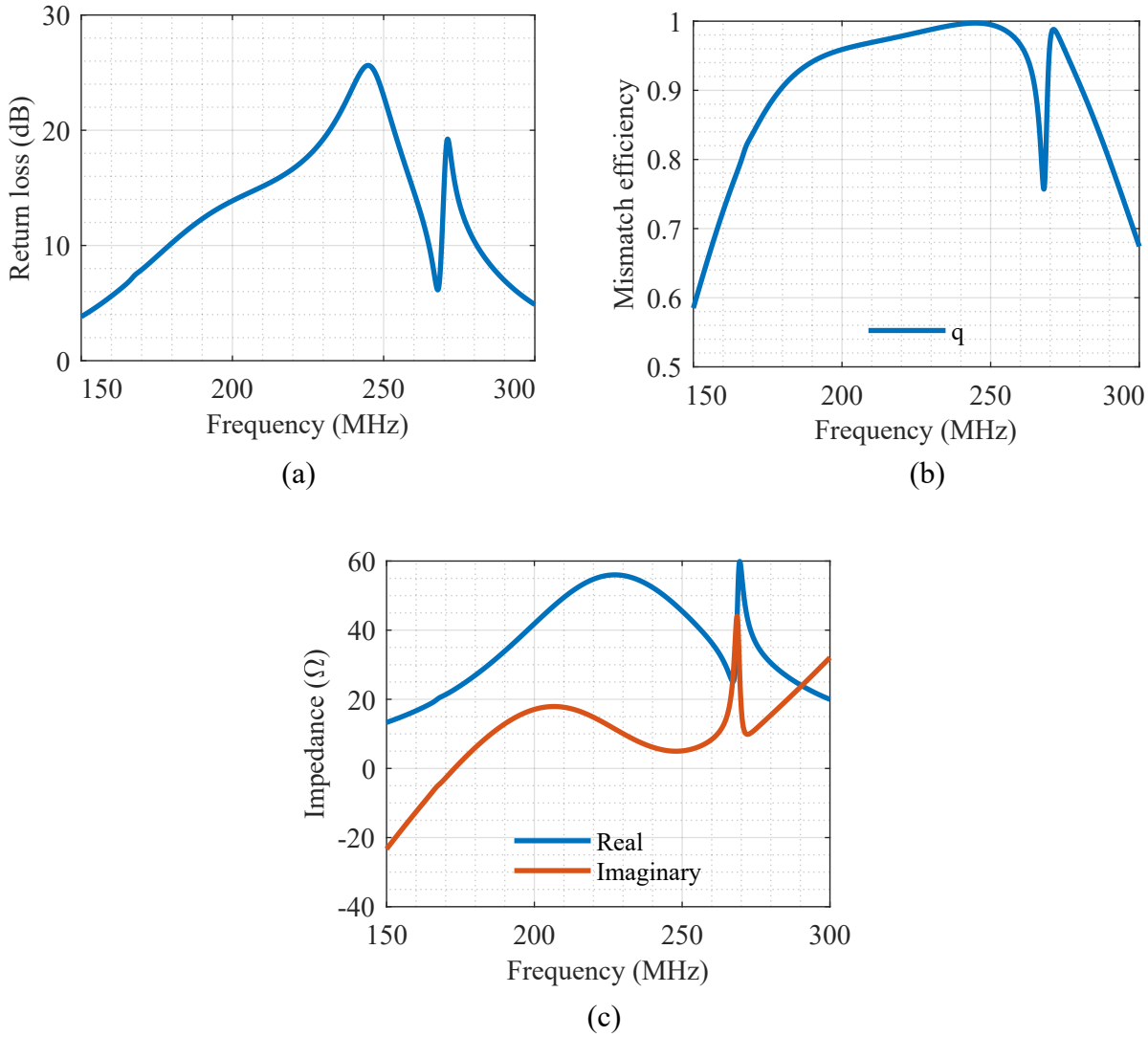

Figure 6.6: RDS isolated antenna performance parameters measured in Feko: (a) return loss referenced to 50 Ω, (b) mismatch efficiency referenced to 50 Ω, (c) antenna input impedance.

associated references.

6.2.3 Inboard Fairing Model

The antenna fairings are aerodynamic enclosures surrounding the subarrays, allowing them to suspend from hard points on the aircraft in flight. The original design, which was driven by NASA's airworthiness certification requirements [87], was modified to improve measured return loss over several design iterations following the inaugural flight of the RDS P-3 sub-

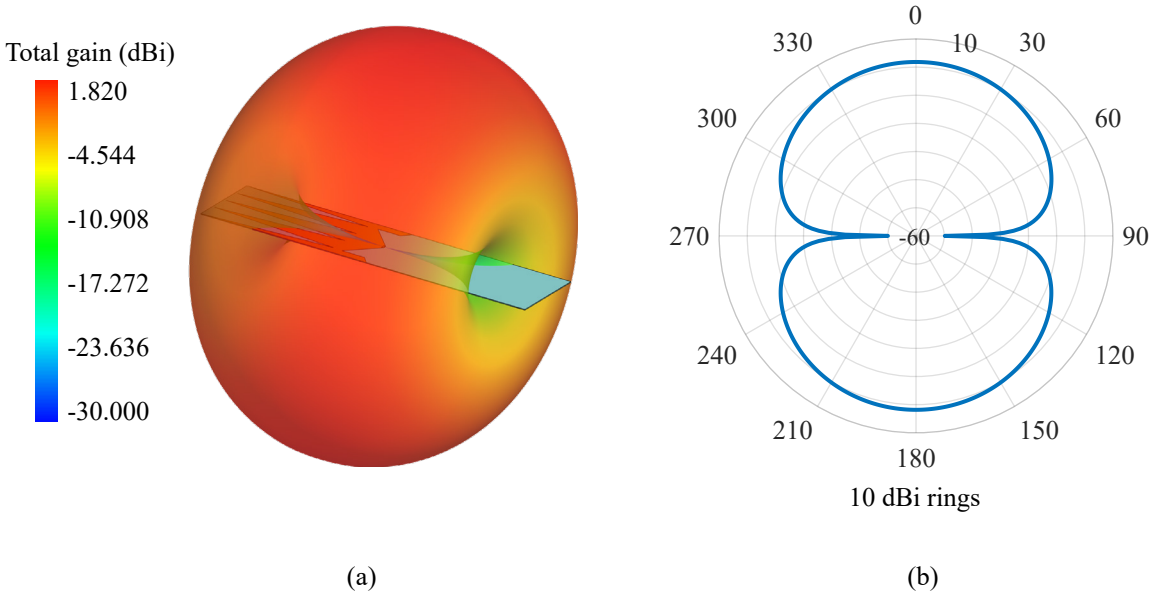

Figure 6.7: RDS isolated element gain pattern at 195 MHz simulated in Feko [4]: (a) 3-D overlay on element model and (b) polar plot.

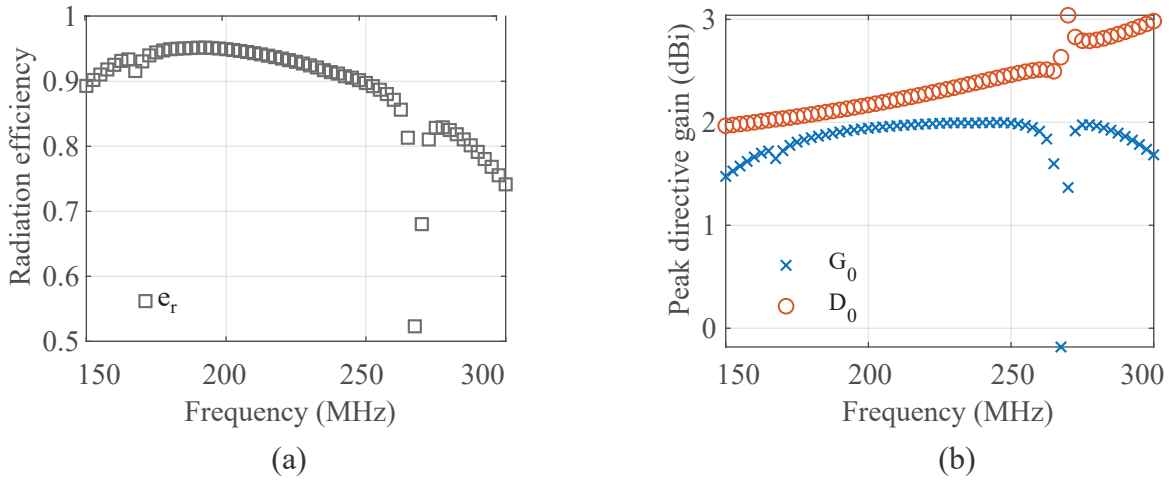

Figure 6.8: RDS isolated element performance characteristics over 150 to 300 MHz band: (a) radiation efficiency and (b) peak gain and directivity.

arrays at NASA Wallops Flight Facility in the Spring of 2010. In an attempt to faithfully represent the state of the array flown during the 2014 IceBridge mission, the following sources are consulted and referenced in development of the Feko model: [87], [107], [3], [7]. The section that follows reports the representation of the primary structural components in the

Table 6.1: Summary of conductive materials in model.

Material	σ_c(S/m)	μ_r	$\tan\delta$	*Components*
Perfect conductor	inf	1	0	Antenna conductors
Aluminum	38,160,000	1	0	Doublers Gang channels Junction ribs Rib inserts Aircraft skin

Table 6.2: Summary of dielectric materials in model.

Material	ε_r	$\tan\delta$	$\rho\,(\mathrm{kg/m^3})$	*Reference*	*Components*
FR-4 Epoxy	4.8	0.017	1,000	[4]	Antenna substrate
S-2 Glass	5.3	0.002	2,488	[103]	Bottom skin Top skin Spars Fairing ribs Outer edges
Rohacell 71 IG	1.09	0.0003	75	[104], [105], [106]	Bottom skin layer

electromagnetic model including bottom and top fairing skins, leading and trailing edges and spars, and non-embedded aluminum components.

The legacy model [7] provides the geometry of the platform as well as the dimensions, shapes, and relative orientation of structural components needed to model the inboard fairing. When possible, basic structural components are rebuilt in Feko with parameterized dimensions. Parameterization of lengths enables the model to be modified by simply changing user-defined dimensional variables which in turn updates the entire model in Feko. The more complex shapes including the glass ribs, junction ribs, and spars are taken directly from the legacy model and assigned the appropriate material properties based on Table 6.2

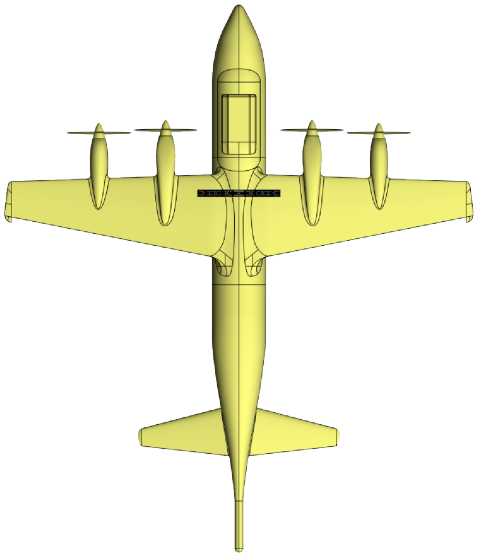

Figure 6.9: Placement of the inboard fairing on P-3 model in Feko. Original HFSS model provided courtesy of Emily Arnold [6].

and Table 6.1. The placement of the inboard fairing relative to the aircraft is demonstrated in Figure 6.9.

The inboard fairing consists of three sections shown in Figure 6.10 The outer sections slope upwards from horizontal to conform to the curvature of the P-3 belly. The angle of the outer sections measured relative to the x-y plane is indicated in Figure 6.10. The port section houses Antennas 1-3 while the starboard section houses Antennas 5-7 and the center section encloses only Antenna 4. When developing the model in Feko, the geometric parameters such as component length in each dimension and offsets from the origin are parameterized and one outboard section of the inboard fairing is built and mirrored across the x axis. The outer sections of the inboard fairing are hence modeled as symmetric *for this study*. In practice, the array and it's fairing enclosure are not perfectly symmetric.

6.2.4 Bottom Skin

The bottom skin is modeled as a layered dielectric substrate following the descriptions in [3], [87], and [6] which illustrate the lower skin as being a thick core of Rohacell 71 IG

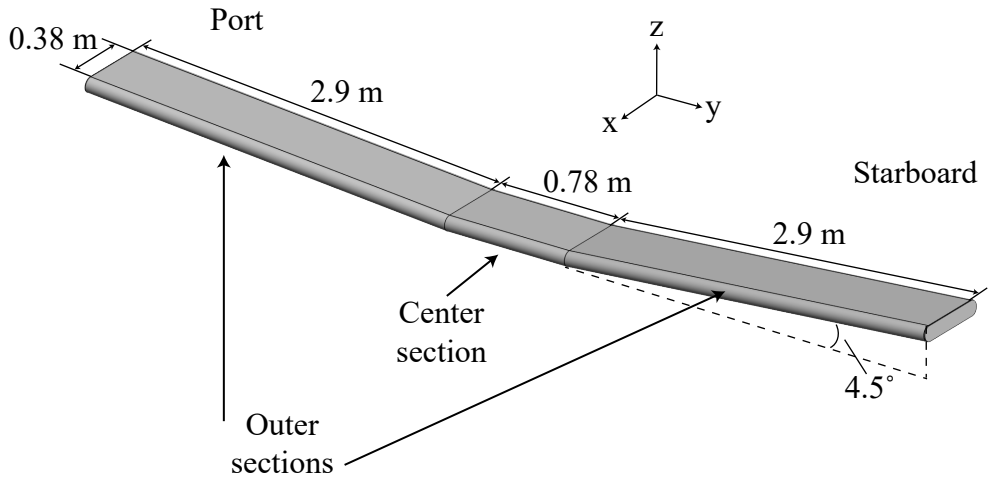

Figure 6.10: Dimensions of fairing sections and dihedral angle of the outer sections assumed in the Feko model (as inherited from the HFSS model). A more recent lidar survey of the subarrays on the P-3 indicates that rotation of the outer sections of the inboard fairing off of the x-y plane may be slightly less than shown.

foam sandwiched between two layers of S-2 glass. Embedded strips of 2024-T3 aluminum doublers line the edges of the very bottom layer of S-2. The original design which included a continuous edge of aluminum along the edges of the bottom skin [87] were found to degrade array performance [107]. Modifications and optimizations to the original design reported in [6] document improvements to the doubler design which involve breaking up the path of aluminum to restore overall return loss of the array elements.

The approach for modeling the bottom skin in Feko departs from the HFSS model which does not embed the aluminum doublers within the S-2 glass nor does it model the layered materials described in [87], [3], and [6]. This was likely a simplification to make the model more computationally tractable at the time it was developed. These structural details are included in the Feko model in order to improve the fidelity of the model in the near field of the radiators. The layered substrate with embedded aluminum doublers is reconstructed in Feko using aspects of the legacy model [7] and details from [87]. The layered media of one of the outer sections is illustrated in Figure 6.12. Detailed descriptions and dimensions of the individual structural components as well as the differences between the center and outer

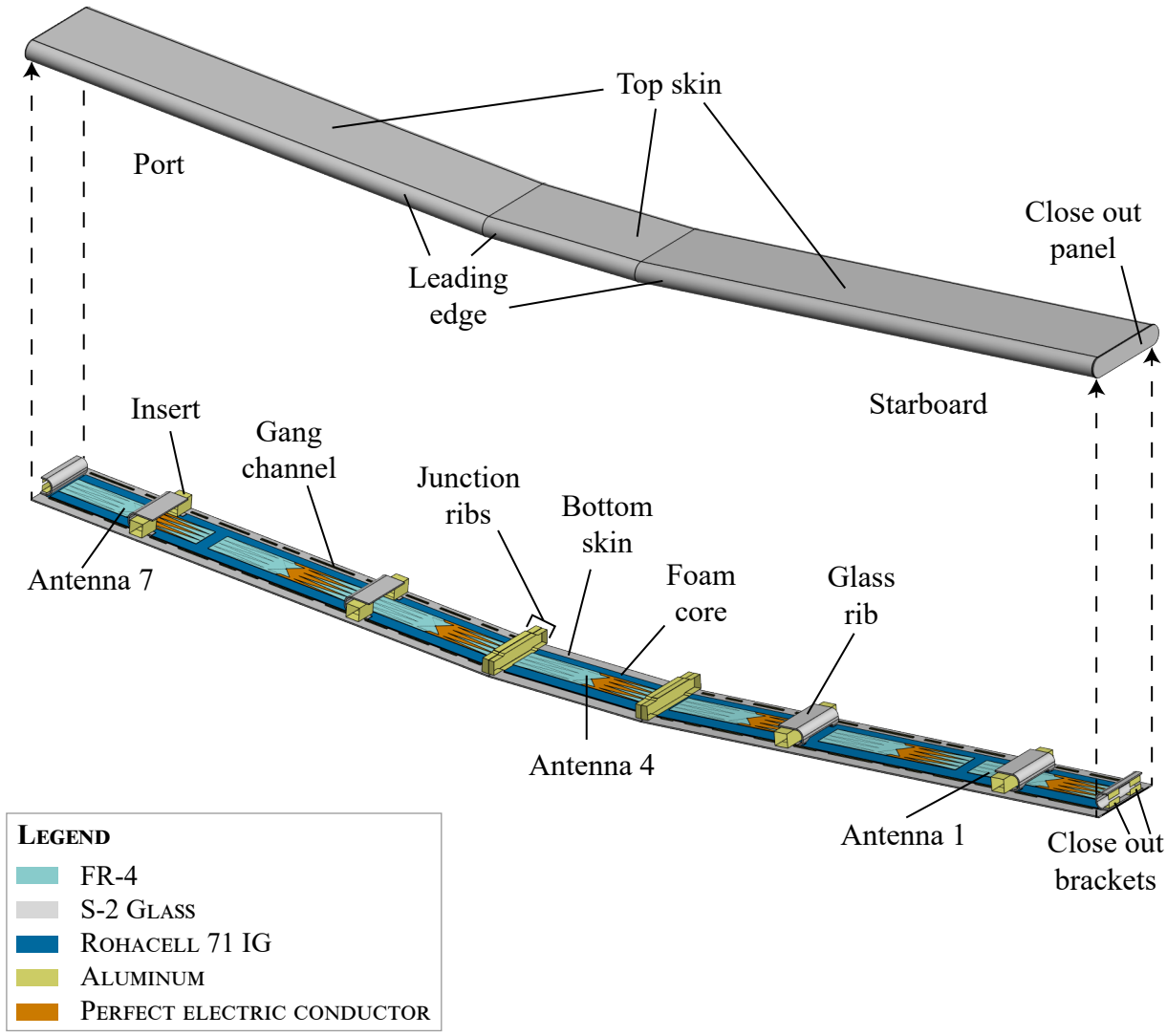

Figure 6.11: Feko inboard fairing model with array antennas in position and bottom skin dropped to show internal structure and antenna placement. The Feko adaptation is partially developed using structural components from a legacy HFSS model provided courtesy of Emily Arnold [7].

assemblies of the inboard fairing are allocated to Appendix F for the sake of completeness and to support future work with the model.

One approach for embedding a conductor in a dielectric medium in Feko may be realized by first creating voids in the host dielectric with physical dimensions that are consistent with those of the conductor. The empty region must be enclosed by a surface (a sphere or cube for example) and declared as free space. The inside faces of the voided region are defined as the corresponding conductive material. For any material other than a perfect electric conductor,

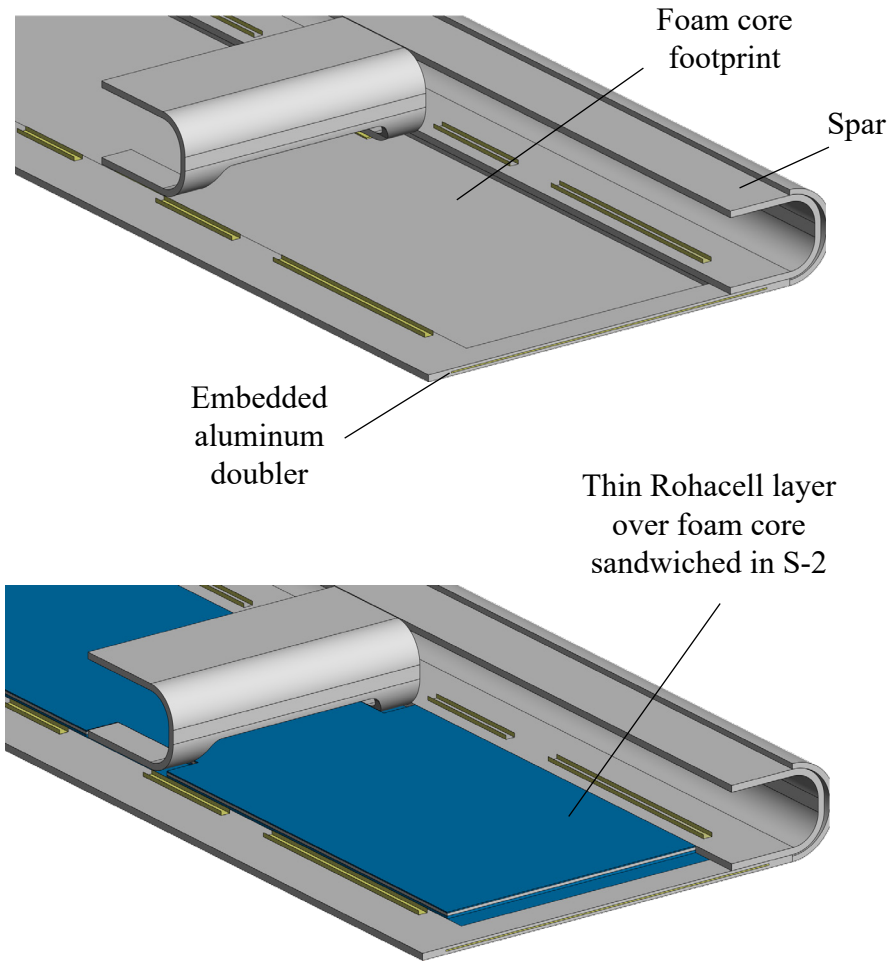

Figure 6.12: Detail of the bottom skin model showing the voided footprint for the foam core (top) and filled in footprint (bottom) as well as one of the embedded doublers.

the user must define the thickness of the enclosing faces. In this model, the thickness is assigned using a parameterized thickness corresponding to the frequency-dependent skin depth of aluminum as

$$\delta_{AL}(f) = \frac{1}{\sqrt{\pi f \mu_0 \sigma_{AL}}}, \tag{6.5}$$

Where σ_{AL} is the conductivity of aluminum defined in Table 6.1 and μ_0 is the free space magnetic permeability. This modeling technique ensures that the MoM solver will properly handle the boundary conditions at a dielectric interface encountered in the model.

6.3 Pattern Prediction from Full Wave Model

Feko is used to simulate θ dependent complex voltages captured across the array on receive. The simulations are designed to develop an understanding of the error mechanisms influencing the phase response of elements embedded within the array. In particular, the tests intend to demonstrate the impacts of mutual coupling, the fairing enclosure, and the irregular ground plane presented to the center subarray by the belly of the P-3. Receive manifolds are presented for the following configurations:

1. **Test 1** *(Free space RDS array)*: Free space array of RDS wideband dipole elements with the conformal geometry specified in Table 6.3. Residual phase after removing propagation phase is interpreted as error due to mutual coupling.

2. **Test 2** (*RDS array with P-3, no fairing)*: RDS wideband dipole array with conformal geometry and positioned below P-3 belly.

3. **Test 3** (*RDS array with fairing and P-3)*: RDS wideband dipole array with conformal geometry is enclosed in the fairing and positioned below P-3 belly.

6.3.1 Lever Arms in Feko Model

Both linear and conformal geometries of the RDS wideband dipole array are considered in the simulations in studying the array. The conformal geometry is approximately representative of the actual RDS antenna positions within the fairing. The feed point of the center element, Antenna 4, is taken to be the origin of both the linear and conformal geometries as well as the global origin in Feko of each individual model. The feed point positions in the linear configuration are determined by rotating the conformal geometry of the outer sections back to the x-y plane.

It is emphasized here that the Feko models presented in this chapter have assumed geometries that preserve perfect symmetry across the x axis. This is not necessarily an

Table 6.3: RDS lever arms in Feko model.

	Linear			**Conformal**		
Antenna	x (m)	y (m)	z (m)	x (m)	y (m)	z (m)
1	0	2.279	0	0	2.274	0.149
2	0	1.530	0	0	1.527	0.090
3	0	0.780	0	0	0.780	0.031
4	0	0	0	0	0	0
5	0	-0.780	0	0	-0.780	0.031
6	0	-1.530	0	0	-1.527	0.090
7	0	-2.279	0	0	-2.274	0.149

accurate representation of the array geometry that was hand fitted to the underside of the aircraft during fairing integration. To this point, it is emphasized that the rotation of the outer fairing panels off the x-y plane by 4.5° as specified in Figure 6.10 is an assumption of the geometry in the Feko model that is inherited from the legacy HFSS model. A recent more recent lidar survey of the P-3 subarrays carried out in 2017 indicates that this angle may be slightly smaller in actuality (by approximately 1°-1.5°). The RDS lever arms specified in Table 3.2 reflect the model adopted from this survey and indicate the positions assumed in determination of the phase center position vectors of the nominal manifold inside the array processor. Small discrepancies between the various models and truth justify a broader need to estimate geometric errors from the multichannel array data as proposed in Chapter 4.

6.3.2 CEM Methodology

With respect to array manifold calibration in the direction of arrival problem, we require θ dependent complex voltage patterns to model the manifold over angle. Antenna reciprocity ensures that we can characterize the antennas on transmit or receive. Reciprocity is verified in Feko by comparing far field gain patterns on transmit to current measured through a load

when an antenna is presented with a plane wave excitation over a ϑ grid. The normalized amplitude quantities produce equivalent patterns. In our problem however, we need angle-dependent phase measurements for each channel as well. Prediction of the complex receive manifold from field quantities simulated on transmission is possible but requires careful tracking of coordinate systems and additional post-processing of Feko outputs to properly convert complex electric field vector quantities.

A more straightforward receive characterization is proposed that eliminates sources of error introduced in the interpretation of Feko outputs and obviates the need for carrying out P independent runs. Receive manifolds are instead simulated for this dissertation by terminating the array elements with a common load impedance and presenting an ideal far field source over a uniformly sampled grid in elevation angle. The origin of the coordinate system is placed at the feedpoint of the center element, Antenna 4. For each plane wave position, the complex currents are measured through the loads. With no loss of generality, these are phase referenced to the measurement on Antenna 4 in the $\theta = 0^\circ$ position. The receive mode setup is illustrated in Figure 6.13, showing a far field source that is presented to the array over a ϑ grid. The plane wave propagation vector is indicated in blue and its polarization vector is indicated in red.

While the manifolds presented further below in this chapter correspond to predictions from receive mode simulation, both transmit and receive simulations are carried out when studying aspects of the array performance. When obtaining field quantities while operating an antenna element in transmission, an ideal voltage source is used with a 50 Ω generator impedance. To evaluate far field directivity, the voltage source is set to unity. In cases 2 and 3 from the enumerated list above, where the array is tested with the P-3 included in the model, surface currents on the aircraft skin may be requested in simulation; in these cases, each antenna is driven with 150 Watts. A receive manifold is simulated with all elements terminated in 50 Ω loads. Hence $\mathbf{Z_L} = 50 \cdot I_P$, where I_P is the $P \times P$ identity matrix.

The procedure for measuring the receive manifold is validated by verifying the reciprocity

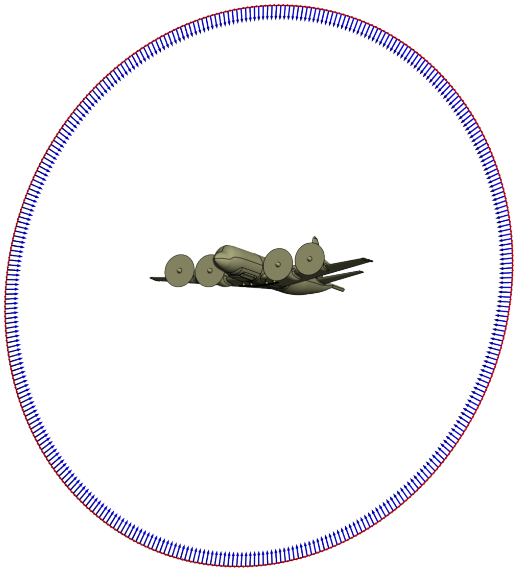

Figure 6.13: Grid of ideal, linearly polarized far field sources in Feko [4] simulations of receive manifolds. Blue vectors indicate planewave propagation vectors and red vectors indicate electric field polarization state.

of the array using the mutual coupling model proposed in [32] and given in Equation 2.54 of Chapter 2. The model, restated below for the convenience of the reader, specifies the predicted multichannel response of an array on receive given its complex open circuit voltage patterns (characterized in transmission), its associated Z-parameters denoted by the matrix $\mathbf{Z_A} \in \mathbb{C}^{P \times P}$ and terminating multichannel load, $\mathbf{Z_L}$:

$$\mathbf{a}(\theta) = \mathbf{Z_L} \left(\mathbf{Z_L} + \mathbf{Z_A} \right)^{-1} \mathbf{a}_{\text{oc}}(\theta). \tag{6.6}$$

The model above is derived assuming an asymptotically thin and perfectly conducting wire dipole in [35]. The form is interpreted for our purposes as an approximation of the coupled manifold of a free space dipole array. Following a description of the open circuit voltage quantity based on induced electromotive force (EMF) outlined in [34], the open circuit manifold is interpreted as follows:

$$\mathbf{a}_{\text{oc}}(\theta) \propto -\mathbf{Z_A} \mathbf{e}_\theta. \tag{6.7}$$

Here $\mathbf{Z_A}$ refers to the Z-parameters measured under unit excitation. The vector $\mathbf{e}_\theta \in \mathbb{C}^{P\times 1}$ is a vector whose p^{th} entry contains the complex electric field measured at given angle θ due to the *open circuit* pattern of element p, obtained by driving antenna p on transmit with all other antenna ports left open. The proportionality above assumes $\mathbf{e}_\phi$ is sufficiently small relative to $\mathbf{e}_\theta$ such that it can be neglected; such an assumption is taken to be valid for practical dipoles but may not necessarily be valid for other element types. The assumption is only made here to enable a coarse validation of the receive configuration and a verification that Feko outputs are properly interpreted in post-processing.

The open circuit element pattern refers to the transmit pattern measured when an element in the array is excited with a unit voltage and all other elements are left open (not terminated). Note that the phase reference of the p^{th} open circuit pattern is the phase center of the p^{th} antenna in the array. In Feko, $[\mathbf{e}_\theta]_p$ is simulated by driving element p with a unit voltage source and measuring the complex field over a θ grid. Hence the global origin of the Feko coordinate system translates to the feed point of the antenna under test in evaluating the open circut pattern of a specified element.

Figures 6.14 and 6.15 demonstrate the results of the reciprocity test used to confirm proper interpretation of Feko outputs. Similar to the measured manifolds in Chapter 5, the curves here are presented as row-wise pairs obtained from antennas sharing approximate even symmetry about Antenna 4. Each curve specifies the real and imaginary component of simulated quantities, normalized to the value measured on Antenna 4 at $\theta = 0^\circ$ in the simulation. In receive mode, the quantities refer to currents in the terminating loads of the array measured on receive for a given plane wave excitation. These quantities are plotted as solid lines and compared to the *predictions* of the receive manifold derived from transmit field quantities using the model in Equation 6.6 and the simplifying assumption in Equation 6.7. The predictions are laid on top of each receive manifold using circular and square markers to indicate the real and imaginary points respectively.

The structural and material complexity of the fairings pose distinct challenges in speci-

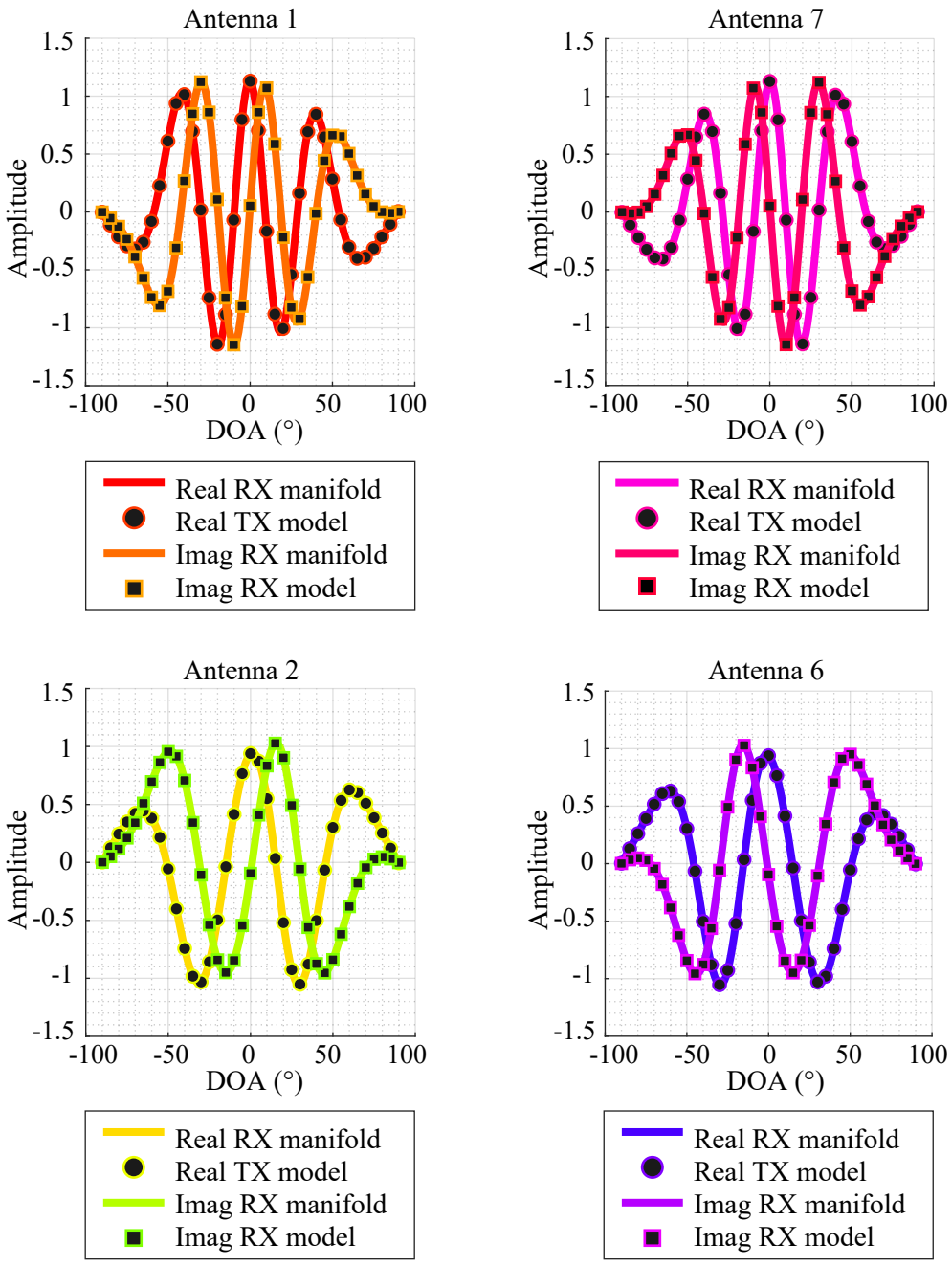

Figure 6.14: Reciprocity validation comparing measured received manifold to predicted manifold based on transmit field quantities for Antennas 1 and 7 and Antennas 2 and 6. Manifolds presented as antenna pairs based on symmetry in array.

fying a method for numerically solving Maxwell's equations. For example the lower skins of the fairings are made up of a bottom substrate of S-2 glass containing strips of embedded aluminum cured inside the material and lined on its surface with aluminum channels at at-

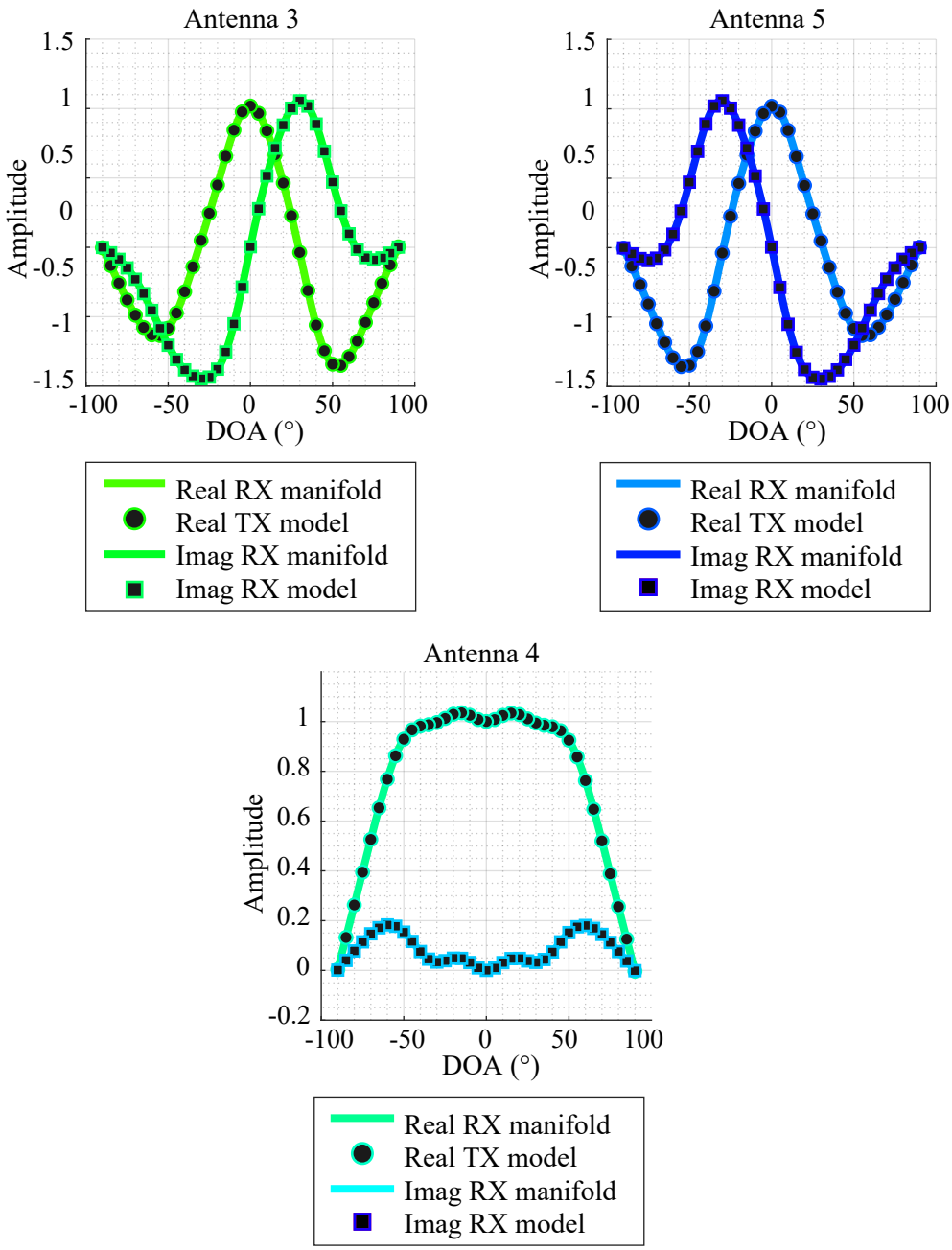

Figure 6.15: Reciprocity validation comparing measured received manifold to predicted manifold based on transmit field quantities for Antennas 3 and 5 and Antenna 4. Manifolds presented as antenna pairs based on symmetry in array.

tachment points that are electrically very small with respect to our wavelength but are known to alter the resonance of the antennas [3]. This portion of the model is better suited for a volume-meshing Finite Element Method (FEM) solver for solving for fields within dielectric

regions while the surface-meshing Method of Moments (MoM) solvers are more appropriate for computing field interactions with the fuselage, wings, and propellers. Both solvers lead to extremely large mesh sizes due to the large range of electrical dimensions in our problem, mandating extremely large RAM requirements needed to carry out computations.

Our problem requires a solver that simultaneously handles *both* electrically small and electrically large scales in one simulation while also accurately representing dielectric regions and fields at surface boundaries simultaneously. The complexity of modeling the RDS subarray when enclosed in the fairing and installed on the aircraft indicates a need for a software package that efficiently implements hybrid solvers. Electrically large problems can often be solved with fast numerical techniques like the MoM-based Multilevel Fast Multipole Method (MLFMM) which leverages sparseness of the near field coupling of an antenna relative to a large background structure to approximate the integral equation. The fine detail of features known to influence array performance inside the fairing and which must be included in the model disqualifies the P-3 model from leveraging the fast MLFMM solver.

The simulations carried out for the dissertation (specified as cases 1-3 above) implement the full Method of Moments solver in producing the receive manifolds. The validity of the MoM solutions in handling dielectric regions with embedded conductors is not studied here but should be revisited in the future to understand differences imparted by a solver method on the predicted manifolds. The full model including the array enclosed in the complete fairing and installed on the aircraft leads to an extremely large computational problem. Application of standard meshing in Feko (where triangle edges are on the order of approximately $\frac{\lambda}{12}$) leads to 264,359 triangles; a CEM problem of this size requires approximately 1.9 TB of memory (which may distribute across cores) for computation.

The simulations outlined in this chapter are run on a machine with 256 GB of available RAM. This motivates two changes to reduce the computational load. First, the leading and trailing edges of the fairing are identified as introducing a significant number of unknowns to the CEM problem. This is attributed to the fine mesh requirement needed to avoid triangle

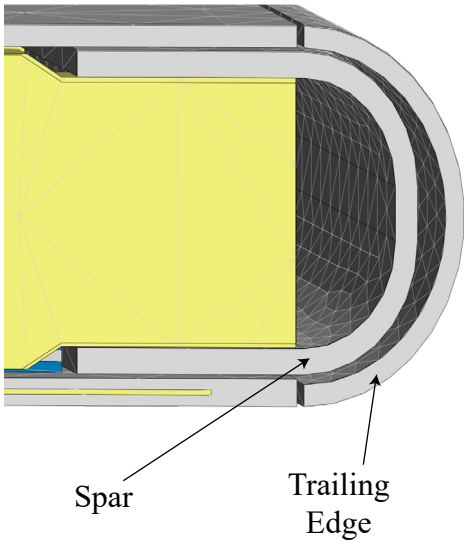

Figure 6.16: Detailed view of a spar nested inside the fairing's trailing edge with simulation mesh overlaid. The tight curvature of these components requires a very fine mesh to avoid intersecting triangles in the areas where the pieces nest together.

intersection where the components cup together. The spar and trailing edge with overlaid simulation mesh are illustrated in Figure 6.16. When the simulation mesh is too coarse, the inner triangles of the trailing edge's mesh intersect with the spar's mesh in the regions where these components nest together, leading to errors in simulation. To avoid triangle intersection in the meshed model, 1 mm gaps are inserted between components throughout the model; this can be noted in Figure 6.16. The trailing edges are omitted in simulation to reduce the number of unknowns. Omission of the leading and trailing edges of the fairing is not expected to significantly alter the pattern cuts through $\phi = 90°$; this simplification reduces the number of triangles and the RAM requirement to 236,638 and 1.32 TB respectively.

The most significant reduction in computational scale is realized in applying local meshing rules to specific faces in the model. Local meshing rules allow the creation of mesh that relaxes the average triangle edge length on specific faces (such as the back of the fuselage and the tail) and also enforces a finer mesh in areas closer to the radiators. The final meshing solution of the full problem (including the array, fairings and platform) requires approximately 155 GB of RAM. Here it is emphasized that the mesh on the body of the aircraft may not be sufficient for modeling the effects of the ground plane. In the vicinity

Table 6.4: Mesh summary for modeling receive manifolds.

		Edge Lengths (cm)			
Model	Triangles	Average	Standard Deviation	Min	Max
Free space	5,318	2.54	1.56	0.075	8.38
Free space, P-3	65,548	15.99	3.09	0.061	38.63
Fairing, P-3	85,788	14.06	3.98	0.061	29.37

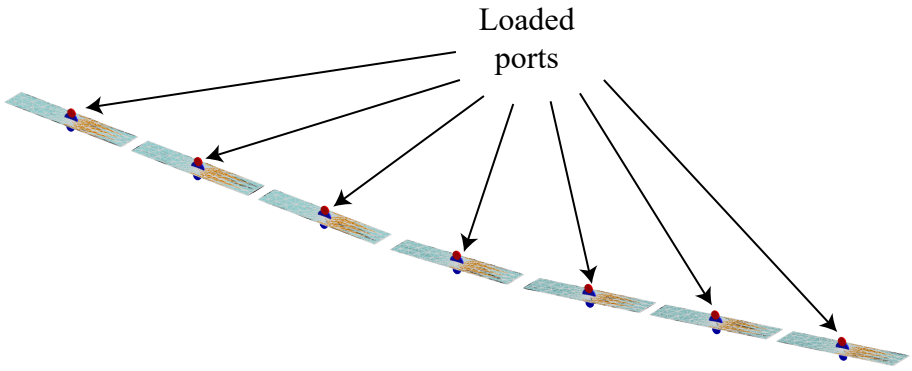

Figure 6.17: Feko [4] model of RDS free space array with overlaid simulation mesh. Arrows point out loaded, ideal edge ports with positive face indicated in red.

where the elements see their image, the local mesh is specified at $\frac{\lambda}{10}$ because a finer mesh leads to a problem that cannot be solved given the computational resource limitation (of 256 GB of RAM). The final simulation sizes are defined in Table 6.4.

An example of the simulation mesh for the free space test is shown in Figure 6.17. The mesh overlays the model in this illustration. Arrows are used to indicate the markers on the loads on the ideal edge ports. Positive marker ends refer to the edge that is treated as the positive port edge in the simulation. Figures demonstrating the models that include the P-3 are shown in 6.18a and 6.18b with overlaid meshes.

6.3.3 Predicted Embedded Element Patterns

The directivity patterns of each embedded element are presented for the three test cases as co-polarized and cross-polarized directive gains. The embedded element patterns are

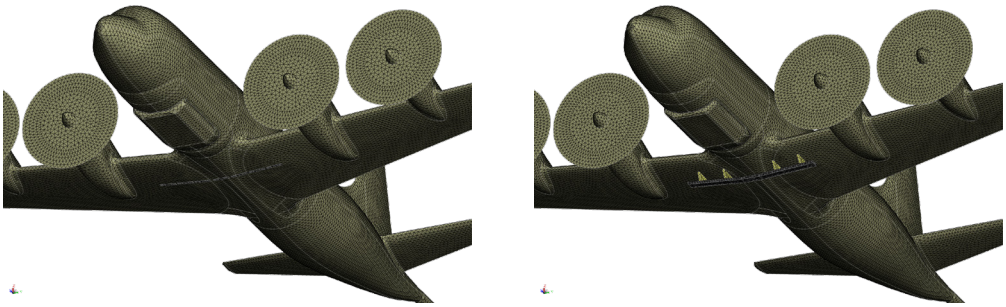

Figure 6.18: FEKO [4] model of (a) the RDS array with P-3 ground plane and (b) the RDS array inside the fairing and integrated onto the P-3.

simulated by exciting one element at a time on transmit with all other elements terminated in 50 Ω. Feko computes directivity by referencing in the far field to radiated power and hence does not account for losses in the structure. Directivity results are presented as polar plots on a dBi scale in Figures 6.19-6.22. Antenna pairs are presented side by side based on their approximate symmetry in the array. Each figure illustrates predicted directivities for each of the tests, organized in order of increasing model complexity. The free space array is considered the simplest setup, shown at the top of each figure, while the full model (with fairing and P-3) is interpreted as the most intricate case, shown at the bottom. Antenna 4 is presented in its own figure. The radial limits on all plots span 110 dBi which increments from -100 dBi to 10 dBi in 10 dBi steps. All plots are shown in terms of the DOA, θ. Thus $|\theta| \leq 90^\circ$ corresponds to the field of regard with 0° referring to nadir and $\pm 180^\circ$ mapping to zenith. The region of angles $|\theta| > 90^\circ$ is regarded as the backlobe of the array.

The figures confirm symmetry in the patterns of antenna pairs that is consistent with the approximate symmetry of elements in the array. In the free space case for example, a null of the Antenna 1 pattern appears in the field of view, near approximately -86° while Antenna 7 has a null at 86°. The nulls in the visible region appear to fill in slightly when the P-3 is placed behind the array. The conformal geometry of the array tilts the dipole patterns in θ. It is worth noting that a linear array case was tested. The results are not shown in this chapter but the patterns show squinting of the outer elements that is attributed to mutual

Table 6.5: Predicted total directivity of embedded patterns at nadir for each test.

	Antenna						
Model	1	2	3	4	5	6	7
Free space	1.5	0.011	0.775	0.432	0.778	0.011	1.49
Free space, P-3	6.86	3.15	6.1	2.75	6.13	3.24	6.85
Fairing, P-3	5.87	4.94	2.86	5.43	3.05	4.83	5.97
	$D_T(\theta = 0°)$ dBi						

coupling. Figure 2.10 in Chapter 2 illustrates the open circuit patterns simulated for that case.

The cuts predicting performance when the array is placed inside the fairing and installed on the platform suggest the dipole nulls are much more filled in these regions. The results confirm the gain improvement with the ground plane in place behind the array, evidenced by an average increase in directive gain in the visible region. Though the patterns show rippling across θ that is not easily observed on the polar plots. The rippling is more visible in the receive manifolds presented further below. The values of the total predicted directivity at nadir are reported in Table 6.5 and demonstrate an alternating of high to low directivities from channel to channel at one grid point in θ. The presence of the rippling in the simplest setups such as the linear array of RDS dipoles in free space indicates that this phenomenon is largely attributable to mutual coupling.

Two additional observations drawn from the element directivity patterns are noted here. First, the dipole nulls appear largely filled in when the RDS array operates inside the fairing. The element patterns predicted with the full model show reduced element rolloff in the regions of $60° \leq |\theta| \leq 90°$. This suggests that the rolloff of signal to noise ratio for the angles far off nadir may not have as much of an impact on manifold measurement as originally anticipated. The patterns also indicate a decreasing polarization isolation as the platform effects increase. Antennas 2 and 6 show less than 10 dB of isolation in the cross-polarization at the angles

$-60°$ and $60°$ respectively. This may justify additional study to determine the impacts of degraded polarization isolation on manifold characterization.

6.3.4 Predicted RDS Receive Manifolds

To help describe the complex patterns that are presented in the following sections, some notation is introduced here. The vectors $\mathbf{i}(\theta) \in \mathbb{C}^{P\times 1}$ and $\mathbf{a_R}(\theta) \in \mathbb{C}^{P\times 1}$ are adopted to refer to a θ dependent multichannel current, $\mathbf{i}(\theta)$, that leads to a predicted receive manifold $\mathbf{a_R}(\theta)$. Feko provides a multichannel vector of complex currents measured across the loaded ports for each position of the far field source over the user specified θ grid, illustrated in Figure 6.13. The p^{th} entry of $\mathbf{i}(\theta)$ is proportional to an embedded gain pattern measured by driving antenna p with a voltage source and an appropriate generator impedance while all other elements in the array are terminated in an impedance Z_L. The measured receive currents can be converted back to directive gains with additional processing of the Feko outputs that accounts for the polarization of the far field source to obtain a gain relative to an isotropic radiator.

The multichannel current vectors are normalized with respect to the complex current on the reference sensor, Antenna 4, at $\theta = 0°$ to obtain $\mathbf{a_R}(\theta)$. This is summarized as

$$\mathbf{a_R}(\theta) = \frac{1}{[\mathbf{i}(0)]_4}\mathbf{i}(\theta). \tag{6.8}$$

This form, which describes offsets of each channel relative to the complex current on Antenna 4 at array boresight, preserves the angle dependent rolloff of the embedded elements and represents the multichannel data after channel equalization. A manifold correction, denoted by the quantity $\mathbf{d}(\theta)$, is introduced to describe the offset of each manifold vector from the isotropic form, evaluated in terms of the true geometry. Evaluation of this correction is carried out by scaling $\mathbf{a_R}(\theta)$ by its norm in each direction and removing the propagation

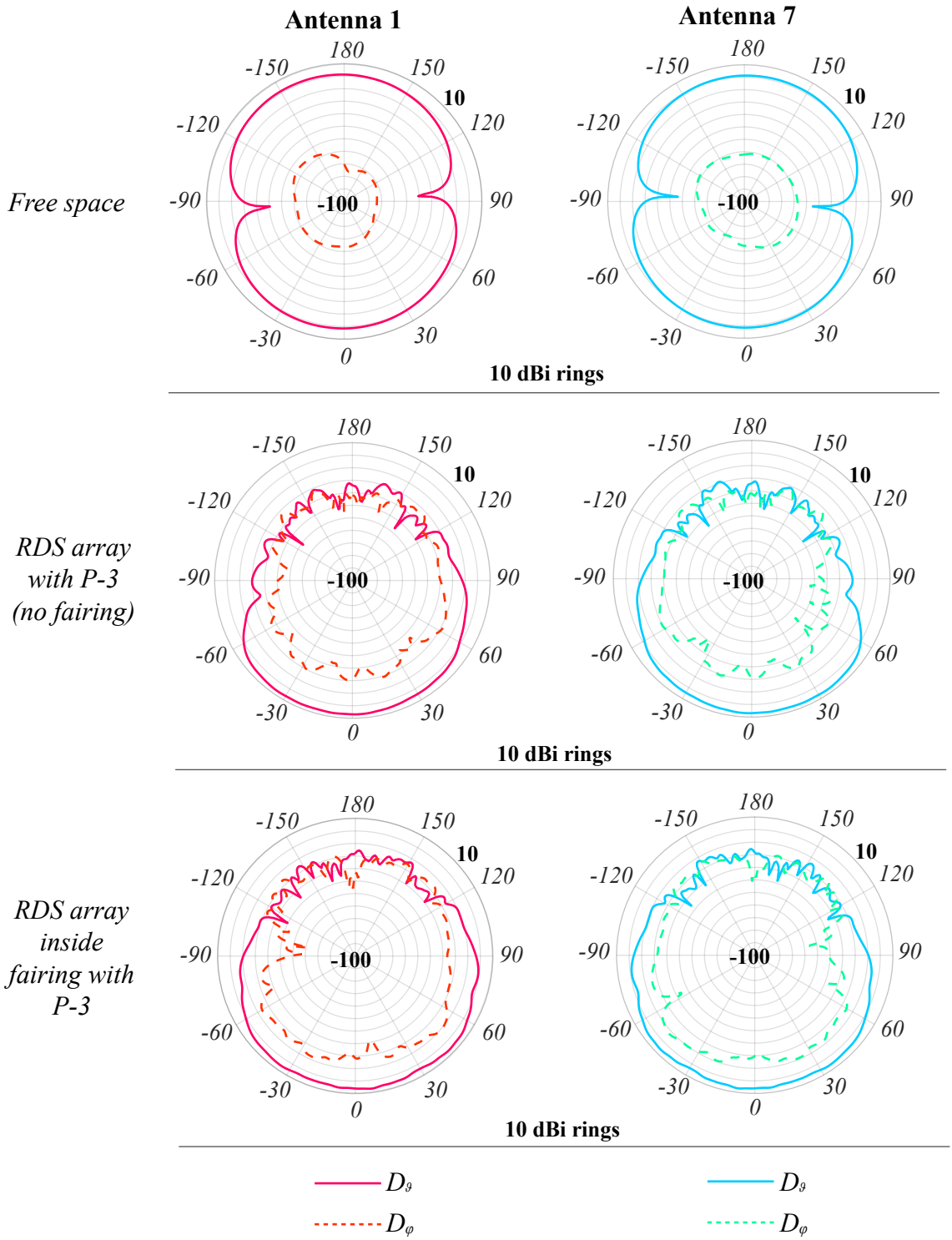

Figure 6.19: Predicted embedded element directivity patterns of Antennas 1 and 7 for each test. Both co-polarized (solid line, labeled as D_ϑ) and cross-polarized (dashed lines, labeled as D_φ) gains are reported.

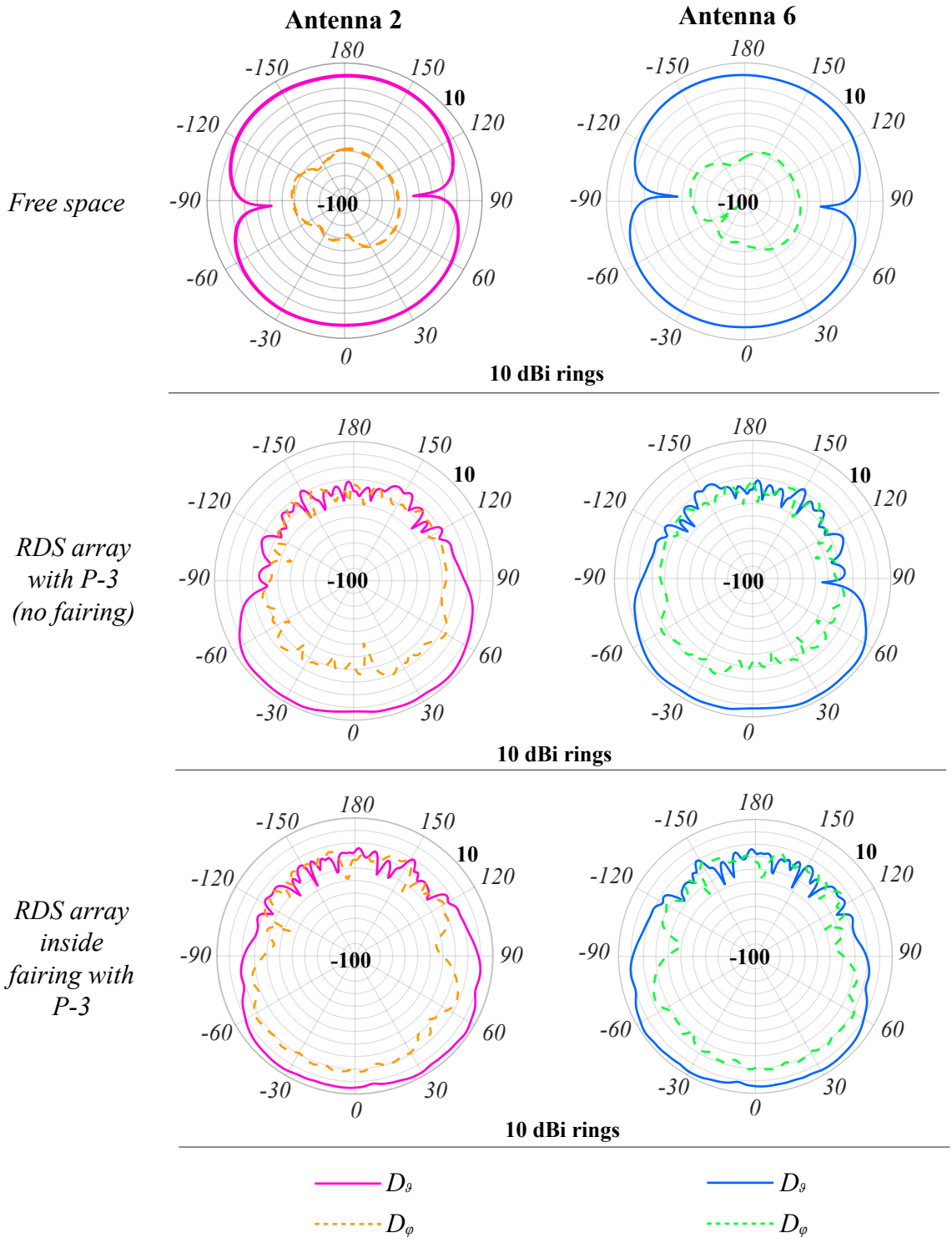

Figure 6.20: Predicted embedded element directivity patterns of Antennas 2 and 6 for each test. Both co-polarized (solid line, labeled as D_ϑ) and cross-polarized (dashed lines, labeled as D_φ) gains are reported.

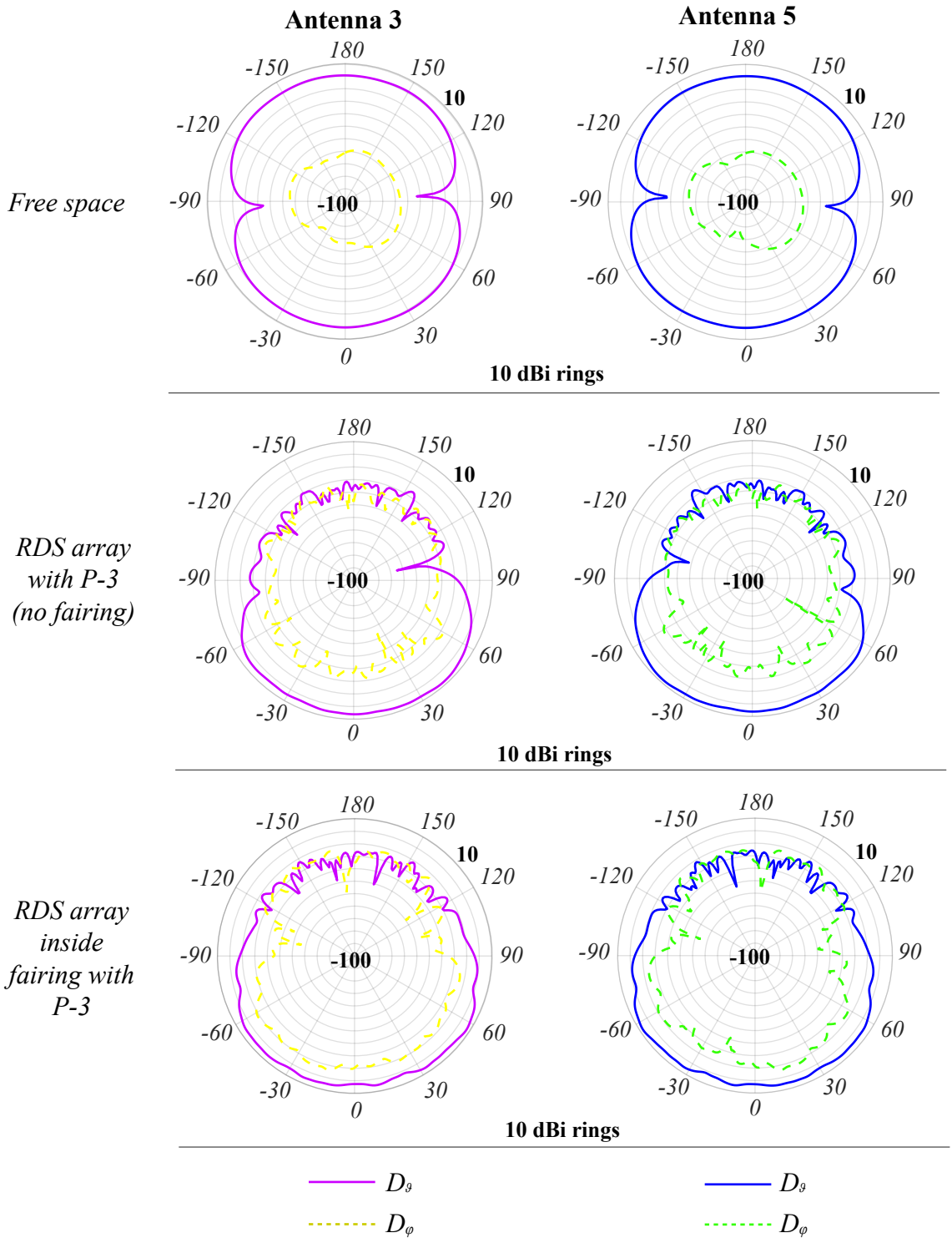

Figure 6.21: Predicted embedded element directivity patterns of Antennas 3 and 5 for each test. Both co-polarized (solid line, labeled as D_ϑ) and cross-polarized (dashed lines, labeled as D_φ) gains are reported.

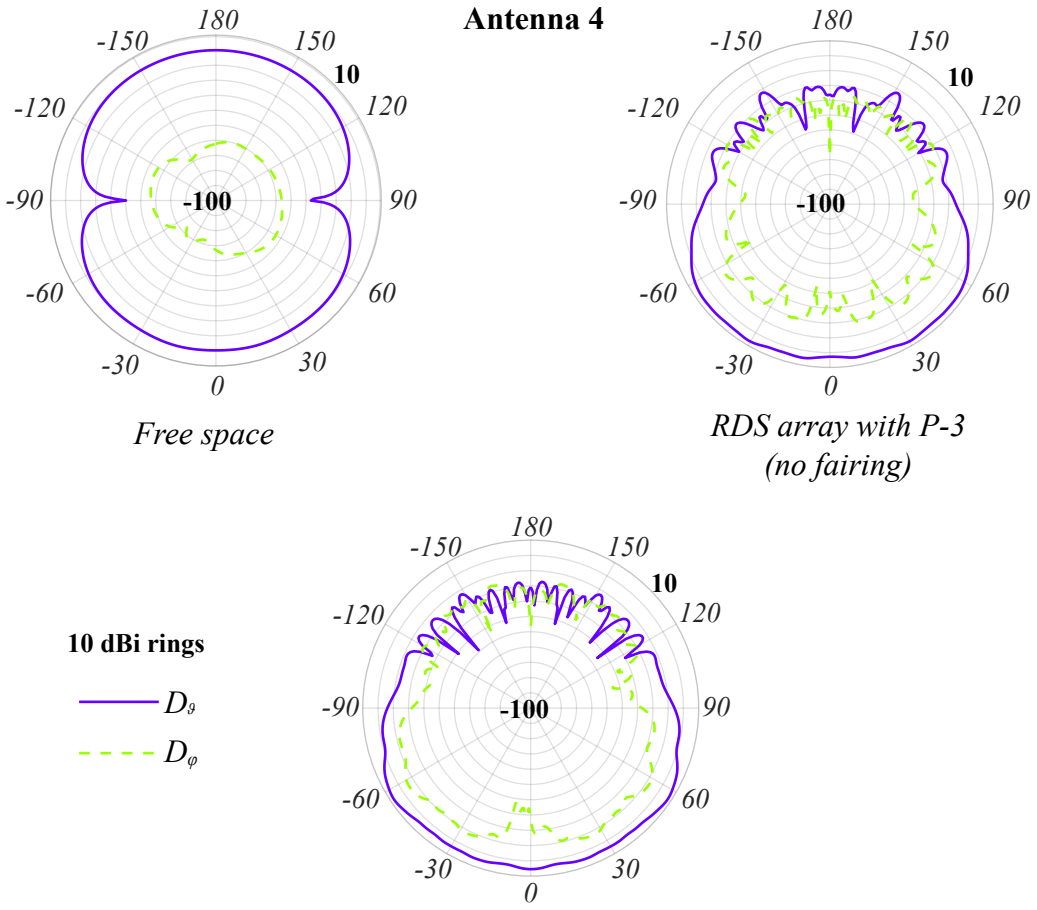

Figure 6.22: Predicted embedded element directivity patterns of Antenna 4 for each test. Both co-polarized (solid line, labeled as D_ϑ) and cross-polarized (dashed lines, labeled as D_φ) gains are reported.

phase based on the true model of the sensor positions.

$$\mathbf{d}(\theta) = \frac{\mathbf{a_R}(\theta)}{\|\mathbf{a_R}(\theta)\|} \odot \mathbf{a}_0^*(\theta). \tag{6.9}$$

Here $\odot$ is a Hadamard product (corresponding to element-wise multiplication of vector entries) and $\mathbf{a}_0^*(\theta)$ is the conjugated isotropic steering vector whose p^{th} entry is restated as having the following form:

$$\Big[\mathbf{a}_0(\theta)\Big]_p = e^{-j\mathbf{r}_p^T\mathbf{k}(\theta)}. \tag{6.10}$$

Note that the feed point of the reference sensor, Antenna 4, is taken to be the origin of the

geometry. Hence the phase of the manifold references this point in the array geometry. It is emphasized here that the propagation to the feed points are removed and not the propagation to our assumption of a phase center. Manifold correction plots are meant to be consistent with the conventions in the measured manifolds with the only difference being that the measured manifolds remove a propagation phase based on our model of the effective phase center of each channel. Discrepancies exist between our initial model of the lever arms, the model assumed in Feko, and the lever arms measured in survey. In Feko, the measurement of the offsets of each feed relative to a corresponding surface normal on the underside of the aircraft is prone to error and the choice was made to avoid introducing these uncertainties into the plotted patterns.

Figure 6.23 presents the receive manifolds and manifold corrections for Test 1 (where the RDS array is operated in free space). Figures 6.24a and 6.24b correspond to the multichannel complex currents, corrected to Antenna 4 at nadir. The phase unwraps about the value at 0°. The outputs help to confirm the simulation setup. For example, Antenna 1 leads the reference element for $\theta > 0°$ which is consistent the assumed geometry in the CReSIS toolbox. The results show a transition in the direction of the unwrapped phase responses near approximately ±85°. The major to minor axial ratio (obtained from the transmit characterization of the elements carried out above) in these regions, which align with the nulls of the dipoles, is much greater than one and indicates an increase in the cross-polarization component of the field. The manifold corrections in these areas suggest that small changes in θ lead to much larger changes in phase, perhaps justifying a finer grid spacing when binning snapshots further off nadir. Mutual coupling is interpreted as the dominant mechanism inside of ±80°.

The predicted manifolds for the Test 2 simulation (where the array is placed below the aircraft without the fairing) are shown in Figure 6.24. The receive manifold confirms rippling of the patterns over θ. The outer elements appear to show the smallest swing in values from peak to trough. Antennas 2, 4, and 6 show a large dip at nadir relative to Antennas 1, 3, 5,

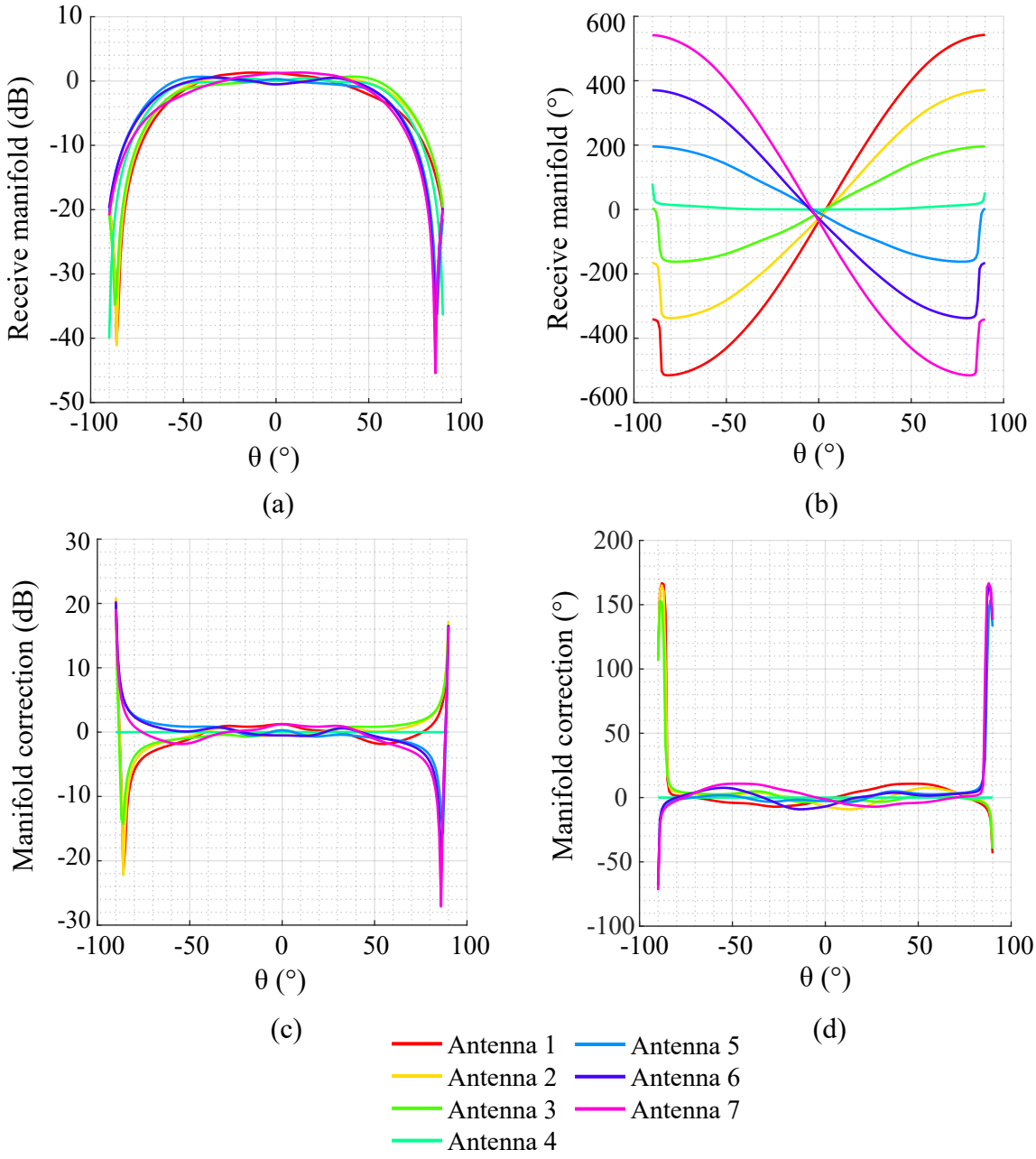

Figure 6.23: Receive manifold predictions of the RDS array in free space (corresponding to Test 1) in response to a linearly polarized plane wave. The magnitude and phase of the receive manifold, normalized to the Antenna 4 pattern at boresight, are shown in (a) and (b) respectively. The magnitude and phase of the manifold corrections, normalized to the Antenna 4, are shown in (c) and (d) respectively. The corrections of each channel are presented in a consistent manner to the measured manifolds in Chapter 5.

and 7. The gain offsets of the channels relative to Antenna 4 at $\theta = 0°$ and listed in order from Antennas 1 to 7 are $[5.099, 0.0467, 3.5422, 0.000, 2.9258, 0.3076, 4.2260]$ dB. Note these

values are very close to the relative gains in the directivity patterns at nadir, cited in Table 6.5. Small differences between the two sets are possibly attributable to differences in the meshes. It is worth noting here that the gain offsets listed are expected to be symmetric across the antenna pairs because the EM model is symmetric. The differences such as those observed in the gain offsets of Antennas 2 and 6 are interpreted being caused by asymmetry in the mesh that perhaps indicates that the ground plane mesh is too coarse.

The predicted receive manifolds with the fully modeled inboard array are presented in Figure 6.25. The magnitude patterns show a large amount of variation per channel in θ. The dipole nulls are all visible in the field of view but show filling over the channels. The range of the predicted magnitude corrections is similar to that of the measured manifolds presented in Chapter 5. The predicted receive manifolds exhibit asymmetric values despite the perfect symmetry of the model. For example we would expect the phase correction of Antenna 1 at a particular θ_0 to be very close to the value observed in the Antenna 7 pattern at the corresponding angle $-\theta_0$ but examples can be drawn from these results that violate this anticipated symmetry. The phase offset of Antenna 1 at $\theta = -56°$ is measured at 23.49° while on the opposite side of the array, Antenna 7 shows a phase offset of 37.26° at $\theta = 56°$. It is worth noting here that in the free space case, symmetry in the phase responses is verifiable within $\pm 85°$ indicating even symmetry in the mutual coupling across 0° for the antenna pairs in the EM model. Again it is emphasized that the EM model exhibits symmetry that we do not anticipate in true array geometry due to the hand fitting of the fairing to the aircraft during integration.

The predicted manifolds of Test 3 are compared to the measured RDS manifolds in Figures 6.26 - 6.21 below. It is acknowledged here that variation is anticipated due to differences in the lever arms assumed in the toolbox and those inherited from the legacy EM model. Perfect agreement is especially not anticipated in the phase corrections. Unwrapped phase is presented, showing measured and predicted values against the nominal model of θ dependent propagation phase on each channel. Magnitude corrections are shown in dB

relative to Antenna 4. On some patterns, peak locations in the magnitude curves appear consistent between predictions and measurements. Antenna 5 for example exhibits peaks in the response at $\pm 10^\circ$ in both the Feko and measured results. Similarly Antenna 7 shows a peak in both the EM manifold and measured manifold at 36°. Some portions of the patterns appear to show dilation or contraction over finite angular windows.

6.4 Electromagnetic Manifold Application in Angle Estimation

Despite the differences observed in comparison of predictions to measurements, the EM manifold is applied in angle estimation using the edited snapshot sets. The performance is compared to measured and nominal manifold angle estimator error. Results are produced that are consistent with those used to assess the performance of the measured manifolds in Chapter 5 (see Figures 5.19 and 5.20). The bias and RMS errors measured in this test are presented in Figure 6.29. The observed bias and RMS errors over $\pm 40^\circ$ indicate that the EM manifold performs better over the angular window of $-40^\circ < \theta < 0^\circ$ compared to the $0^\circ < \theta < 40^\circ$ range. RMS errors over $|\theta| \leq 40^\circ$ are all bound within 3°. The EM manifold leads to lower errors compared to the nominal case over $-90^\circ \leq \theta \leq -18^\circ$ and $40^\circ < \theta \leq 90^\circ$. The measured bias suggests that the EM manifold consistently produces biased estimates of angle with the exception of a small window near -30°.

Similar to the result presented in Figure 5.21 of Chapter 5, an error reduction factor is offered to help in quantifying angle estimation performance improvement. Following the form of Equation 5.34, this is computed as the following ratio of RMS errors measured between the nominal and predicted manifolds as:

$$\text{Error Reduction}(\theta) = \frac{\text{RMSE}_{\text{nom}}(\theta)}{\text{RMSE}_{\text{feko}}(\theta)}. \tag{6.11}$$

This form is interpreted as a reduction when the ratio is at least one. The error reduction factor comparing MUSIC angle estimates under nominal and predicted RDS manifolds is

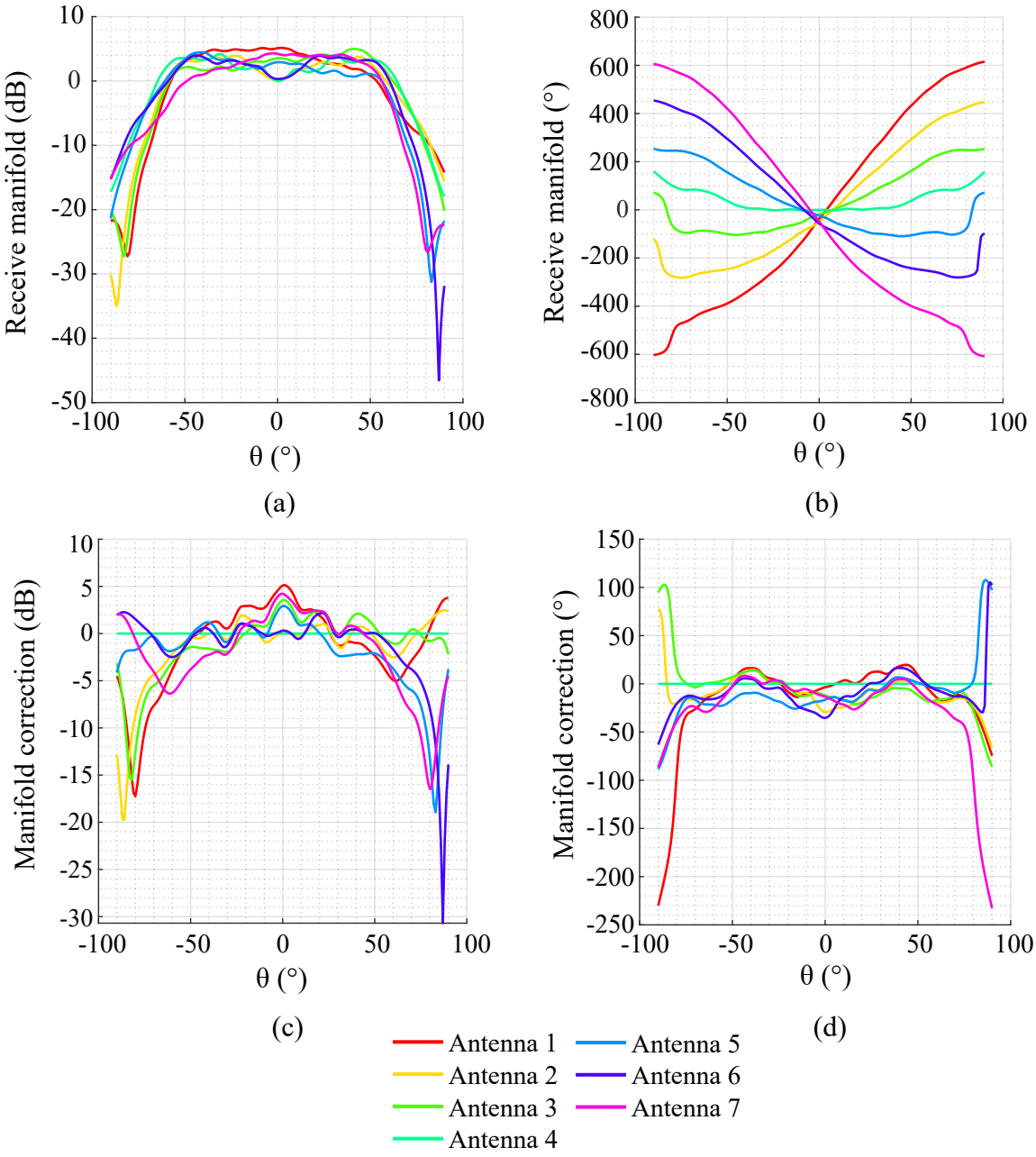

Figure 6.24: Receive manifold predictions of the RDS array when P-3 is included in the model (corresponding to Test 2). The fairing is not used in this simulation. The magnitude and phase of the receive manifold, normalized to the Antenna 4 pattern at boresight, are shown in (a) and (b) respectively. The magnitude and phase of the manifold corrections, normalized to the Antenna 4, are shown in (c) and (d) respectively. In plotting corrections, only the propagation to the feed point of the antenna is removed (and does not account for the offset of the feed from the ground plane). Phase residuals on each channel contain propagation from the feed to the unknown effective phase center.

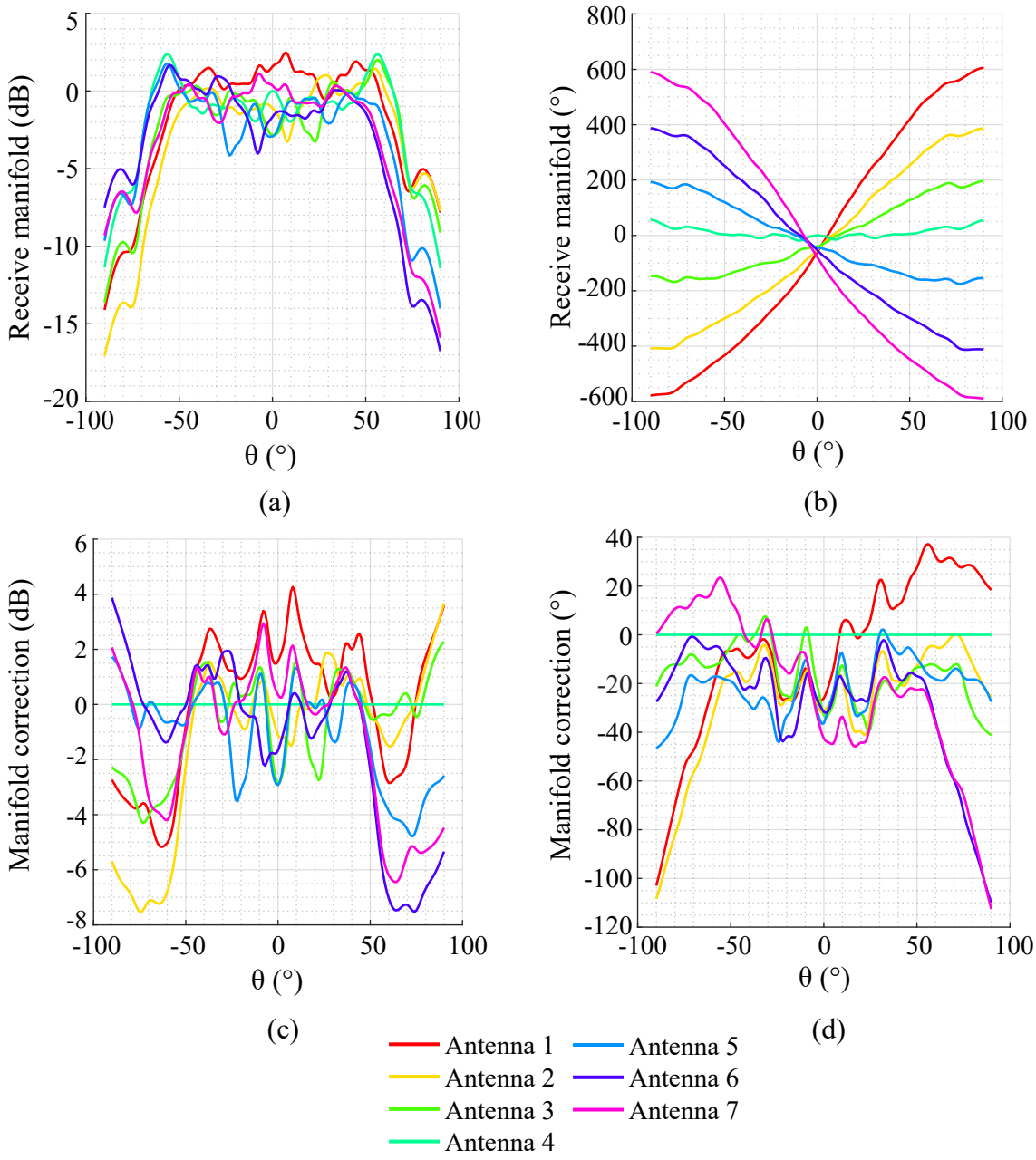

Figure 6.25: Receive manifold predictions of the RDS array inside the fairing and attached to the P-3 (corresponding to Test 3). The magnitude and phase of the receive manifold, normalized to the Antenna 4 pattern at boresight, are shown in (a) and (b) respectively. The magnitude and phase of the manifold corrections, normalized to the Antenna 4, are shown in (c) and (d) respectively. In plotting corrections, only the propagation to the feed point of the antenna is removed (and does not account for the offset of the feed from the ground plane). Phase residuals on each channel contain propagation from the feed to the unknown effective phase center.

shown in Figure 6.30. The ratio of RMS errors is plotted in green and the black markers indicate regions where the *nominal* result outperforms the prediction. We observe that the nominal manifold leads to better angle estimation outcomes (where the ratio is at least one) over the windows of -17° $\leq \theta \leq -8°$ and $0° \leq \theta \leq 40°$. The predicted manifold provides an average error reduction (evaluated over the values that are at least one) of 3 in angle estimation.

6.5 Discussion

Interpretation of the deterministic manifolds produced with the full wave solver is likely limited in Test 2 and Test 3 where the full aircraft is meshed for the simulation. Although the mesh technically satisfies common surface meshing rules of thumb adopted in CEM communities, these may not be sufficient for representing the ground plane. Symmetric responses across 0° are expected based on the symmetry of the CAD model. The Feko model exploits symmetry to simplify construction of the fairing. One outer panel is constructed and the mirrored across the x axis to force symmetry before dropping the antennas inside. Component positions are parameterized at onset to ensure precise translations and rotations in construction. Although the RDS array is not perfectly symmetric across the center line of the fuselage, forced symmetry in the model helps to reveal the artifacts imposed by the solver and its configuration. We may use this knowledge to levy requirements on the simulation that ensure minimal error is imparted on the predicted manifolds when the model is perfectly symmetric. Once the relationships between simulator parameters and predicted patterns are better understood, the model may be modified to reflect the true nuances of the actual system.

The tests that include the aircraft demonstrate asymmetries in the complex patterns (both in magnitude and phase) that are not observed in the free space array simulation. It is possible that the P-3 CAD model is not symmetric across the x axis. It is also possible that the center line of the P-3 CAD is not perfectly aligned to the x axis. If the aircraft model

is symmetric and properly aligned in the full model, the multipath presented in simulation is also expected to exhibit symmetry. The most plausible explanation for small differences between antenna pairs is due to the asymmetry of the surface mesh. Given the coarse mesh used on the body (needed to scale the problem to fit within the constraints of the available computational resources), the ground plane which curves above the array is likely too faceted to accurately represent the image of each antenna. It is recommended that manifold predictions are recreated with a minimum triangle edge length of $\frac{\lambda}{16}$ on the faces behind the array once computational resources become available.

The predicted patterns indicate that at the edges of the field of view, for example for $|\theta| > 70^\circ$, the phase response changes more rapidly with angle. This may offer insight into the consistent increase in RMS errors observed in angle estimation with the measured manifold and justifies some localized testing in these regions with finer calibration bin spacing than the 1° grid used for this work. The measured angle estimation performance under varying manifold types indicates that the EM predictions lead to better performances at the large angles. Additional testing is recommended to evaluate the potential of using the EM predictions to compute the subspace clustering measure in the angular regions where we suspect the measure degrades due to the reliance on the nominal manifold. Improving angle estimation at the large angles is critical for using automated tracking of the surface in extracting bed topography.

The predicted array response computed with the full model suggests that a large number of coefficients will be needed to model the relative magnitude and phase within a parametric framework. Several attempts were made to apply the parametric framework to the EM manifold of a geometrically perturbed linear array of RDS dipoles in free space using a manifold model that relied on a sum of complex exponential basis functions with an unknown propagation phase, expressed in terms of the geometric perturbation model discussed in Chapter 4. The number of complex exponentials in each summation was estimated from the number of significant terms in the Fourier Transform of each channel's measured complex

pattern, estimated to be between 15 and 20 (per antenna). In simulation, the reference antenna was always unperturbed. When the manifold model included propagation phase to represent unknown geometric errors, the optimization problem grew to involve more than 100 unknowns. Attempts to solve this problem with a global search algorithm and a particle swarm approach suggest that the optimizer was converging on local minima as evidenced by a large number of coefficients that were left unchanged at the output of the optimization routine. This behavior was observed even when initializing the unknown geometric terms with their real answers (known from the EM simulation).

It is emphasized here that the evidence of failed convergence is observed when using a deterministic manifold result from a perturbed linear geometry of RDS dipoles in free space. MATLAB's curve fitting tools [94] are applied to both measurements and predictions. Both cases are examined with Fourier series fits to the real and imaginary components. The results are not included here but indicate at least 17 parameters are needed to represent each channel (judged by the number of coefficients that result in R-squared goodness of fit measures over 0.9 for all channels). This indicates approximately 102 unknown parameters are expected for the full model if Antenna 4 is regarded as a reference. The predicted manifolds from Feko are expected to be critical in validating the parametric framework. It is recommended that the EM manifold be fit with a Fourier series using the built in curve fitting tools in MATLAB [94]. This will help to initialize the optimizer when all of the coefficients are exactly known so that the range on the search bounds can be studied.

6.6 Conclusion

The computational electromagnetic modeling methodology presented in this chapter lays down a foundation for understanding the error mechanisms influencing the RDS manifold on the P-3 aircraft. The chapter documents the refactoring of a legacy EM model to study the manifold calibration problem. RDS receive manifolds are presented for three scenarios, designed to capture an increasing complexity of environmental effects. The predicted pat-

terns indicate that finer grid spacing of calibration bins in manifold characteriztion is likely justified at the large off-nadir angles where small changes in elevation angle correspond to large changes in the phase response of a given channel. The predicted manifold is applied to RDS snapshots and demonstrated improved angle estimation performance relative to the nominal manifold in certain angular regions, suggesting that potential performance gains may be realized by using the EM results to evaluate the subspace alignment measure for harvesting calibration targets in the SAR pixels in these regions. The predicted manifolds are expected to improve algorithm development in support of the parametric framework outlined in Chapter 4 that will lead to the application of a multitarget calibration strategy.

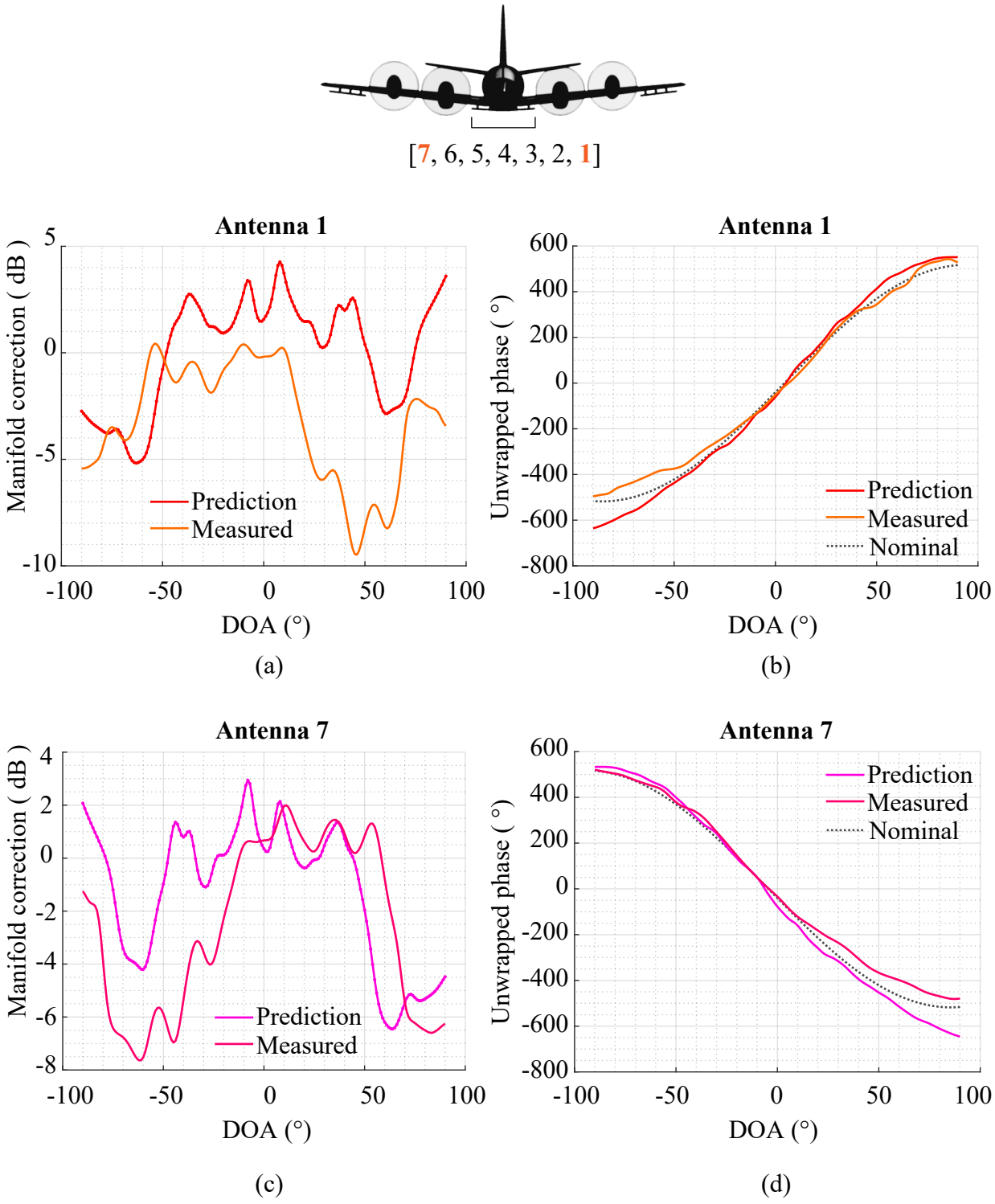

Figure 6.26: Comparison of predicted receive manifolds to measurements for Antennas 1 and 7, reported as magnitude and unwrapped phase in (a),(b) and (c),(d) respectively. The measured manifold is an aggregated result from three measured RDS receive manifolds that are reported individually in Chapter 5. This result represents a season level manifold correction for the 2014 Greenland P-3 data set.

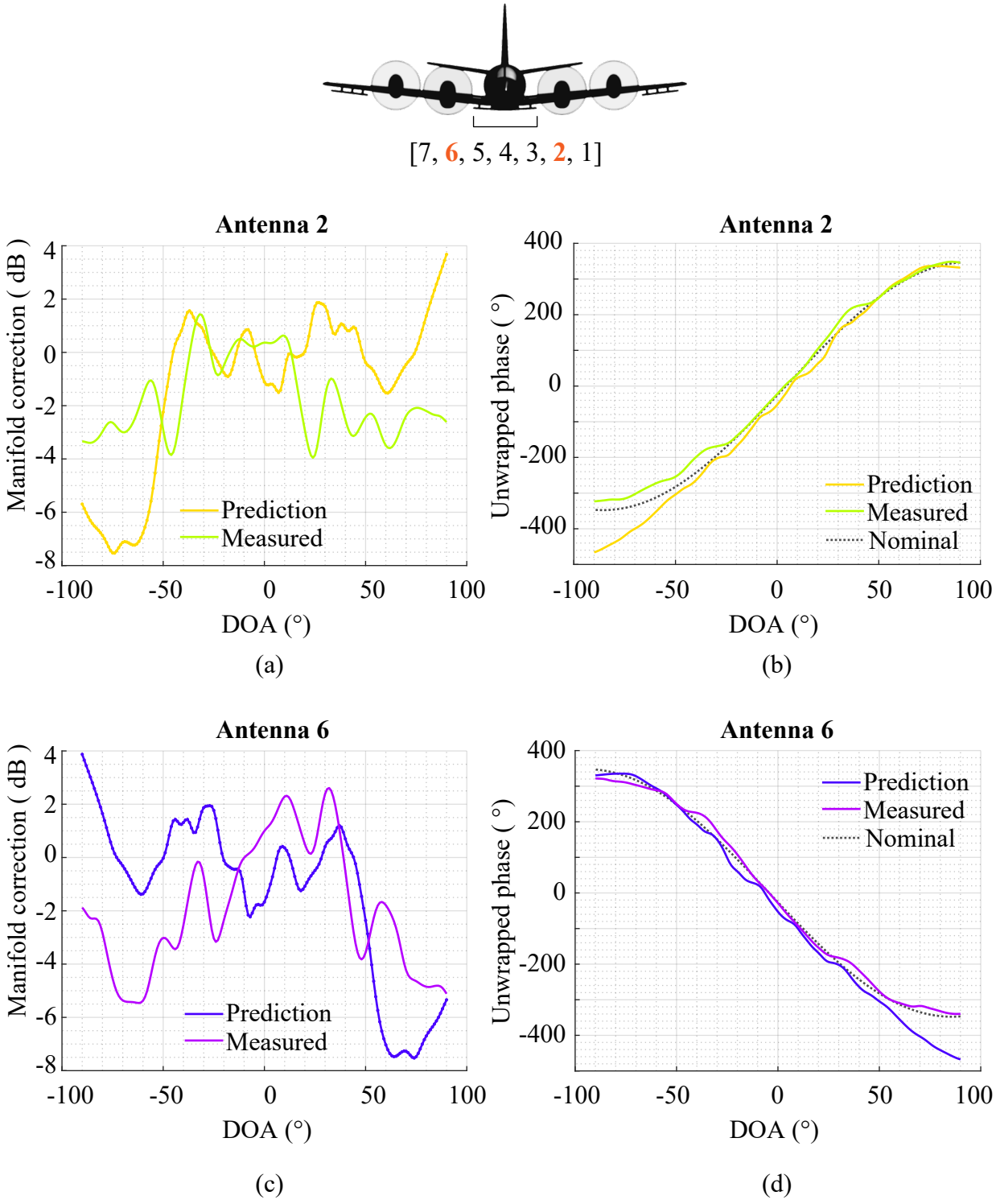

Figure 6.27: Comparison of predicted receive manifolds to measurements for Antennas 2 and 6, reported as magnitude and unwrapped phase in (a),(b) and (c),(d) respectively. The measured manifold is an aggregated result from three measured RDS receive manifolds that are reported individually in Chapter 5. This result represents a season level manifold correction for the 2014 Greenland P-3 data set.

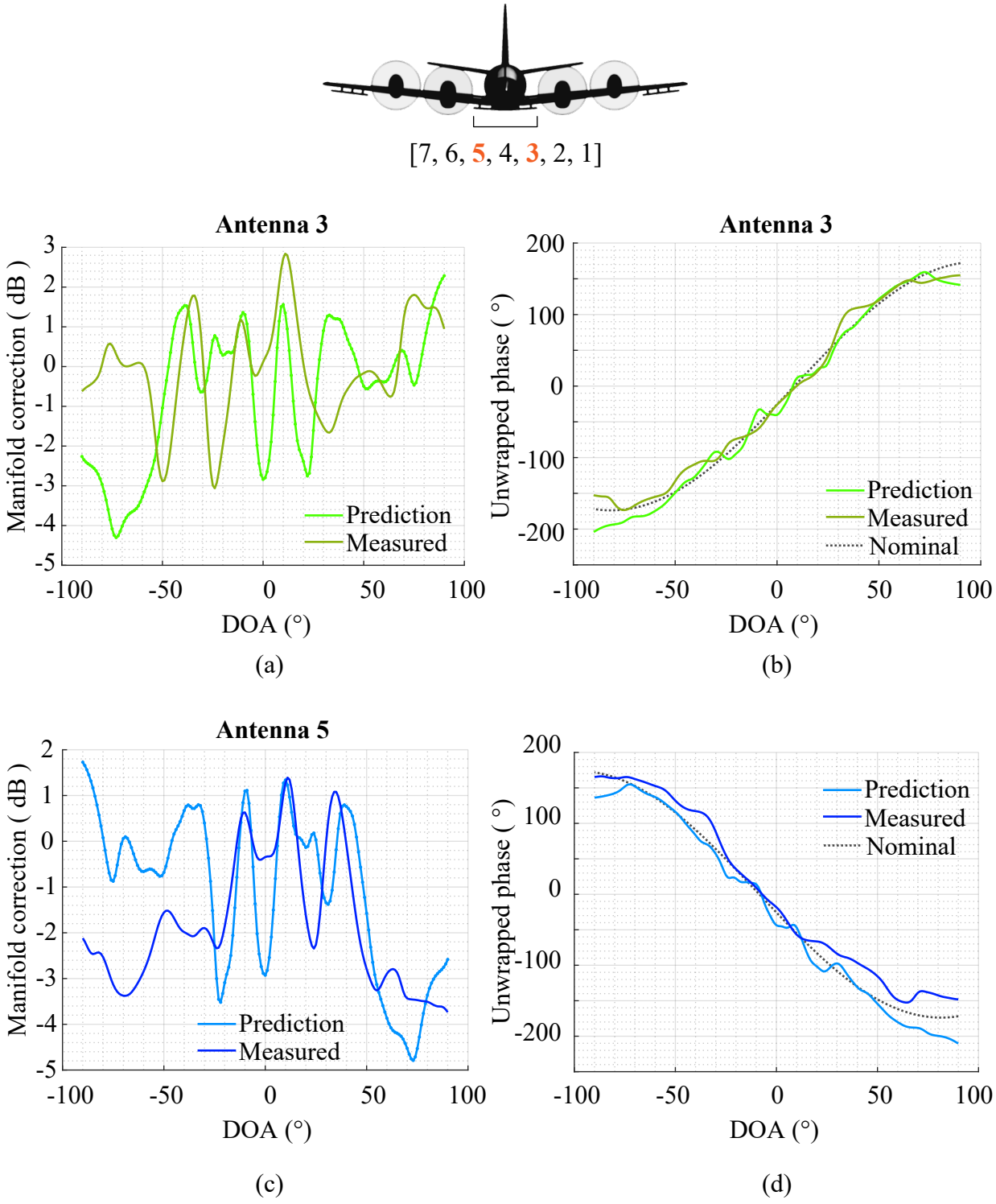

Figure 6.28: Comparison of predicted receive manifolds to measurements for Antennas 3 and 5, reported as magnitude and unwrapped phase in (a),(b) and (c),(d) respectively. The measured manifold is an aggregated result from three measured RDS receive manifolds that are reported individually in Chapter 5.This result represents a season level manifold correction for the 2014 Greenland P-3 data set.

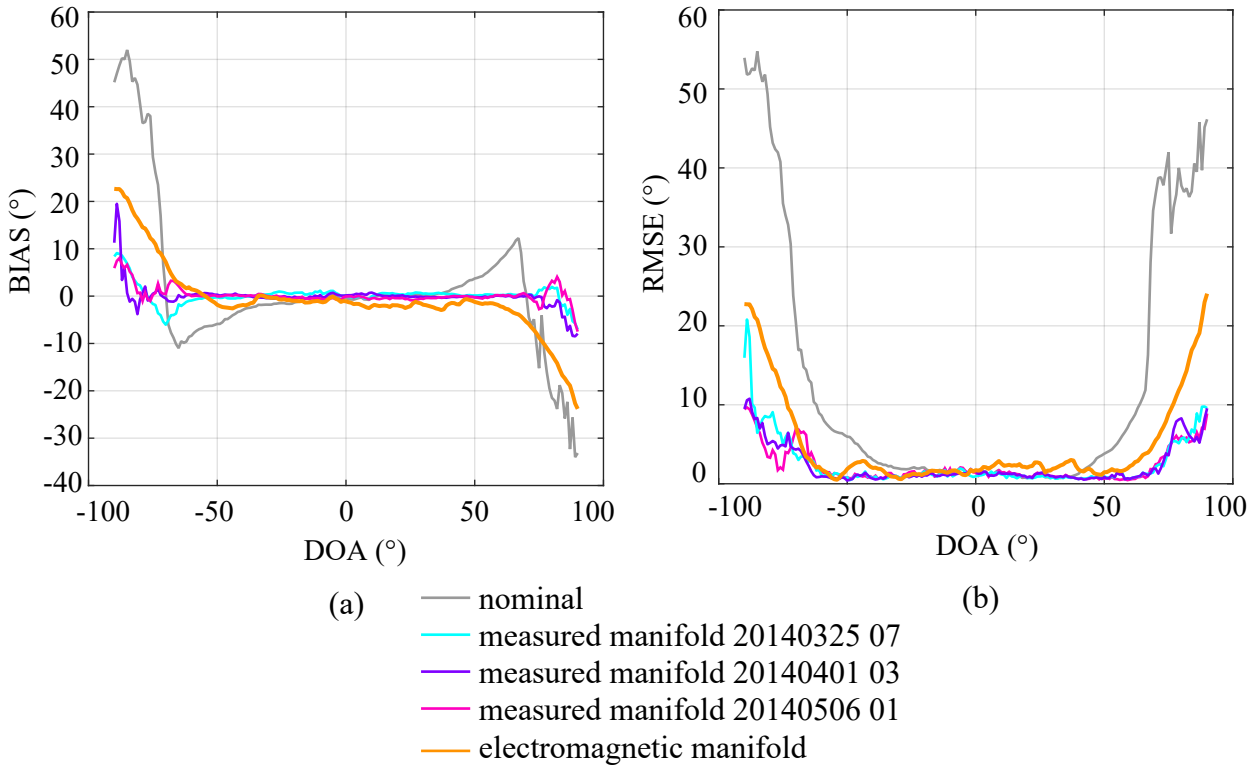

Figure 6.29: MUSIC DOA estimation performance for comparing manifold models, reported as (a) bias in degrees and (b) root mean squared error in degrees. The nominal model refers to the isotropic steering vector evaluated in terms of our current model of phase center positions. Measured manifolds correspond to those presented in Chapter 5. The EM manifold is the result of a full wave solution which outputs complex multichannel data in response to an ideal, linearly polarized plane wave source.

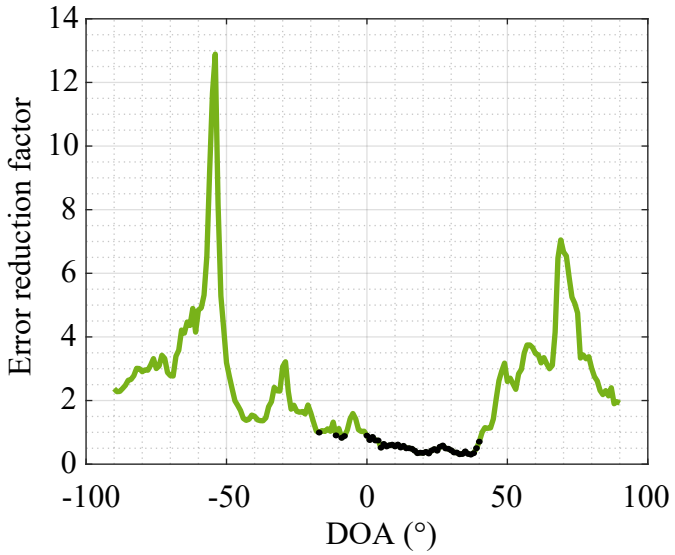

Figure 6.30: Average RMS error reduction demonstrated with predicted manifold, defined as the average ratio of RMS angle estimation error of the nominal model to the RMS error observed with a EM manifold. The black portions indicate where this ratio is less than one and hence interpreted as a localized degradation (where the predicted manifold does not outperform the nominal in angle estimation).

Chapter 7

Application of Manifold Calibration in Tomography

Abstract

The nonparametric manifold calibration approach outlined in Chapter 5 leads to improved angle estimation outcomes when the measured manifold is applied in MUSIC. The reduction of the estimated bias and RMS error reported in Chapter 5 suggests that the measured manifold will lead to improved outcomes in tomography when the measured manifold is applied in the angle estimation step of 3-D image formation. This chapter documents the application of measured manifolds in tomography and the assessment of 16 RDS-derived DEMs of sea ice and rocky terrain in the Canadian Arctic. Comparison of the vertical elevation errors of RDS DEMs generated with the nominal array response model to those generated with measured manifold model confirm significant reductions in elevation errors measured over the 3 dB illuminated swath. This chapter presents quantitative evidence that confirms the significant reduction in vertical elevation errors of RDS-derived DEMs produced with the measured manifold, judged by comparing mean and RMS elevation errors before and after calibration. It is shown that the measured manifold on average reduces RMS elevation errors by as much as 14.7 meters over the 3 dB swath width. Qualitative results are presented that substantiate better surface tracking outcomes after calibration, enabling a wider swath to be imaged before the tracker pulls off into noise..

7.1 Introduction

Chapter 5 presents three measured RDS receive manifolds that characterize the response of the inboard P-3 subarray to directional sources. The manifolds are measured by estimating the principal component of the array covariance matrix obtained from the edited snapshots in a calibration bin. The quality of manifolds is assessed by carrying out angle estimation with the MUSIC algorithm on cleaned snapshot bins and comparing estimator bias and RMS error to estimator errors observed when the nominal manifold is applied. Recall that the assessment tests a measured manifold against snapshots from a different day to avoid testing with the training data. The results reveal bias in the angle estimates obtained with the nominal model that increase as the elevation angle progresses further off nadir. DOA estimation with the measured manifold reduces angle estimator uncertainty and bounds the error well below 2° over a 120° angular extent about nadir.

Based on the initial assessment described above, we expect significantly improved outcomes in tomography. This chapter confirms the improvements realized when the measured manifold is applied in the angle estimation step of tomography. This chapter summarizes the results documented in [53] offering frame level detail of measured errors for each combination of measured manifold and tested frame. Qualitative examples are presented that illustrate the more focused scattering signatures observed in the 3-D images formed with measured manifolds.

7.2 RDS DEM Generation for Assessing Manifold Quality

Calibration performance is assessed by applying various manifold models in the direction of arrival stage of tomography and comparing RDS-derived DEMs to the ArcticDEM model of the surface. In this assessment, only non-penetrative surfaces are considered including sea ice and rocky terrain; subsurface returns are excluded. Manifolds are tested against a subset of the frames processed in nonparametric calibration that were reported in Table 5.2

Table 7.1: Frames processed in tomography.

Day Segment	*Frame List*	*Mission*
20140325_07	[2]	Axel Heiberg - Eureka
20140401_03	[4,5, 13, 15-16, 19, 34-35, 38, 41,42,45]	North Canada Glaciers
20140506_01	[41, 42, 45]	South Canada Glaciers

of Chapter 5. Table 7.1 reports the frames processed in tomography. The multichannel data are SAR processed for targets on the surface; the permittivity is assigned for free space propagation, $\varepsilon_r = 1$, in f-k migration. The MUSIC algorithm is applied for estimating angle in array processing. The number of sources, which remains fixed over a frame, is assigned to two in angle estimation.

7.2.1 Surface Reconstruction with CReSIS Toolbox

In tomographic processing with the MUSIC mode enabled, we estimate a pseudospectrum for every synthesized aperture and two-way delay gate in the scene. This produces a set of slices in two-way propagation and wavenumber space which we collectively refer to as the three-dimensional image. A nominal result is produced for each of the tested frames. Recall that the nominal model refers to the isotropic steering vector whose propagation phase is evaluated in terms of our understanding of the phase center positions based on a CAD description of the P-3 subarrays and a lidar survey. The nominal result is interpreted as the *uncalibrated* case and represents the baseline of the RDS tomography work preceding this dissertation research.

The array processor is modified to support three-dimensional image formation with measured manifold models. Both MUSIC and MLE methods are upgraded to handle angle estimation with a measured manifold, gridded in θ, by interpolating between grid points when evaluating their respective cost functions. To date, RDS DEMs produced with tomography apply the nominal steering vector in angle estimation. Hence the results presented

in this chapter and the resulting manuscript documented in [53] are the first examples in literature that demonstrate manifold calibration in ice sheet tomography.

The CReSIS toolbox implements a sequential tree reweighted (TRW-S) message passing algorithm for tracking surfaces in the 3-D image. The adaptation of TRW-S to ice sheet tomography, documented in [108], relies on a model of the air-to-ice interface to track the ice subsurface. Layer tracking aided by a surface model is disabled in TRW-S when reconstructing surface terrain for assessing manifold calibration in this research; the tracker does not use the ArticDEM in extracting a surface from the 3-D image in the results that follow. Additional support is implemented to update the surface layer extracted from the 3-D image with the binary ice mask described in Chapter 3. This step allows the coregistered mask to be carried through DEM generation so that any point on an RDS-derived DEM grid is associated with a binary value indicating the presence or absence of glacial ice. This ensures that subsurface targets are excluded from the error analysis presented below.

7.2.2 DEM Accuracy Assessment

DEM vertical elevation errors are reported for the portion of the 3-D image lying approximately within the 3 dB beamwidth of the scanned transmit beams, $|\theta| \leq 47^\circ$ and whose corresponding ice mask is false. The elevation height error of the n^{th} point on a the gridded DEM is determined as

$$e_n^h = h_n^{RDS} - h_n^{ADEM}, \tag{7.1}$$

Where h_n^{RDS} and h_n^{ADEM} refer to the n^{th} elevation point on the RDS and ArcticDEMs respectively. A sample mean elevation error and standard error are evaluated for the N_T ice-free grid points as

$$m_e^h = \frac{1}{N_T} \sum_{n=1}^{N_T} e_n^h, \tag{7.2a}$$

$$s_e^h = \sqrt{\frac{1}{N_T - 1} \sum_{n=1}^{N_T} \left(h_n^{RDS} - m_e^h \right)^2}. \tag{7.2b}$$

The total RMS elevation error and mean error (ME) are reported for each frame processed in tomography. Due to the sensitivity of the RMSE to outliers, outliers are identified as those elevation measurements lying more than 3 standard deviations from the mean error in Equation 7.1 before computing an RMSE and ME. These measures are evaluated over the $N_{T'}$ remaining grid points (after outlier removal) using the following expressions

$$ME = \frac{1}{N_{T'}} \sum_{n=1}^{N_{T'}} h_n^{RDS} - h_n^{ADEM}, \tag{7.3a}$$

$$RMSE = \sqrt{\frac{1}{N_{T'}} \sum_{n=1}^{N_{T'}} \left(h_n^{RDS} - h_n^{ADEM} \right)^2}. \tag{7.3b}$$

When reporting RMSE and ME for a frame, outliers are removed at the frame level. When reporting an RMSE and ME per manifold, all of the ice-free elevation points from the tested frames are aggregated prior to rejecting outliers.

7.3 Application of Measured Manifolds in Tomography

The measured manifolds presented in Chapter 5 are applied in tomography to produce RDS-derived DEMs for the 16 test frames specified in Table 7.1. Note that the frames tested in tomography are drawn from the larger calibration data sets (originally specified in Table 5.2). The reason for choosing test frames from the calibration set is because these frames provide the most comprehensive set of collections over non-penetrative terrain. Tomographic image formation is carried out with each of the three measured manifolds. It is acknowledged here that errors evaluated by testing a measured manifold against a frame from its training set may not provide a fair performance assessment (such as error reported when generating a DEM with the 20140325_07 measured manifold against the 20140325_07_002 frame). These occurrences are emphasized when reporting statistics on a frame by frame basis in

a comprehensive table. This table is reserved for Appendix E due to its large size. These cases are still reported for the sake of completeness in the figure of frame-level summary statistics with the disclaimer that the manifolds and test frames of coincident days may not be independent.

The ME and RMSE per frame are plotted in Figure 7.1 by manifold model. The measured manifolds demonstrate elevation error reduction in all cases relative to the nominal result, indicated by the green curve in these figures. In most cases the manifold measured from the 20140325_07 data set admits slightly larger errors than the 20140401_03 and 20140506_01 manifolds. This may be attributable to the fact that the 20140325_07 manifold is measured from the smallest number of frames (4 in this case as compared to 12 and 13 frames in the cases of the 20140401_03 and 20140506_01 manifolds respectively). The mean errors appear to track somewhat across the measured and nominal models with the nominal results appearing to show amplified biases. The large biases presented in the nominal results confirm the angle biases observed in the measured angle estimation performance. The measured elevation errors for each of the days tested are also reported by frame in Tables E.1-E.4 of Appendix E. The summary statistics are rolled up in Table 7.2 over all of the frames to present a summary mean elevation error and RMS elevation error for each manifold. The reported errors demonstrate bias in the DEMs produced with the nominal manifold model. In all cases, the measured manifold DEMs lead to significant reduction of elevation errors. The largest RMS elevation errors are observed with the 20140325 07 manifold, attributed to the fact that the 20140325 07 manifold is measured from the smallest number of frames.

The reduction in RDS elevation errors indicates better performance with the TRW-S tracking algorithm. This is supported with qualitative examples that are demonstrative of the large performance improvements observed with the measured manifold. The first example in Figure 7.2 shows fast-time/cross-track MUSIC slices from the 3-D image corresponding to returns from a frozen channel crossing. We expect the sea ice in the channel to present a smooth, non-penetrative interface to the RDS which should lead to a parabolic signature in

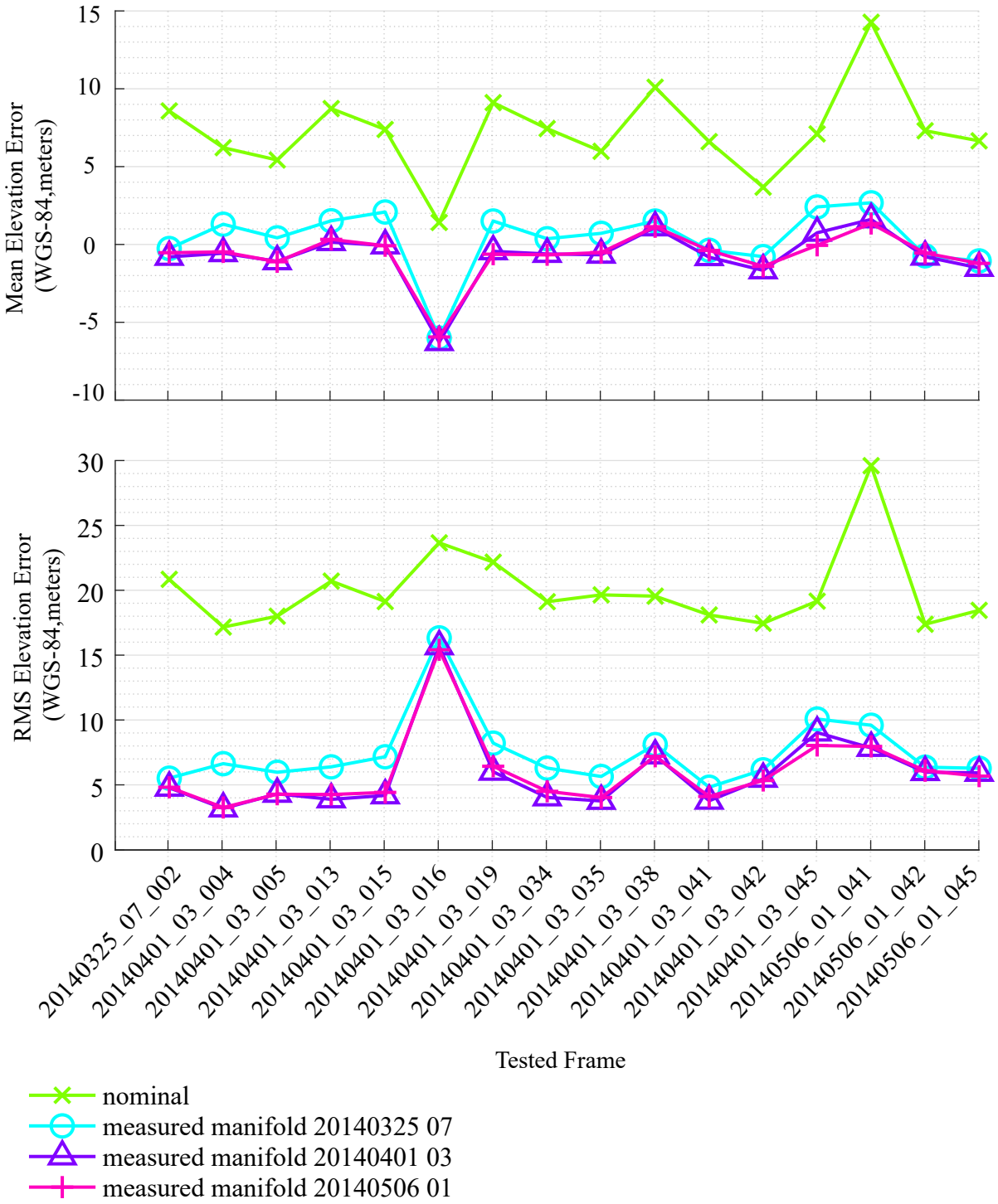

Figure 7.1: Measured elevation errors of RDS DEMs (reported as meters with respect to the WGS-84 ellipsoid) for 16 tested frames, comparing vertical accuracy when varying manifold model applied in tomography.

the slice. The DEMs estimated with the nominal and measured manifolds are presented in Figures 7.2a and 7.2b respectively, draped over Landsat-7 imagery. A black solid line crosses the flight line at along-track bin 2,200 to indicate the corresponding platform position. The MUSIC slices pulled from the nominal and measured manifold results are shown in 7.2c and 7.2d respectively. The slices confirm the anticipated improvements in the 3-D images produced with the measured manifold in angle estimation and show that the measured manifold outputs lead to a more focused scattering signature with higher intensity values. We anticipate these features to lead to more accurate layer tracking in surface extraction.

Figure 7.3 offers an example that points to better performance in layer tracking with the calibrated result. This figure follows a consistent format with Figure 7.2. From a side-by-side comparison of the DEMs, we can observe that the measured manifold result is smoother, especially in the drainage channels (corresponding to the low elevation valleys on the maps). The slices validate the anticipated tracking improvements, showing better agreement between the ArcticDEM and the RDS surfaces in the calibrated result. This result also shows that the calibrated result enables TRW-S to track the surface longer in fast-time (corresponding to *further* in cross-track). In the nominal result we more commonly observe that the low pixel intensities pull the tracker off into noise much earlier. In the DEM, this behavior appears as increased elevation at the edges of the swath. This is observable in the next example.

The final example shows the terminus of an outlet glacier on Ellesmere Island in Figure 7.4 Note that this example is produced to assess the vertical elevation error of RDS-derived DEMs. This means that the layer tracker is modified to ensure that it does not use the ArcticDEM in tracking and the bottom is not tracked. In mapping glacier beds with tomography, TRW-S also tracks the bottom. Thus in typical tomographic image formation, we would have a third layer to indicate the TRW-S picks of the bottom interface in the slices. It is pointed out that the lower parabolic scattering signature (meaning the signature that starts at a later propagation time) observed in the slices corresponds to scattering from the bottom of the glacier. Where the lower parabola intersects with the surface signature rep-

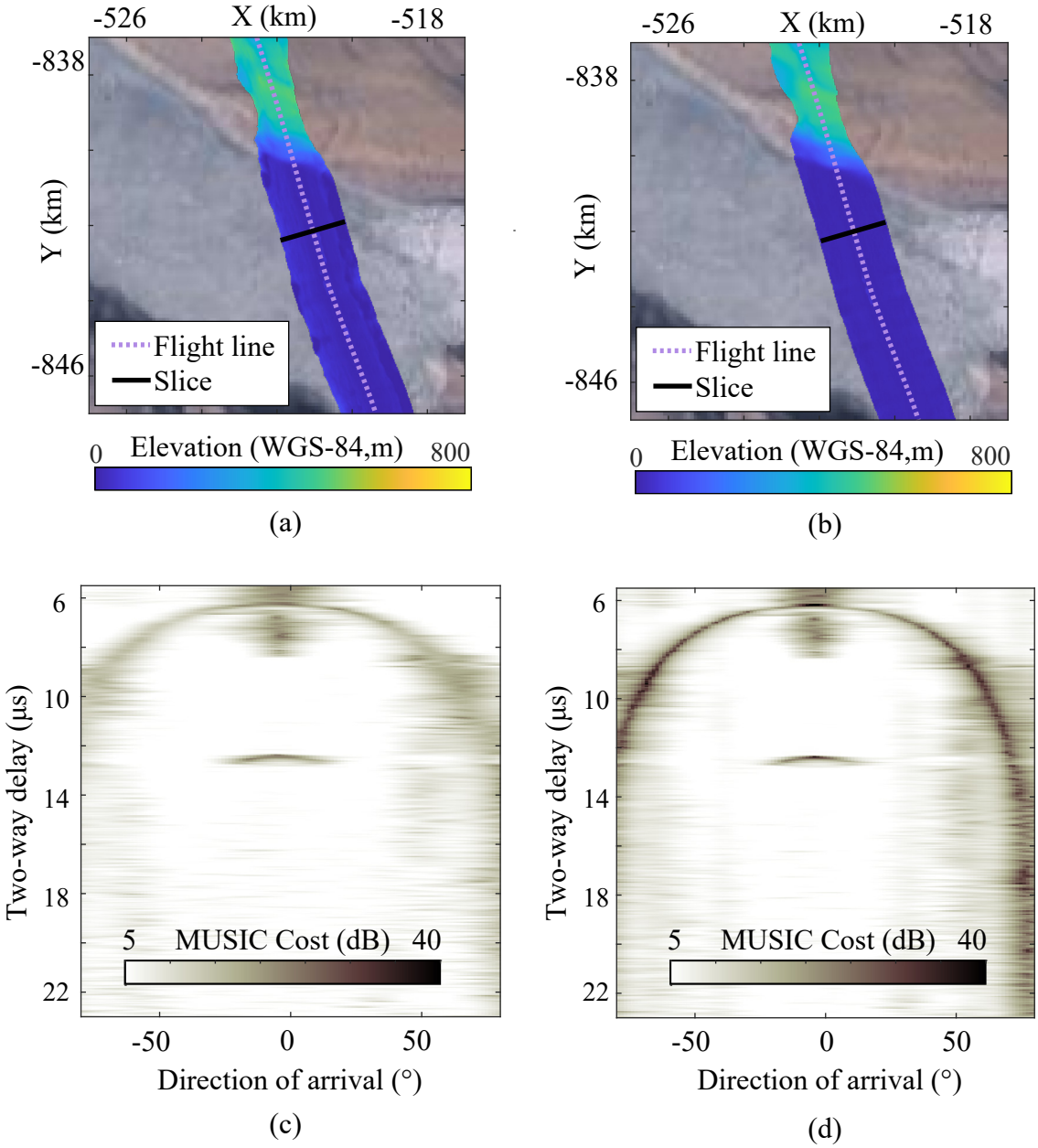

Figure 7.2: Comparison of RDS-derived DEMs and an example of fast-time/cross-track MUSIC slices showing scattering from a frozen channel, pulled from the 3-D images of the 20140401_03_035 frame. Figure (a) presents the RDS-derived DEM produced with the nominal manifold model and draped over Landsat-7 imagery. Figure (b) presents the RDS-derived DEM produced with the 20140506_01 measured RDS manifold presented in Chapter 5. The MUSIC slices produced with nominal and measured manifolds are shown in (c) and (d) respectively and correspond to the along-track position (range line 2,200) indicated by a black solid line on the DEMs. The slices demonstrate observed improvements after calibration, evidenced through the more focused scattering signatures and higher value of the MUSIC cost functions. Landsat-7 image courtesy of the U.S. Geological Survey.

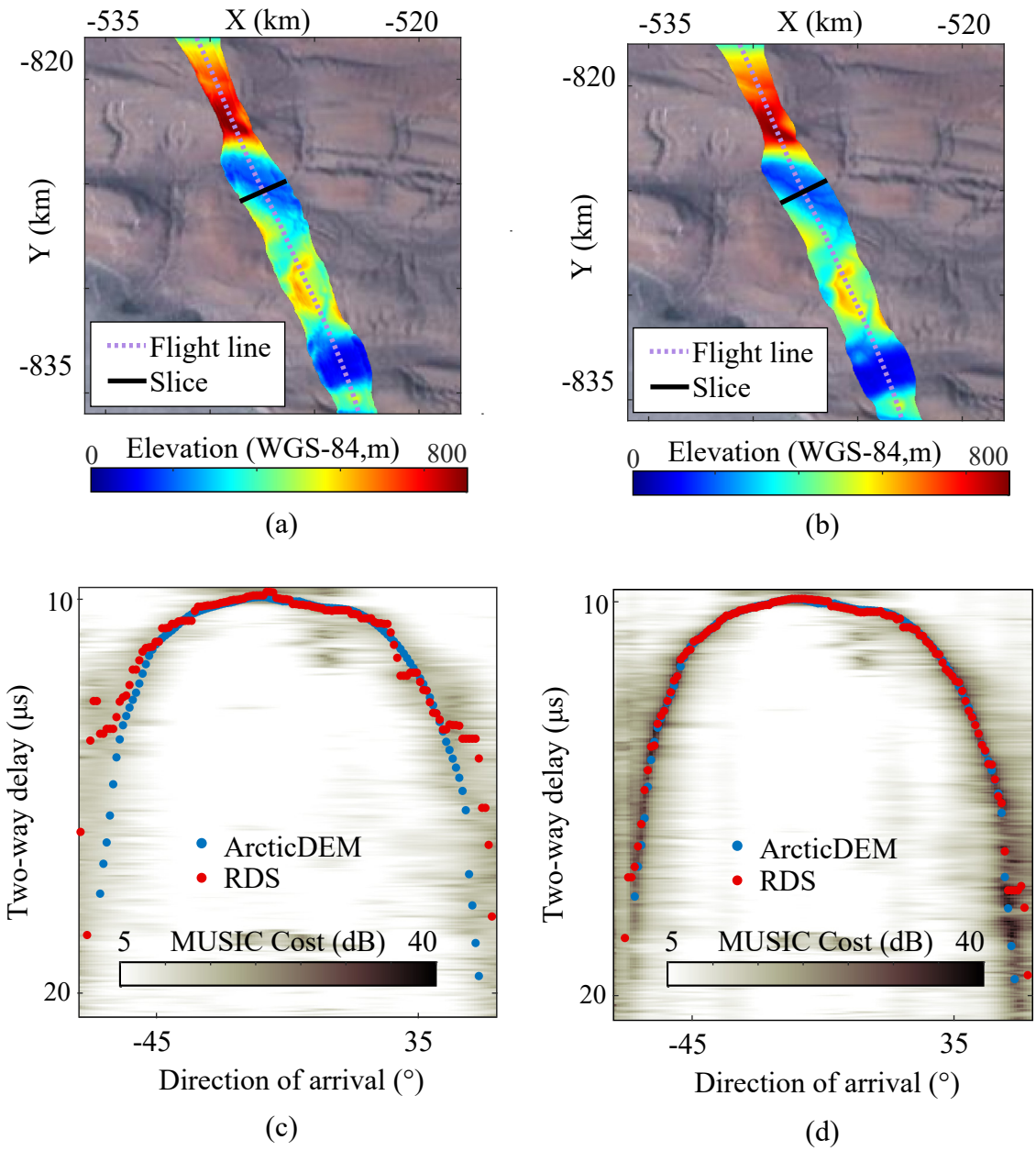

Figure 7.3: Comparison of RDS-derived DEMs and an example of fast-time/cross-track MUSIC slices showing scattering over rocky terrain, pulled from the 3-D images of the 20140401_03_035 frame. Figure (a) presents the RDS-derived DEM produced with the nominal manifold model and draped over Landsat-7 imagery. Figure (b) presents the RDS-derived DEM produced with the 20140506_01 measured RDS manifold presented in Chapter 5. The MUSIC slices produced with nominal and measured manifolds are shown in (c) and (d) respectively and correspond to the along-track position (range line 940) indicated by a black solid line on the DEMs. The ArcticDEM surface layer is plotted in blue with TRW-S surface picks plotted in red. The result confirms improved surface tracking performance in the slice produced with the measured manifold in angle estimation. Landsat-7 image courtesy of the U.S. Geological Survey.

Table 7.2: Summary of elevation errors (WGS-84, meters) of RDS-Derived DEMs relative to the ArcticDEM by manifold model [9].

Manifold	$\mathbf{N_T}$	**Outliers**	**Rejection (%)**	**ME (m)**	**RMSE (m)**
Nominal	1,227,632	26,740	2.13	7.0299	19.7090
20140325 07	1,279,866	24,163	1.85	0.5810	6.1548
20140401 03	1,286,332	25,146	1.92	-0.6374	5.0240
20140506 01	1,285,332	24,377	1.85	-0.5326	5.1309

resents the physical margins of the glacier where the bottom layer and surface layer should merge. The slice from the calibrated 3-D image demonstrates resolution of the margins of the glacier. In the nominal result, these portions of the image are comparatively much noisier.

7.4 Discussion

The quantitative and qualitative results presented in this chapter offer substantial evidence of the consistent reduction in the vertical elevation accuracy of RDS DEMs produced with the application of the measured manifolds in angle estimation. The three manifolds all lead to significant reduction of mean elevation errors and RMS elevation errors. This is important because the manifolds are measured from three independent data sets collected on flights at the beginning, middle, and end of the season. This suggests that the manifolds are stable in time. The measured manifolds do not mandate an underlying model of the error mechanisms. The technique simply measures the offset of the manifold from nominal and the source of that offset (be it mutual coupling, perturbed geometry, or higher order platform effects) is arbitrary.

It is emphasized that hardware changes on the receive path will likely change the manifold and it is recommended that a new manifold be measured following such a change mid-season (if possible). The 2014 Greenland IceBridge mission is unique from other seasons because the hardware was not removed from the aircraft after the preceding mission as the P-3 was

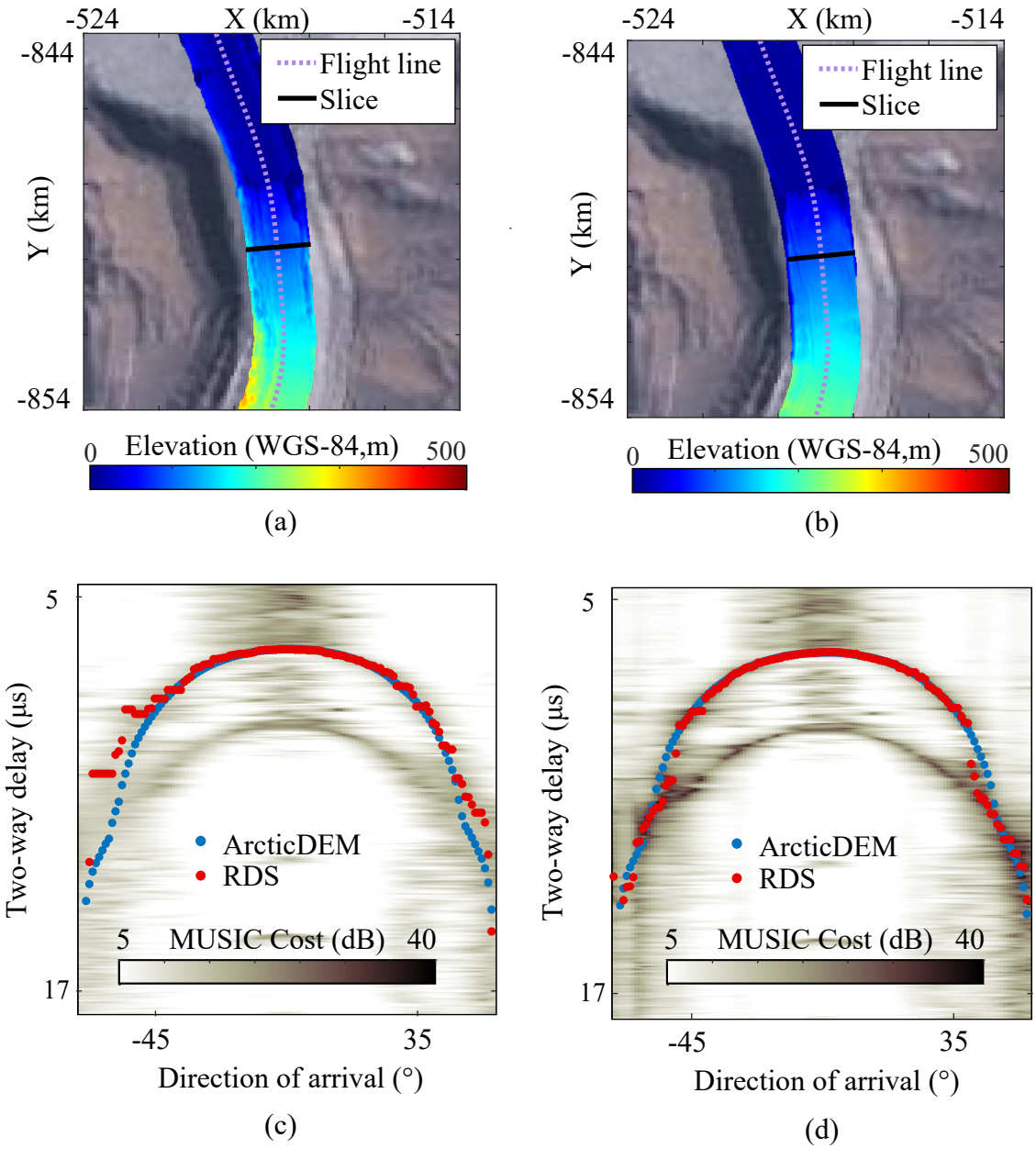

Figure 7.4: Comparison of RDS-derived DEMs and an example fast-time/cross-track MUSIC slices showing scatteringover the terminus of a glacier on Ellesmere Island, pulled from the 3-D images of the 20140401_03_035 frame. Figure (a) presents the RDS-derived DEM produced with the nominal manifold model and draped over Landsat-7 imagery. Figure (b) presents the RDS-derived DEM produced with the 20140506_01 measured RDS manifold presented in Chapter 5. The MUSIC slices produced with nominal and measured manifolds are shown in (c) and (d) respectively and correspond to the along-track position (range line 2,749) indicated by a black solid line on the DEMs. The slices demonstrate observed improvements after calibration and increased agreement between the TRW-S picks. We also observe better resolution of the glacier margins in the calibrated result. Landsat-7 image courtesy of the U.S. Geological Survey.

used in both the preceding 2013 Antarctic IceBridge mission and the 2014 Arctic campaign. The measured manifolds presented in this dissertation are expected to improve performance for the previous mission as well and it is recommended that the 2013 data set be reprocessed with these corrections.

An important implication of the results presented in this chapter is emphasized here. The slices from the calibrated 3-D image exhibit larger pixel intensities over broader angular extents in comparison with the nominal images. The nominal images exhibit low intensity pixels that pull the tracker off into noise much earlier in fast-time. TRW-S is able to track the surface in the calibrated images longer in fast-time, indicating that the calibrated results will increase the width of the RDS swath in 3-D imaging. This is an important outcome of this research: *manifold calibration enables 3-D imaging over a wider swath.* Hence more area can be imaged in a single pass with higher accuracy. We expect the improved fine resolution 3-D swath maps of the subsurface to support morphometric analyses and process studies such as [14] and [15]. The 2014 Greenland P-3 data set tested in this chapter stands to support the AtaaMap project, a multi-disciplinary research effort focused on producing bed maps that will help to constrain the contributions of the Canadian Arctic Archipelago to sea level rise.

The measured manifolds admit more accurate angle estimates and it is anticipated that null steering accuracy will improve with the RDS receive manifolds measured for this work. This indicates the potential to recover detection performance in areas where the basal returns are dominated by surface clutter (such as over the marine terminating outlet glaciers of Greenland's margins). Improved nulling of the surface returns is also important for high-altitude sounding configurations. It is recommended that the methodology outlined here be applied to historic data sets to assess profiling performance with the measured manifold.

7.5 Conclusion

This chapter confirms that manifold calibration leads to more accurate DEMs produced with tomography. The results put forth in this chapter indicate that the RDS-derived DEMs produced with the nominal manifold are biased in elevation (by approximately 7.03 meters). The total RMS elevation errors of the nominal DEMs are on average 19.71 meters over the 3 dB swath width. The mean elevation errors of the calibrated DEMs range from -0.64 meters to 0.58 meters with RMS elevation errors ranging from 5.02 meters to 6.2 meters. On average, the RDS-derived DEMs produced with the measured manifolds reduce vertical elevation uncertainty by a factor of 3.7 in tomography. Qualitative results from the 3-D images indicate that the layer tracker benefits from the more focused scattering signatures and higher pixel intensities produced with the calibrated result. The improved layer tracking outcomes means that the application of the measured manifold in the angle estimation step of 3-D image formation enables imaging over a wider swath and with higher accuracy in a single pass.

Chapter 8

Summary and Conclusions

The research summarized in this dissertation establishes a framework for handling the array manifold calibration problem of airborne ice-penetrating SARs that rely on parametric angle estimation to resolve scattering interfaces in elevation as part of the 3-D image formation step in tomography. Several outcomes of this study merit highlighting. First, the research proves that the SAR sounder imagery can be coregistered to a surface DEM and land classification map to identify calibration pixels with known arrival angles. The creation of snapshot databases as described in Chapter 3 will be crucial in calibrating seasons which lack collections on dedicated calibration flights from a maneuvering platform over smooth extended surface targets. Building an observation database facilitates both parametric and nonparametric forms of manifold calibration described in Chapters 4 and 5. The data processing architecture holds the potential to evolve in the future in order to support calibration frameworks where the arrival angles are only approximately known. Additional lidar data could be ingested to improve our knowledge of truth in the calibration bins. Because a vast majority of the observations that feed into manifold measurement correspond to rocky terrain returns, one can envision using surface altimetery from many collections to ensure good ground control. The current code does not support this yet but could easily augmented to improve correction of the ArcticDEM.

Both parametric and nonparametric forms of manifold calibration are advanced in this dissertation. A parametric estimation framework is derived in Chapter 4 that lays the groundwork for calibration with multiple sources simultaneously. The derivation interprets the snapshot database as a superset of statistically independent subsets which share com-

mon unknown nonlinear manifold parameters and casts a large separable Gaussian estimation problem composed of many smaller Gaussian estimation problems, leading to a total likelihood expression that is a simple summation of compressed likelihoods from each of the subsets. The mathematics suggest that the large estimator is suitable for multitarget calibration provided that the manifold admits an analytic form that is parameterized by some nonlinear unknowns and arrival angle. We show analytically that the proposed estimator does not rely on the scan dependent length of the manifold vectors from which we conclude that only the *orientation* of the manifold vector in $\mathbb{C}^P$ space is needed to leverage the parametric form. This analysis justifies the principal components based characterization derived under a unit norm constraint in Chapter 5 as sufficient for application of the parametric form. Although the framework is not yet applied to real measurements, the estimator performance is established numerically and evidence is presented that explores the influence of spatial bandwidth (determined by the angular extent of calibration sources) and number of calibration bins on angle estimation outcomes.

Chapter 5 outlines nonparametric manifold calibration for the SAR sounder. The principal components characterization is derived for a single spatial source under the unit norm constraint on the manifold vector. Evidence is presented that emphasizes the challenge of applying nonparametric manifold calibration techniques to our data sets. In particular it is shown that the RDS snapshots when binned into 1° grids do not lead to a sufficient number of single source observations for carrying out the nonparametric characterization. The sparsity of single source observations in angle forces us to consider measurements with two sources in the nonparametric framework, contradicting the traditional procedures found in literature. A methodology is described that circumvents the single source requirement by applying a subspace measure to the two source SAR pixels to extract high SINR measurements for calibration. The technique *edits* out the observations that appear more correlated to an interference source, leading to improved angle estimation outcomes when manifolds are measured with the edited snapshot set. The editing technique is not derived here but

adopts the form of generalized likelihood ratio test that is expected to hold provided that the manifold errors are sufficiently small relative to the nominal array response model. The validity of this assumption is not easily verified without further study using a CEM model. When applied in angle estimation, the measured manifolds reduce angle estimation errors by a factor of 4.8 on average foreshadowing reductions of vertical elevation errors in their associated RDS-derived DEMs in tomography.

The RDS manifold is studied in Chapter 6. Groundwork is laid that is necessary in using the CEM model to predict the RDS manifolds. Although the model has yet to be fully validated with a forced symmetric geometry to understand errors imparted by the asymmetric mesh, the predicted manifold is applied in angle estimation and compared to measured and nominal manifolds. This leads to an unexpected result. The observed RMS error as a function of angle indicates that the Feko predictions are better matched to the true array response outside of $\pm 50^{\circ}$, in the areas where the nominal errors grow extremely large in angle estimation and the snapshot editing is expected to break down. The predicted manifolds on average reduce angle estimation error over the nominal manifold model by a factor of 3. The improved angle estimation outcomes at the large incidence angles measured when applied to real RDS snapshots are signficant for two reasons. The improvements provide the first confirmation of the utility of the CEM model in predicting the embedded element patterns of our integrated P-3 subarrays. The reduced angle estimation errors measured at the large incidence angles indicate that the predictions should be used to compute the editing measure at the edges of the field of regard where we suspect the measure to degrade.

The parametric framework is tested on a deterministic manifold predicted by Feko for a linear array of RDS wideband dipoles with perturbed geometry. Multiple attempts to fit the observations to an array response model where an element pattern is expressed as a sum of complex exponential basis functions that includes a term to account for the propagation error were unsuccessful. The minimization carried out with built in MATLAB search functions has not yet reproduced the receive patterns on any of the channels, even when the problem

is initialized with the known geometric errors and the global search framework is provided. Convergence failures in optimization are attributed to poor initialization of the coeffcients of the basis functions and the complexity of the problem. The test only imposes geometric error on 5 out 7 sensors. Position errors in two dimensions leads to 10 unknowns. The number of nontrivial terms in the Fourier transform of a channel's θ dependent manifold indicates at least 15 coefficients are needed to fit a pattern to the model, leading to 105 unknowns in optimization (when the position errors are treated as known).

The measured manifolds are demonstrated in tomography and compared to the nominal results using RDS-derived DEMs of rocks and sea ice collected in the Canadian Arctic. Both quantitative and qualitative evidence is presented that confirms the significant performance improvements realized with the calibrated manifold. The findings substantiate the bias of the nominal manifold that leads to biased estimates of topography. On average, the nominal manifold produces DEMs with a mean elevation error of 7.03 meters and an RMS elevation error of 19.71 meters. The RDS DEMs produced with the measured manifold in angle estimation lead to mean elevation errors that range from -0.64 meters to 0.58 meters and RMS elevation errors ranging from 5.02 meters to 6.15 meters. The more focused scattering signatures with higher pixel intensities realized with the application of the measured manifold lead to better tracking outcomes that enable the TRW-S algorithm to track the surface for a longer duration in time (corresponding to a longer cross-track extent) before pulling off into noise. The improved tracking performance during surface extraction enables a wider swath to imaged in tomography.

8.1 Recommendations and Future Work

It is recommended that the parametric framework be validated with an electromagnetic manifold predicted from the full-wave solver. The validation should model a very simple free space array of RDS dipoles using the conformal geometry of the inboard subarray with no perturbations. The real and imaginary components of the θ dependent complex pattern of

each channel should be fit with a Fourier series using MATLAB's built in curve fitting tools. Using a cost function expressed in terms of the following Fourier series

$$\begin{aligned} a_p(\theta) = &\sum_{n=1}^{N_p} \alpha_{r0} + \alpha_{rn}\cos(w_r\theta n) + \beta_{rn}\sin(w_r\theta n) + \dots \\ &j \cdot \sum_{n=1}^{N_p} \alpha_{i0} + \alpha_{in}\cos(w_i\theta n) + \beta_{in}\sin(w_i\theta n) \end{aligned} \tag{8.1}$$

The problem can be cast into a regression and minimized as demonstrated in Chapter 4. The first step should be to verify that initialization with the correct coefficients (from the MATLAB curve fitting) and a definition of tight windows leads the solver to converge to truth. Once the convergence is verified by initializing with truth, the search windows can be broadened to understand the behavior of the optimization problem.

It is recommended that the CEM model be run with a much finer mesh to verify that the asymmetric mesh leads to marginal phase differences across geometrically symmetric channels. The predicted manifolds produced with a finer mesh should be applied to the snapshot bins to confirm that the angle estimation performance is at least as good as what was observed with a coarse mesh of the ground plane. Additional study is warranted to determine if the application of the predicted manifold in snapshot editing (using the prediction to evaluate the subspace alignment measure) leads to better angle estimation outcomes and more accurate RDS-derived DEMs.

Reprocessing the 2014 Greenland data set with both a geometric nulling beamformer and an adaptive generalized sidelobe canceller is recommended to study potential basal detection improvements over areas known to suffer sensitivity loss by masking surface clutter. This season includes flights over Jakobshavn glacier. These frames are good candidates to carry out such a study. Finally it is recommended that the measured manifold be used to produce 3-D bed maps of the Canadian Arctic Archipelago data set to support the Ataamap effort

currently underway that aims to constrain the estimated volume of freshwater ice in the Canadian Arctic.

References

[1] I. Ziskind and M. Wax, "Maximum likelihood localization of multiple sources by alternating projection," *IEEE Transactions on Acoustics, Speech, and Signal Processing*, vol. 36, no. 10, pp. 1553–1560, 1988.

[2] R. O. Schmidt, "A signal subspace approach to multiple emitter location and spectral estimation," Ph.D. dissertation, Stanford University, 1982. [Online]. Available: https://www-proquest-com.

[3] K. J. Byers, A. R. Harish, S. A. Seguin, C. J. Leuschen, F. Rodriguez-Morales, J. Paden, E. J. Arnold, and R. D. Hale, "A modified wideband dipole antenna for an airborne VHF ice-penetrating radar," *IEEE Transactions on Instrumentation and Measurement*, vol. 61, no. 5, pp. 1435–1444, 2012.

[4] Altair, *FEKO [computer software]*. Altair Engineering, Inc. Digital Media, 2021, Version 2021.1. https://www.altair.com/feko/. [Online]. Available: https://www.altair.com/feko/.

[5] W. Stutzmann and G. Thiele, "Feeding Wire Antennas," in *Antenna Theory and Design*, 3rd ed. John Wiley & Sons, Ltd, 2012, ch. 6, p. 181, figure 6-36.

[6] E. J. Arnold, "Development and improvement of airborne remote sensing radar platforms," Ph.D. dissertation, University of Kansas, 2013.

[7] E. Arnold, Personal communication, 2021.

[8] F. Rodríguez-Morales, S. Gogineni, C. J. Leuschen, J. D. Paden, J. Li, C. C. Lewis, B. Panzer, D. Gomez-Garcia Alvestegui, A. Patel, K. Byers, R. Crowe, K. Player,

R. D. Hale, E. J. Arnold, L. Smith, C. M. Gifford, D. Braaten, and C. Panton, "Advanced multifrequency radar instrumentation for polar research," *IEEE Transactions on Geoscience and Remote Sensing*, vol. 52, no. 5, pp. 2824–2842, 2014.

[9] T. Moore and J. Paden, "Nonparametric array manifold calibration for ice sheet sar tomography," in *Proc. IEEE Int. Geoscience and Rem. Sens. Symp. (IGARSS 2021)*, 2021, pp. 2919–2922.

[10] IPCC, 2019, "Summary for policy makers," in *Climate Change 2021: The Physical Science Basis. Contribution of Working Group I to the Sixth Assessment Report of the Intergovernmental Panel on Climate Change*, V. MassonDelmotte, P. Zhai, A. Pirani, S. Connors, C. Péan, S. Berger, N. Caud, Y. Chen, L. Goldfarb, M. Gomis, M. Huang, K. Leitzell, E. Lonnoy, J. Matthews, T. Maycock, T. Waterfield, O. Yelekçi, R. Yu, and B. Zhou, Eds. Geneva, Switzerland: Cambridge University Press. In Press, 2021.

[11] M. Morlighem, C. N. Williams, E. Rignot, L. An, J. E. Arndt, J. L. Bamber, G. Catania, N. Chauché, J. A. Dowdeswell, B. Dorschel *et al.*, "Bedmachine v3: Complete bed topography and ocean bathymetry mapping of Greenland from multibeam echo sounding combined with mass conservation," *Geophysical research letters*, vol. 44, no. 21, pp. 11–051, 2017.

[12] M. Morlighem, E. Rignot, T. Binder, D. Blankenship *et al.*, "Deep glacial troughs and stabilizing ridges unveiled beneath the margins of the Antarctic Ice Sheet," *Nature Geoscience*, vol. 13, pp. 219–137, 2019.

[13] A. Shepherd, E. Ivins, E. Rignot, B. Smith, M. Van Den Broeke, I. Velicogna, P. Whitehouse, K. Briggs, I. Joughin, G. Krinner *et al.*, "Mass balance of the antarctic ice sheet from 1992 to 2017," *Nature*, vol. 558, pp. 219–222, 2018.

[14] N. Holschuh, K. Christianson, J. Paden, R. Alley, and S. Anandakrishnan, "Linking postglacial landscapes to glacier dynamics using swath radar at Thwaites Glacier,

Antarctica," *Geol.*, vol. 48, no. 3, pp. 268–272, 01 2020. [Online]. Available: https://doi.org/10.1130/G46772.1

[15] D. Medrzycka, L. Copland, W. Van Wychen, and D. Burgess, "Seven decades of uninterrupted advance of Good Friday Glacier, Axel Heiberg Island, Arctic Can." *J. of Glaciology*, vol. 65, no. 251, p. 440–452, 2019.

[16] J. Paden, T. Akins, D. Dunson, C. Allen, and P. Gogineni, "Ice-sheet bed 3-D tomography," *J. of Glaciology*, vol. 56, no. 195, pp. 3–11, 2010.

[17] X. Wu, K. Jezek, E. Rodríguez, S. Gogineni, F. Rodríguez-Morales, and A. Freeman, "Ice sheet bed mapping with airborne SAR tomography," *IEEE Trans. Geosci. Remote Sens.*, vol. 49, no. 10, pp. 3791–3802, 2011.

[18] A. Ferreol, P. Larzabal, and M. Viberg, "Performance prediction of maximum likelihood direction-of-arrival estimation in the presence of modeling errors," *IEEE Transactions on Signal Processing*, vol. 56, no. 10, pp. 4785–4793, 2008.

[19] ——, "On the resolution probability of MUSIC in presence of modeling errors," *IEEE Transactions on Signal Processing*, vol. 56, no. 5, pp. 1945–1953, 2008.

[20] A. J. Weiss and B. Friedlander, "Effects of modeling errors on the resolution threshold of the MUSIC algorithm," *IEEE Transactions on Signal Processing*, vol. 42, no. 6, pp. 1519–1526, 1994.

[21] B. Friedlander, "A sensitivity analysis of the MUSIC algorithm," *IEEE Transactions on Acoustics, Speech, and Signal Processing*, vol. 38, no. 10, pp. 1740–1751, 1990.

[22] ——, "Sensitivity analysis of the maximum likelihood direction-finding algorithm," *IEEE Transactions on Aerospace and Electronic Systems*, vol. 26, no. 6, pp. 953–968, 1990.

[23] A. L. Swindlehurst and T. Kailath, "A performance analysis of subspace-based methods in the presence of model errors. I. the MUSIC algorithm," *IEEE Transactions on Signal Processing*, vol. 40, no. 7, pp. 1758–1774, 1992.

[24] J. Yan, J. Li, F. Rodríguez-Morales, R. Crowe, D. Gomez-Garcia, E. Arnold, J. Paden, C. Leuschen, and S. Gogineni, "Meas. of in-flight cross-track antenna patterns of radar depth sounder/imager," *IEEE Trans. Antennas Propag.*, vol. 60, no. 12, pp. 5669–5678, 2012.

[25] J. J. Smith, Y. H. Leung, and A. Cantoni, "The cramér-rao lower bound for towed array shape estimation with a single source," *IEEE Transactions on Signal Processing*, vol. 44, no. 4, pp. 1033–1036, 1996.

[26] ——, "The partitioned eigenvector method for towed array shape estimation," *IEEE Transactions on Signal Processing*, vol. 44, no. 9, pp. 2273–2283, 1996.

[27] J. J. Fuchs, "Shape calibration for a nominally linear equispaced array," *IEEE Transactions on Signal Processing*, vol. 43, no. 10, pp. 2241–2248, 1995.

[28] A. J. Weiss and B. Friedlander, "Array shape calibration using sources in unknown locations-a Maximum Likelihood approach," *IEEE Transactions on Acoustics, Speech, and Signal Processing*, vol. 37, no. 12, pp. 1958–1966, 1989.

[29] ——, "Array shape calibration using eigenstructure methods," in *Twenty-Third Asilomar Conference on Signals, Systems and Computers, 1989.*, vol. 2, 1989, pp. 925–929.

[30] Y. Rockah and P. M. Schultheiss, "Array shape calibration using sources in unknown locations-part I: Far-field sources," *IEEE Transactions on Acoustics, Speech, and Signal Processing*, vol. 35, no. 3, pp. 286–299, Mar. 1987.

[31] ——, "Array shape calibration using sources in unknown locations-part II: Near-field sources and estimator implementation," *IEEE Transactions on Acoustics, Speech, and Signal Processing*, vol. AASP-35, no. 6, pp. 724–735, Jun. 1987.

[32] B. Friedlander, "Antenna array manifolds for high-resolution direction finding," *IEEE Transactions on Signal Processing*, vol. 66, no. 4, pp. 923–932, 2018.

[33] B. Friedlander, "The extended manifold for antenna arrays," *IEEE Transactions on Signal Processing*, vol. 68, pp. 493–502, 2020.

[34] S. Henault, Y. M. Antar, S. Rajan, R. Inkol, and S. Wang, "The multiple antenna induced emf method for the precise calculation of the coupling matrix in a receiving antenna array," *Progress in Electromagnetics Research M*, vol. 8, pp. 103–118, 2009.

[35] J. W. Wallace and R. Mehmood, "On the accuracy of equivalent circuit models for multi-antenna systems," *IEEE Transactions on Antennas and Propagation*, vol. 60, no. 2, pp. 540–547, 2012.

[36] E. J. Arnold, J.-B. Yan, R. D. Hale, F. Rodriguez-Morales, and P. Gogineni, "Identifying and compensating for phase center errors in wing-mounted phased arrays for ice sheet sounding," *IEEE Transactions on Antennas and Propagation*, vol. 62, no. 6, pp. 3416–3421, 2014.

[37] E. J. Arnold, J.-B. Yan, R. D. Hale, F. Rodriguez-Morales, P. Gogineni, J. Li, and M. Ewing, "Effects of vibration on a wing-mounted ice-sounding antenna array," *IEEE Antennas and Propagation Magazine*, vol. 56, no. 6, pp. 41–52, 2014.

[38] A. Santori, J. Barrere, G. Chabriel, C. Jauffret, and D. Medynski, "Sensor self-localization for antenna arrays subject to bending and vibrations," *IEEE Transactions on Aerospace and Electronic Systems*, vol. 46, no. 2, pp. 884–898, 2010.

[39] R. Moore, "Modern coherent radar for ice-sheet sounding," *Antarctic Journal of the United States*, vol. 22, no. 5, pp. 83–84, 1987.

[40] K. Demarest, R. Garudachar, and R. Moore, "A modern radar for ice-sheet sounding," *Antarctic Journal of the United States*, vol. 23, no. 5, pp. 63–64, 1988.

[41] R. K. Moore, G. Raju, W. Xin, C. Davis, K. R. Demarest, and D. I. Rummer, "A 150-MHz coherent radar system (ice cap sounding)," in *Proceedings of the IEEE National Radar Conference*, 1989, pp. 42–47.

[42] C. Allen, B. Wohletz, and S. Gogineni, "Radar sounding of glaciers in Greenland," in *IGARSS '96. 1996 International Geoscience and Remote Sensing Symposium*, vol. 4, 1996, pp. 1932–1934 vol.4.

[43] S. Gogineni, T. Chuah, C. Allen, K. Jezek, and R. Moore, "An improved coherent radar depth sounder," *Journal of Glaciology*, vol. 44, no. 148, pp. 659–669, 1998.

[44] S. Gogineni, D. Tammana, D. Braaten, C. Leuschen, T. Akins, J. Legarsky, P. Kanagaratnam, J. Stiles, C. Allen, and K. Jezek, "Coherent radar ice thickness measurements over the Greenland ice sheet," *Journal of Glaciology*, vol. 106, no. D24, pp. 33,761–33,772, 2001.

[45] D. A. Braaten, S. P. Gogineni, D. Tammana, S. Namburi, J. Paden, and K. K. Gurumoorthy, "Improvement of radar ice-thickness measurements of Greenland outlet glaciers using SAR processing," *Annals of Glaciology*, vol. 35, p. 73–78, 2002.

[46] F. Rodriguez-Morales, P. Gogineni, K. Jezek, C. Allen, C. Leuschen, K. Marathe, V. Jara-Olivares, A. Hoch, J. Li, and J. Ledford, "Dual-frequency and multi-receiver radars for sounding and imaging polar ice sheets," in *7th European Conference on Synthetic Aperture Radar*, 2008, pp. 1–4.

[47] C. Allen, J. Paden, D. Dunson, and P. Gogineni, "Ground-based multi-channel synthetic-aperture radar for mapping the ice-bed interface," in *2008 IEEE Radar Conference*, 2008, pp. 1–6.

[48] Y. Rockah, H. Messer, and P. M. Schultheiss, "Localization performance of arrays subject to phase errors," *IEEE Transactions on Aerospace and Electronic Systems*, vol. 24, no. 4, pp. 402–410, 1988.

[49] A. L. Swindlehurst and T. Kailath, "A performance analysis of subspace-based methods in the presence of model error. II. multidimensional algorithms," *IEEE Transactions on Signal Processing*, vol. 41, no. 9, pp. 2882–2890, 1993.

[50] P. Snoeij and A. R. Vellekoop, "A statistical model for the error bounds of an active phased array antenna for SARapplications," *IEEE Transactions on Geoscience and Remote Sensing*, vol. 30, no. 4, pp. 736–742, 1992.

[51] C. Leuschen, S. Gogineni, and D. Tammana, "SAR processing of radar echo sounder data," in *Proc. IEEE Int. Geoscience and Rem. Sens. Symp. (IGARSS 2000) (Cat. No.00CH37120)*, vol. 6, 2000, pp. 2570–2572 vol.6.

[52] H. Van Trees, "Arrays and spatial filters," in *Optimum Array Processing*. John Wiley & Sons, Ltd, 2002, ch. 2, pp. 17–89.

[53] T. Moore, J. Paden, C. Leuschen, and F. Rodríguez-Morales, "Nonparametric array manifold calibration for ice sheet tomography," *IEEE Transactions on Geoscience and Remote Sensing*, pp. 1–1, 2021.

[54] T. Moore and J. Paden, "Array manifold calibration for multichannel radar ice sounders," in *Proc. IEEE Int. Geoscience and Rem. Sens. Symp. (IGARSS 2020)*, 2020, pp. 92–95.

[55] H. Van Trees, "Optimum waveform estimation," in *Optimum Array Processing*. John Wiley & Sons, Ltd, 2002, ch. 6, pp. 428–709.

[56] B. D. Van Veen and K. M. Buckley, "Beamforming: a versatile approach to spatial filtering," *IEEE ASSP Magazine*, vol. 5, no. 2, pp. 4–24, 1988.

[57] J. Capon, "High-resolution frequency-wavenumber spectrum analysis," *Proceedings of the IEEE*, vol. 57, no. 8, pp. 1408–1418, 1969.

[58] J. Li, J. Paden, C. Leuschen, F. Rodriguez-Morales, R. D. Hale, E. J. Arnold, R. Crowe, D. Gomez-Garcia, and P. Gogineni, "High-altitude radar measurements of ice thickness over the Antarctic and Greenland ice sheets as a part of operation icebridge," *IEEE Transactions on Geoscience and Remote Sensing*, vol. 51, no. 2, pp. 742–754, 2012.

[59] B. Miller, B. Randolph, J. Paden, and E. Arnold, "Effects of known and unknown antenna position errors on MVDR," in *2019 IEEE International Symposium on Phased Array Systems and Technology*. IEEE, 2019.

[60] A. Moreira, P. Prats-Iraola, M. Younis, G. Krieger, I. Hajnsek, and K. P. Papathanassiou, "A tutorial on synthetic aperture radar," *IEEE Geoscience and Remote Sensing Magazine*, vol. 1, no. 1, pp. 6–43, 2013.

[61] H. A. Zebker and R. M. Goldstein, "Topographic mapping from interferometric synthetic aperture radar observations," *Journal of Geophysical Research: Solid Earth*, vol. 91, no. B5, pp. 4993–4999, 1986.

[62] N. Marechal, "Tomographic formulation of interferometric SAR for terrain elevation mapping," *IEEE Transactions on Geoscience and Remote Sensing*, vol. 33, no. 3, pp. 726–739, 1995.

[63] A. Reigber and A. Moreira, "First demonstration of airborne SAR tomography using multibaseline L-band data," *IEEE Transactions on Geoscience and Remote Sensing*, vol. 38, no. 5, pp. 2142–2152, 2000.

[64] G. Fornaro and V. Pascazio, "Chapter 20 - SAR interferometry and tomography: Theory and applications," in *Academic Press Library in Signal Processing: Volume 2*, ser. Academic Press Library in Signal Processing, N. D. Sidiropoulos, F. Gini, R. Chellappa, and S. Theodoridis, Eds. Elsevier, 2014, vol. 2, pp. 1043 – 1117.

[65] R. Schmidt, "Multiple emitter location and signal parameter estimation," *IEEE Transactions on Antennas and Propagation*, vol. 34, no. 3, pp. 276–280, 1986.

[66] H. Van Trees, "Parameter estimation II," in *Optimum Array Processing*. John Wiley & Sons, Ltd, 2002, ch. 9, pp. 1139–1317.

[67] P. Stoica and A. Nehorai, "MUSIC, Maximum Likelihood, and Cramér-Rao bound," *IEEE Transactions on Acoustics, Speech, and Signal Processing*, vol. 37, no. 5, pp. 720–741, 1989.

[68] H. Van Trees and K. Bell, "General Gaussian Estimation," in *Detection, Estimation, and Modulation. Part I: Detection, Estimation, and Filtering Theory*, 2nd ed. John Wiley & Sons, Ltd, 2013, ch. 5, pp. 400–510.

[69] S. Haykin, *Wiener Filters*, 4th ed. Prentice Hall, Inc, 2002, ch. 2, pp. 94–125.

[70] D. Manolakis, V. Ingle, and S. Kogon, *Array Processing*. Artech House Publishing, 2005, ch. 11, pp. 621–684.

[71] W. Stutzmann and G. Thiele, *Antenna Fundamentals*, 3rd ed. John Wiley & Sons, Inc, 2013, ch. 2, pp. 23–69.

[72] ——, *Array Antennas*, 3rd ed. John Wiley & Sons, Inc, 2013, ch. 8, pp. 271–335.

[73] I. Gupta and A. Ksienski, "Effect of mutual coupling on the performance of adaptive arrays," *IEEE Transactions on Antennas and Propagation*, vol. 31, no. 5, pp. 785–791, 1983.

[74] A. T. D. Hoop, "The N-port receiving antenna and its equivalent electrical network," *Philips Research Reports*, vol. 30, pp. 302–315, 1975.

[75] C. Craeye and D. González-Ovejero, "A review on array mutual coupling analysis," *Radio Science*, vol. 46, no. 02, pp. 1–25, 2011.

[76] H. Van Trees, "Characterization of space-time processes," in *Optimum Array Processing.* John Wiley & Sons, Ltd, 2002, ch. 5, pp. 332–427.

[77] H. Van Trees and K. Bell, "Classical Parameter Estimation," in *Detection, Estimation, and Modulation. Part I: Detection, Estimation, and Filtering Theory*, 2nd ed. John Wiley & Sons, Ltd, 2013, ch. 4, pp. 230–399.

[78] S. Fortunati, F. Gini, M. S. Greco, and C. D. Richmond, "Performance bounds for parameter estimation under misspecified models: Fundamental findings and applications," *IEEE Signal Processing Magazine*, vol. 34, no. 6, pp. 142–157, 2017.

[79] M. Viberg and A. L. Swindlehurst, "A Bayesian approach to auto-calibration for parametric array signal processing," *IEEE Trans. Signal Process.*, vol. 42, no. 12, pp. 3495–3507, 1994.

[80] B. Flanagan, "Self calibration of antenna arrays with large perturbation errors," Ph.D. dissertation, George Mason University, 2000.

[81] B. Flanagan and K. Bell, "Array self-calibration with large position errors," *Signal Processing*, vol. 81, no. 10, pp. 2201–2214, 2001.

[82] N. Fistas and A. Manikas, "A new general global array calibration method," in *Proceedings of ICASSP '94. IEEE International Conference on Acoustics, Speech and Signal Processing*, vol. iv, 1994, pp. IV/73–IV/76 vol.4.

[83] A. J. Weiss and B. Friedlander, "Algorithm for steering vector estimation using second order moments," in *Conference Record of The Twenty-Ninth Asilomar Conference on Signals, Systems and Computers*, vol. 2, 1995, pp. 782–786 vol.2.

[84] M. Viberg, M. Lanne, and A. Lundgren, "Calibration in array processing," in *Classical and Modern Direction-of-Arrival Estimation*, T. Tuncer and B. Friedlander, Eds. Elsevier, 2009, ch. 3, pp. 39–124.

[85] T. Akins, S. Gogineni, P. Kanagaratnam, J. Legarsky, and A. Wong, "Airborne ice thickness measurements: status report and future work," in *Program for Arctic Regional Climate Assessment (PARCA): Greenland Science and Planning Meeting*, S. Gogineni, R. H. Thomas, and W. Abdalati, Eds. National Aeronautics and Space Administration, 1999.

[86] E. Arnold, C. Leuschen, F. Rodriguez-Morales, J. Li, J. Paden, R. Hale, and S. Keshmiri, "CReSIS airborne radars and platforms for ice and snow sounding," *Annals of Glaciology*, pp. 1–10, 2019.

[87] R. Hale, E. Arnold, K. Balaji, W. Liu, K. Po, and A. Thakur, "Aerodynamic and structural analysis of the P-3 antenna assembly," Technical Report, The University of Kansas, February 2010.

[88] CReSIS, *Radar Depth Sounder Data*. Lawrence KS, USA. Digital Media, 2021, Accessed: January 1, 2021. [Online]. Available: http://data.cresis.ku.edu/.

[89] C. Porter, P. Morin, I. Howat, M. Noh, B. Bates, K. Peterman, S. Keesey, M. Schlenk, J. Gardiner, K. Tomko, M. Willis, C. Kelleher, M. Cloutier, E. Husby, S. Foga, H. Nakamura, M. Platson, M. W. Jr., C. Williamson, G. Bauer, J. Enos, G. Arnold, W. Kramer,

P. Becker, A. Doshi, C. D'Souza, P. Cummens, F. Laurier, and M. Bojesen, "ArcticDEM," *Harvard Dataverse, V1*, 2018.

[90] M.-J. Noh and I. M. Howat, "Automated stereo-photogrammetric DEM generation at high latitudes: Surface extraction with TIN-based search-space minimization (SETSM) validation and demonstration over glaciated regions," *GIScience & Remote Sensing*, vol. 52, no. 2, pp. 198–217, 2015.

[91] B. Raup, A. Racoviteanu, S. J. S. Khalsa, C. Helm, R. Armstrong, and Y. Arnaud, "The glims geospatial glacier database: A new tool for studying glacier change," *Global and Planetary Change*, vol. 56, no. 1, pp. 101–110, 2007, climate Change Impacts on Mountain Glaciers and Permafrost. [Online]. Available: https://www.sciencedirect.com/science/article/pii/S0921818106001597

[92] A. Arendt, A. Bliss, T. Bolch, J. Cogley, A. Gardner, J. Hagen, R. Hock, M. Huss, G. Kaser, C. Kienholz, W. Pfeffer, G. Moholdt, F. Paul, V. Radic, L. Andreassen, S. Bajracharya, N. Barrand, M. Beedle, E. Berthier, R. Bhambri, and I. Brown et al, *Randolph Glacier Inventory – A Dataset of Global Glacier Outlines: Version 5.0 [03 Arctic Canada (North)].* Boulder, Colorado USA. NASA National Snow and Ice Data Center Distributed Active Archive Center. Digital Media., 2015, Accessed: September 6, 2016. [Online]. Available: http://dx.doi.org/10.7265/N5V98602

[93] W. J. Bangs, "Array processing with generalized beamformers," Ph.D. dissertation, Yale University, 1971.

[94] Mathworks, *Matlab [computer software].* Mathwords, Inc. Digital Media, 2015, Version 2015b. [Online]. Available: https://www.mathworks.com/products/matlab.html.

[95] S. M. Kay, "Summary of Important PDFs," in *Fundamentals of Statistical Signal Processing: Detection Theory.* Prentice Hall, 1998, ch. 2, pp. 20–38.

[96] L. Scharf and B. Friedlander, "Matched subspace detectors," *IEEE Trans. Signal Process.*, vol. 42, no. 8, pp. 2146–2157, 1994.

[97] L. Scharf, "4.11. matched subspace filters," in *Statist. Signal Process.: Detect., Estimation, and Time Series Anal.* Addison-Wesley, Reading, PA, USA, 1991, ch. 4, pp. 145–147.

[98] O. Besson, L. Scharf, and F. Vincent, "Matched direction detectors and estimators for array processing with subspace steering vector uncertainties," *IEEE Trans. Signal Process.*, vol. 53, no. 12, pp. 4453–4463, 2005.

[99] O. Besson and L. Scharf, "Cfar matched direction detector," *IEEE Trans. Signal Process.*, vol. 54, no. 7, pp. 2840–2844, 2006.

[100] E. J. Kelly, "A Maximum-Likelihood Multiple-Hypothesis Testing Algorithm, with an application to monopulse data editing," MIT-LL, Tech. Rep., 1973.

[101] S. M. Kay, "Complex/vector extensions and array processing," in *Fundamentals of Statistical Signal Processing: Detection Theory.* Prentice Hall, 1998, ch. 2, pp. 473–535.

[102] W. Stutzmann and G. Thiele, *Antenna Theory and Design*, 3rd ed. John Wiley & Sons, Ltd.

[103] M. Sergolle, X. Castel, M. Himdi, P. Besnier, and P. Parneix, "Structural composite laminate materials with low dielectric loss: Theoretical model towards dielectric characterization," *Composites Part C: Open Access*, vol. 3, 2020. [Online]. Available: https://www.sciencedirect.com/science/article/pii/S2666682020300505

[104] *Dielectric Properties.* Evonik Industries, 2011, theodore, AL, USA. https://www.rohacell.com/en/down-loads/product-information. Accessed: Septem-

ber 2021. [Online]. Available: https://www.rohacell.com/en/down-loads/product-information/

[105] *Rohacell IG-F: Product Information.* Evonik Corporation, 2011, theodore, AL, USA. https://www.rohacell.com/en/down-loads/product-information. Accessed: September 2021. [Online]. Available: https://www.rohacell.com/en/down-loads/product-information/

[106] *Rohacell - The Dielectric Leader.* Evonik Corporation, 2020, theodore, AL, USA. https://www.rohacell.com/en/down-loads/product-information. Accessed: September 2021. [Online]. Available: https://www.rohacell.com/en/down-loads/product-information/

[107] K. Byers, "Integration of a 15-element, vhf bow-tie antenna array into an aerodynamic fairing on a nasa p-3 aircraft," Master's thesis, University of Kansas, Lawrence, KS, 2011.

[108] V. Berger, X. Mingze, M. Al-Ibadi, S. Chu, D. Crandall, J. Paden, and G. Fox, "Automated ice-bottom tracking of 2D and 3D ice radar imagery using Viterbi and TRW-S," *Journal of Selected Topics on Applied Earth Observation and Remote Sensing*, vol. 12, no. 9, pp. 3272–3285, 2019.

[109] S. M. Kay, "Generalized Matched Filter," in *Fundamentals of Statistical Signal Processing: Detection Theory.* Prentice Hall, 1998, ch. 4, pp. 94–140.

[110] H. Van Trees, "Parameter estimation I: Maximum likelihood," in *Optimum Array Processing.* John Wiley & Sons, Ltd, 2002, ch. 8, pp. 917–1138.

[111] S. Kay, "Cramér-Rao lower bound," in *Fundamentals of Statistical Signal Processing: Estimation Theory.* Upper Saddle River, New Jersey: Prentice Hall PTR, 1993, vol. I, ch. 15, pp. 27–77.

[112] H. Van Trees, "Appendix A: Matrix operations," in *Optimum Array Processing.* John Wiley & Sons, Ltd, 2002, pp. 1340–1406.

[113] H. Van Trees and K. Bell, "General Gaussian Estimation," in *Detection, Estimation, and Modulation. Part I: Detection, Estimation, and Filtering Theory*, 2nd ed. John Wiley & Sons, Ltd, 2013, ch. 5, p. 410, equation 5.75.

Appendix A

Optimal Beamformer Derivations

A.1 Problem Statement

Beamforming weight vectors are derived for an array of sensors that spatially samples a field presented by Q directional sources in the presence of observation noise. We assume the narrowband snapshot model in equation 2.1 restated here as

$$\mathbf{x}_m = \mathbf{A}(\mathbf{\Theta})\mathbf{s}_m + \mathbf{n}_m, \tag{A.1}$$

Where the terms have the same meanings as described in Chapter 2. We derive the optimal combining weights by treating sources as deterministic but unknown and regard $\mathbf{n}$ as a realization of a zero-mean random process with covariance $\mathbf{R}_n = E\left\{\mathbf{n}\mathbf{n}^H\right\}$. We seek an estimate of a source waveform, s_m, at the output of the beamformer. The general form of the beamformer output assumed in the derivations that follow is stated as:

$$y_m = \mathbf{w}^H\mathbf{x}_m. \tag{A.2}$$

A.2 Spatial Matched Filter

The spatial matched filter is sometimes referred to as the Maximum SNR beamformer [55], [56] because the weights are derived to maximize the signal-to-noise ratio at the output of array processor. To derive the spatial matched filter, we assume that a single plane wave ($Q = 1$) from a source of interest with an associated arrival angle θ_t is incident on the array

leading to the following model of our observation:

$$\mathbf{x}_m = \mathbf{a}(\theta_t)s_m + \mathbf{n}_m. \tag{A.3}$$

The spatial matched filter weights are given by the solution to the following optimization

$$\mathbf{w}_{MF} = \max_{\mathbf{w}} \left\{ SNR_{out} \right\}, \tag{A.4}$$

Where SNR_{out} denotes the signal to noise ratio at the beamformer output. Let P_s denote the average power of the source. Dropping the discrete time arguments (so the math reads more easily), the average power at the beamformer output is

$$\begin{aligned}
E\left\{y^*y\right\} &= E\left\{ \left(\mathbf{w}^H\mathbf{x}\right)^H \left(\mathbf{w}^H\mathbf{x}\right) \right\}, \\
&= E\left\{ \left(\mathbf{w}^H\left(\mathbf{a}(\theta_t)s + \mathbf{n}\right)\right)^H \left(\mathbf{w}^H\left(\mathbf{a}(\theta_t)s + \mathbf{n}\right)\right) \right\}, \\
&= E\left\{ \left(\mathbf{w}^H\mathbf{a}(\theta_t)s + \mathbf{w}^H\mathbf{n}\right)^H \left(\mathbf{w}^H\mathbf{a}(\theta_t)s + \mathbf{w}^H\mathbf{n}\right) \right\}, \\
&= E\left\{ \left(s^*\mathbf{a}^H(\theta_t)\mathbf{w} + \mathbf{n}^H\mathbf{w}\right) \left(\mathbf{w}^H\mathbf{a}(\theta_t)s + \mathbf{w}^H\mathbf{n}\right) \right\}, \\
&= E\left\{ s^*\mathbf{a}^H(\theta_t)\mathbf{w}\mathbf{w}^H\mathbf{a}(\theta_t)s + s^*\mathbf{a}(\theta_t)^H\mathbf{w}\mathbf{w}^H\mathbf{n} + \mathbf{n}^H\mathbf{w}\mathbf{w}^H\mathbf{a}(\theta_t)s + \mathbf{n}^H\mathbf{w}\mathbf{w}^H\mathbf{n} \right\}.
\end{aligned} \tag{A.5}$$

We simplify the expectations to obtain

$$\begin{aligned}
E\left\{y^*y\right\} &= E\left\{ s^*\mathbf{a}^H(\theta_t)\mathbf{w}\mathbf{w}^H\mathbf{a}(\theta_t)s + s^*\mathbf{a}^H(\theta_t)\mathbf{w}\mathbf{w}^H\mathbf{n} + \mathbf{n}^H\mathbf{w}\mathbf{w}^H\mathbf{a}(\theta_t)s + \mathbf{n}^H\mathbf{w}\mathbf{w}^H\mathbf{n} \right\}, \\
&= \underbrace{\mathbf{w}^H\mathbf{a}(\theta_t)P_s\mathbf{a}^H(\theta_t)\mathbf{w}}_{\text{signal}} + \underbrace{\mathbf{w}^H\mathbf{R}_n\mathbf{w}}_{\text{noise}}.
\end{aligned} \tag{A.6}$$

Using the signal and noise terms from Equation A.6 and letting $\mathbf{R}_s = P_s\mathbf{a}(\theta_t)\mathbf{a}^H(\theta_t)$, we write the output SNR as the following ratio of two quadratic forms

$$SNR_{out} = \frac{\mathbf{w}^H\mathbf{R}_s\mathbf{w}}{\mathbf{w}^H\mathbf{R}_n\mathbf{w}} \tag{A.7}$$

And restate the optimization in A.4 as

$$\mathbf{w}_{MF} = \max_{\mathbf{w}} \left\{ \frac{\mathbf{w}^H\mathbf{R}_s\mathbf{w}}{\mathbf{w}^H\mathbf{R}_n\mathbf{w}} \right\}. \tag{A.8}$$

We solve Equation A.8 by taking a complex gradient with respect to $\mathbf{w}^H$ and solving for $\mathbf{w}$ at the critical point. Using the quotient rule we have the following

$$\frac{\partial SNR_{out}}{\partial \mathbf{w}^H} = \frac{\mathbf{R}_s\mathbf{w}\mathbf{w}^H\mathbf{R}_n\mathbf{w} - \mathbf{R}_n\mathbf{w}\mathbf{w}^H\mathbf{R}_s\mathbf{w}}{\left(\mathbf{w}^H\mathbf{R}_n\mathbf{w}\right)^2}. \tag{A.9}$$

Setting A.9 equal to zero leads to

$$\mathbf{R}_s\mathbf{w}\left(\mathbf{w}^H\mathbf{R}_n\mathbf{w}\right) = \mathbf{R}_n\mathbf{w}\left(\mathbf{w}^H\mathbf{R}_s\mathbf{w}\right). \tag{A.10}$$

We can divide through by $\mathbf{w}^H\mathbf{R}_n\mathbf{w}$ and write this form in terms of A.7 as

$$\mathbf{R}_s\mathbf{w} = \mathbf{R}_n\mathbf{w}SNR_{out}. \tag{A.11}$$

Finally we left multiply by the inverse $\mathbf{R}_n$ to obtain the expression below

$$\mathbf{R}_n^{-1}\mathbf{R}_s\mathbf{w} = SNR_{out}\mathbf{w}. \tag{A.12}$$

In this form we recognize that the spatial matched filter is an eigenvector of the matrix $\mathbf{R}_n^{-1}\mathbf{R}_s$. We simplify this further to garner some additional insight. If we assume the noise to be independent and identically distributed, we can rewrite the noise covariance as $\mathbf{R}_n = \sigma_n^2 I_P$

where I_p refers to the $P \times P$ identity matrix. Assuming a noise covariance of this form and expanding $\mathbf{R}_s$, we obtain the following

$$\frac{P_s}{\sigma_n^2}\mathbf{a}(\theta_t)\mathbf{a}^H(\theta_t)\mathbf{w} = SNR_{out}\mathbf{w}. \tag{A.13}$$

At this point we can recognize the input SNR on the left hand side of this expression (corresponding to the SNR on a single element). We restate the previous result and relate it to the orginal optimization criterion below:

$$\begin{aligned} \mathbf{a}(\theta_t)\mathbf{a}^H(\theta_t)\mathbf{w} &= \frac{SNR_{out}}{SNR_{in}}\mathbf{w}, \\ &\Downarrow \\ \mathbf{a}(\theta_t)\mathbf{a}^H(\theta_t)\mathbf{w}_{MF} &= \lambda_{max}\mathbf{w}_{MF} \end{aligned} \tag{A.14}$$

Hence the optimal weights are given by the eigenvector of the matrix $\mathbf{a}(\theta_t)\mathbf{a}^H(\theta_t)$ corresponding to the largest eigenvalue λ_{max}. The matrix $\mathbf{a}(\theta_t)\mathbf{a}^H(\theta_t)$ is the rank one positive semi-definite matrix whose only non-trivial eigenvalue corresponds to the eigenvector given by a unitary vector that is parallel to $\mathbf{a}(\theta_t)$. This is simply the normalized steering vector given by:

$$\frac{\mathbf{a}(\theta_t)}{\sqrt{\mathbf{a}^H(\theta_t)\mathbf{a}(\theta_t)}}. \tag{A.15}$$

Thus the spatial matched filter solution is the steering vector scaled by its Euclidean length

$$\mathbf{w}_{MF} = \frac{\mathbf{a}(\theta_t)}{\|\mathbf{a}(\theta_t)\|_2}. \tag{A.16}$$

We determine corresponding eigenvalue by substituting Equation A.16 into A.14 and assuming that the magnitude of any entry in $\mathbf{w}_{MF}$ is unity (i.e. $a_i^* a_i, 1 \leq i \leq P$).

$$\begin{aligned} \mathbf{a}(\theta_t)\mathbf{a}^H(\theta_t)\mathbf{w}_{MF} &= \lambda_{max}\mathbf{w}_{MF}, \\ \mathbf{a}(\theta_t)\mathbf{a}^H(\theta_t)\frac{\mathbf{a}(\theta_t)}{\|\mathbf{a}(\theta_t)\|_2} &= \lambda_{max}\mathbf{w}_{MF}, \\ \frac{\mathbf{a}(\theta_t)}{\|\mathbf{a}(\theta_t)\|_2}\mathbf{a}^H(\theta)\mathbf{a}(\theta) &= \lambda_{max}\mathbf{w}_{MF}, \\ P\mathbf{w}_{MF} &= \lambda_{max}\mathbf{w}_{MF}. \end{aligned} \tag{A.17}$$

From this expression we find that the largest eigenvalue (and equivalently the largest SNR improvement) is given by

$$\lambda_{max} = \frac{SNR_{out}^{max}}{SNR_{in}} = P. \tag{A.18}$$

This derivation confirms a well-known result for the maximum SNR improvement of P realized by the matched filter for the beamforming problem formulation. The result is consistent with the SNR improvement realized in the temporal problem which can be shown to be equal to the number of digital samples in the filter [109].

A.3 Minimum Power Distortionless Response Beamformer

Here we derive the MPDR beamformer using the array model in A.1 and the form of the beamformer output in A.2, restated here with discrete time dependence suppressed

$$\mathbf{x} = \mathbf{A}(\boldsymbol{\Theta})\mathbf{s} + \mathbf{n}, \tag{A.19a}$$

$$y = \mathbf{w}^H\mathbf{x}. \tag{A.19b}$$

Following [55], we treat sources as deterministic and unknown and assume $\mathbf{n}$ to be a zero-mean random vector with covariance $\mathbf{R}_n = E\left\{\mathbf{n}\mathbf{n}^H\right\}$. In the MVDR and MPDR formulations, the vector $\mathbf{n}$ contains noise plus interference. We seek a minimum variance and

unbiased estimate of a signal s_t which corresponds to a source with DOA θ_t.

$$\begin{aligned} \text{minimize:} \quad & \mathbf{w}^H \mathbf{R}_\mathbf{x} \mathbf{w} \\ \text{subject to:} \quad & \mathbf{w}^H \mathbf{a}(\theta_t) = 1. \end{aligned} \tag{A.20}$$

The second statement in $A.20$ is the linear constraint that admits a non-trivial solution to the minimization of the quadratic form $\mathbf{w}^H \mathbf{R}_\mathbf{x} \mathbf{w}$. We can show that the distortionless constraint above ensures that the estimator of the source s_t will be unbiased.

We want to constrain our solution $\mathbf{w}$ such that $y = \hat{s}_t = \mathbf{w}^H \mathbf{x}$ is unbiased. As such, the estimator must satisfy the following

$$E\left\{\hat{s}_t\right\} = s_t. \tag{A.21}$$

We expand the expected value of the beamformer output as

$$\begin{aligned} E\left\{\hat{s}_t\right\} &= E\left\{\mathbf{w}^H \left(\mathbf{a}(\theta_t) s_t + \mathbf{n}\right)\right\}, \\ &= E\left\{\mathbf{w}^H \mathbf{a}(\theta_t) s_t + \mathbf{w}^H \mathbf{n}\right\}, \\ &= E\left\{\mathbf{w}^H \mathbf{a}(\theta_t) s_t\right\} + E\left\{\mathbf{w}^H \mathbf{n}\right\}, \\ &= \mathbf{w}^H \mathbf{a}(\theta_t) s_t. \end{aligned} \tag{A.22}$$

This leads us to the final statement

$$E\left\{\hat{s}_t\right\} = \mathbf{w}^H \mathbf{a}(\theta_t) s_t. \tag{A.23}$$

From this form we can conclude that for the unbiased estimator, the following must be true

$$\mathbf{w}^H \mathbf{a}(\theta_t) = 1. \tag{A.24}$$

Thus the *distortionless* constraint ensures an unbiased estimate of the signal of interest at

the output of the spatial filter. We solve the constrained minimization in A.20 using the method of Lagrange multipliers which leads to the following form of the cost function

$$J(\mathbf{w}) = \mathbf{w}^H \mathbf{R}_\mathbf{x} \mathbf{w} + \mathrm{Re}\left\{\lambda^* \left(\mathbf{w}^H \mathbf{a}(\theta_t) - 1\right)\right\}. \tag{A.25}$$

Taking the gradient with respect to $\mathbf{w}^H$

$$\frac{\partial J(\mathbf{w})}{\partial \mathbf{w}^H} = \mathbf{R}_\mathbf{x} \mathbf{w} + \lambda^* \mathbf{a}(\theta_t). \tag{A.26}$$

Setting this equal to zero gives the following

$$\mathbf{w} = -\lambda^* \mathbf{R}_\mathbf{x}^{-1} \mathbf{a}(\theta_t). \tag{A.27}$$

Taking the conjugate transpose both sides, we get

$$\mathbf{w}^H = -\lambda \mathbf{a}^H(\theta_t) \mathbf{R}_\mathbf{x}^{-1} \tag{A.28}$$

Where we have made the assumption that $\left(\mathbf{R}_\mathbf{x}^{-1}\right)^H = \mathbf{R}_\mathbf{x}^{-1}$. We right multiply by $\mathbf{a}(\theta_t)$ and apply the constraint to solve for λ

$$\begin{aligned} \mathbf{w}^H \mathbf{a}(\theta_t) &= -\lambda \mathbf{a}^H(\theta_t) \mathbf{R}_\mathbf{x}^{-1} \mathbf{a}(\theta_t) = 1, \\ \lambda &= \frac{1}{\mathbf{a}^H(\theta_t) \mathbf{R}_\mathbf{x}^{-1} \mathbf{a}(\theta_t)}. \end{aligned} \tag{A.29}$$

Thus

$$\mathbf{w}_{MPDR} = \frac{\mathbf{a}^H(\theta_t) \mathbf{R}_\mathbf{x}^{-1}}{\mathbf{a}^H(\theta_t) \mathbf{R}_\mathbf{x}^{-1} \mathbf{a}(\theta_t)}. \tag{A.30}$$

Appendix B

Derivation of Arrival Angle Estimators

B.1 MUltiple SIgnal Classification (MUSIC)

The MUSIC pseudospectrum is formulated here for the general linear model presented in Equation 2.1 and restated (with time dependence suppressed) as

$$\mathbf{x} = \mathbf{A}(\boldsymbol{\Theta})\mathbf{s} + \mathbf{n}, \tag{B.1}$$

Where the terms have the same meanings as described in Chapter 2. We suppress the angle dependence in $\mathbf{A}(\boldsymbol{\Theta})$ to simplify the discussion that follows. To formulate the MUSIC pseudospectral estimator, we state the following assumptions upfront:

A1: The number of spatial sources is strictly less than the number of sensors ($Q < P$) and the steering vectors are linearly independent. This ensures that $\mathbf{A}$ has full column rank and that the mapping of the signal subspace to its image in our observation space is injective. In other words, every $\mathbf{s} \in \mathbb{C}^{Q\times 1}$ in the signal subspace maps to a unique $\mathbf{As} \in \mathbb{C}^{P\times 1}$.

A2: The multichannel noise observation vector is a zero-mean random vector whose entries are independent and identically distributed. The distribution of $\mathbf{n}$ is not assumed however we require the following: $E\{\mathbf{n}\} = \mathbf{0}$, $E\left\{\mathbf{nn}^H\right\} = \sigma_n^2 I_P$, and $E\left\{\mathbf{nn}^T\right\} = 0 \times I_P$. The final assertion guarantees that the real and imaginary components of an arbitrary element of $\mathbf{n}$ will have the same second moments.

A3: The observation covariance matrix $E\left\{\mathbf{xx}^H\right\}$ is positive definite (hence non-singular).

MUSIC is referred to in literature as a subspace technique. This is because given Equation B.1, we can view the array observation model through the lens of linear algebra. Based on the first of our stated assumptions, we know that the steering vectors must form a basis for the image of the signal subspace in the observation space, $\mathbb{C}^{P\times 1}$. The image of the signal subspace is exactly equal to the column space $\mathrm{C}(\mathbf{A}) \subseteq \mathbb{C}^{P\times 1}$ and in the absence of observation noise $\mathbf{x} \in \mathrm{C}(\mathbf{A})$.

Given the initial assumptions, the array covariance matrix takes the following form

$$\mathbf{R}_{\mathbf{x}} = \mathbf{A}\mathbf{R}_{\mathbf{s}}\mathbf{A}^H + \sigma_n^2 I_p. \tag{B.2}$$

Here $\mathbf{R}_{\mathbf{s}} \in \mathbb{C}^{Q\times Q}$ is assumed to be a positive definite matrix defined as

$$\mathbf{R}_{\mathbf{s}} = E\left\{\mathbf{s}\mathbf{s}^H\right\}. \tag{B.3}$$

The $P \times P$ matrix $\mathbf{A}\mathbf{R}_{\mathbf{s}}\mathbf{A}^H$ is a positive semi-definite matrix with Q non-trivial eigenvalues. The observation covariance in Equation B.2 is a non-singular $P \times P$ Hermitian matrix from which we can conclude that there exists a set of P orthonormal eigenvectors whose corresponding eigenvalues are all real and non-trivial.

If we assume the sources to be uncorrelated, we may write $\mathbf{R}_{\mathbf{s}}$ as a diagonal matrix whose main diagonal contains the source powers:

$$\mathbf{R}_{\mathbf{s}} = \begin{pmatrix} p_1 & 0 & \dots & 0 \\ 0 & p_2 & \dots & 0 \\ \vdots & \vdots & \ddots & \vdots \\ 0 & 0 & \dots & p_q \end{pmatrix}. \tag{B.4}$$

We can then express $\mathbf{A}\mathbf{R}_\mathbf{s}\mathbf{A}^H$ as the following weighted sum of Q rank-one matrices

$$\mathbf{A}\mathbf{R}_\mathbf{s}\mathbf{A}^H = \sum_{i=1}^{Q} p_i \mathbf{a}_i \mathbf{a}_i^H. \tag{B.5}$$

The matrix $\mathbf{A}\mathbf{R}_\mathbf{s}\mathbf{A}^H$ has Q nontrivial eigenvalues associated with Q principal eigenvectors and $Q - P$ trivial eigenvalues whose corresponding eigenvectors are an orthonormal set and orthogonal to each $\mathbf{a}_i$. When $\mathbf{R}_\mathbf{x}$ can be written in the following form

$$\mathbf{R}_\mathbf{x} = \sum_{i=1}^{Q} p_i \mathbf{a}_i \mathbf{a}_i^H + \sigma_n^2 I_p, \tag{B.6}$$

Then the eigenvectors of $\mathbf{R}_\mathbf{x}$ are the eigenvectors of $\mathbf{A}\mathbf{R}_\mathbf{s}\mathbf{A}^H$. Let $\mathbf{u}_i$ be the i^{th} principal eigenvector of $\mathbf{R}_\mathbf{x}$ with eigenvalue λ_i. From the eigenequation we can write the following

$$\mathbf{R}_\mathbf{x}\mathbf{u}_i = \lambda_i \mathbf{u}_i. \tag{B.7}$$

By definition $\mathbf{u}_i$ is a principal eigenvector of $\mathbf{A}\mathbf{R}_\mathbf{s}\mathbf{A}^H$ with a corresponding eigenvalue λ_i^s that is not equal to λ_i. Equation B.7 can be rewritten as

$$\begin{aligned}
\mathbf{R}_\mathbf{x}\mathbf{u}_i = \left(\mathbf{A}\mathbf{R}_\mathbf{s}\mathbf{A}^H + \sigma_n^2 I_p\right)\mathbf{u}_i &= \lambda_i \mathbf{u}_i, \\
\mathbf{A}\mathbf{R}_\mathbf{s}\mathbf{A}^H\mathbf{u}_i + \sigma_n^2\mathbf{u}_i &= \lambda_i \mathbf{u}_i, \\
\lambda_i^s\mathbf{u}_i + \sigma_n^2\mathbf{u}_i &= \lambda_i \mathbf{u}_i, \\
\left(\lambda_i^s + \sigma_n^2\right)\mathbf{u}_i &= \lambda_i \mathbf{u}_i.
\end{aligned} \tag{B.8}$$

Hence the eigenvalues of $\mathbf{R}_\mathbf{x}$ are given by

$$\lambda_i = \begin{cases} \lambda_i^s + \sigma_n^2, & i = 1, \ldots, Q, \\ \sigma_n^2, & i = Q+1, \ldots, P. \end{cases} \tag{B.9}$$

Based on the orthogonality of the eigenvectors, we can write the eigenexpansion of $\mathbf{R}_\mathbf{x}$ as

the following sum of orthogonal subspaces

$$\mathbf{R_x} = \mathbf{U}\boldsymbol{\Lambda}\mathbf{U}^H = \mathbf{U}_s\boldsymbol{\Lambda}_s\mathbf{U}_s^H + \mathbf{U}_n\boldsymbol{\Lambda}_n\mathbf{U}_n^H. \tag{B.10}$$

The matrix $\mathbf{U}_s \in \mathbb{C}^{P\times Q}$ is the matrix whose columns span the signal subspace and takes the following form

$$\mathbf{U}_s = \left[\mathbf{u}_1^s, \ldots, \mathbf{u}_Q^s\right], \tag{B.11}$$

And $\boldsymbol{\Lambda}_s$ is the $Q \times Q$ matrix of eigenvalues

$$\boldsymbol{\Lambda}_s = \operatorname{diag}\left[\lambda_1^s + \sigma_n^2, \ldots, \lambda_Q^s + \sigma_n^2\right]. \tag{B.12}$$

The matrix of orthonormal noise eigenvectors are stored in $\mathbf{U_n} \in \mathbb{C}^{P\times(P-Q)}$ which takes the general form

$$\mathbf{U}_n = \left[\mathbf{u}_1^n, \ldots, \mathbf{u}_{P-Q}^n\right], \tag{B.13}$$

And maps to the eigenvalues

$$\boldsymbol{\Lambda}_n = \sigma_n^2 I_{P-Q}. \tag{B.14}$$

From here we can note that there will be a noise component in the signal subspace but more importantly the noise subspace contains no signal contribution. Hence we can write the following statement

$$\mathbf{R_x}\mathbf{U}_n = \mathbf{A}\mathbf{R_s}\mathbf{A}^H\mathbf{U}_n + \sigma_n^2 I_p\mathbf{U}_n = \sigma_n^2\mathbf{U}_n, \tag{B.15}$$

From which we can conclude

$$\mathbf{A}^H\mathbf{u}_i^n = \mathbf{0} \quad \forall \quad \mathbf{u}_i^n \in \mathbf{U}_n. \tag{B.16}$$

Therefore the vectors in $\mathbf{U}_n$ span the left null space of $\mathbf{A}$ and we may write

$$\operatorname{span}\left\{\mathbf{a}_1, \ldots, \mathbf{a}_Q\right\} \perp \operatorname{span}\left\{\mathbf{u}_1^n, \ldots, \mathbf{u}_{P-Q}^n\right\}. \tag{B.17}$$

Also we know that the Hermitian symmetry of $\mathbf{AR_s A}^H$ and $\mathbf{R_x}$ ensures the orthogonality of all of the eigenvectors thus we may equivalently write

$$\text{span}\left\{\mathbf{u}_1^s, \ldots, \mathbf{u}_Q^s\right\} \perp \text{span}\left\{\mathbf{u}_1^n, \ldots, \mathbf{u}_{P-Q}^n\right\}. \tag{B.18}$$

From Equations B.17 and B.18 we can infer that the principal eigenvectors span the signal subspace. Following the rationale outlined above, we conclude that

$$\|\mathbf{U}_n \mathbf{a}_i\|^2 = 0, \quad i = 1, \ldots, Q. \tag{B.19}$$

Restoring the θ dependence of the steering vectors, we state the MUSIC pseudospectrum as the following one-dimensional function of the DOA as

$$S_{music}(\theta) = \frac{1}{\mathbf{a}^H(\theta)\mathbf{U}_n\mathbf{U}_n^H\mathbf{a}(\theta)}. \tag{B.20}$$

This form will produce large peaks when a steering vector under test is orthogonal (or at least nearly orthogonal) to the noise subspace.

B.2 Maximum Likelihood Estimator

We derive a Maximum Likelihood Estimator of parameters of the linear model presented in Equation 2.2 and restated here:

$$\mathbf{X} = \mathbf{A}(\boldsymbol{\Theta})\mathbf{S} + \mathbf{N}, \tag{B.21}$$

Whose terms are given by

$$\mathbf{X} = \Big[\mathbf{x}_1, \ldots, \mathbf{x}_M\Big], \tag{B.22a}$$

$$\mathbf{A}(\boldsymbol{\Theta}) = \Big[\mathbf{a}(\theta_1), \ldots, \mathbf{a}(\theta_Q)\Big], \tag{B.22b}$$

$$\mathbf{N} = \Big[\mathbf{n}_1, \ldots, \mathbf{n}_M\Big], \tag{B.22c}$$

$$\mathbf{S} = \Big[\mathbf{s}_1, \ldots, \mathbf{s}_M\Big]. \tag{B.22d}$$

Here derive Maximum Likelihood Estimates of the following parameters of the linear model

1. The noise power σ_n^2,
2. The set of bearing angles, $\boldsymbol{\Theta} = [\theta_1, \ldots, \theta_Q]^T$,
3. The source signals $\mathbf{S}$.

We must first determine the distribution of $\mathbf{X}$ conditioned on one of the aforementioned unknowns. To do this, we state a set of assumptions up front

A1 : The linear model is overdetermined, hence $Q < P$,

A2 : The columns of $\mathbf{A}(\boldsymbol{\Theta})$ are linearly independent,

A3 : The noise process $\mathbf{N}$ is an ergodic and stationary complex Gaussian random process of zero mean and covariance $\sigma_n^2 \mathcal{I}_P$,

A4 : The noise snapshots are statistically independent, $p(\mathbf{n}_i, \mathbf{n}_j) = p(\mathbf{n}_i)p(\mathbf{n}_j)$,

A5 : Sources are modeled as deterministic but unknown,

A6 : The number of sources is known.

The Maximum Likelihood Estimator is derived from the density of $\mathbf{X}$ conditioned on an unknown parameter. A snapshot of array data is regarded as an observation of a deterministic

signal in the presence of observation noise. Hence we consider $\mathbf{x}_m$ to be a complex Gaussian random vector with mean $\boldsymbol{\mu}_{\mathbf{x}m} = \mathbf{A}(\boldsymbol{\Theta})\mathbf{s}_m$ and covariance $\sigma_n^2\mathcal{I}_P$, in other words $\mathbf{x}_m \sim (\boldsymbol{\mu}_{\mathbf{x}}, \sigma_n^2\mathcal{I}_P)$. The distribution of $\mathbf{x}_m$ conditionally distributed on the directional sources and noise variance is

$$p\left(\mathbf{x}_m; \boldsymbol{\Theta}, \mathbf{s}_m, \sigma_n^2\right) = \pi^{-P}\sigma_n^{-2P} \exp\left[-\frac{1}{\sigma_n^2} \left\|\mathbf{x}_m - \mathbf{A}(\boldsymbol{\Theta})\mathbf{s}_m\right\|^2 \right], \tag{B.23}$$

Where the operator $\| \|^2$ gives the square of the Euclidean norm (equivalent to the inner product of its argument).

From the independence of the snapshots of $\mathbf{N}$, we assume that the snapshots of $\mathbf{X}$ are also independent. We then write the distribution of $\mathbf{X}$ as a joint probability of the snapshots which becomes a product of the marginals based on the independence of adjacent snapshots:

$$\begin{aligned} p\left(\mathbf{X}; \boldsymbol{\Theta}, \mathbf{S}, \sigma_n^2\right) &= p\left(\left(\mathbf{x}_1; \boldsymbol{\Theta}, \mathbf{s}_1, \sigma_n^2\right), \ldots, \left(\mathbf{x}_M; \boldsymbol{\Theta}, \mathbf{s}_M, \sigma_n^2\right)\right), \\ &= \prod_{i=1}^{M} p\left(\mathbf{x}_i; \boldsymbol{\Theta}, \mathbf{s}_i, \sigma_n^2\right), \\ &= \pi^{-MP}\sigma_n^{-2MP} \prod_{i=1}^{M} \exp\left[-\frac{1}{\sigma_n^2} \left\|\mathbf{x}_i - \mathbf{A}(\boldsymbol{\Theta})\mathbf{s}_i\right\|^2 \right], \\ &= \pi^{-MP}\sigma_n^{-2MP} \exp\left[-\frac{1}{\sigma_n^2} \sum_{i=1}^{M} \left\|\mathbf{x}_i - \mathbf{A}(\boldsymbol{\Theta})\mathbf{s}_i\right\|^2 \right]. \end{aligned} \tag{B.24}$$

Define the log likelihood function to be the natural logarithm of the conditional density determined above,

$$\begin{aligned} L\left(\mathbf{X}; \boldsymbol{\Theta}, \mathbf{S}, \sigma_n^2\right) &= \ln p\left(\mathbf{X}; \boldsymbol{\Theta}, \mathbf{S}, \sigma_n^2\right), \\ &= -MP\ln(\pi) - MP\ln(\sigma_n^2) - \frac{1}{\sigma_n^2} \sum_{i=1}^{M} \left\|\mathbf{x}_i - \mathbf{A}(\boldsymbol{\Theta})\mathbf{s}_i\right\|^2. \end{aligned} \tag{B.25}$$

From this point forward, we ignore the constant term $-MP\ln(\pi)$ since it has no bearing on

the maximization and use the following expression for $L\left(\mathbf{\Theta}, \mathbf{S}, \sigma_n^2; \mathbf{X}\right)$

$$L\left(\mathbf{\Theta}, \mathbf{S}, \sigma_n^2; \mathbf{X}\right) = -MP\ln(\sigma_n^2) - \frac{1}{\sigma_n^2}\sum_{i=1}^{M}\left\|\mathbf{x}_i - \mathbf{A}(\mathbf{\Theta})\mathbf{s}_i\right\|^2. \tag{B.26}$$

B.2.1 Maximum Likelihood Estimator of Noise Power

The Maximum Likelihood Estimate of σ_n^2 is determined by solving the following maximization problem

$$\hat{\sigma}_n^2 = \max_{\sigma_n^2} \frac{\partial L\left(\mathbf{\Theta}, \mathbf{S}, \sigma_n^2; \mathbf{X}\right)}{\partial \sigma_n^2}. \tag{B.27}$$

We solve this maximization by differentiating (B.26), setting it equal to zero and solving for the parameter of interest σ_n^2

$$\frac{\partial L\left(\mathbf{\Theta}, \mathbf{S}, \sigma_n^2; \mathbf{X}\right)}{\partial \sigma_n^2} = \frac{-2MP}{\sigma_n} + \frac{2}{\sigma_n^3}\sum_{i=1}^{M}\left\|\mathbf{x}_i - \mathbf{A}(\mathbf{\Theta})\mathbf{s}_i\right\|^2. \tag{B.28}$$

Setting this equal to zero and solving for σ_n^2 we have the following ML estimator for the noise variance

$$\hat{\sigma}_n^2 = \frac{1}{MP}\sum_{i=1}^{M}\left\|\mathbf{x}_i - \mathbf{A}(\mathbf{\Theta})\mathbf{s}_i\right\|^2. \tag{B.29}$$

We substitute this solution into $L\left(\mathbf{X}; \mathbf{\Theta}, \mathbf{S}, \sigma_n^2\right)$ to eliminate σ_n^2 from our expression, leaving the likelihood of an observation matrix $\mathbf{X}$ conditioned on $\mathbf{\Theta}$ and $\mathbf{S}$

$$L\left(\mathbf{\Theta}, \mathbf{S}; \mathbf{X}\right) = -MP\ln\left[\frac{1}{MP}\sum_{i=1}^{M}\left\|\mathbf{x}_i - \mathbf{A}(\mathbf{\Theta})\mathbf{s}_i\right\|^2\right] - MP. \tag{B.30}$$

This expression is a monotonically *decreasing* function (based on the negative scaling) that is maximized when the argument of the natural logarithm is minimized. Hence the following

form is an equivalent likelihood function

$$L\left(\boldsymbol{\Theta}, \mathbf{S}; \mathbf{X}\right) = \frac{1}{MP} \sum_{i=1}^{M} \left\|\mathbf{x}_i - \mathbf{A}(\boldsymbol{\Theta})\mathbf{s}_i\right\|^2 . \tag{B.31}$$

B.2.2 Maximum Likelihood Estimator of Waveform

The ML estimate of $\mathbf{s}_i$ is obtained from a ML estimate of the $\mathbf{S}$ matrix, found by minimizing the cost function $L\left(\boldsymbol{\Theta}, \mathbf{S}; \mathbf{X}\right)$ as defined in (B.31) with respect to $\mathbf{S}$. This is stated as the following minimization problem (where the $\frac{1}{MP}$ may be ignored)

$$\hat{\mathbf{S}} = \min_{\mathbf{S}} \left\{ \sum_{i=1}^{M} \left\|\mathbf{x}_i - \mathbf{A}(\boldsymbol{\Theta})\mathbf{s}_i\right\|^2 \right\}. \tag{B.32}$$

The solution of (B.32) is one that minimizes a for each single snapshot. We write this likelihood as

$$L\left(\boldsymbol{\Theta}, \mathbf{s}_i; \mathbf{x}_i\right) = \left\|\mathbf{x}_i - \mathbf{A}(\boldsymbol{\Theta})\mathbf{s}_i\right\|^2 . \tag{B.33}$$

Thus to solve (B.32), we first solve the following

$$\hat{\mathbf{s}}_i = \min_{\mathbf{s}_i} L\left(\boldsymbol{\Theta}, \mathbf{s}_i; \mathbf{x}_i\right) = \min_{\mathbf{s}_i} \left\{ \left\|\mathbf{x}_i - \mathbf{A}(\boldsymbol{\Theta})\mathbf{s}_i\right\|^2 \right\}. \tag{B.34}$$

$L\left(\boldsymbol{\Theta}, \mathbf{s}_i; \mathbf{x}_i\right)$ has a quadratic form which we minimize by differentiating the expression with respect to our parameter of interest, setting it equal to zero and solving for a ML estimator. We solve the partial derivative with respect to $\mathbf{s}_i^H$ to simplify the solution for $\mathbf{s}_i$.

$$\begin{aligned}\frac{\partial L\left(\boldsymbol{\Theta}, \mathbf{s}_i; \mathbf{x}_i\right)}{\partial \mathbf{s}^H} &= \frac{\partial}{\partial \mathbf{s}^H}\left(\left(\mathbf{x}_i - \mathbf{A}(\boldsymbol{\Theta})\mathbf{s}_i\right)^H \left(\mathbf{x}_i - \mathbf{A}(\boldsymbol{\Theta})\mathbf{s}_i\right) \right), \\ &= \frac{\partial}{\partial \mathbf{s}^H}\Bigg(\mathbf{x}_i^H\mathbf{x}_i - \mathbf{s}_i^H\mathbf{A}^H(\boldsymbol{\Theta})\mathbf{x}_i - \dots \\ &\qquad\qquad \mathbf{x}_i^H\mathbf{A}(\boldsymbol{\Theta})\mathbf{s}_i + \mathbf{s}_i^H\mathbf{A}^H(\boldsymbol{\Theta})\mathbf{A}(\boldsymbol{\Theta})\mathbf{s}_i \Bigg), \\ &= -\mathbf{A}^H(\boldsymbol{\Theta})\mathbf{x}_i + \mathbf{A}^H(\boldsymbol{\Theta})\mathbf{A}(\boldsymbol{\Theta})\mathbf{s}_i.\end{aligned}$$

Setting this expression equal to zero leads to

$$\begin{aligned}\mathbf{A}^H(\boldsymbol{\Theta})\mathbf{A}(\boldsymbol{\Theta})\mathbf{s}_i - \mathbf{A}^H(\boldsymbol{\Theta})\mathbf{x}_i &= 0, \\ \mathbf{A}^H(\boldsymbol{\Theta})\mathbf{A}(\boldsymbol{\Theta})\mathbf{s}_i &= \mathbf{A}^H(\boldsymbol{\Theta})\mathbf{x}_i.\end{aligned}$$

Here we acknowledge assumptions **A1** and A2 from which we conclude that the matrix $\mathbf{A}(\boldsymbol{\Theta})$ has full column rank (equal to Q). The product $\mathbf{A}^H(\boldsymbol{\Theta})\mathbf{A}(\boldsymbol{\Theta})$ is a $Q \times Q$ non-singular matrix with full rank. By definition this means that $\left(\mathbf{A}^H(\boldsymbol{\Theta})\mathbf{A}(\boldsymbol{\Theta})\right)^{-1}$ exists. Multiplying both sides by $\left(\mathbf{A}^H(\boldsymbol{\Theta})\mathbf{A}(\boldsymbol{\Theta})\right)^{-1}$, we find the well known Maximum Likelihood Estimator of $\mathbf{s}_i$ obtained by applying a pseudo-inverse to the observation

$$\hat{\mathbf{s}}_i = \left(\mathbf{A}^H(\boldsymbol{\Theta})\mathbf{A}(\boldsymbol{\Theta})\right)^{-1}\mathbf{A}^H(\boldsymbol{\Theta})\mathbf{x}_i. \tag{B.35}$$

From this, we write the ML estimate of $\mathbf{S}$ as

$$\hat{\mathbf{S}} = \left(\mathbf{A}^H(\boldsymbol{\Theta})\mathbf{A}(\boldsymbol{\Theta})\right)^{-1}\mathbf{A}^H(\boldsymbol{\Theta})\mathbf{X}. \tag{B.36}$$

We use the result in (B.35) to present a likelihood function of $\mathbf{X}$ conditioned on the unknown parameter $\boldsymbol{\Theta}$ by substituting this solution into (B.31)

$$\begin{aligned} L\Big(\boldsymbol{\Theta};\mathbf{X}\Big) &= L\Big(\boldsymbol{\Theta},\mathbf{S};\mathbf{X}\Big)\Big|_{\mathbf{s}_i=\hat{\mathbf{s}}_i} \\ &= \sum_{i=1}^{M} \left\|\mathbf{x}_i - \mathbf{A}(\boldsymbol{\Theta})\hat{\mathbf{s}}_i\right\|^2, \\ &= \sum_{i=1}^{M} \left\|\mathbf{x}_i - \mathbf{A}(\boldsymbol{\Theta})\left(\mathbf{A}^H(\boldsymbol{\Theta})\mathbf{A}(\boldsymbol{\Theta})\right)^{-1}\mathbf{A}^H(\boldsymbol{\Theta})\mathbf{x}_i\right\|^2. \end{aligned} \tag{B.37}$$

B.2.3 Maximum Likelihood Estimator of DOA

The likelihood determined above may now be solved for a MLE of $\boldsymbol{\Theta}$ as the solution to the minimization problem

$$\begin{aligned} \hat{\boldsymbol{\Theta}} &= \min_{\boldsymbol{\Theta}} \left\{ L\Big(\boldsymbol{\Theta};\mathbf{X}\Big)\right\}, \\ &= \min_{\boldsymbol{\Theta}} \left\{ \sum_{i=1}^{M} \left\|\mathbf{x}_i - \mathbf{A}(\boldsymbol{\Theta})\left(\mathbf{A}^H(\boldsymbol{\Theta})\mathbf{A}(\boldsymbol{\Theta})\right)^{-1}\mathbf{A}^H(\boldsymbol{\Theta})\mathbf{x}_i\right\|^2 \right\}. \end{aligned} \tag{B.38}$$

Here we introduce the projection matrix $\mathbf{P}_{\mathbf{A}(\boldsymbol{\Theta})}$ which projects a vector onto the subspace spanned by the columns of $\mathbf{A}(\boldsymbol{\Theta})$. We define this matrix as

$$\mathbf{P}_{\mathbf{A}(\boldsymbol{\Theta})} = \mathbf{A}(\boldsymbol{\Theta})\left(\mathbf{A}^H(\boldsymbol{\Theta})\mathbf{A}(\boldsymbol{\Theta})\right)^{-1}\mathbf{A}^H(\boldsymbol{\Theta}). \tag{B.39}$$

By definition, the matrix $\mathbf{P}^{\perp}_{\mathbf{A}(\boldsymbol{\Theta})}$ is the matrix that projects a vector onto the orthogonal compliment of the subspace spanned by $\mathbf{A}(\boldsymbol{\Theta})$. This projection matrix is defined as

$$\mathbf{P}^{\perp}_{\mathbf{A}(\boldsymbol{\Theta})} = \mathcal{I} - \mathbf{P}_{\mathbf{A}(\boldsymbol{\Theta})}. \tag{B.40}$$

Hence the ML estimate of $\boldsymbol{\Theta}$ is obtained by solving the following minimization problem

$$\hat{\boldsymbol{\Theta}} = \min_{\boldsymbol{\Theta}} \left\{ \sum_{i=1}^{M} \left\| \mathbf{P}^{\perp}_{\mathbf{A}(\boldsymbol{\Theta})} \mathbf{x}_i \right\|^2 \right\}, \tag{B.41}$$

Which is equivalent to the solution of the maximization problem stated as

$$\hat{\boldsymbol{\Theta}} = \max_{\boldsymbol{\Theta}} \left\{ \sum_{i=1}^{M} \left\| \mathbf{P}_{\mathbf{A}(\boldsymbol{\Theta})} \mathbf{x}_i \right\|^2 \right\}. \tag{B.42}$$

So an equivalent likelihood function is

$$L(\boldsymbol{\Theta}; \mathbf{X}) = \sum_{i=1}^{M} \left\| \mathbf{P}_{\mathbf{A}(\boldsymbol{\Theta})} \mathbf{x}_i \right\|^2. \tag{B.43}$$

This may be rewritten in terms of a sample covaraince matrix estimated from the array snapshots as

$$\mathbf{R} = \frac{1}{M} \sum_{i=1}^{M} \mathbf{x}_i \mathbf{x}_i^H. \tag{B.44}$$

We start by rewriting (B.43) in terms of the inner product as follows

$$\begin{aligned} L(\boldsymbol{\Theta}; \mathbf{X}) &= \sum_{i=1}^{M} \left\| \mathbf{P}_{\mathbf{A}(\boldsymbol{\Theta})} \mathbf{x}_i \right\|^2, \\ &= \sum_{i=1}^{M} \left(\mathbf{P}_{\mathbf{A}(\boldsymbol{\Theta})} \mathbf{x}_i \right)^H \left(\mathbf{P}_{\mathbf{A}(\boldsymbol{\Theta})} \mathbf{x}_i \right), \\ &= \sum_{i=1}^{M} \mathbf{x}_i^H \mathbf{P}^H_{\mathbf{A}(\boldsymbol{\Theta})} \mathbf{P}_{\mathbf{A}(\boldsymbol{\Theta})} \mathbf{x}_i. \end{aligned} \tag{B.45}$$

Here we leverage the following two properties of the projection matrix. Consider an arbitrary projection matrix $\mathbf{P}_{\mathbf{A}} = \mathbf{A} \left(\mathbf{A}^H \mathbf{A} \right)^{-1} \mathbf{A}^H$, where $\mathbf{A}$ is a matrix with full column rank. Since $\mathbf{A}$ has full column rank, we know that $\mathbf{A}^H \mathbf{A}$ is a square invertible matrix with non-zero determinant. The follow properties of $\mathbf{P}_{\mathbf{A}}$ hold

1. The projection matrix $\mathbf{P}_{\mathbf{A}}$ is Hermitian, $\mathbf{P}_{\mathbf{A}} = \mathbf{P}_{\mathbf{A}}{}^H$.

Proof:

$$\begin{aligned}
\mathbf{P_A}^H &= \left(\mathbf{A}\left(\mathbf{A}^H\mathbf{A}\right)^{-1}\mathbf{A}^H\right)^H, \\
&= \left(\left(\mathbf{A}^H\mathbf{A}\right)^{-1}\mathbf{A}^H\right)^H\mathbf{A}^H, \\
&= \mathbf{A}\left(\left(\mathbf{A}^H\mathbf{A}\right)^{-1}\right)^H\mathbf{A}^H, \\
&= \mathbf{A}\left(\mathbf{A}^H\mathbf{A}\right)^{-1}\mathbf{A}^H, \\
&= \mathbf{P_A}
\end{aligned}$$

2. The projection matrix is idempotent, $\mathbf{P_A}\mathbf{P_A} = \mathbf{P_A}$.

   Proof:

$$\begin{aligned}
\mathbf{P_A}\mathbf{P_A} &= \mathbf{A}\left(\mathbf{A}^H\mathbf{A}\right)^{-1}\mathbf{A}^H\mathbf{A}\left(\mathbf{A}^H\mathbf{A}\right)^{-1}\mathbf{A}^H, \\
&= \mathbf{A}\left(\mathbf{A}^H\mathbf{A}\right)^{-1}\mathcal{I}\mathbf{A}^H, \\
&= \mathbf{A}\left(\mathbf{A}^H\mathbf{A}\right)^{-1}\mathcal{I}\mathbf{A}^H, \\
&= \mathbf{A}\left(\mathbf{A}^H\mathbf{A}\right)^{-1}\mathbf{A}^H, \\
&= \mathbf{P_A}.
\end{aligned}$$

Using the Hermitian and Idempotent properties of $\mathbf{P}_{\mathbf{A}(\mathbf{\Theta})}$, (B.45) simplifies further as follows

$$\begin{aligned}
L(\mathbf{\Theta};\mathbf{X}) &= \sum_{i=1}^{M}\mathbf{x}_i^H\mathbf{P}_{\mathbf{A}(\mathbf{\Theta})}^H\mathbf{P}_{\mathbf{A}(\mathbf{\Theta})}\mathbf{x}_i, \\
&= \sum_{i=1}^{M}\mathbf{x}_i^H\mathbf{P}_{\mathbf{A}(\mathbf{\Theta})}\mathbf{P}_{\mathbf{A}(\mathbf{\Theta})}\mathbf{x}_i, \\
&= \sum_{i=1}^{M}\mathbf{x}_i^H\mathbf{P}_{\mathbf{A}(\mathbf{\Theta})}\mathbf{x}_i.
\end{aligned} \tag{B.46}$$

Because multiplication by a scalar will not change the maximization of (B.46), an equivalent cost function is

$$L(\boldsymbol{\Theta}; \mathbf{X}) = \frac{1}{M} \sum_{i=1}^{M} \mathbf{x}_i^H \mathbf{P}_{\mathbf{A}(\boldsymbol{\Theta})} \mathbf{x}_i. \tag{B.47}$$

We now use an identity that relates the inner product of two arbitrary vectors $\mathbf{x}$ and $\mathbf{y}$ to the trace (sum of the diagonal elements) of their outer product. This is stated as

$$\mathbf{y}^T \mathbf{x} = \mathrm{tr}(\mathbf{x}\mathbf{y}^T). \tag{B.48}$$

We pull the $\frac{1}{M}$ inside the summation and use this identity to rewrite (B.47) as

$$\begin{aligned} L(\boldsymbol{\Theta}; \mathbf{X}) &= \sum_{i=1}^{M} \frac{1}{M} \mathbf{x}_i^H \mathbf{P}_{\mathbf{A}(\boldsymbol{\Theta})} \mathbf{x}_i, \\ &= \sum_{i=1}^{M} \mathrm{tr}\left(\frac{1}{M} \mathbf{P}_{\mathbf{A}(\boldsymbol{\Theta})} \mathbf{x}_i \mathbf{x}_i^H \right), \\ &= \mathrm{tr}\left(\frac{1}{M} \mathbf{P}_{\mathbf{A}(\boldsymbol{\Theta})} \mathbf{x}_1 \mathbf{x}_1^H \right) + \ldots + \mathrm{tr}\left(\frac{1}{M} \mathbf{P}_{\mathbf{A}(\boldsymbol{\Theta})} \mathbf{x}_M \mathbf{x}_M^H \right). \end{aligned} \tag{B.49}$$

Finally we recognize an important property of the trace that allows us to express the sum of traces as the trace of a sum. For two arbitrary square matrices $\mathbf{A}$ and $\mathbf{B}$,

$$\mathrm{tr}(\mathbf{A}) + \mathrm{tr}(\mathbf{B}) = \mathrm{tr}(\mathbf{A} + \mathbf{B}). \tag{B.50}$$

Hence (B.49) is rewritten as

$$\begin{aligned} L(\boldsymbol{\Theta}; \mathbf{X}) &= \mathrm{tr}\left(\frac{1}{M} \mathbf{P}_{\mathbf{A}(\boldsymbol{\Theta})} \mathbf{x}_1 \mathbf{x}_1^H \right) + \ldots + \mathrm{tr}\left(\frac{1}{M} \mathbf{P}_{\mathbf{A}(\boldsymbol{\Theta})} \mathbf{x}_M \mathbf{x}_M^H \right), \\ &= \mathrm{tr}\left(\sum_{i=1}^{M} \frac{1}{M} \mathbf{P}_{\mathbf{A}(\boldsymbol{\Theta})} \mathbf{x}_i \mathbf{x}_i^H \right), \\ &= \mathrm{tr}\left(\frac{1}{M} \sum_{i=1}^{M} \mathbf{P}_{\mathbf{A}(\boldsymbol{\Theta})} \mathbf{x}_i \mathbf{x}_i^H \right). \end{aligned} \tag{B.51}$$

Because $\mathbf{P}_{\mathbf{A}(\boldsymbol{\Theta})}$ is constant with respect to the summation, (B.51) is equivalent to

$$L(\boldsymbol{\Theta}; \mathbf{X}) = \mathrm{tr}\left(\mathbf{P}_{\mathbf{A}(\boldsymbol{\Theta})} \frac{1}{M} \sum_{i=1}^{M} \mathbf{x}_i \mathbf{x}_i^H \right). \tag{B.52}$$

Finally we recognize

$$\mathbf{R}_{\mathbf{x}} = \frac{1}{M} \sum_{i=1}^{M} \mathbf{x}_i \mathbf{x}_i^H,$$

Which we substitue into (B.52) to obtain our final form of the likelihood function

$$\boxed{L(\boldsymbol{\Theta}; \mathbf{X}) = \mathrm{tr}\left(\mathbf{P}_{\mathbf{A}(\boldsymbol{\Theta})} \mathbf{R}_{\mathbf{x}} \right).} \tag{B.53}$$

The Maximum Likelihood Estimator of $\boldsymbol{\Theta}$ is the solution to the following maximization

$$\boxed{\hat{\boldsymbol{\Theta}} = \max_{\boldsymbol{\Theta}} \left\{ \mathrm{tr}\left(\mathbf{P}_{\mathbf{A}(\boldsymbol{\Theta})} \mathbf{R}_{\mathbf{x}} \right) \right\}.} \tag{B.54}$$

Appendix C

Cramér-Rao Lower Bound

In estimation theory, the Cramér-Rao Lower Bound (CRLB) is used to benchmark the accuracy of unbiased estimators by providing a theoretical lower bound on estimator variance. For unbiased estimators of a real *vector* of N_η deterministic parameters, $\boldsymbol{\eta} \in \mathbb{R}^{N_\eta}$, the CRLB bounds the covariance matrix of the estimates [110] which we denote as $\mathbf{C}_{\boldsymbol{\eta}}$. The estimator covariance takes the following general form

$$\mathbf{C}_{\boldsymbol{\eta}} \triangleq E\left\{\left(\hat{\boldsymbol{\eta}} - \boldsymbol{\eta}\right)\left(\hat{\boldsymbol{\eta}} - \boldsymbol{\eta}\right)^T\right\}, \tag{C.1}$$

where $\hat{\boldsymbol{\eta}}$ denotes the estimate of the true parameter $\boldsymbol{\eta}$. The CRLB of the estimator of the true parameter vector $\boldsymbol{\eta}$, denoted $\mathbf{C}_{\mathbf{CR}}(\boldsymbol{\eta})$, is given by the inverse of the Fisher Information Matrix, $\mathbf{J}(\boldsymbol{\eta})$

$$\mathbf{C}_{\boldsymbol{\eta}} \geq \mathbf{C}_{\mathbf{CR}}(\boldsymbol{\eta}) \triangleq \mathbf{J}^{-1}(\boldsymbol{\eta}). \tag{C.2}$$

The definition of the $N_\eta \times N_\eta$ Fisher Information Matrix (FIM) is stated as

$$\mathbf{J}(\boldsymbol{\eta}) \triangleq E\left\{\left[\nabla_{\boldsymbol{\eta}} L\left(\mathbf{x};\boldsymbol{\eta}\right)\right]\left[\nabla_{\boldsymbol{\eta}} L\left(\mathbf{x};\boldsymbol{\eta}\right)\right]^H\right\} = -E\left\{\nabla_{\boldsymbol{\eta}}\left[\nabla_{\boldsymbol{\eta}} L\left(\mathbf{x};\boldsymbol{\eta}\right)\right]\right\}, \tag{C.3}$$

Where $\nabla_{\boldsymbol{\eta}}$ and $L\left(\mathbf{x};\boldsymbol{\eta}\right)$ represent the gradient vector and likelihood function respectively. These terms are defined as

$$\nabla_{\boldsymbol{\eta}} \triangleq \left[\frac{\partial}{\partial \eta_1}, \quad \cdots \quad, \frac{\partial}{\partial \eta_{N_\eta}}\right]^T, \tag{C.4}$$

And

$$L\left(\mathbf{x};\boldsymbol{\eta}\right)=\ln\left[p_{\mathbf{x};\boldsymbol{\eta}}(\mathbf{x};\boldsymbol{\eta})\right]. \tag{C.5}$$

The general form of the (i,j) element of the Fisher Information Matrix is given by

$$\left[\mathbf{J}(\boldsymbol{\eta})\right]_{i,j}\triangleq E\left\{\frac{\partial L\left(\mathbf{x};\boldsymbol{\eta}\right)}{\partial\eta_i}\cdot\frac{\partial L\left(\mathbf{x};\boldsymbol{\eta}\right)}{\partial\eta_j}\right\}=-E\left\{\frac{\partial^2 L\left(\mathbf{x};\boldsymbol{\eta}\right)}{\partial\eta_i\partial\eta_j}\right\}. \tag{C.6}$$

Where the expectation is taken with respect to the parameterized density function, $p_{\mathbf{x};\boldsymbol{\eta}}(\mathbf{x};\boldsymbol{\eta})$. This appendix summarizes the relevant expressions with appropriate citations. For the complete derivation, which can be tedious and at times detracts from the mathematical intuition of some of the results, the interested reader is referred to the following texts [110], [111], [68].

C.1 CRLB for Parameters of Interest and Nuissance Parameters

Van Trees often frames interpretations of the Fisher information with respect to parameters of interest and nuisance parameters [110] in order to organize $\mathbf{J}(\boldsymbol{\eta})$ into a convenient block partitioned form which admits an identity for finding the inverse of a sub block. We start by partitioning the parameter vector $\boldsymbol{\eta}$ into wanted and unwanted (or nuisance) parameters denoted by the parameter vectors $\boldsymbol{\eta}_{\mathbf{w}}$ and $\boldsymbol{\eta}_{\mathbf{u}}$ respectively

$$\boldsymbol{\eta}=\begin{bmatrix}\boldsymbol{\eta}_{\mathbf{w}}\\ \\ \boldsymbol{\eta}_{\mathbf{u}}\end{bmatrix}. \tag{C.7}$$

The FIM may be written as a block partitioned matrix in terms of the information from wanted and unwanted parameters as

$$\mathbf{J}(\boldsymbol{\eta}) = \left[\begin{array}{c:c} \mathbf{J}(\boldsymbol{\eta}_\mathbf{w}) & \mathbf{J}(\boldsymbol{\eta}_\mathbf{w}, \boldsymbol{\eta}_\mathbf{u}) \\ \hdashline \mathbf{J}(\boldsymbol{\eta}_\mathbf{u}, \boldsymbol{\eta}_\mathbf{w}) & \mathbf{J}(\boldsymbol{\eta}_\mathbf{u}) \end{array}\right]. \tag{C.8}$$

The CRLB matrix may similarly be partitioned as

$$\mathbf{C}_{\mathbf{CR}}(\boldsymbol{\eta}) = \left[\begin{array}{c:c} \mathbf{C}_{\mathbf{CR}}(\boldsymbol{\eta}_\mathbf{w}) & \mathbf{C}_{\mathbf{CR}}(\boldsymbol{\eta}_\mathbf{w}, \boldsymbol{\eta}_\mathbf{u}) \\ \hdashline \mathbf{C}_{\mathbf{CR}}(\boldsymbol{\eta}_\mathbf{u}, \boldsymbol{\eta}_\mathbf{w}) & \mathbf{C}_{\mathbf{CR}}(\boldsymbol{\eta}_\mathbf{w}) \end{array}\right]. \tag{C.9}$$

In this form we can use the identity for inverting block matrices in [112] to obtain a CRLB of the parameters of interest

$$\mathbf{C}_{\mathbf{CR}}(\boldsymbol{\eta}_\mathbf{w}) = \left[\mathbf{J}(\boldsymbol{\eta}_\mathbf{w}) - \mathbf{J}(\boldsymbol{\eta}_\mathbf{w}, \boldsymbol{\eta}_\mathbf{u})\mathbf{J}^{-1}(\boldsymbol{\eta}_\mathbf{w})\mathbf{J}(\boldsymbol{\eta}_\mathbf{u}, \boldsymbol{\eta}_\mathbf{w})\right]^{-1}. \tag{C.10}$$

C.2 General Form of CRLB for Gaussian Estimation Model

The closed form expression of the (i, j) element for the general Gaussian estimation model is presented in [110] for a snapshot modeled as a complex random vector distributed as $\mathbf{x} \sim \mathcal{C}(\boldsymbol{\mu}_\mathbf{x}(\boldsymbol{\eta}), \mathbf{R}_\mathbf{x}(\boldsymbol{\eta}))$ with likelihood function given by

$$L(\mathbf{x}; \boldsymbol{\eta}) = -\ln\det\left[\pi\mathbf{R}_\mathbf{x}\right] - \left\{\left(\mathbf{x} - \boldsymbol{\mu}_\mathbf{x}(\boldsymbol{\eta})\right)^H \mathbf{R}_\mathbf{x}^{-1}(\boldsymbol{\eta})\left(\mathbf{x} - \boldsymbol{\mu}_\mathbf{x}(\boldsymbol{\eta})\right)\right\}, \tag{C.11}$$

It can be shown that when the likelihood function takes this form, then Equation C.6 is given by

$$[\mathbf{J}(\boldsymbol{\eta})]_{i,j} = \text{tr}\left[\mathbf{R}_{\mathbf{x}}^{-1}(\boldsymbol{\eta})\frac{\partial \mathbf{R}_{\mathbf{x}}(\boldsymbol{\eta})}{\partial \eta_i}\mathbf{R}_{\mathbf{x}}^{-1}(\boldsymbol{\eta})\frac{\partial \mathbf{R}_{\mathbf{x}}(\boldsymbol{\eta})}{\partial \eta_j}\right] + 2Re\left[\frac{\partial \boldsymbol{\mu}_{\mathbf{x}}^{H}(\boldsymbol{\eta})}{\partial \eta_i}\mathbf{R}_{\mathbf{x}}^{-1}(\boldsymbol{\eta})\frac{\partial \boldsymbol{\mu}_{\mathbf{x}}(\boldsymbol{\eta})}{\partial \eta_j}\right]. \quad \text{(C.12)}$$

The result in Equation C.12 is attributed to [93]. We can use the definitions above to determine the information in a single snapshot of array data which we could denote as $\mathbf{J}(\boldsymbol{\eta}; m)$. Assuming independence between observations of a random vector $\mathbf{x}$, the total information in M snapshots is the summation of the information in each observation [68]

$$\mathbf{J}(\boldsymbol{\eta}) = \sum_{m=1}^{M} \mathbf{J}(\boldsymbol{\eta}; m). \quad \text{(C.13)}$$

Recall the separable Gaussian form introduced in Chapter 2 which regarded a snapshot as an instantiation of a multivariate Gaussian random vector distributed as $\mathbf{x} \sim \mathcal{C}\left(\boldsymbol{\mu}_{\mathbf{x}}(\boldsymbol{\eta}_{\boldsymbol{\mu}}), \mathbf{R}_{\mathbf{x}}(\boldsymbol{\eta}_{\mathbf{c}})\right)$, where the terms $\boldsymbol{\eta}_{\boldsymbol{\mu}}$ and $\boldsymbol{\eta}_{\mathbf{c}}$ were introduced to delineate the parameters of the mean and covariance of the observation vector. When the parameter vector can be partitioned in the following form

$$\boldsymbol{\eta} = \begin{bmatrix} \boldsymbol{\eta}_{\boldsymbol{\mu}} \\ \\ \boldsymbol{\eta}_{\mathbf{c}} \end{bmatrix} \quad \text{(C.14)}$$

Then in a similar fashion to the case where we partitioned the Fisher Information into wanted and unwanted blocks, we may also partition $\mathbf{J}(\boldsymbol{\eta})$ based on the parameters associated with the mean and the covariance as [113]

$$\mathbf{J}(\boldsymbol{\eta}) = \left[\begin{array}{c:c} \mathbf{J}(\boldsymbol{\eta}_{\boldsymbol{\mu}}) & \mathbf{J}(\boldsymbol{\eta}_{\boldsymbol{\mu}}, \boldsymbol{\eta}_{\mathbf{c}}) \\ \hdashline \mathbf{J}(\boldsymbol{\eta}_{\mathbf{c}}, \boldsymbol{\eta}_{\boldsymbol{\mu}}) & \mathbf{J}(\boldsymbol{\eta}_{\mathbf{c}}) \end{array}\right]. \quad \text{(C.15)}$$

In the separable Gaussian problem, $\mathbf{J}(\boldsymbol{\eta}_\mathbf{c}, \boldsymbol{\eta}_\boldsymbol{\mu}) = \mathbf{J}(\boldsymbol{\eta}_\boldsymbol{\mu}, \boldsymbol{\eta}_\mathbf{c}) = \mathbf{0}$ and the FIM reduces to the following block diagonal form

$$\mathbf{J}(\boldsymbol{\eta}) = \left[\begin{array}{c:c} \mathbf{J}(\boldsymbol{\eta}_\boldsymbol{\mu}) & \mathbf{0} \\ \hdashline \mathbf{0} & \mathbf{J}(\boldsymbol{\eta}_\mathbf{c}) \end{array}\right]. \tag{C.16}$$

From this form, we see that the estimator performance of the mean and covariance parameters are decoupled in the separable Gaussian problem.

The array snapshot model is described as separable Gaussian when we treat the directional sources as time samples of deterministic but unknown variables. The mean of our observation in this case is given by

$$\boldsymbol{\mu}_\mathbf{x}(\boldsymbol{\eta}_\boldsymbol{\mu}) = \mathbf{A}(\boldsymbol{\eta}_{nl})\boldsymbol{\eta}_l. \tag{C.17}$$

The parameters associated with the mean are

$$\boldsymbol{\eta}_\boldsymbol{\mu} = \begin{bmatrix} \boldsymbol{\eta}_{nl} \\ \\ \boldsymbol{\eta}_l \end{bmatrix} \tag{C.18}$$

Where $\boldsymbol{\eta}_{nl}$ and $\boldsymbol{\eta}_l$ are the nonlinear and linear parameters respectively. In the separable Gaussian problem, the block diagonal structure of $\mathbf{J}(\boldsymbol{\eta})$ simplifies the matrix inverse calculation and we find that

$$\mathbf{C}_{\mathbf{CR}}(\boldsymbol{\eta}_\boldsymbol{\mu}) = \mathbf{J}^{-1}(\boldsymbol{\eta}_\boldsymbol{\mu}), \tag{C.19a}$$

$$\mathbf{C}_{\mathbf{CR}}(\boldsymbol{\eta}_\mathbf{c}) = \mathbf{J}^{-1}(\boldsymbol{\eta}_\mathbf{c}). \tag{C.19b}$$

The FIM associated with the mean parameters can be similarly organized as

$$\mathbf{J}(\boldsymbol{\eta}_{\boldsymbol{\mu}}) = \left[\begin{array}{c:c} \mathbf{J}(\boldsymbol{\eta}_{nl}) & \mathbf{J}(\boldsymbol{\eta}_{nl}, \boldsymbol{\eta}_{l}) \\ \hdashline \mathbf{J}(\boldsymbol{\eta}_{l}, \boldsymbol{\eta}_{nl}) & \mathbf{J}(\boldsymbol{\eta}_{l}) \end{array}\right]. \tag{C.20}$$

When the observations are complex, the real vector of linear parameters is written in terms of its real and imaginary components as

$$\boldsymbol{\eta}_{l} = \begin{bmatrix} \boldsymbol{\eta}_{I} \\ \\ \boldsymbol{\eta}_{R} \end{bmatrix}. \tag{C.21}$$

Note that this doubles the number of unknown parameters in $\boldsymbol{\eta}_{l}$ over the case of real observations. For complex observations, the FIM for the parameters of the mean $\mathbf{J}(\boldsymbol{\eta}_{\boldsymbol{\mu}})$ is a 3×3 block matrix given by

$$\mathbf{J}(\boldsymbol{\eta}_{\boldsymbol{\mu}}) = \left[\begin{array}{c:c:c} \mathbf{J}(\boldsymbol{\eta}_{nl}) & \mathbf{J}(\boldsymbol{\eta}_{nl}, \boldsymbol{\eta}_{R}) & \mathbf{J}(\boldsymbol{\eta}_{nl}, \boldsymbol{\eta}_{I}) \\ \hdashline \mathbf{J}(\boldsymbol{\eta}_{R}, \boldsymbol{\eta}_{nl}) & \mathbf{J}(\boldsymbol{\eta}_{R}) & \mathbf{J}(\boldsymbol{\eta}_{R}, \boldsymbol{\eta}_{I}) \\ \hdashline \mathbf{J}(\boldsymbol{\eta}_{I}, \boldsymbol{\eta}_{nl}) & \mathbf{J}(\boldsymbol{\eta}_{I}, \boldsymbol{\eta}_{R}) & \mathbf{J}(\boldsymbol{\eta}_{I}) \end{array}\right]. \tag{C.22}$$

We now define the blocks of the FIM in Equation C.22 assuming the observation noise to be a vector of complex Gaussian noise distributed as $\mathbf{n} \sim C\left(\mathbf{0}, \sigma_n^2 I\right)$. The computational steps are not included but result from evaluating the form in C.12 with the mean and

covariance of the observation vector defined as

$$\boldsymbol{\mu}_{\mathbf{x}}(\boldsymbol{\eta}_{\boldsymbol{\mu}}) = \mathbf{A}(\boldsymbol{\eta}_{nl})\tilde{\boldsymbol{\eta}}_l \tag{C.23a}$$

$$\mathbf{R}_{\mathbf{x}} = \sigma_n^2 I. \tag{C.23b}$$

The tilde is used here to emphasize that the linear variable is a complex vector containing the real and imaginary parameters, i.e.

$$\tilde{\boldsymbol{\eta}}_l = \boldsymbol{\eta}_R + j\boldsymbol{\eta}_I, \tag{C.24}$$

And the vector of real linear parameters is as defined in C.21. The nine submatrices needed to populate the FIM in C.22 are then defined as follows:

$$\mathbf{J}(\boldsymbol{\eta}_{nl}) = \frac{2}{\sigma_n^2} Re\left\{ \left(\nabla_{\boldsymbol{\eta}_{nl}} \left[\tilde{\boldsymbol{\eta}}_l^H \mathbf{A}^H(\boldsymbol{\eta}_{nl}) \right] \right) \left(\nabla_{\boldsymbol{\eta}_{nl}} \left[\tilde{\boldsymbol{\eta}}_l^H \mathbf{A}^H(\boldsymbol{\eta}_{nl}) \right] \right)^H \right\} \tag{C.25a}$$

$$\mathbf{J}(\boldsymbol{\eta}_{nl}, \boldsymbol{\eta}_I) = -\frac{2}{\sigma_n^2} Im\left\{ \left(\nabla_{\boldsymbol{\eta}_{nl}} \left[\tilde{\boldsymbol{\eta}}_l^H \mathbf{A}^H(\boldsymbol{\eta}_{nl}) \right] \right) \mathbf{A}(\boldsymbol{\eta}_{nl}) \right\} \tag{C.25b}$$

$$\mathbf{J}(\boldsymbol{\eta}_{nl}, \boldsymbol{\eta}_R) = \frac{2}{\sigma_n^2} Re\left\{ \left(\nabla_{\boldsymbol{\eta}_{nl}} \left[\tilde{\boldsymbol{\eta}}_l^H \mathbf{A}^H(\boldsymbol{\eta}_{nl}) \right] \right) \mathbf{A}(\boldsymbol{\eta}_{nl}) \right\} \tag{C.25c}$$

$$\mathbf{J}(\boldsymbol{\eta}_I, \boldsymbol{\eta}_{nl}) = \frac{2}{\sigma_n^2} Im\left\{ \mathbf{A}^H(\boldsymbol{\eta}_{nl}) \left(\nabla_{\boldsymbol{\eta}_{nl}} \left[\tilde{\boldsymbol{\eta}}_l^H \mathbf{A}^H(\boldsymbol{\eta}_{nl}) \right] \right)^H \right\} \tag{C.25d}$$

$$\mathbf{J}(\boldsymbol{\eta}_R, \boldsymbol{\eta}_{nl}) = \frac{2}{\sigma_n^2} Re\left\{ \mathbf{A}^H(\boldsymbol{\eta}_{nl}) \left(\nabla_{\boldsymbol{\eta}_{nl}} \left[\tilde{\boldsymbol{\eta}}_l^H \mathbf{A}^H(\boldsymbol{\eta}_{nl}) \right] \right)^H \right\} \tag{C.25e}$$

$$\mathbf{J}(\boldsymbol{\eta}_R) = \frac{2}{\sigma_n^2} Re\left\{ \mathbf{A}^H(\boldsymbol{\eta}_{nl}) \mathbf{A}(\boldsymbol{\eta}_{nl}) \right\} \tag{C.25f}$$

$$\mathbf{J}(\boldsymbol{\eta}_I) = \frac{2}{\sigma_n^2} Re\left\{ \mathbf{A}^H(\boldsymbol{\eta}_{nl}) \mathbf{A}(\boldsymbol{\eta}_{nl}) \right\} \tag{C.25g}$$

C.2.1 Example: CRLB on Estimators of the DOA

We can use the results above to determine the estimator bounds for the classic angle of arrival problem where $\boldsymbol{\eta}_{nl}$ is our vector of unknown arrival angles and $\boldsymbol{\eta}_l$ contains the real and imaginary parts of the source vector $\mathbf{s}$. The mean and covariance of the observation vector are defined as

$$\boldsymbol{\mu}_{\mathbf{x}} = \mathbf{A}(\boldsymbol{\Theta})\mathbf{s}, \tag{C.26a}$$

$$\mathbf{R}_{\mathbf{x}} = \sigma_n^2 I. \tag{C.26b}$$

We typically limit our interest to the parameters of the mean specified by the following

$$\boldsymbol{\eta}_{nl} = \boldsymbol{\Theta} \tag{C.27a}$$

$$\boldsymbol{\eta}_l = \begin{bmatrix} Re\,(\mathbf{s}) \\ \\ Im\,(\mathbf{s}) \end{bmatrix}. \tag{C.27b}$$

The FIM in C.22 with blocks as defined in C.25a can be used to determine the CRB on estimators of $\boldsymbol{\Theta}$ and $\mathbf{s}$. We first define a $Q \times Q$ matrix $\mathbf{R}_{\mathbf{s}}$ to be the diagonal matrix whose only nonzero entries correspond to the source powers down its main diagonal

$$\mathbf{R}_{\mathbf{s}} = \begin{pmatrix} s_1^* s_1 & 0 & \dots & 0 \\ \\ 0 & s_2^* s_2 & \ddots & 0 \\ \\ \vdots & \ddots & \ddots & \vdots \\ \\ 0 & 0 & \dots & s_Q^* s_Q \end{pmatrix}. \tag{C.28}$$

We also define a matrix $\mathbf{D} \in \mathbb{C}^{P \times Q}$ whose i^{th} column, $\mathbf{d}_i$ is the gradient of the i^{th} steering vector with respect to θ_i

$$\mathbf{d}_i = \frac{\partial \mathbf{a}(\theta_i)}{\partial \theta_i}, \tag{C.29}$$

Assuming M available snapshots, the CRB matrix of bounds on the unknown angle estimates is given by

$$\mathbf{C_{CR}}(\mathbf{\Theta}) = \frac{\sigma_n^2}{2M} \left\{ Re\left[\mathbf{R_s} \odot \left[\mathbf{D}^H \mathbf{P}^{\perp}_{\mathbf{A}(\mathbf{\Theta})} \mathbf{D} \right]^T \right] \right\}^{-1}, \tag{C.30}$$

Where the matrix $\mathbf{P}^{\perp}_{\mathbf{A}(\mathbf{\Theta})} \in \mathbb{C}^{Q \times Q}$ is the projection matrix onto the null-space of $\mathbf{A}(\mathbf{\Theta})$. This form is derived in section 8.4.4 of [110] and can be found by populating the FIM as described above, performing the matrix inverse to obtain the corresponding CRB matrix and just retaining the submatrix associated with $\mathbf{\Theta}$.

Appendix D

Snapshot Editing Algorithm

D.1 Snapshot Editing Algorithms

Algorithm 1 Single source snapshot editing

Input: $\mathbf{X}_{n1}$, θ_n^c, γ_1
Output: $\mathbf{X}_1^{\text{clean}}$

$\mathbf{X}_1^{\text{clean}} = [\quad]$ ▷ Initialize edited snapshot matrix to empty.
$\mathbf{a}_c \leftarrow \tilde{\mathbf{a}}(\theta_n^c)$ ▷ Assign array response to θ_c^n based on *nominal model*.
$\mathbf{P}_{\mathbf{a}_c} \leftarrow \mathbf{a}_c \left(\mathbf{a}_c^H \mathbf{a}_c\right)^{-1} \mathbf{a}_c^H$ ▷ Projection onto span $\{\mathbf{a}_c\}$.
$\mathbf{P}_{\mathbf{a}_c}^{\perp} \leftarrow \mathbf{I}_P - \mathbf{P}_{\mathbf{a}_c}$ ▷ Projection onto span $\left\{\mathbf{a}_c^{\perp}\right\}$.
for $m_{n1} \leftarrow 1, M_{n1}$ **do** ▷ Loop over single source measurements in the bin.
    $\mathbf{x} \leftarrow \mathbf{x}_{m_{n1}}$ ▷ Test measurement is one column of $\mathbf{X}_{n1}$.
    $T_1 \leftarrow \dfrac{\mathbf{x}^H \mathbf{P}_{\mathbf{a}_c} \mathbf{x}}{\mathbf{x}^H \mathbf{P}_{\mathbf{a}_c}^{\perp} \mathbf{x}}$ ▷ Compute the subspace alignment measure.
    if $T_1 > \gamma_1$ **then** ▷ Compare test measurement to the threshold.
        $\mathbf{X}_1^{\text{clean}} = \left[\mathbf{X}_1^{\text{clean}} \mid \mathbf{x}_{m_{n1}}\right]$ ▷ Keep $\mathbf{x}$ if measure exceeds threshold.
    end if
end for

Algorithm 2 Two source snapshot editing

Input: $\mathbf{X}_{n2}$, θ_n^c, $\boldsymbol{\theta}_{n2}^i$, γ_1, γ_2, θ_{null}
Output: $\mathbf{X}_2^{\text{clean}}$

$\mathbf{X}_2^{\text{clean}} = [\quad]$ ▷ Initialize edited snapshot matrix to empty.
$\mathbf{a}_c \leftarrow \tilde{\mathbf{a}}(\theta_n^c)$ ▷ Assign array response to θ_c^n based on *nominal model*.
$\mathbf{P}_{\mathbf{a}_c} \leftarrow \mathbf{a}_c \left(\mathbf{a}_c^H \mathbf{a}_c\right)^{-1} \mathbf{a}_c^H$ ▷ Projection onto span $\{\mathbf{a}_c\}$.
$\mathbf{P}_{\mathbf{a}_c}^{\perp} \leftarrow \mathbf{I}_P - \mathbf{P}_{\mathbf{a}_c}$ ▷ Projection onto span $\left\{\mathbf{a}_c^{\perp}\right\}$.
for $m_{n2} \leftarrow 1, M_{n2}$ **do** ▷ Loop over $Q = 2$ snapshots.
    $\theta_i \leftarrow [\boldsymbol{\theta}_{n2}^i]_{m_{n2}}$ ▷ Assign interference angle.
    $\Delta\theta \leftarrow |\theta_n^c - \theta_i|$ ▷ Determine angular separation between sources.
    $\mathbf{a}_i \leftarrow \tilde{\mathbf{a}}(\theta_i)$ ▷ Assign array response to θ_i based on *nominal model*.
    $\mathbf{x} \leftarrow \mathbf{x}_{m_{n2}}$
    $\mathbf{P}_{\mathbf{a}_i} \leftarrow \mathbf{a}_i \left(\mathbf{a}_i^H \mathbf{a}_i\right)^{-1} \mathbf{a}_i^H$ ▷ Projection onto span $\{\mathbf{a}_i\}$.
    $\mathbf{P}_{\mathbf{a}_i}^{\perp} \leftarrow \mathbf{I}_P - \mathbf{P}_{\mathbf{a}_i}$ ▷ Projection onto span $\left\{\mathbf{a}_i^{\perp}\right\}$.
    $T_1 \leftarrow \dfrac{\mathbf{x}^H \mathbf{P}_{\mathbf{a}_c} \mathbf{x}}{\mathbf{x}^H \mathbf{P}_{\mathbf{a}_c}^{\perp} \mathbf{x}}$ ▷ Calibration subspace alignment measure.
    $T_2 \leftarrow \dfrac{\mathbf{x}^H \mathbf{P}_{\mathbf{a}_i} \mathbf{x}}{\mathbf{x}^H \mathbf{P}_{\mathbf{a}_i}^{\perp} \mathbf{x}}$ ▷ Interference subspace alignment measure.
    if $\Delta\theta > \theta_{null}$ **then** ▷ Angular separation requirement between sources.
        if $T_1 - T_2 > \gamma_1 - \gamma_2$ and $T_1 > \gamma_1$ **then** ▷ Assert culling rule.
            $\mathbf{X}_2^{\text{clean}} = \left[\mathbf{X}_2^{\text{clean}} \mid \mathbf{x}_{m_{n2}}\right]$
        end if
    end if
end for

Appendix E

Elevation Errors

E.1 Elevation Errors Reported for Tested Frames

This section offers a frame level summary of elevation errors summarized in Chapter 7. The *manifold* column indicates the model assumed in angle estimation while the *frame* column specifies the tested frame. Red is used to indicate cases where the manifold measured from a particular day is tested against a frame from the same data set. These correspond to cases where the test data is drawn from the training set. The elevation errors reported in Tables E.1 - E.4 provide frame level detail of the rolled up mean elevation error and root mean squared elevation error reported for each manifold model in [53] and also in Chapter 7.

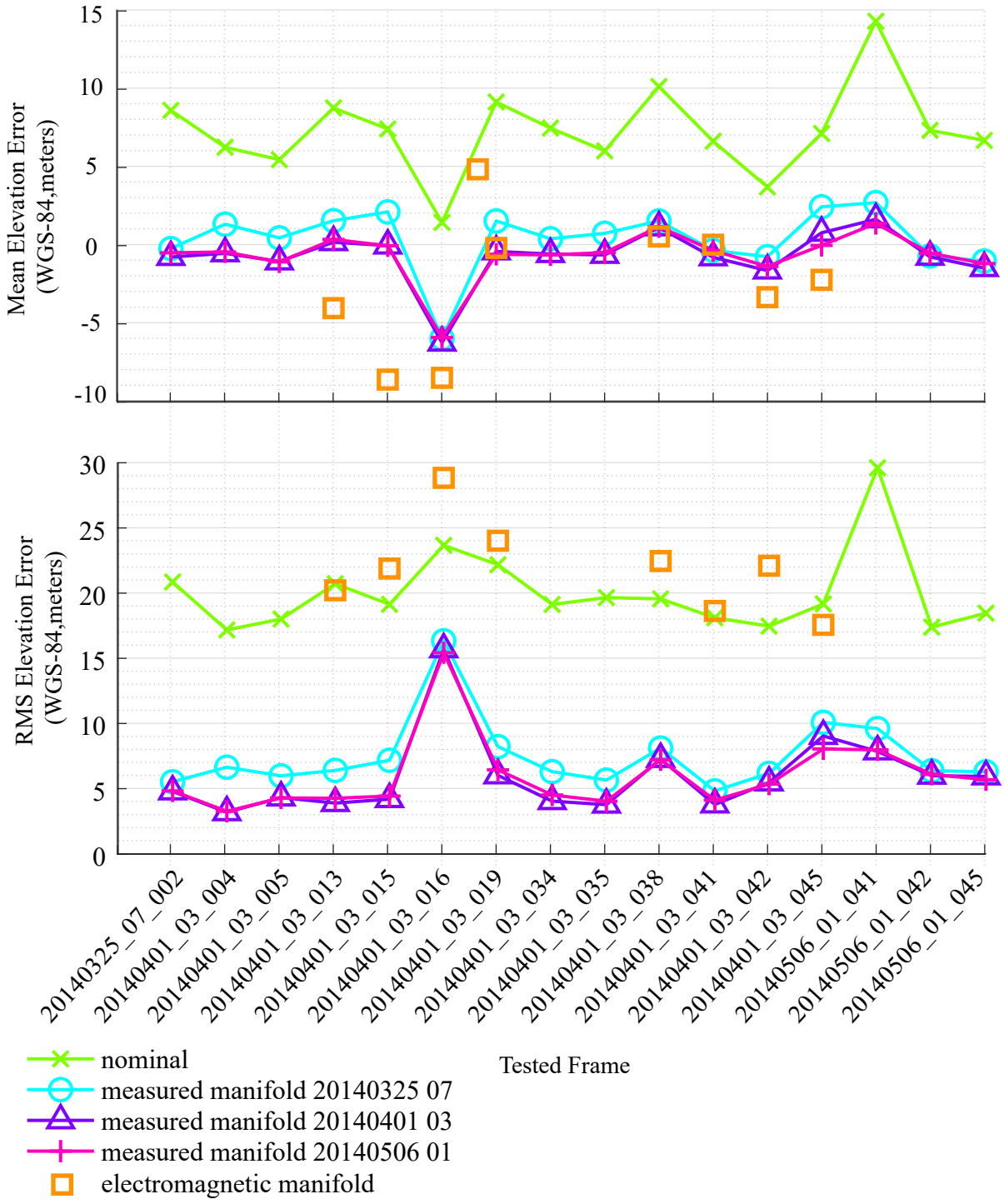

Figure E.1: Measured elevation errors of RDS DEMs (reported as meters with respect to the WGS-84 ellipsoid) for 16 frames tested with measured manifolds and including errors for subset of 20140401_03 frames tested with the electromagnetic manifold model.

Table E.1: Summary of elevation errors (WGS-84, meters) from 20140325 07 test frames.

Frame	Manifold	N_T	Outliers	Rejection (%)	ME (m)	RMSE (m)
002	Nominal	102,387	2,219	2.17	8.575	20.8433
	20140325 07	106,528	1,748	1.64	-0.2610	5.5166
	20140401 03	106,881	2,024	1.89	-0.8003	4.7752
	20140506 01	106,778	1,622	1.52	-0.5312	4.8124

Table E.2: Summary of elevation errors (WGS-84, meters) from 20140401 03 test frames.

Frame	Manifold	N_T	Outliers	Rejection (%)	ME (m)	RMSE (m)
004	Nominal	145,818	3,184	2.18	6.2164	17.1631
	20140325 07	150,385	1,243	0.83	1.2986	6.6333
	20140401 03	151,639	1,706	1.13	-0.5635	3.1773
	20140506 01	151,456	1,789	1.18	-0.4779	3.2560
005	Nominal	131,642	2,938	2.23	5.4239	18.0012
	20140325 07	135,714	1,309	0.96	0.4258	5.9720
	20140401 03	136,576	1,491	1.09	-1.0850	4.3074
	20140506 01	136,363	1,469	1.08	-1.1118	4.2756
013	Nominal	89,746	1,694	1.89	8.7277	20.7070
	20140325 07	93,620	1,587	1.70	1.5197	6.3888
	20140401 03	94,228	1,094	1.16	0.1489	3.8803
	20140506 01	94,107	1,349	1.43	0.3255	4.2538
015	Nominal	23,822	479	2.01	7.3865	19.1307
	20140325 07	24,954	282	1.13	2.0847	7.1665
	20140401 03	25,098	342	1.36	-0.0685	4.1857
	20140506 01	25,060	328	1.31	-0.0836	4.4189
016	Nominal	51,803	949	1.83	1.4140	23.6574
	20140325 07	54,085	1,324	2.45	-6.0128	16.3317
	20140401 03	54,256	1,526	2.81	-6.2778	15.6783
	20140506 01	54,206	1,428	2.63	-5.9464	15.4123
019	Nominal	151,829	3,227	2.13	9.1100	22.1687
	20140325 07	158,742	3,424	2.16	1.5057	8.2149
	20140401 03	159,885	3,577	2.24	-0.4424	6.0053
	20140506 01	159,546	3,801	2.38	-0.6274	6.4325

Table E.3: Summary of elevation errors (WGS-84, meters) from 20140401 03 test frames.

Frame	Manifold	N_T	Outliers	Rejection (%)	ME (m)	RMSE (m)
034	Nominal	38,937	729	1.87	7.442	19.1181
	20140325 07	40,012	498	1.24	0.3681	6.2939
	20140401 03	40,363	568	1.41	-0.6115	4.0296
	20140506 01	40,229	556	1.37	-0.6619	4.5018
035	Nominal	132,697	3,203	2.41	5.9842	19.6467
	20140325 07	138,597	1,654	1.19	0.7145	5.6460
	20140401 03	139,539	1,563	1.12	-0.6646	3.7598
	20140506 01	139,323	1,438	1.03	-0.5198	4.0230
038	Nominal	58,226	1,027	1.76	10.098	19.5464
	20140325 07	60,129	1,471	2.45	1.5048	8.1048
	20140401 03	60,292	1,424	2.36	1.0931	7.2635
	20140506 01	60,278	1,454	2.41	1.1382	7.2037
041	Nominal	56,842	1,484	2.61	6.6041	18.0980
	20140325 07	59,617	939	1.58	-0.3732	4.8190
	20140401 03	60,007	744	1.24	-0.8198	3.7732
	20140506 01	59,900	787	1.31	-0.3844	4.1054
042	Nominal	100,742	2,264	2.25	3.6788	17.4560
	20140325 07	104,636	2,708	2.59	-0.7809	6.1608
	20140401 03	105,022	2,806	2.67	-1.6653	5.4631
	20140506 01	104,948	2,592	2.47	-1.4049	5.3361
045	Nominal	17,977	530	2.95	7.1013	19.1607
	20140325 07	18,592	426	2.29	2.4102	10.0747
	20140401 03	18,707	454	2.43	0.7477	9.0282
	20140506 01	18,662	458	2.45	-0.0571	8.0363

Table E.4: Summary of elevation errors (WGS-84, meters) from 20140506 01 test frames.

Frame	Manifold	N_T	Outliers	Rejection (%)	ME (m)	RMSE (m)
041	Nominal	34,916	725	2.08	14.2723	29.6026
	20140325 07	36,877	1,060	2.87	2.6762	9.5964
	20140401 03	37,026	1,042	2.81	1.6084	7.8443
	20140506 01	37,073	1,062	2.86	1.3458	7.9620
042	Nominal	46,706	867	1.86	7.3034	17.3808
	20140325 07	48,729	1,056	2.17	-0.7300	6.3632
	20140401 03	48,816	1,043	2.14	-0.7898	5.9799
	20140506 01	48,816	969	1.99	-0.5533	6.0895
045	Nominal	70,282	1,830	2.60	6.6554	18.4534
	20140325 07	72,812	1,480	1.93	-1.0560	6.2789
	20140401 03	73,002	1,381	1.89	-1.5090	5.9233
	20140506 01	72,954	1,387	1.90	-1.2163	5.6722

Table E.5: Summary of elevation errors (WGS-84, meters) from 20140401 03 test frames.

Frame	Manifold	N_T	Outliers	Rejection (%)	ME (m)	RMSE (m)
034	Nominal	38,937	729	1.87	7.442	19.1181
	20140325 07	40,012	498	1.24	0.3681	6.2939
	20140401 03	40,363	568	1.41	-0.6115	4.0296
	20140506 01	40,229	556	1.37	-0.6619	4.5018
035	Nominal	132,697	3,203	2.41	5.9842	19.6467
	20140325 07	138,597	1,654	1.19	0.7145	5.6460
	20140401 03	139,539	1,563	1.12	-0.6646	3.7598
	20140506 01	139,323	1,438	1.03	-0.5198	4.0230
038	Nominal	58,226	1,027	1.76	10.098	19.5464
	20140325 07	60,129	1,471	2.45	1.5048	8.1048
	20140401 03	60,292	1,424	2.36	1.0931	7.2635
	20140506 01	60,278	1,454	2.41	1.1382	7.2037
041	Nominal	56,842	1,484	2.61	6.6041	18.0980
	20140325 07	59,617	939	1.58	-0.3732	4.8190
	20140401 03	60,007	744	1.24	-0.8198	3.7732
	20140506 01	59,900	787	1.31	-0.3844	4.1054
042	Nominal	100,742	2,264	2.25	3.6788	17.4560
	20140325 07	104,636	2,708	2.59	-0.7809	6.1608
	20140401 03	105,022	2,806	2.67	-1.6653	5.4631
	20140506 01	104,948	2,592	2.47	-1.4049	5.3361
045	Nominal	17,977	530	2.95	7.1013	19.1607
	20140325 07	18,592	426	2.29	2.4102	10.0747
	20140401 03	18,707	454	2.43	0.7477	9.0282
	20140506 01	18,662	458	2.45	-0.0571	8.0363

Table E.6: Summary of elevation errors (WGS-84, meters) from 20140401 03 test frames.

Frame	**Manifold**	$\mathbf{N_T}$	**Outliers**	**Rejection (%)**	**ME (m)**	**RMSE (m)**
004	GLRT	151,456	1,789	1.18	-0.4779	3.2560
	Pseudo	151,450	1,624	1.07	0.0225	3.3675
005	GLRT	136,363	1,469	1.08	-1.1118	4.2756
	Pseudo	136,259	1,525	1.12	-0.8453	4.4022
013	GLRT	94,107	1,349	1.43	0.3255	4.2538
	Pseudo	94,053	1,317	1.40	0.7908	4.5930
015	GLRT	25,060	328	1.31	-0.0836	4.4189
	Pseudo	25,079	326	1.30	-0.1065	4.5335
016	GLRT	54,206	1,428	2.63	-5.9464	15.4123
	Pseudo	54,196	1,418	2.62	-5.9629	16.3622
019	GLRT	159,546	3,801	2.38	-0.6274	6.4325
	Pseudo	159,533	3,755	2.35	-0.2637	6.5172
034	GLRT	40,229	556	1.37	-0.6619	4.5018
	Pseudo	40,266	517	1.28	0.0017	4.6310
035	GLRT	139,323	1,438	1.03	-0.5198	4.0230
	Pseudo	139,237	1,468	1.05	-0.1562	4.1753
038	GLRT	60,278	1,454	2.41	1.1382	7.2037
	Pseudo	60,239	1,427	2.37	1.6738	7.5150

Appendix F

Structural Detail of Modeled P-3 Inboard Fairing

F.1 Doubler Dimensions of Outer Sections

The dimensions of the embedded doublers assumed in the CEM model of the bottom skin are specified here. The dimensions for an outboard panel of the inboard P-3 subarray are summarized in Table F.1 relating the physical dimensions with designators that are labeled in Figure F.1

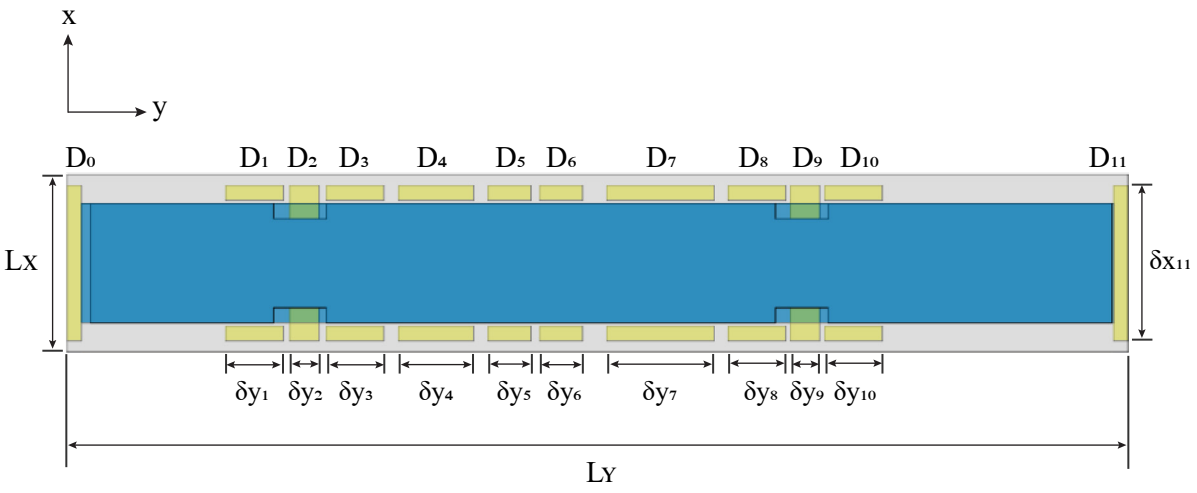

Figure F.1: Bottom skin of an outboard panel in the CEM model, showing embedded doublers.

Table F.1

Designator	δx (cm)	δy (cm)
D_0	33.3	3.1
D_1	3.1	12.4
D_2	7.1	6.35
D_3	3.1	12.4
D_4	3.1	16.3
D_5	3.1	9.3
D_6	3.1	9.3
D_7	3.1	23.2
D_8	3.1	12.4
D_9	7.1	12.4
D_{10}	3.1	12.4
D_{11}	33.3	3.1